Studies on Linear and Non Linear Optical Properties of Pulsed Laser Deposited Si, SiO_x and SiC Nanostructured Thin Films

A Thesis submitted in partial fulfillment of the requirements for the award of the degree of

DOCTOR OF PHILOSOPHY

by

PARTHA PRATIM DEY

Laser and Photonics Laboratory

DEPARTMENT OF PHYSICS

INDIAN INSTITUTE OF TECHNOLOGY GUWAHATI

February 2018

TH-1680_10612114

Dedicated to my Parents

TH-1680_10612114

TH-1680_10612114

भारतीय प्रौद्योगिकी संस्थान गुवाहाटी
Indian Institute of Technology Guwahati
Department of Physics
Guwahati-781039, Assam State, INDIA
Phone: +91 361 2582705, 2582701, 2690321 to 328 (extn. 2705),
Fax: +91 361 2582749
Dr. Alika Khare
Professor
E-mail: alika@iitg.ernet.in, k_alika@yahoo.com

Date: Aug 2017

Certificate

This is to certify that work contained in the thesis entitled '**Studies on Linear and Non Linear Optical Properties of Pulsed Laser Deposited Si, SiO_x and SiC Nanostructured Thin Films**' by **Mr Partha Pratima Dey** (Roll no: 10612114), a student of Department of Physics, Indian Institute of Technology Guwahati, for the award of degree of Doctor of Philosophy, has been carried out under my supervision and that the same has not been submitted elsewhere for any other degree.

(Alika Khare)

TH-1680_10612114

TH-1680_10612114

Partha Pratim Dey
Registration No. 10612114
Department of Physics
Indian Institute of Technology Guwahati
Guwahati-781039, Assam, India

Statement

I hereby declare that the matter embodied in this thesis is the result of investigations carried out by me at the Department of Physics, Indian Institute of Technology Guwahati, Guwahati, India, under the supervision of **Prof. Alika Khare**. This thesis has not been submitted to any university, institute or elsewhere for the award of the any degree, diploma or associate-ship.

Date: ………………. **Partha Pratim Dey**

TH-1680_10612114

TH-1680_10612114

ACKNOWLEDGEMENTS

I would like to thank all the people who contributed in some way or other to the work described in this thesis. First and foremost, I would like to thank my research supervisor, Prof. Alika Khare, for accepting me into her group. During my tenure, her continuous care, encouragement, and supervision of the research kept me going and helped completing the PhD thesis. She gave me intellectual freedom in my work and demanded quality work in all my endeavors.

My gratitude goes to my doctoral committee members, Prof. Pratima Agarwal, Dr. Bosanta Ranjan Boruah and Dr. Shrikrishna N. Joshi for their timely and invaluable suggestions, which helped me to improve the work pertaining to PhD thesis.

I owe full gratitude to the Department of Physics, IIT Guwahati and CIF, IIT Guwahati for providing me the necessary facilities to fulfill my PhD thesis objectives. In particular, I would like to extend my sincere thanks to Dr. Sidananda Sarma, Mr. Chandan Burgohain, Dr. K. K. Senapati, Mr. Madhurjya Borah and all the staffs of Physics dept. of IIT Guwahati for their kind help with various instruments.

I would like to thank DRDO (India), Project No. ERIP/ER/07003/30/M/01/1138 as well as MHRD, India and IIT Guwahati for providing financial assistance during my Ph.D. tenure.

It was pleasure to work with my research lab members Dr. Gaurav, Dr. Arpita, Dr. Abu, Dr. Satchi, Dr. Indrajeet, Gyan Prakash, Dr. Shanta Kumar, Rahul, Prahlad, Eshita, Gobinda, Sasmita and Sumit. Thanks to them for their suggestions, time, help in experiments and kindness throughout my PhD. I am also indebted to Dr. Indrajeet Kumar who deserves the credit for developing the Matlab program used for retrieving data of modified Z-scan measurements. I convey my thanks also to Mr. Rahul Kesarwani specially for helping me with Ellipsometric measurements and their data analysis.

I am deeply indebted to all my friends at IIT Guwahati; Abhijit, Ruhit, Himangshu, Bhaskar, Kuntal and others for providing a soothing environment and helping in the critical situations during my PhD, whenever I needed. I must acknowledge all my friends, my PhD. batch mates for their love, encouragement and support.

My special thanks and appreciation goes to my amazing parents, my lovely wife as well as my family for their blessings, love, patience, support and understanding throughout my studies and most of all to the Almighty Nature who governs everything.

Date: ………………

Partha Pratim Dey

TH-1680_10612114

TH-1680_10612114

ABSTRACT

The present research work was aimed towards the fabrication and characterization of nc-Si, SiO_x and SiC semiconductor thin films via PLD technique in order to study the effect of substrate temperature and background gas pressure on their stoichiometry, crystallinity, linear as well as nonlinear optical (NLO) and photoluminescence (PL) properties.

The nc-Si thin films fabricated via PLD as a function of substrate temperature (T_s) displayed polycrystalline nature. Raman maps confirmed that the films were comprised of nc-Si domains embedded in a-Si matrix. The static refractive index was found to be in the range of 3.3- 3.9 while optical band gap energy was varying non-monotically from 1.35 to 1.56 eV as a function of T_s. The crystallinity as well as optical properties were observed to be influenced by T_s. The SiO_x films having stoichiometry, x=0.03 to 2.1, were fabricated via PLD simply by controlling the background pressure of oxygen during deposition in the range of 10^{-4} to 0.5 mbar. XRD spectra confirmed the polycrystalline nature of these films. The SiO_x films exhibited the micron-sized clusters containing nc-Si embedded in otherwise uniform background composed of oxidized amorphous Si. The average crystallite size of nc-Si was observed to be reducing from around 18.3 to 3.2 nm with increasing O_2 pressure. Their static refractive index was found to reduce from 3.57 to 1.57 while band gap energy blue shifted from ~ 1.55 to 2.80 eV with increasing O_2 pressure. Laser excited PL spectra were observed for films fabricated at O_2 pressure of 0.01, 0.1 and 0.5 mbar only, exhibiting peaks around 1.43, 1.53 and 2.51 eV, respectively. These PL spectra possessed multi-component peaks originated due to quantum confined nc-Si as well as oxygen related defects; NBOH and V_o centers.

Amorphous SiC thin films were deposited onto fused silica by PLD at various T_s (RT to 750 °C) to study its effect on their structural and linear optical properties. A transition from

Si-rich SiC to nearly stoichiometric SiC was observed with increasing T_s which resulted in decrease in the refractive index from 3.00 to 2.64 and blue shift in the optical band gap from 1.59 to 2.33 eV. The structural disorders in these films tend to decrease with increasing T_s.

The third order NLO characteristics of all the PLD thin films of Si, SiO_x and a-SiC was performed by modified Z-scan set up using cw He-Ne laser at 632.8 nm wavelength. The NLA coefficient, β and NLR coefficient, n_2, were determined from open aperture (OA) and closed aperture (CA) Z-scan, respectively. The OA Z-scan of the nc-Si, SiO_x and SiC thin films showed feature of strong reverse saturation absorbtion while the CA Z-scan indicated the presence of self focusing property in all the films, which corresponds to positive nonlinear refraction. The values of third order optical suceptibility, $\chi^{(3)}$, in nc-Si films of the order of 10^{-1} *esu*. The values of $\chi^{(3)}$ for SiO_x was observed to be of the order of 10^{-1} to 10^{-3}esu with increasing oxygen content while for that of a-SiC films was ~ 10^{-3} esu. The optical limiting (OL) property was exhibited by the nc-Si and SiO_x thin films where the OL threshold varies inversely with β.

Finally, in order to grow the nanostructures of Si locally on Si wafer, direct laser ablation of c-Si wafer was performed in air. The structural and compositional modification of c-Si wafers as a function of irradiated laser fluence was studied. The laser ablation resulted in the formation of crater, containing crystalline central region surrounded by the micron sized cauliflower-like clusters of a-Si embedded in SiO_2 matrix (a-Si:SiO_2). These nanostructured a-Si:SiO_2 exhibited luminescence in far red region. The effect of laser fluence on the RT PL properties and its possible origin were also discussed.

TH-1680_10612114

Contents

List of Figures... *v*

List of Tables..

xiii

Abbreviations .... *xv*

Symbols..

xvii

1.Introduction.. **1**

1.1 Silicon nanostructures and thin films 2

1.2 Silicon carbide thin films 4

1.3 Pulsed laser deposition technique 7

1.4 Characterization of Si-based Thin Films 10

1.5 Third order Nonlinear optical properties of nc-Si, SiOx and a-SiC PLD thin films.. 11

1.6 Organization of the Present Thesis.. 13

2. Experimental Details.. **23**

2.1 Experimental setup for fabrication of a-Si:SiO_2 via direct laser irradiation of silicon wafer:.. 24

2.2 Pulsed laser deposition (PLD) setup for fabrication of Si, SiO_x and SiC thin films.. 25

2.3 Characterization of thin films.. 27

2.4 Modified Z-Scan set-up for measurement of the third order NLO coefficients of Si, SiO_x and SiC thin films 37

2.5 Optical limiting set-up.. 41

3. Fabrication of lumunescent Si:SiO_2 nanostructures by direct laser irradiation of Si wafer in air.. **47**

3.1 Experimental Details.. 47

3.2 Results and discussions......... 48

3.2.1 Study of morphological, structural and photoluminescence property of laser irradiated Si target at a laser fluence of ~ 1.46 Jcm^{-2} after 6,000 laser shots.. 48

TH-1680_10612114

3.2.2 Compositional analysis of a-Si:SiO_2 nanostructures as a function of laser fluence........ 51
3.2.3 Structural characterization of a-Si:SiO_2 nanostructures as a function of laser fluence........ 52
3.2.4 Surface morphology characterization of a-Si:SiO_2 nanostructures as a function of laser fluence........ 57
3.2.5 TEM analysis of a-Si:SiO_2 nanostructures as a function of laser fluence.58
3.2.6 Photoluminescence studies of a-Si:SiO_2 nanostructures as a function of laser fluence........60
3.3 Conclusion........ 66
4. Fabrication and characterization of PLD Si and SiO_x thin films 69
4.1 Experimental Details........70
4.2 Effect of substrate temperature and O_2 pressure on Si-based thin films via PLD........71
4.2.1 Effect of substrate temperature on the properties of Si films........72
4.2.2.1 Structural properties of nc-Si thin films 72
4.2.2.2 Linear optical properties of Si thin films........77
4.2.2 Effect of background oxygen pressure during deposition on the properties of SiO_x films........85
4.2.2.1 Structural and Compositional properties of SiO_x thin films........85
4.2.2.2 Linear optical properties of SiOx thin films........94
4.2.2.3 Photoluminescence studies of SiO_x films........ 100
4.3 Conclusion........ 107
5. Fabrication and characterization of PLD amorphous SiC thin films 113
5.1 Experimental Details........114
5.2 Effect of substrate temperature in properties of SiC films........115
5.2.1 Surface morphology of PLD a-SiC thin films by FESEM images........115
5.2.2 TEM images and SAED patterns of PLD a-SiC thin films........ 116
5.2.3 Structural and compositional studies of PLD a-SiC thin films........117
5.2.4 Linear optical properties of PLD a-SiC thin films........ 128
5.3 Conclusion........ 134
6. Third order Non-linear optical properties of PLD Si, SiO_x and SiC thin films... 137
6.1 Experimental Details 138

TH-1680_10612114

6.2 Effect of substrate temperature on the third order NLO response and OL property of PLD nc-Si films……………………………………140
6.2.1 Third order NLA and NLR coefficients of PLD nc-Si films……...140
6.2.2 Optical limiting in PLD nc-Si thin films…………………………..146
6.3 Effect of oxygen pressure on the third order NLO response and OL property of PLD SiO_x thin films…………………………………………………………147
5.2.1 Third order NLA and NLR coefficients by modified Z-scan technique………………………………………………………………148
5.2.2 Optical limiting in PLD SiO_x thin films……………………………151
6.4 Effect of substrate temperature on the third order NLO properties of a-SiC thin films……………………………………………………………………..152
6.5 Conclusion…………………………………………………………………156
7. Conclusions……………………………………………………………………..161
8. List of publications……………………………………………………............167

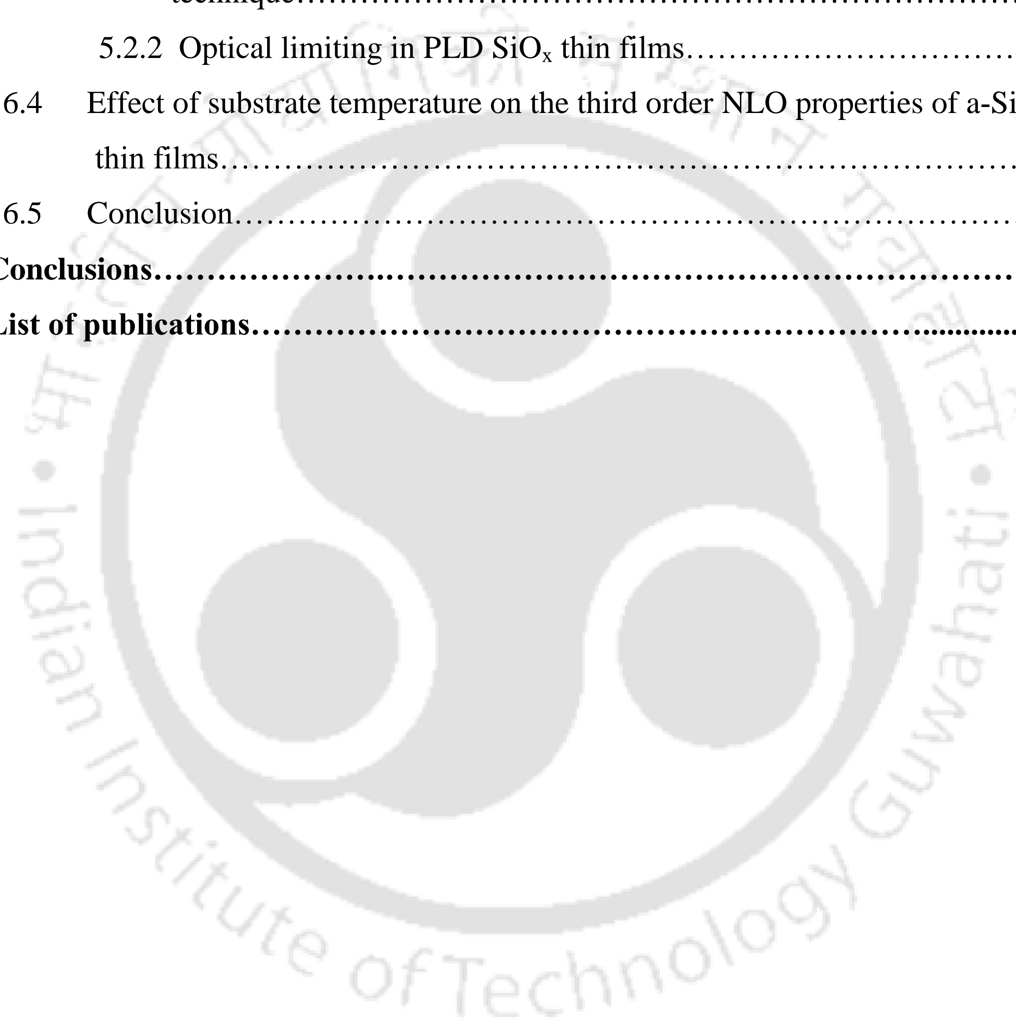

TH-1680_10612114

TH-1680_10612114

LIST OF FIGURES

Figure	Description	Page No.
1.1	*Schematic of pulsed laser deposition setup……………………………………..*	7
2.1	*Schematic of experimental setup for direct laser irradiation of silicon ……*	24
2.2	*Schematic of PLD setup…………………………………………………………*	25
2.3	*Photograph of PLD setup ………………...*	26
2.4	*UV-Vis-NIR transmission spectrum of PLD Si (~430 nm thickness) thin film exhibiting T_{max} and T_{min} curves by Swanepoel's envelop approximation……*	31
2.5	*Absorption coefficient of a PLD nanocrystalline Si film (~330 nm) exhibiting Tauc region and Urbach region ……………………………………..*	32
2.6	*Schematic depicting reflection of polarized light on film-substrate surface and geometrical interpretation of ellipsometric parameters (ψ, Δ)…………..*	34
2.7	*Schematic of modified Z-scan setup ……………………………………………….*	38
2.8	*Photograph of modified Z-scan setup ….…………………………………………….*	38
2.9	*Schematic of optical limiting measuring set-up ………………………………..*	42
3.1	*SEM image of laser irradiated Si target at a laser fluence of ~ 1.46 Jcm^{-2} after 6,000 shots…………………………………………………………………..*	49
3.2	*(a) SEM image, (b) Raman spectrum and (c) RT Photoluminescence spectrum of whitish clusters formed at a laser fluence of 1.46 Jcm^{-2} (6000 laser shots)….*	50
3.3	*(a) SEM image, (b) Raman spectrum and (c) RT Photoluminescence spectrum of dark central region formed at a laser fluence of 1.46 Jcm^{-2} (6000 laser shots).……………………………………………………………………*	50

TH-1680_10612114

Figure	Description	Page No.
3.4	*EDX spectra of whitish area of sample fabricated at laser fluences of (a) 0.35 Jcm^{-2}, (b) 0.67 Jcm^{-2} and (c) 1.46 Jcm^{-2} with 6000 laser shots and (d) 2.67 Jcm^{-2} with 3000 laser shots.……………………………………………….*	52
3.5	*The de-convoluted RT Raman spectra of whitish clusters of a-Si:SiO_2 formed at laser fluences of (a) 0.35 Jcm^{-2}, (b) 0.67 Jcm^{-2} and (c) 1.46 Jcm^{-2} with 6000 laser shots and (d) 2.67 Jcm^{-2} with 3000 laser shots.……………………………………………………………………….*	54
3.6	*FTIR transmission spectra of whitish clusters of a-Si:SiO_2 formed at different laser fluences ………………………………………………………….*	56
3.7	*SEM images of whitish clusters formed at different laser fluences (a) 0.35 Jcm^{-2}, (b) 0.67 Jcm^{-2} and (c) 1.46 Jcm^{-2} with 6000 laser shots and (d) 2.67 Jcm^{-2} with 3000 laser shots …………………………………………………………*	58
3.8	*TEM micrographs (a-d) and corresponding SAED pattern (e-h) of whitish clusters formed at laser fluences of 0.35 Jcm^{-2}, 0.67 Jcm^{-2} and 1.46 Jcm^{-2} with 6000 laser shots and 2.67 Jcm^{-2} with 3000 laser shots, respectively. Inset in (c) shows the HRTEM of nanostructures formed at laser fluence of 1.46 Jcm^{-2}……………………………………………………………………………*	59
3.9	*Histograms depicting the particle size distribution estimated from TEM images of whitish clusters formed at laser fluences of (a) 1.46 and (b) 2.67 Jcm^{-2}……………………………………………………………………………….*	60
3.10	*RT Photoluminescence spectra of whitish clusters of a-Si:SiO_2 formed at different laser fluences~ 0.35 Jcm^{-2} (6000 shots), 0.67 Jcm^{-2} (6000 shots), 1.46 Jcm^{-2} (6000 shots), and 2.67 Jcm^{-2} (3000 shots).…………………………*	61
3.11	*Curve-fitted and de-convoluted RT Photoluminescence spectra of whitish clusters of a-Si:SiO_2 formed at different laser fluences (a) 0.35 Jcm^{-2} (6000 shots),(b) 0.67 Jcm^{-2} (6000 shots), (c) 1.46 Jcm^{-2} (6000 shots), and 2.67 Jcm^{-2} (3000 shots) showing two peak centers (in eV).…………..........................*	62

TH-1680_10612114

Figure	Description	Page No.
3.12	*Plot showing variation of PL peak energy of peak 1 (at low energy) and peak 2 (at high energy) versus increasing irradiating laser fluence ……….*	64
3.13	*(a) Variation of atomic percentage of O/Si (from EDX) and peak 2 PL intensity as a function of irradiating laser fluence and (b) variation in PL intensity of peak 2 as a function of atomic % of O/Si (from EDX)……….*	65
4.1	*XRD spectra of the substrate and PLD nc-Si thin films fabricated at different T_s…………………………………………………………*	72
4.2	*(a) Optical micrograph images (30μm × 30μm), (b) corresponding Raman mapping and (c) Raman spectra of micron sized clusters and background of nc-Si thin film deposited at T_s of 400 ˚C …………………………………*	74
4.3	*(i) Optical micrograph, (ii) Raman spectra of micron sized crystalline clusters and (iii) Raman spectra of background amorphous matrix along with respective de-convoluted spectra of the PLD nc-Si thin films deposited at T_s of (a) RT, (b) 200 ˚C, (c) 400 ˚C, (d) 600 ˚C and (e) 700 ˚C…………………….*	76
4.4	*UV-Vis-NIR Transmittance spectra of SiO_x thin films deposited at different T_s ………………………………………………………………………*	77
4.5	*Plot of refractive index as a function of wavelength for nc-Si films deposited at different T_s. Inset shows static refractive indices (n_0) for nc-Si thin films deposited as a function of T_s…………………………………………………….*	78
4.6	*Tauc plots for determining optical band gap of nc-Si films and the inset shows the variation of optical band gap (E_g) of the films with increasing T_s...*	80
4.7	*Measured ellipsometric spectra for (a) real (ε_1) and (b) imaginary (ε_2) parts of dielectric functions of Si films deposited at various T_s. The solid lines depict the fitted curves ……………………………………………………….*	82
4.8	*Measured ellipsometric spectra for (a) real (ε_1) and (b) imaginary (ε_2) parts of dielectric functions of Si film deposited at 700 °C at different angle of incidence, Φ = 65°, 70° and 75°. The solid lines depict the fitted curves*	

TH-1680_10612114

Figure	Description	Page No.
	using BEMA. Inset of figure (a) and (b) show the layered structure used in BEMA modeling and Tauc plot of α (hv) estimated using BEMA, respectively……………………………………………………………………….	83
4.9	*(a) The refractive index and (b) extinction coefficient as a function of wavelength of the Si films deposited at RT, 400 and 700º C…………………..*	84
4.10	*XRD spectra of the substrate and PLD SiO_x thin films fabricated at various ambient O_2 pressure …………………………………………………………*	85
4.11	*SEM images (a-c) and corresponding EDX spectra (d-f) of SiO_x thin films deposited at O_2 pressure of 10^{-4}, 10^{-2} and 0.5 mbar, respectively…………*	87
4.12	*Optical micrograph (a-c), corresponding Raman map (d-f) and Raman spectra of micron sized clusters and background (g-i) of SiO_x thin films deposited at O_2 pressure of 10^{-4}, 10^{-2} and 0.5 mbar, respectively…………..*	88
4.13	*Enlarged view of Raman spectra of micron sized clusters of SiO_x thin films deposited at O_2 pressure of 10^{-4} mbar to 0.5 mbar. Peak position of TO mode of bulk c-Si is marked as broken line at 521 cm^{-1} ………………………..*	90
4.14	*Variation of crystal size (D) of nc-Si present within the micron sized clusters of SiO_x thin films as a function of O_2 pressure* …………………………………………………………………………………	91
4.15	*De-convoluted Raman spectra of background amorphous matrix of SiO_x thin films deposited at O_2 pressure of (a) 10^{-4}, (b) 10^{-3}, (c) 10^{-2}, (d) 10^{-1} and (e) 0.5 mbar, respectively. Open circle and solid lines represents experimental data and fitted data respectively. (f) the variation of I_{TA}/I_{TO} and FWHM of TO Raman peak of SiO_x films as a function of different O_2 pressure…………………………………………………………………………..*	92
4.16	*UV-Vis-NIR Transmission spectra of SiO_x thin films deposited at different O_2 pressure…………………………………………………………………*	94
4.17	*UV-Vis-NIR transmission spectrum of SiO_x thin film deposited at 10^{-4} mbar*	

TH-1680_10612114

Figure	Description	Page No.
	of O_2 pressure showing T_{max} and T_{min} curves plotted by interpolation to envelop transmission maxima and minima …………………..……………	95
4.18	*Refractive index as a function of wavelength for SiO_x films deposited at various O_2 pressure. Inset shows variation of x in SiO_x films and corresponding static refractive index as a function of O_2 pressure………….*	96
4.19	*(a) Tauc plots for determining optical band gaps of SiO_x films and (b) variation of optical band gaps (E_g) of SiO_x films as a function of different O_2 pressure ………………………………………………………………………*	97
4.20	*(a) Plot of absorption coefficient as a function of photon energy for SiO_x thin films deposited at different O_2 pressure and (b) showing the plot of ln α vs hν of SiO_x thin films.…………………………………………………………..*	99
4.21	*Variations of E_U and B parameter of SiO_x thin films fabricated with increasing O_2 pressure from 10^{-4} to 0.5 mbar.…………………….................*	99
4.22	*PL spectra of SiO_x thin films fabricated at different O_2 pressure from 10^{-4} to 0.5 mbar………………………………………………………………………........*	101
4.23	*(a) De-convoluted PL spectra of SiO_x thin film fabricated at O_2 pressure of 0.1 and (b) the energy level schematic of possible PL mechanism while (c) shows de-convoluted PL spectra of the film fabricated at O_2 pressure of 0.5 mbar………………………………………………………………………………*	103
4.24	*PL spectra of SiO_x thin film fabricated at 0.1 mbar O_2 pressure as a function of excitation laser power………………………………………………..*	105
4.25	*Variation of QC PL peak position (E_{PL}^{QC}) and corresponding integrated intensity in SiO_x thin film fabricated at O_2 pressure of 0.1 mbar as a function of excitation laser power………………………………………………..*	105
4.26	*(a) TEM image with inset containing corresponding SAED pattern and (b) UHRTEM of selected region of SiO_x thin film fabricated at O_2 pressure of 0.1 mbar……………………………………………………………………….*	106

TH-1680_10612114

Figure	Description	Page No.
5.1	*FESEM images of PLD a-SiC thin films fabricated at (a) RT, (b) 250°C, (c) 500°C and (d) 750°C, respectively. The inset shows the corresponding images at higher magnification…………………………………………….…………*	116
5.2	*TEM images of PLD a-SiC thin films deposited at (a) RT and (b) 750 ^{o}C. Inset shows corresponding SAED patterns …………………………………….....*	117
5.3	*XRD spectra of PLD SiC thin films fabricated at different substrate temperatures (T_s) from RT to 750 °C. Inset shows the zoomed view of 3C-SiC (111) XRD peak for SiC deposited at 750 °C……………………………….....*	118
5.4	*(a) Raman spectra of PLD a-SiC thin films at different T_s and (b) corresponding C-C band of Raman spectra…………………………………….*	119
5.5	*De-convoluted Raman spectra of PLD a-SiC thin films at T_s –(a) RT, (b) 250 °C, (c) 500 °C and (d) 750 °C. The peak positions (in cm^{-1}) are listed on right side (colour coded) in the graphs…………………………………..………*	121
5.6	*Normalized integrated intensities of acoustic modes of a-SiC ($I_{SiC,\ LA+TA}$) overlapped with Raman modes of a-SiC, optical modes of a-SiC ($I_{SiC,\ LO+TO}$) and C-C (I_{C-C}) in a-SiC films as a function of substrate temperature, T_s…….*	122
5.7	*FTIR absorbance spectra of PLD a-SiC thin films fabricated at T_s from RT to 750 °C. The inset shows the corresponding absorption coefficients (Y-axis scale = 10^4 cm^{-1})…………………………………………………….…………*	124
5.8	*Absorption coefficient of PLD a-SiC thin films fabricated at different T_s - (a) RT, (b) 250°C, (c) 500°C and (d) 750°C, respectively……………………..*	125
5.9	*Variation of FTIR (a) peak wavenumber and (b) corresponding FWHM of Si-C peak in a-SiC thin films as a function of T_s………………………………..*	125
5.10	*Variation of Si-C bond density of PLD a-SiC thin films as a function of T_s….*	126
5.11	*EDX spectra of PLD a-SiC films deposited at T_s of (a) RT, (b) 500°C and (c) 750°C respectively, while (d) shows the variation of atomic percentages*	

TH-1680_10612114

Figure	Description	Page No.
	of Si, C and O with increasing T_s.……………………………………………………	127
5.12	*UV-Vis-IR transmission spectra of PLD a-SiC thin films deposited at different T_s.……………………………………………………………………….*	128
5.13	*UV-Vis-NIR transmission spectrum of PLD a-SiC thin film deposited at 750 °C substrate temperature along with interpolated T_{max} and T_{min} curves……*	129
5.14	*Variation of refractive index as a function of wavelength for PLD a-SiC films deposited at different T_s……………………………………………………*	130
5.15	*Plot of absorption coefficient as a function of photon energy for PLD a-SiC films deposited at different T_s. Inset shows the plot of ln α vs. hυ at different T_s………………………………………………………………………………………*	131
5.16	*(a) Tauc plots for determining optical band gap (E_g) of a-SiC films deposited at different T_s and (b) variation of E_g of PLD a-SiC thin films with T_s……………………………………………………………………………………….*	132
5.17	*Variations of E_U and B parameter of PLD a-SiC thin films fabricated with increasing T_s from RT to 750°C…………………………………………………….*	133
6.1	*CCD image of transmitted beam through PLD nc-Si film, fabricated at T_s=400 °C, positioned at 10 mm from the focal point: (a) open aperture and (b) closed aperture Z-scan for S~0.40……………………………………………*	139
6.2	*Open aperture Z-scan Normalized Transmittance curve of nc-Si thin films deposited at substrate temperature of (a) RT, (b) 200 °C, (c) 400°C, (d) 600 °C and (e) 700 °C while (f) shows variation of ß as a function of substrate temperature………………………………………………………………………….*	142
6.3	*Closed aperture Z-scan Normalized Transmittance curve of nc-Si thin films deposited at substrate temperature of (a) RT, (b) 200 °C, (c) 400°C, (d) 600 °C and (e) 700 °C while (f) shows variation of n_2 as a function of substrate temperature…………………………………………………………………………..*	143

TH-1680_10612114

Figure	Description	Page No.
6.4	*Variation of nonlinear absorption coefficient (β) and nonlinear coefficient of refraction (n_2) of nc-Si thin films as a function of T_s. Dotted lines are not fitted lines but are only guide for eyes. Inset shows the variation of linear absorption coefficient (α) at λ = 632 nm, with increasing T_s…………………….*	144
6.5	*Optical limiting response of nc-Si films deposited at various T_s. The variation of OL threshold as a function T_s is depicted by broken red line……*	147
6.6	*Z scan spectra of SiO_x films (a) Open aperture and (b) Closed aperture (Symbols: measured data points, continuous line: fitted curve)……………….*	149
6.7	*Variation of nonlinear absorption coefficient (β) and nonlinear coefficient of refraction (n_2) of SiO_x thin films with increasing O_2 pressure (broken lines are not fitted lines but are only guide for eyes). Inset shows the variation of linear absorption coefficient (α) at λ = 632 nm, with increasing O_2 pressure……………………………………………………………………………..*	150
6.8	*Optical limiting response of SiO_x thin films. The red line shows the OL threshold variation as a function O_2 pressure……………………………………*	152
6.9	*Open Z-scan Normalized Transmission intensity for a-SiC thin films deposited at T_s = (a) RT, (b) 250 ^{0}C, (c) 500 ^{0}C and (d) 750 ^{0}C……………..*	153
6.10	*Closed Z-scan Normalized Transmission intensity of PLD a-SiC thin films deposited at T_s = (a) RT, (b) 250 ^{0}C, (c) 500 ^{0}C and (d) 750 ^{0}C……………..*	154
6.11	*$\chi^{(3)}$ values for the different band gap engineered PLD Si-based thin films deposited under different deposition parameters…………………………………..*	156

TH-1680_10612114

LIST OF TABLES

Table	Description	Page No.
3.1	*Peak centers and FWHMs of de-convoluted RT Raman spectra of whitish clusters of a-Si:SiO_2 formed as a function of laser fluences along with appropriate peak assignments* ………………………....................................	57
4.1.	*Deposition parameters for the fabrication of Si-based films*…………………	71
4.2	*XRD peak positions, corresponding FWHMs and respective Si crystallite size for the Si thin films as a function of T_s* ……………………………………....	73
4.3	*Measured film thickness and optical properties of thin Si films measured by means of SE and compared with other relevant techniques*…………….........	82
4.4	*XRD peak positions, corresponding FWHMs and respective Si crystallite size for the SiO_x thin films as a function of O_2 pressure* ………………………	85
5.1	*Static refractive indices (n_0), film thicknesses estimated by envelop method (d_{avg}) and measured by step profilometer (d_{step}) for PLD a-SiC thin films as a function of T_s*……………………………………………………………	129
6.1	*n_2, α, β, $\chi_R^{(3)}$, $\chi_I^{(3)}$ and $\chi^{(3)}$ for the PLD nc-Si thin films deposited at different T_s*………………………………………………………………..	145
6.2	*n_2, α, β, $\chi_R^{(3)}$, $\chi_I^{(3)}$ and $\chi^{(3)}$ for the PLD SiO_x thin films deposited at different O_2 pressure*………………………………………………….……	150
6.3	*n_2, α, β, $\chi_R^{(3)}$, $\chi_I^{(3)}$ and $\chi^{(3)}$ for PLD a-SiC thin films deposited at different T_s*…………………………………………………………………………	155

TH-1680_10612114

TH-1680_10612114

ABBREVIATIONS

AFM – Atomic Force Microscopy

BEMA - Bruggeman's effective medium approximation

CVD – Chemical Vapor Deposition

CA – Closed Aperture

CCD - Charged Coupled Device

EBD – Electron Beam Deposition

EDX – Energy Dispersive X-ray

FTIR – Fourier Transform Infra Red

FWHM – Full Width at Half Maximum

HRTEM – High Resolution Transmission Electron Microscope

LA- Longitudinal Acoustic

LO- Longitudinal Optical

LED- Light Emitting Diode

LIP – Laser Induced Plasma

Nd:YAG - Neodymium-doped Yttrium Aluminium Garnet

NLO – Non Linear Optical

NRL – Non Linear Refraction

OA – Open Aperture

OL – Optical Limiting

PL – Photo Luminescence

PLD – Pulsed Laser Deposition

QC – Quantum Confinement

RF – Radio Frequency

RSA- Reverse Saturation Absorption

RMSE- Root Mean Square Error

SAED–Selected Area Electron Diffraction

SE – Spectroscopic Ellipsometry

SEM – Scanning Electron Microscope

sscm- Standard cubic centimetres per minute

TA – Transverse Acoustic

TEM – Transmission Electron Microscope

TL- Tauc Lorentz

TLL - Tauc Lorentz Lorentz

TO – Transverse Optical

UV-Vis-NIR – Ultra Violet-Visible-Near Infrared

XRD – X-Ray Diffraction

w.r.t – with respect to

TH-1680_10612114

TH-1680_10612114

SYMBOLS

~	approximately	**μm**	micrometre
A	Absorbance	**cm**	centimetre
α	linear absorption coefficient	**eV**	electron volt
β	nonlinear absorption coefficient	$\mathbf{E_i}$	incident electric field
B	B parameter (Tauc slope)	$\mathbf{E_{ip}}$	incident electric field for *p*-polarization
c	speed of light	$\mathbf{E_{is}}$	incident electric field for *s*-polarization
d	film thickness	E_g	optical band gap
D	crystallite size	$\mathbf{E_p}$	energy corresponding to plasma frequency
ε_1	real part of dielectric function	$\mathbf{E_r}$	reflected electric field
ε_2	imaginary part of dielectric function	$\mathbf{E_{rp}}$	reflected electric field for *p*-polarization
λ	wavelength of light	$\mathbf{E_{rs}}$	reflected electric field for *s*-polarization
ν	frequency of light	E_U	Urbach energy
ρ	Fresnel reflection coefficient	f	focal length
ϕ	incident angle of plane polarized light	h	Plank's constant
Δ	phase difference between *p*- and *s*- polarization	**Hz**	hertz
$\Delta\phi_o$	phase distortion	I_o	peak intensity at focus
Δm	plasma flux supersaturation	**J**	joule
$\Delta T_{p\text{-}v}$	difference in the normalized transmission of peak and valley	k	extinction coefficient
$\Delta z_{p\text{-}v}$	separation between peak and valley position	k_B	Boltzmann constant
°C	degree Celsius	K	Kelvin
		keV	kilo electron volt
		L_{eff}	effective sample length

TH-1680_10612114

mbar	millibar
min	minutes
n	refractive index
n_0	static refractive index
n_2	nonlinear refractive index coefficient
nm	nanometre
ns	nanosecond
O_2	oxygen
S	aperture size
Si	Silicon
SiC	Silicon Carbide
SiO_x	Non stoichiometric Silicon dioxide
T_{max}	Transmittance maxima
T_{min}	Transmittance minima
T_{cl}	closed aperture transmittance
T_{op}	open aperture transmittance
T_s	Substrate temperature
W	Watt
w_o	Beam diameter at focus
$\chi^{(3)}$	Third order nonlinear susceptibility
z	sample position w.r.t. focus
z_o	Rayleigh length

TH-1680_10612114

Chapter 1

Introduction

The semiconductor nanostructure research has created enormous global interest over the past decades for its fascinating properties which helped in realizing devices usable in several day-to-day life applications. The most studied semiconductors in nanoscale dimensions include Si, C, Ge, ZnO, TiO_2, GaAs, CdS, CdSe, GaN etc. and these have been extensively explored as potential material for nanoscale electronics, optoelectronics, chemical/bio/optical sensors/detectors, energy harvesting and environmental purification owing to their size related interesting physical properties [1-3]. Silicon (Si) continues to be the most popular functional material for commercial electronic applications due to the following benefits: (i) the most abundant semiconductor on Earth; (ii) high stability and non-toxic nature; (iii) high carrier mobility; (iv) the well-established fabrication techniques; and (v) flexibility to create hetero-structures with other nanostructured materials. Si has a face-centered diamond cubic structure with lattice constant of 5.431 Å and belongs to the space group of *Fd-3m*. Excellent optical, electrical, and mechanical properties made Si an ideal material for optoelectronics, renewable power source as solar cells, optical communication and integrated microelectronics [4-7]. Silicon is realized to be the best material for fabricating photovoltaic solar cells among various proposed materials till date. But crystalline silicon (c-Si) has some shortcomings due to its high price and low absorption coefficient in visible light spectrum, for photovoltaic applications. The bulk crystalline silicon is inefficient photo-emitter due to its indirect optical band gap of 1.12 eV. This is a considerable weakness in contrast to some fabulous optical properties of c-Si viz; the successful realization of Raman lasing [8, 9] and the demonstration of ultrafast electro-optic modulation [10, 11]. In order to achieve full Si-

TH-1680_10612114

based optoelectronic integration, high performance in all aspects of optical functionality is highly desired. This would pave the way to integrated low-cost Si-based devices. Compared to Si, Silicon carbide (SiC), another semiconductor material, possesses superior chemical, mechanical and thermal robustness and is most suitable for high-power, high-frequency, and high-temperature applications [12]. In addition, SiC can be used to fabricate metal-oxide-semiconductor (MOS) device for extreme conditions [13]. The Si-based materials have also been reported to exhibit non-linear optical (NLO) properties both in bulk and nanostructured forms. The enhanced NLO in Si-based nano-materials have attracted much attention in the recent years since they can be potentially applied in many kinds of optoelectronic devices because of its compatibility with well established Si-based micro-electronics technology.

1.1 Silicon nanostructures and thin films:

Nanocrystalline silicon (nc-Si) has some advantageous features in contrast to its bulk form. It absorbs light better than c-Si and exhibits better electronic properties. The crystalline, micro/polycrystalline and amorphous forms of film-based Si solar cells have not been able to surpass the efficiency of its bulk counterpart due to reduced net absorption of the former. Therefore, implementation of light-trapping schemes like nanopatterning, quantum confinement (QC) and surface-induced effects in Si nanostructures could offer interesting features that might boost the photovoltaic energy conversion efficiency and overcome the restraints that lead to the Shockley–Queisser limit [14, 15]. A variety of nanostructured silicon, viz. nano-crystalline Si (nc-Si), nano structured amorphous Si (a-Si), nc Si or a-Si embedded in amorphous SiO_2 matrix and porous Silicon (po-Si), have been studied intensively over the past decade which

TH-1680_10612114

exhibited visible and near infrared photoluminescence (PL) owing to enhanced electronic transition probability [16, 17]. The nanostructured Si can be of the forms of free standing nanoparticle, direct nano-patterning on Si, nanorod or as films etc. For light emission applications involving nc-Si, excitonic and defect related emissions are most common. It has been reported that the excitonic emission from Si nanocrystals exhibit blue shift with decreasing crystal size and its intensity increases [18]. This observation indicates the increase of the band gap and the enhancement of the radiative recombination rate, due to QC effect while the transition remains indirect. Though in excitonic emission, there is an advantage of size-related wavelength tunability, yet it suffers from the low efficiency of phonon-assisted recombination and hence devices based on this emission channel remain a challenge till date. Defect related emission (oxygen or carbon-related) has been proven to be more successful, and light emitting devices with higher efficiencies have been reported using SiO_x and $Si_{1-x}C_x$ thin film structures [19-22]. However, no light emitting devices based on Si nanocrystals have reached the market till date. Visible PL from nanostructured Si films, as well as its oxides, carbides and nitrides grown by various deposition techniques has been reported in the literature [17, 19, 21-24]. Though different forms of Si based films were fabricated by various deposition techniques, yet in some cases, it is important to produce local nanostructured area directly on a silicon-based device or on assembled integrated chip. The local etching of a Si based film can be performed by irradiating it with nano second pulsed laser with a high precision in air or any other suitable ambient to produce various photoluminescent nanostructures of Si and SiO_x (which has Si nanoparticles embedded in a silicon oxide matrix/Si:SiO_2) [7]. By changing oxygen content (x), the compositional, structural, morphological, and optical properties of SiO_x can be tuned. The SiO_x thin films can be potential candidate for the

TH-1680_10612114

fabrication of tunable light-emitting silicon-based devices [19, 25]. SiO_x layers have been also used as protective coatings in metallic mirrors, antireflection coatings, or low refractive index layers in the mid infrared range [26-28]. These films can also be used as insulating dielectric films, passivation layers, and interlayers in microelectronics [29-31].

The Si-based films have been fabricated by thermal evaporation [32], RF sputtering [33], variety of chemical vapor deposition (CVD) techniques [34, 35], and pulsed-laser deposition (PLD) [36] etc. The PLD technique offers the advantage of low temperature deposition for fabrication of Si and SiO_x thin films. The ability to control the size and structure of Si nanoparticles as well as the oxygen content in the surrounding SiO_2 matrix by PLD technique might allow the fabrication of band gap engineered SiO_x films having tunable linear as well as nonlinear optical properties desired for various optoelectronic device applications.

1.2 Silicon carbide thin films:

SiC is another very useful Si-based material which is more robust than Si for microelectronics and optoelectronics devices. It possesses high breakdown field, excellent thermal conductivity, chemical inertness, high electron mobility, high thermal stability and mechanical hardness [37-39]. It exists in numerous polytypes, viz; cubic(C), hexagonal (H) and rhombohedral (R). Among these polytypes, 3C-SiC, 4H-SiC and 6H-SiC are the more important for technological applications due to some superior physical, chemical, electronic and optical properties [12]. These polytypes of SiC have indirect wide band gap ranging from 2.7 to 3.3 eV [37, 40]. This wide band gap gives it a very high breakdown field (about 10 times higher than that of Si or GaAs)[41]. It has optical phonons of high energy in the range of 100–120 meV [42] which leads to a high electron-

TH-1680_10612114

saturation drift velocity of 2×10^7 cm/s in 6H-SiC [43], high acoustic velocity of 13730 ms^{-1} [44] and a high thermal conductivity of 4.9 W/K cm [38]. It posses high temperature stability and is preferred over other semiconductor for radiation detectors under hazardous environment [45, 46]. Due to strong bonding in SiC, it is a very hard substance having Young's modulus around 400 GPa [47] and hence can be used as tools for cutting and abrasion. Bulk SiC shows weak optical emission at room temperature on account of its indirect band gap. But nanostructured SiC due to QC effect and its higher light-emission efficiency can have potential applications as emitters in blue and UV spectral range [48]. Band gap of nc-SiC can be also tuned by changing the size of the nanostructures. Luminescent SiC films can be fabricated by incorporating various defects (dislocations, oxygen and hydrogen related defects and surface states) during the growth process [49]. The nc-SiC also exhibits greater elasticity and strength as compared to that of bulk SiC [50].

Another technologically useful low-cost SiC material is its amorphous form. Amorphous hydrogenated silicon carbide (a-$Si_{1-x}C_x$:H) was first prepared by Anderson and Spear in 1976 [51] by the glow discharge technique. Since then, amorphous SiC (a-SiC) films continued to be of considerable interest for both fundamental understanding as well as technologically in electronic and optoelectronics devices. The ratio of Si to carbon (C) as well as hybridization of C-C bonds in the film is responsible in shaping up the structural, electrical and optical properties of the a-$Si_{1-x}C_x$ films. The optical band gap and refractive index of the film are function of its carbon content (x). By varying the carbon concentrations in a-$Si_{1-x}C_x$ the optical band gap can be tuned over a wide range (1.6-2.8 eV) [51]. This makes a-SiC thin films a potential candidate for applications in many kinds of optoelectronic devices with spectral tunability, such as tunable light-emitting diodes,

TH-1680_10612114

image sensors, solar cells and wide spectral range photodetectors [52-56] The a-SiC thin films have been used as a protective coating for extreme UV optics due to its high reflectivity in this spectral region [57]. It can effectively be used as a thermally stable surface passivation material for highly efficient thin film silicon-based photovoltaic devices [58]. Furthermore, a-SiC films are chemically and mechanically stronger and more durable in terms of temperature resistance than a-Si films. As such, a-SiC films can be applied in silicon micromachining [39]. It is also foreseen as a robust material for the NLO applications [59].

Amorphous SiC films have been prepared by the glow discharge technique [51], reactive sputtering [60], R.F. sputtering [61, 62], chemical vapor deposition (CVD) [63-65] and more recently via PLD [66-68]. The structural and electrical properties of these films depend on the deposition conditions. PLD offers the advantages of fabrication of stoichiometric as well as non-stoichiometric thin films in a single step by controlling the deposition parameters without the use of any hazardous gas. The structural and crystalline quality of the films fabricated via PLD process depends on substrate, laser wavelength, laser fluence, target-to-substrate distance, background ambient gas and substrate temperature [64, 66, 69, 70]. Therefore, there is a need to optimize some of these PLD parameters to tune the stoichiometry of a-SiC films for obtaining band gap engineered SiC films with possible tunable photoluminescence as well as linear and non linear optical properties.

A brief description of the PLD technique, employed for fabrication of various Si-based thin films in the present thesis work, is given in the following section.

TH-1680_10612114

1.3 Pulsed laser deposition technique:

PLD is a versatile deposition technique because of its ability to ablate any material to yield thin films of desired composition and thickness ranging from few nanometers to hundreds of microns [71, 72]. A wide variety of thin films of metals, metal oxides, semiconductors, ceramic, composite etc. have been reported to be fabricated via PLD [70, 72-78]. The composition of the thin film can be controlled by the composition of target material, laser power, target-substrate distance and the background gas and its pressure in PLD technique. The crystalline films can be deposited even at room temperature easily by this technique [79, 80]. PLD technique was first proposed by Smith and Turner in 1965 immediately after the advent of high power lasers [81]. Later on, it has emerged as a powerful deposition tool for the fabrication of various materials, multilayer, nanostructures since 1980's. The schematic diagram of PLD system is shown in *Figure 1.1*. It consists of a multiport vacuum chamber having a programmable target holder, substrate holder and viewport for focusing the laser beam onto the target. The PLD

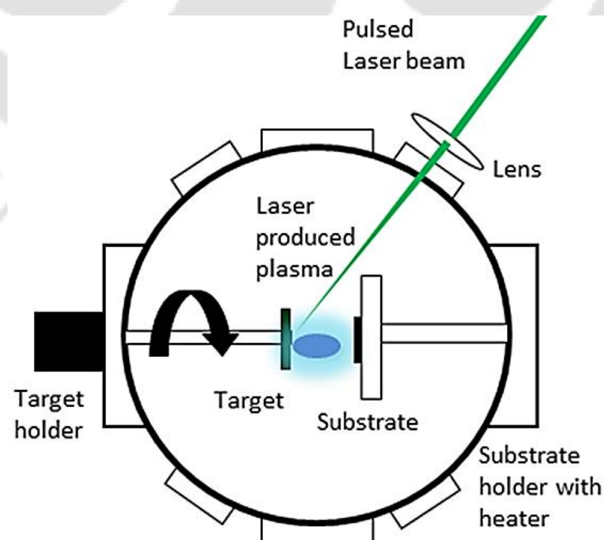

Figure 1.1 *Schematic of Pulsed Laser Deposition set-up.*

TH-1680_10612114

chamber is initially evacuated to a base pressure of ~ 10^{-6} mbar and if required it can be pressurized with the desired background gas. The focusing of a high power laser beam (laser intensity ~ 10^{9} – 10^{11} W/cm^{2}) onto the target results in the formation of Laser induced plasma (LIP) of target material. The LIP plume comprises of highly energetic electrons, ions and atoms/molecules of target material. This plume expands adiabatically and cools down while moving forward towards the substrate placed few tens of mm apart from target and gets deposited on it. When the condensation rate is higher than the rate of particles supplied by ablation, thermal equilibrium condition can be reached quickly and then film grows on the substrate surface at the expense of the direct flow of the particles from LIP. When the target is placed in a non-inert gaseous ambient then the surrounding gas molecules also undergo ionization/ dissociation/ plasma formation via multiphoton absorption of laser energy in the vicinity of focal spot as well as via interaction of highly energetic plasma plume of the target material. Both these plasmas (target plasma and background gas plasma) undergo adiabatic cooling and under suitable dynamics undergo the reaction phase to form the molecular species [82-84]. In such situation, it is termed sometime as reactive PLD. Usually the substrate holder is fitted with a substrate heater to raise the substrate temperature up to 800° C or more during the film growth. Based on the requirements, the PLD chamber can be pressurized by various types of working gases using appropriate gas inlet ports. The role of the background gas is also to thermalize the highly energetic plasma species, to compensate for the loss of an elemental component from the plasma plume of the target within deposited film and hence prohibiting the formation of non-stoichiometric films [85, 86] apart from reactive PLD for the formation of new molecules. The laser beam steering system for focusing the laser on to the target is placed out side the vacuum chamber and hence avoiding the contamination of expensive

TH-1680_10612114

high damage threshold optics. The multiple-target holder assembly can also be adopted for the PLD system for the growth of multicomponent/multilayer/hetero-structure thin films [73].

In general, the growth process of the film is very complicated. However it can be classified into three modes; Volmer-Weber growth (island only), Frank-van der Merwe growth (layer-by-layer) and Stranski-Krastanov growth (layer-plus-island) [70, 87]. In Volmer–Weber (VW) growth, adatom–adatom interactions are stronger than those of the adatom with the surface, leading to the formation of three-dimensional (3D) adatom clusters or islands. Growth of these clusters results in rough surface of the films grown on the substrate. But during Frank–van der Merwe (FM) growth, adatom-substrate interaction being stronger than adatom-adatom interactions, this adatoms attach preferentially onto surface sites during the growth in the form of atomically smooth layers, resulting layer-by-layer growth. The third mode, Stranski–Krastanov growth is an intermediary process characterized by both 2D layer and 3D island growth. Transition from the layer-by-layer to island-based growth occurs at a critical layer thickness which is highly dependent on the chemical and physical properties of substrate and adatoms. Depending upon the substrate surface energy, lattice orientation and dynamics of the laser induced target plasma; these atoms /molecules condense and deposit in the form of thin film, following any of the three modes, onto the surface of a cleaned substrate. The nucleation process depends on the interfacial energies between the three phases present – substrate, the condensing material and the vapor. Nucleation-and-growth of films being crystalline, amorphous or both depends on the density, kinetic energy, degree of ionization, and the type of the depositing material, as well as the substrate temperature and its physical-chemical properties. The two main thermodynamic parameters for the

TH-1680_10612114

growth mechanism are the substrate temperature T_s and the supersaturation Δm. They can be related by the following equation, $\Delta m = k_B T_s \ln(R/R_e)$, where k_B is the Boltzmann constant, R is the actual deposition rate, and R_e is the equilibrium value at temperature T_s [88]. The growth of the crystalline film depends on the surface mobility of the adatom. Normally, the adatom will diffuse through several atomic distances before sticking to a stable position over the freshly formed film. The surface temperature of the substrate determines the adatom's surface diffusion ability. High temperature favours rapid and defect free crystal growth, whereas under low temperature or large supersaturation, crystal growth may be overwhelmed by energetic particle impingement, resulting in disordered or even amorphous structures. Hence, the substrate temperature and kinetic energy of the arriving species toward substrate are key factors determining the degree of crystallinity of the films in PLD.

1.4 Characterization of Si-based Thin Films:

The physical properties of the thin films can be studied by variety of characterization tools. The structural characterization of the thin films to unveil their crystalline nature and bonding structure can be performed by X-Ray Diffraction (XRD) technique and micro Raman spectroscopy. Raman mapping offers the additional advantage of probing the film locally for any structural inhomogeneity present in the film. Fourier transform infrared (FTIR) spectrum measures the vibrational modes of the molecules. It is a very handy tool for identification of a variety of materials, their bonding structures and estimation of respective bond densities. Scanning Electron Microscopy (SEM) and Field-effect Scanning Electron Microscopy (FESEM) images can be captured to investigate the surface morphology of thin films. The atomic composition of the thin

TH-1680_10612114

films can be determined using the Electron Diffraction X-Ray spectroscopic (EDX) technique attached with SEM or FESEM instrument. For the lattice structure characterization and crystalline size determination of nanostructures and films, Transmission Electron Microscopy (TEM) images can be recorded and analyzed. UV-Vis-NIR transmission spectra of films can be studied to determine the optical constants, film thickness and band gap of the films. Film thickness can also be measured using step profilometer. Spectroscopic Ellipsometric (SE) measurements is another optical characterization technique which can also be used to determine refractive index, extinction coefficient, thickness, absorption coefficient and optical band gap of single layer as well as multilayer thin films. PL spectra of the thin film are recorded to investigate the photo-emission properties, band structures and defect levels present in films.

1.5 Third order Nonlinear optical properties of nc-Si, SiO_x and a-SiC thin films:

The NLO properties of materials have been utilized for optical switching, optical waveguide, optical limiting, harmonic generation and information storage [89]. Self-focusing observed due to positive nonlinear refraction phenomena may be useful in reducing the optical beam-spot size below the diffraction limit and hence can be applied for enhanced density of optical data storage [90]. The NLO response of bulk crystalline Si and SiO_2 is poor restricting its applications in devices [91]. The NLO susceptibilities enhances manifold in nanoscale dimensions due to manifestations of quantum size effects. The enhancement of NLO coefficients is attributed to the increase of oscillator strengths because of the quantum confinement-induced localization of electron–hole pairs [59]. The NLO coefficient can be size dependent for the particle size less than or close to

TH-1680_10612114

its excitonic Bohr radius [59, 92]. Several forms of Si-based materials such as silicon nanoparticles in suspensions [93], porous silicon [94, 95], nanostructured Si formed by etching and deposited on quartz substrates [96, 97] or embedded in silica matrix [92, 98] and SiC have been reported to exhibit NLO behaviour.

A variety of techniques have been developed to measure the NLO properties of materials. These techniques include nonlinear interferometry, degenerate four-wave mixing, ellipse rotation, *Z*-scan technique and beam distortion measurements [99-103]. The first three techniques are sensitive but require relatively complex experimental setup whereas the beam distortion measurement is relatively less sensitive and need detailed wave propagation analysis. *Z*-scan technique involves comparatively simple experimental setup. The *Z*-scan technique, proposed by Sheik-Bahae *et al.* in 1989, is a single beam scan method based on the spatial beam distortion during beam propagation through the nonlinear medium [102]. In this technique, the sample is translated longitudinally along the optic axis around the focal plane of a focused laser beam. The translation of the sample leads to the change of irradiance at the sample, resulting in changes in the intensity dependent optical properties. The intensity transmitted through the sample is recorded as a function of sample location z with respect to the focal plane. The plot of transmitted intensity as a function of z gives the information about the order of the nonlinearity as well as its sign and magnitude. The technique includes open aperture (OA) and closed aperture (CA) Z-scan measurements which determine nonlinear absorption (NLA) coefficient and nonlinear refractive index (NLR) coefficient, respectively. The experimental setup and basic theory are briefly explained in *Chapter 2, Section 2.1*.

TH-1680_10612114

1.6 Organization of Present Thesis:

The present research work was aimed towards the fabrication and characterization of Si, SiO_x and SiC semiconductor thin films via PLD technique along with the fabrication of a-Si:SiO_2 nanostructures by direct laser ablation of Si target. The effect of substrate temperature and background gas pressure on the stoichiometry and crystallinity of the thin films via PLD have been carried out, which in turn control their optical properties. The room temperature (RT) photoluminescence properties of some of these films and their possible origins were also investigated. The effect of film stoichiometry on the third order NLO properties and optical limiting (OL) properties under cw-laser irradiation has also been investigated. The NLO properties of thin films under cw-laser irradiation are dependent on its linear absorption coefficient and optical band gap, which can be tuned by changing the stoichiometry and crystallinity of the films. Hence, the major objective of the NLO studies of the Si, SiO_x and SiC films were to understand how film stoichiometry and crystallinity affect their NLA as well as NLR properties so as to achieve tunable NLO coefficients and optical limiting property in these films.

The thesis organization and overview of various chapters is mentioned below:

Chapter 1, "*Introduction*", presents the overview of the literature survey on Si, SiO_x and SiC thin films, basics of PLD technique, various characterization tools for analyzing structural, compositional and the linear as well as nonlinear optical properties of these thin films.

Chapter 2, "*Experimental Details*", describes the PLD setup used for fabrication of Si, SiO_x and SiC thin films. The various commercialized instruments used for the characterization of PLD films are documented in this chapter. It also briefly discusses the modified *Z*-scan setup developed in house to measure the NLO coefficients of all the Si-

TH-1680_10612114

based films documented in the thesis. The experimental set-up assembled for studying the OL properties is also sketched in this chapter.

Chapter 3, "*Fabrication of lumunescent Si:SiO_2 nanostructures by direct laser irradiation of Si wafer in air* ", describes the structural and compositional modification of polished c-Si wafers by pulsed laser irradiation. The effect of laser fluence on their photoluminescence properties and its possible origin are discussed.

Chapter 4, "*Fabrication and charecterization of PLD Si and SiO_x thin films*", presents the fabrication via PLD as well as structural and optical charecterization of Si thin films as a function of substrate temperature. The effect of O_2 pressure on structural and optical properties along with PL properties of SiO_x thin films are also presented.

Chapter 5, "*Fabrication and charecterization of PLD amorphous SiC thin films*", discusses the effect of substrate temperature on structural and optical properties of PLD SiC thin films.

Chapter 6 "*Third order Nonlinear optical properties of PLD nc-Si, SiO_x and SiC thin films*", discusses the measurement of non-linear absorption coefficient, nonlinear refractive index and third order optical susceptibilty of Si, SiO_x and a-SiC thin films. The OL properties of these films are also presented.

The last chapter of the thesis, *Chapter 7* is the *concluding* chapter and it provides salient features of the present research work along with the possibilities of future research.

TH-1680_10612114

Bibliography

[1] H.S. Nalwa, Handbook of Nanostructured Materials and Nanotechnology, Academic Press, Burlington, 1999.

[2] E. Fortunato, P. Barquinha, R. Martins, Oxide Semiconductor Thin-Film Transistors: A Review of Recent Advances, Advanced Materials, 24 (2012) 2945-2986.

[3] J. Valenta, S. Mirabella, Nanotechnology and Photovoltaic Devices: Light Energy Harvesting with Group IV Nanostructures, Pan Stanford Boca Raton, Florida, 2015.

[4] M.R. Esmaeili-Rad, A. Sazonov, A.G. Kazanskii, A.A. Khomich, A. Nathan, Optical Properties of Nanocrystalline Silicon Deposited by PECVD, Journal of Materials Science: Materials in Electronics, 18 (2007) 405-409.

[5] A. Shah, J. Meier, E. Vallat-Sauvain, C. Droz, U. Kroll, N. Wyrsch, J. Guillet, U. Graf, Microcrystalline Silicon and 'Micromorph' Tandem Solar Cells, Thin Solid Films, 403–404 (2002) 179-187.

[6] S. Meister, B. Franke, H.J. Eichler, S. Kupijai, H. Rhee, A.W.S. Al-Saadi, L. Zimmermann, Photonic Integrated Circuits for Optical Communication, Optik & Photonik, 7 (2012) 59-62.

[7] C. Wu, C.H. Crouch, L. Zhao, E. Mazur, Visible Luminescence from Silicon Surfaces Microstructured in Air, Applied Physics Letters, 81 (2002) 1999-2001.

[8] H. Rong, R. Jones, A. Liu, O. Cohen, D. Hak, A. Fang, M. Paniccia, A continuous-wave Raman silicon laser, Nature, 433 (2005) 725-728.

[9] R. Claps, D. Dimitropoulos, V. Raghunathan, Y. Han, B. Jalali, Observation of stimulated Raman amplification in silicon waveguides, Optics Express, 11 (2003) 1731-1739.

[10] G.T. Reed, G. Mashanovich, F.Y. Gardes, D.J. Thomson, Silicon optical modulators, Nature Photonics, 4 (2010) 518-526.

[11] A. Liu, R. Jones, L. Liao, D. Samara-Rubio, D. Rubin, O. Cohen, R. Nicolaescu, M. Paniccia, A high-speed silicon optical modulator based on a metal-oxide-semiconductor capacitor, Nature, 427 (2004) 615-618.

[12] S.E. Saddow, A. Agarwal, Advances in silicon carbide processing and applications, Artech House, 2004.

[13] E. Pippel, J. Woltersdorf, H.Ö. Ólafsson, E.Ö. Sveinbjörnsson, Interfaces between 4H-SiC and SiO2: Microstructure, nanochemistry, and near-interface traps, Journal of Applied Physics, 97 (2005) 034302.

[14] A.J. Nozik, Quantum dot solar cells, Physica E: Low-dimensional Systems and Nanostructures, 14 (2002) 115-120.

[15] A. Polman, H.A. Atwater, Photonic design principles for ultrahigh-efficiency photovoltaics, Nature Materials, 11 (2012) 174-177.

TH-1680_10612114

[16] T.K. Chini, D.P. Datta, S. Facsko, A. Mücklich, Room Temperature Photoluminescence from the Amorphous Si Structure Generated under keV Ar-ion-induced Surface Rippling Condition, Applied Physics Letters, 92 (2008) 101919.

[17] G. Kurumurthy, K.S. Alee, D.N. Rao, Photoluminescence Studies of Si/SiO_2 Nanoparticles Synthesized with Different Laser Irradiation Wavelengths of Nanosecond Pulse Duration, Optics Communications, 282 (2009) 3509-3512.

[18] W.D.A.M. de Boer, D. Timmerman, K. Dohnalova, I.N. Yassievich, H. Zhang, W.J. Buma, T. Gregorkiewicz, Red Spectral Shift and Enhanced Quantum Efficiency in Phonon-free Photoluminescence from Silicon Nanocrystals, Nature Nanotechnology, 5 (2010) 878-884.

[19] K. Dohnalová, L. Ondič, K. Kůsová, I. Pelant, J.L. Rehspringer, R.R. Mafouana, White-emitting Oxidized Silicon Nanocrystals: Discontinuity in Spectral Development with Reducing Size, Journal of Applied Physics, 107 (2010) 053102.

[20] M. Schnabel, C. Summonte, S.A. Dyakov, M. Canino, L. López-Conesa, P. Löper, S. Janz, P.R. Wilshaw, Absorption and emission of silicon nanocrystals embedded in SiC: Eliminating Fabry-Pérot interference, Journal of Applied Physics, 117 (2015) 045307.

[21] C. Huh, B.K. Kim, B.-J. Park, E.-H. Jang, S.-H. Kim, Enhancement in Electron Transport and Light Emission Efficiency of a Si Nanocrystal Light-emitting Diode by a SiCN/SiC Superlattice Structure, Nanoscale Res Lett, 8 (2013) 14

[22] Z. Xia, S. Huang, Structural and Photoluminescence Properties of Silicon Nanocrystals Embedded in SiC matrix prepared by Magnetron Sputtering, Solid State Communications, 150 (2010) 914-918.

[23] Y.Q. Wang, Y.G. Wang, L. Cao, Z.X. Cao, High-efficiency Visible Photoluminescence from Amorphous Silicon Nanoparticles embedded in Silicon Nitride, Applied Physics Letters, 83 (2003) 3474-3476.

[24] L. Cheng, L. Chaorong, J. Ailing, M. Libo, W. Yongqian, C. Zexian, Intense Blue Photoluminescence from Si-in-SiN_x Thin Film with High-density Nanoparticles, Nanotechnology, 16 (2005) 940-943.

[25] V.T. Vu, D.C. Nguyen, H.D. Pham, A.T. Chu, T.H. Pham, Fabrication of a Silicon Nanostructure-based Light Emitting Device, Advances in Natural Sciences: Nanoscience and Nanotechnology, 1 (2010) 025006.

[26] G. Hass, C.D. Salzberg, Optical Properties of Silicon Monoxide in the Wavelength Region from 0.24 to 14.0 Microns, Journal of Optical Society of America, 44 (1954) 181-187.

[27] K.W. Wecht, Large-range Refractive-index Control of Silicon Monoxide Antireflection Coatings using Oblique Incident Thermal Evaporation, Applied Optics, 30 (1991) 4133-4135.

[28] J.A. Savage, Infrared Optical Materials and their Antireflection Coatings, Adam Hilger Ltd. , Bristol, 1985.

[29] M.J. O'Leary, J.H. Thomas, Characterization of Reactively Evaporated SiO_x Thin Films, Journal of Vacuum Science & Technology A: Vacuum, Surfaces, and Films, 5 (1987) 106-109.

TH-1680_10612114

[30] G. Franzò, A. Irrera, E.C. Moreira, M. Miritello, F. Iacona, D. Sanfilippo, G. Di Stefano, P.G. Fallica, F. Priolo, Electroluminescence of silicon nanocrystals in MOS structures, Applied Physics A, 74 (2002) 1-5.

[31] J. Sheng, K. Fan, D. Wang, C. Han, J. Fang, P. Gao, J. Ye, Improvement of the SiOx Passivation Layer for High-Efficiency Si/PEDOT:PSS Heterojunction Solar Cells, Acs Applied Materials & Interfaces, 6 (2014) 16027-16034.

[32] D. Nesheva, C. Raptis, A. Perakis, I. Bineva, Z. Aneva, Z. Levi, S. Alexandrova, H. Hofmeister, Raman scattering and photoluminescence from Si nanoparticles in annealed SiO_x thin films, Journal of Applied Physics, 92 (2002) 4678-4683.

[33] H. Miyazaki, T. Goto, SiOx films prepared using RF magnetron sputtering with a SiO target, Journal of Non-Crystalline Solids, 352 (2006) 329-333.

[34] F. Iacona, G. Franzò, C. Spinella, Correlation between Luminescence and Structural Properties of Si Nanocrystals, Journal of Applied Physics, 87 (2000) 1295-1303.

[35] J.A. Luna-López, G. García-Salgado, T. Díaz-Becerril, J.C. López, D.E. Vázquez-Valerdi, H. Juárez-Santiesteban, E. Rosendo-Andrés, A. Coyopol, FTIR, AFM and PL properties of thin SiOx films deposited by HFCVD, Materials Science and Engineering: B, 174 (2010) 88-92.

[36] D. Riabinina, C. Durand, J. Margot, M. Chaker, G.A. Botton, F. Rosei, Nucleation and Growth of Si Nanocrystals in an Amorphous SiO_2 matrix, Physical Review B, 74 (2006) 075334.

[37] H. Morkoç, S. Strite, G.B. Gao, M.E. Lin, B. Sverdlov, M. Burns, Large-band-gap SiC, III-V nitride, and II-VI ZnSe-based semiconductor device technologies, Journal of Applied Physics, 76 (1994) 1363-1398.

[38] G.A. Slack, Thermal Conductivity of Pure and Impure Silicon, Silicon Carbide, and Diamond, Journal of Applied Physics, 35 (1964) 3460-3466.

[39] A. Klumpp, U. Schaber, H.L. Offereins, K. Kühl, H. Sandmaier, Amorphous silicon carbide and its application in silicon micromachining, Sensors and Actuators A: Physical, 41 (1994) 310-316.

[40] G.L. Harris, Properties of Silicon Carbide, INSPEC-the Institution of Electrical Engineers, London, United Kingdom, 1995.

[41] W. V. Muench, I. Pfaffeneder, Breakdown field in vapor-grown silicon carbide p-n junctions, Journal of Applied Physics, 48 (1977) 4831-4833.

[42] D.W. Feldman, J.H. Parker, W.J. Choyke, L. Patrick, Phonon Dispersion Curves by Raman Scattering in SiC, Polytypes 3C, 4H, 6H, 15R, and 21R, Physical Review, 173 (1968) 787-793.

[43] W. v. Muench, E. Pettenpaul, Saturated electron drift velocity in 6H silicon carbide, Journal of Applied Physics, 48 (1977) 4823-4825.

[44] G. Arlt, G.R. Schodder, Some Elastic Constants of Silicon Carbide, The Journal of the Acoustical Society of America, 37 (1965) 384-386.

[45] F.H. Ruddy, A.R. Dulloo, J.G. Seidel, S. Seshadri, L.B. Rowland, Development of a silicon carbide radiation detector, IEEE Transactions on Nuclear Science, 45 (1998) 536-541.

TH-1680_10612114

[46] G. Bertuccio, R. Casiraghi, Study of silicon carbide for X-ray detection and spectroscopy, IEEE Transactions on Nuclear Science, 50 (2003) 175-185.

[47] J. Tan, P.J. Meadows, D. Zhang, X. Chen, E. López-Honorato, X. Zhao, F. Yang, T. Abram, P. Xiao, Young's modulus measurements of SiC coatings on spherical particles by using nanoindentation, Journal of Nuclear Materials, 393 (2009) 22-29.

[48] J. Xu, J. Mei, Y. Rui, D. Chen, Z. Cen, W. Li, Z. Ma, L. Xu, X. Huang, K. Chen, UV and blue light emission from SiC nanoclusters in annealed amorphous SiC alloys, Journal of Non-Crystalline Solids, 352 (2006) 1398-1401.

[49] J.Y. Fan, X.L. Wu, P.K. Chu, Low-dimensional SiC nanostructures: Fabrication, luminescence, and electrical properties, Progress in Materials Science, 51 (2006) 983-1031.

[50] E.W. Wong, P.E. Sheehan, C.M. Lieber, Nanobeam Mechanics: Elasticity, Strength, and Toughness of Nanorods and Nanotubes, Science, 277 (1997) 1971-1975.

[51] D.A. Anderson, W.E. Spear, Electrical and optical properties of amorphous silicon carbide, silicon nitride and germanium carbide prepared by the glow discharge technique, Philosophical Magazine, 35 (1977) 1-16.

[52] T.S. Jen, J.W. Pan, N.F. Shin, W.C. Tsay, J.W. Hong, C.Y. Chang, Hydrogenated Amorphous Silicon Carbide P-I-N Thin-Film Light-Emitting Diodes with Barrier Layers Inserted at P-I Interface, Japanese Journal of Applied Physics, 33 (1994) 827-831.

[53] T. Ma, J. Xu, J. Du, W. Li, X. Huang, K. Chen, Full color light emission from amorphous SiC_x:H with organic–inorganic structures, Journal of Applied Physics, 88 (2000) 6408-6412.

[54] M. Fernandes, M. Vieira, I. Rodrigues, R. Martins, Large area image sensing structures based on a-SiC:H: a dynamic characterization, Sensors and Actuators A: Physical, 113 (2004) 360-364.

[55] S.Y. Myong, S.S. Kim, K.S. Lim, In situ ultraviolet treatment in an Ar ambient upon p-type hydrogenated amorphous silicon–carbide windows of hydrogenated amorphous silicon based solar cells, Applied Physics Letters, 84 (2004) 5416-5418.

[56] M. Akiyama, M. Hanada, H. Takao, K. Sawada, M. Ishida, Excess Noise Characteristics of Hydrogenated Amorphous Silicon p-i-n Photodiode Films, Japanese Journal of Applied Physics, 41 (2002) 2552-2555.

[57] J.B. Kortright, D.L. Windt, Amorphous silicon carbide coatings for extreme ultraviolet optics, Applied Optics, 27 (1988) 2841-2846.

[58] Y.H. Joung, H.I. Kang, J.H. Kim, H.S. Lee, J. Lee, W.S. Choi, SiC formation for a solar cell passivation layer using an RF magnetron co-sputtering system, Nanoscale Res Lett, 7 (2012) 22.

[59] M.S. Brodyn, V.I. Volkov, V.R. Lyakhovetskii, V.I. Rudenko, V.M. Puzilkov, A.V. Semenov, Nonlinear-optical and Structural Properties of Nanocrystalline Silicon Carbide Films, Journal of Experimental and Theoretical Physics, 114 (2012) 205-211.

[60] T. Shimada, Y. Katayama, K.F. Komatsubara, Compositional and structural properties of amorphous Si_xC_{1-x}:H alloys prepared by reactive sputtering, Journal of Applied Physics, 50 (1979) 5530-5532.

TH-1680_10612114

[61] A.K. Costa, S.S. Camargo Jr, C.A. Achete, R. Carius, Characterization of ultra-hard silicon carbide coatings deposited by RF magnetron sputtering, Thin Solid Films, 377–378 (2000) 243-248.

[62] W.K. Choi, F.L. Loo, C.H. Ling, F.C. Loh, K.L. Tan, Structural and electrical studies of radio frequency sputtered hydrogenated amorphous silicon carbide films, Journal of Applied Physics, 78 (1995) 7289-7294.

[63] A. Gupta, D. Paramanik, S. Varma, C. Jacob, CVD growth and characterization of 3C-SiC thin films, Bulletin of Materials Science, 27 (2004) 445-451.

[64] B.P. Swain, R.O. Dusane, Effect of substrate temperature on HWCVD deposited a-SiC:H film, Materials Letters, 61 (2007) 4731-4734.

[65] M.A. El Khakani, M. Chaker, A. Jean, S. Boily, H. Pépin, J.C. Kieffer, S.C. Gujrathi, Effect of rapid thermal annealing on both the stress and the bonding states of a-SiC:H films, Journal of Applied Physics, 74 (1993) 2834-2840.

[66] H. ElGazzar, E. Abdel-Rahman, H.G. Salem, F. Nassar, Preparation and characterizations of amorphous nanostructured SiC thin films by low energy pulsed laser deposition, Applied Surface Science, 256 (2010) 2056-2060.

[67] A. Keffous, K. Bourenane, M. Kechouane, N. Gabouze, T. Kerdja, Morphological, structural and optical properties of thin SiC layer growth onto silicon by pulsed laser deposition, Vacuum, 81 (2007) 632-635.

[68] Y.S. Katharria, S. Kumar, R.J. Choudhary, R. Prakash, F. Singh, N.P. Lalla, D.M. Phase, D. Kanjilal, Pulsed laser deposition of SiC thin films at medium substrate temperatures, Thin Solid Films, 516 (2008) 6083-6087.

[69] M. Tabbal, A. Said, E. Hannoun, T. Christidis, Amorphous to crystalline phase transition in pulsed laser deposited silicon carbide, Applied Surface Science, 253 (2007) 7050-7059.

[70] D.B. Chrisey, G.K. Hubler, Pulsed Laser Deposition of Thin Films, Wiley-VCH, USA, 2003.

[71] M.N.R. Ashfold, F. Claeyssens, G.M. Fuge, S.J. Henley, Pulsed laser ablation and deposition of thin films, Chemical Society Reviews, 33 (2004) 23-31.

[72] R.D. Vispute, S. Choopun, R. Enck, A. Patel, V. Talyansky, R.P. Sharma, T. Venkatesan, W.L. Sarney, L. Salamancariba, S.N. Andronescu, A.A. Iliadis, K.A. Jones, Pulsed laser deposition and processing of wide band gap semiconductors and related materials, Journal of Electronic Materials, 28 (1999) 275-286.

[73] A.T.T. Mostako, C.V.S. Rao, A. Khare, Mirrorlike pulsed laser deposited tungsten thin film, Review of Scientific Instruments, 82 (2011) 013101.

[74] M. Filipescu, A.P. Papavlu, M. Dinescu, Functional Metal Oxide Thin Films Grown by Pulsed Laser Deposition, in: P. Mandracci (Ed.) Crystalline and Non-crystalline Solids, InTech, Rijeka, 2016, pp. 33-55.

[75] R. Eason, Pulsed Laser Deposition of Thin Films: Applications-led growth of functional materials, John Wiley & Sons, New Jersey, 2007.

TH-1680_10612114

[76] D.H. Lowndes, D.B. Geohegan, A.A. Puretzky, D.P. Norton, C.M. Rouleau, Synthesis of Novel Thin-Film Materials by Pulsed Laser Deposition, Science, 273 (1996) 898-903.

[77] S. Kumari, A. Khare, Optical and structural characterization of pulsed laser deposited ruby thin films for temperature sensing application, Applied Surface Science, 265 (2013) 180-186.

[78] G. Shukla, P.K. Mishra, A. Khare, Effect of annealing and O_2 pressure on structural and optical properties of pulsed laser deposited TiO_2 thin films, Journal of Alloys and Compounds, 489 (2010) 246-251.

[79] J.P. Zheng, H.S. Kwok, Preparation of indium tin oxide films at room temperature by pulsed laser deposition, Thin Solid Films, 232 (1993) 99-104.

[80] A. Suresh, P. Wellenius, A. Dhawan, J. Muth, Room temperature pulsed laser deposited indium gallium zinc oxide channel based transparent thin film transistors, Applied Physics Letters, 90 (2007) 123512.

[81] H.M. Smith, A.F. Turner, Vacuum Deposited Thin Films Using a Ruby Laser, Applied Optics, 4 (1965) 147-148.

[82] S.S. Harilal, Expansion dynamics of laser ablated carbon plasma plume in helium ambient, Applied Surface Science, 172 (2001) 103-109.

[83] R.K. Thareja, A.K. Sharma, Formation of AlN in laser ablated plasma of Al in nitrogen ambient, physica status solidi C, 2 (2005) 2079-2082.

[84] G. Soto, E.C. Samano, R. Machorro, L. Cota, Growth of SiC and SiC_xN_y films by pulsed laser ablation of SiC in Ar and N_2 environments, Journal of Vacuum Science & Technology A, 16 (1998) 1311-1315.

[85] S. Amoruso, B. Toftmann, J. Schou, Thermalization of a UV laser ablation plume in a background gas: From a directed to a diffusionlike flow, Physical Review E, 69 (2004) 056403.

[86] X.Y. Chen, S.B. Xiong, Z.S. Sha, Z.G. Liu, The interaction of ambient background gas with a plume formed in pulsed laser deposition, Applied Surface Science, 115 (1997) 279-284.

[87] J.S. Horwitz, J.A. Sprague, Film Nucleation and Film Growth in Pulsed Laser of Ceramics, in: G.B. Chrisey, B.K. Hubler (Eds.) Pulsed Laser Deposition of Thin Films, John Wiley & Sons, INC, USA, 1994, pp. 229-326.

[88] S. Metev, K. Meteva, Nucleation and growth of laser-plasma deposited thin films, Applied Surface Science, 43 (1989) 402-408.

[89] D. Cotter, R.J. Manning, K.J. Blow, A.D. Ellis, A.E. Kelly, D. Nesset, I.D. Phillips, A.J. Poustie, D.C. Rogers, Nonlinear Optics for High-Speed Digital Information Processing, Science, 286 (1999) 1523-1528.

[90] J. Tominaga, T. Nakano, N. Atoda, An Approach for Recording and Readout beyond the Diffraction Limit with an Sb Thin Film, Applied Physics Letters, 73 (1998) 2078-2080.

[91] M. Ito, K. Imakita, M. Fujii, S. Hayashi, Nonlinear Optical Properties of Silicon Nanoclusters/nanocrystals Doped SiO_2 Films: Annealing Temperature Dependence, Journal of Applied Physics, 108 (2010) 063512.

TH-1680_10612114

[92] G.V. Prakash, M. Cazzanelli, Z. Gaburro, L. Pavesi, F. Iacona, G. Franzò, F. Priolo, Nonlinear optical properties of silicon nanocrystals grown by plasma-enhanced chemical vapor deposition, Journal of Applied Physics, 91 (2002) 4607-4610.

[93] S.B. Korovin, A.N. Orlov, A.M. Prokhorov, V.I. Pustovoi, M. Konstantaki, S. Couris, E. Koudoumas, Nonlinear absorption in silicon nanocrystals, Quantum Electronics, 31 (2001) 817.

[94] F.Z. Henari, K. Morgenstern, W.J. Blau, V.A. Karavanskii, V.S. Dneprovskii, Third-order optical nonlinearity and all-optical switching in porous silicon, Applied Physics Letters, 67 (1995) 323-325.

[95] Y. Kanemitsu, S. Okamoto, A. Mito, Third-order nonlinear optical susceptibility and photoluminescence in porous silicon, Physical Review B, 52 (1995) 10752-10755.

[96] S. Vijayalakshmi, M.A. George, H. Grebel, Nonlinear optical properties of silicon nanoclusters, Applied Physics Letters, 70 (1997) 708-710.

[97] S. Vijayalakshmi, F. Shen, H. Grebel, Artificial Dielectrics: Nonlinear Optical Properties of Silicon Nanoclusters at λ=532 nm, Applied Physics Letters, 71 (1997) 3332-3334.

[98] Y. Zhang, S. Vijayalakshmi, M. Ajgaonkar, H. Grebel, C.W. White, Optical properties of an ordered array of silica nanospheres embedded with silicon nanoclusters, Journal of the Optical Society of America B, 17 (2000) 1967-1972.

[99] S.R. Friberg, P.W. Smith, Nonlinear optical glasses for ultrafast optical switches, IEEE Journal of Quantum Electronics, 23 (1987) 2089-2094.

[100] M. Moran, S. Chiao-Yao, R. Carman, Interferometric measurements of the nonlinear refractive-index coefficient relative to CS_2 in laser-system-related materials, IEEE Journal of Quantum Electronics, 11 (1975) 259-263.

[101] A. Owyoung, Ellipse rotation studies in laser host materials, IEEE Journal of Quantum Electronics, 9 (1973) 1064-1069.

[102] M. Sheik-Bahae, A.A. Said, T.H. Wei, D.J. Hagan, E.W.V. Stryland, Sensitive measurement of optical nonlinearities using a single beam, IEEE Journal of Quantum Electronics, 26 (1990) 760-769.

[103] W.E. Williams, M.J. Soileau, E.W. Van Stryland, Optical switching and n_2 measurements in CS_2, Optics Communications, 50 (1984) 256-260.

TH-1680_10612114

TH-1680_10612114

Chapter 2

Experimental Details

Pulsed laser deposition (PLD) offers the advantages of fabrication of stoichiometric as well as non-stoichiometric thin films in a single step by controlling the deposition parameters [1-8]. It does not require any hazardous gas and hence environment friendly. The growth as well as the structural and crystalline properties of deposited thin films are governed by the kinetics of the laser produced plasma species which in turn can be controlled by a number of deposition parameters like laser wavelength, laser fluence, target-to-substrate distance, background ambient gas and substrate temperature [1, 2, 9-11]. Therefore, these parameters are to be optimized to obtain desired quality films. The present research work was aimed towards the fabrication and characterization of Si, SiO_x (nc-Si:SiO_2) and SiC thin films of sub micron thickness via PLD technique and to study the effect of substrate temperature and background gas pressure on their stoichiometry and crystallinity, which in turn control their optical properties. The room temperature (RT) photoluminescence properties of these films and their possible origins were also investigated. The a-Si:SiO_2 nanostructures were also fabricated directly on crystalline Si (c-Si) wafer by irradiating it with focused beam of a high power pulsed laser. This nanostructures thus formed are free from any contamination. The structural, compositional and photoluminescence properties of these structures as a function of laser fluence were studied. The nonlinear absorption (NLA) and nonlinear refractive index (NLR) coefficients of the films were measured by modified *Z*-scan setup developed in-house [12]. The effect of film stoichiometry on the third order nonlinear optical (NLO) properties and optical limiting (OL) properties of these films were also discussed.

TH-1680_10612114

2.1 Experimental setup for fabrication of a-Si:SiO_2 via direct laser irradiation of silicon wafer:

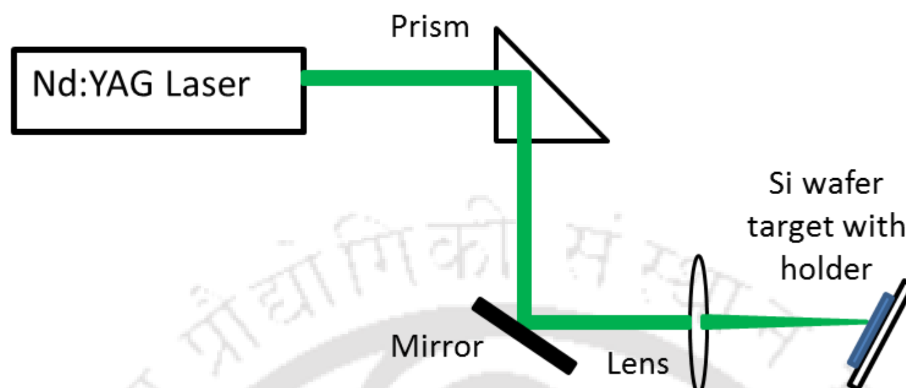

***Figure 2.1** Schematic of experimental setup for direct laser irradiation of silicon.*

The polished crystalline Si (100) wafers were irradiated by loosely focusing a second harmonic (532 nm) of a Q switched high power Nd: YAG laser (*Quanta-System, HYL-101*) having pulse duration of 8 ns and repetition rate of 10 Hz, in air at room temperature as shown in *Figure 2.1*. The laser beam was steered by a 90° prism focused by a convex lens of focal length of 25 cm and irradiated on the c-Si wafer at an incident angle ~ 30˚ (to avoid back reflection going back to the laser). The focal spot of laser beam onto the Si target was elliptical with major and minor axes of ~ 1.9 mm and 1.6 mm, respectively. The focusing of high power laser onto Si target in air results in the breakdown of the material as well as the atmospheric air in the neighborhood of focal region. This produces Si and oxygen ions which reacts and get deposited back onto the target around the periphery of the focal spot to yield a-Si:SiO_2 nanostructures. The laser fluence of 0.35, 0.67, 1.43 and 2.67 Jcm^{-2} was used for irradiation. The laser ablation was carried out for 10 min at all laser fluences except that of at 2.67 Jcm^{-2} where ablation duration was reduced to 5 min in order to avoid piercing of Si wafer.

TH-1680_10612114

2.2 Pulsed laser deposition (PLD) setup for fabrication of Si, SiO_x and SiC thin films:

The schematic of PLD setup and its photograph used for deposition of Si and SiO_x thin films is shown in *Figure 2.2 and Figure 2.3,* respectively. It consists of 12" diameter ultra-high vacuum compatible multiport stainless steel ablation chamber and a high power laser as two major components. The Si target was mounted on the motorized target carrousel and was inserted inside the ablation chamber through one of the 150 CF port.

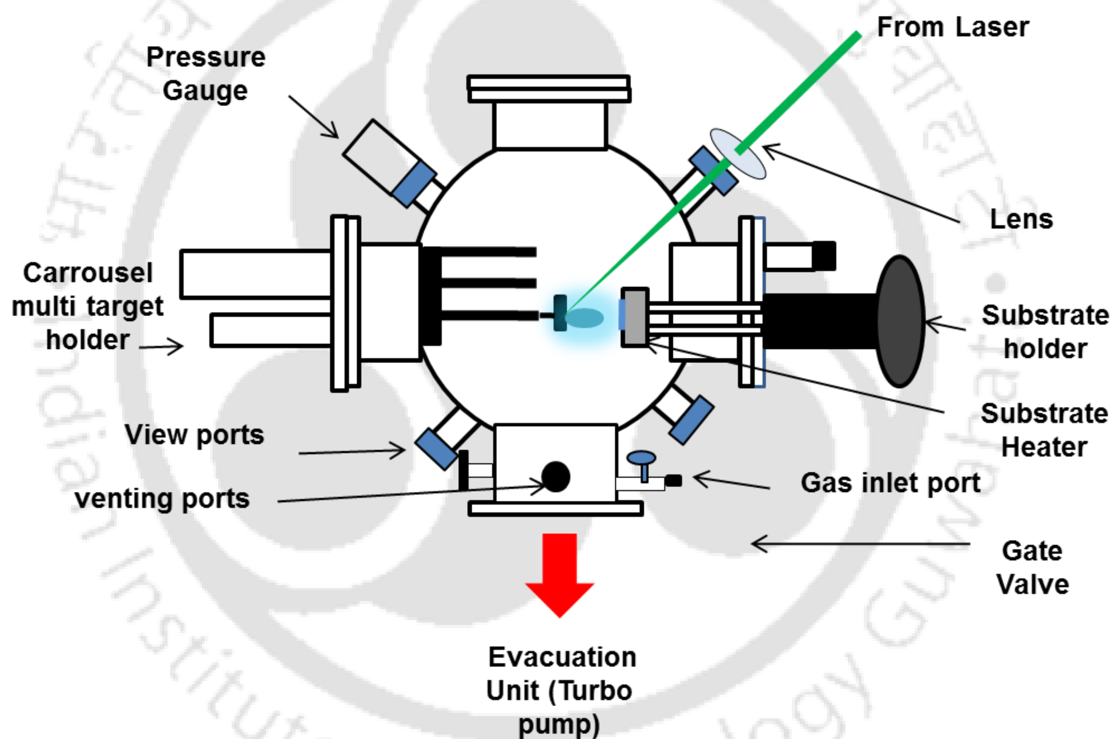

Figure 2.2 *Schematic of PLD setup.*

The substrate (glass and silicon) was mounted on the substrate holder assembly having provision for resistive heater to control the substrate temperature in a programmable manner till 800 °C. The substrate holder assembly was mounted on another 150 CF port of the ablation chamber opposite to the target carrousel. The target to substrate separation was maintained around ~3 cm. The vacuum chamber was evacuated to a base pressure

TH-1680_10612114

~10^{-6} mbar before deposition, using turbo molecular pump (*Pfeiffer, Hi Pace 300 C*) connected to the bottom 100 CF port of the ablation chamber, as shown in *Figure 2.1*.

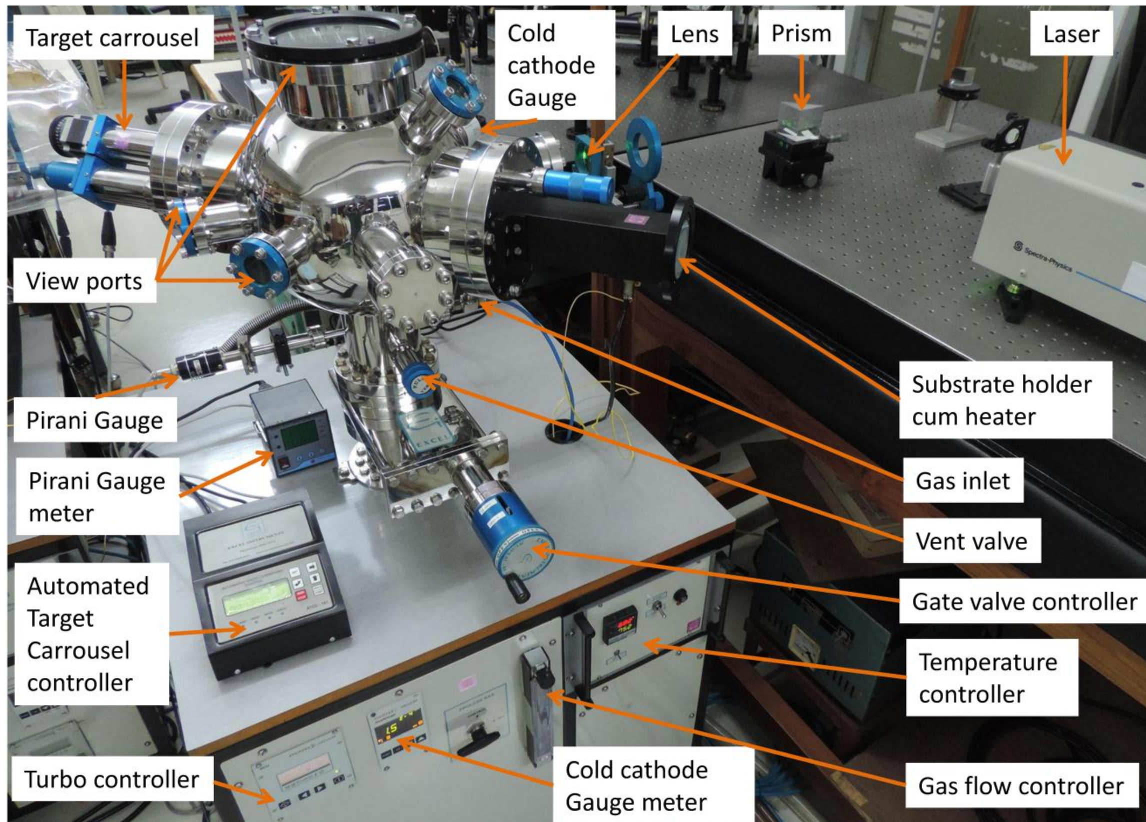

Figure 2.3 *Photograph of PLD setup*

The turbo molecular pump was backed by the rotary pump (*Pfeiffer, DUO 10 MC*). The pressure inside the ablation chamber was monitored using a compact cold cathode gauge (*Pfeiffer, IKR 251*) for low pressure regime (10^{-2} mbar – 10^{-7} mbar) and pirani gauge (*Pfeiffer, PCR 280* and *Hind HiVac, HPS-2*) for high pressure regime (10^{3} mbar - 10^{-3} mbar). The same Q-switched Nd:YAG laser (as mentioned in previous section 2.1) was focused onto the target by a convex lens of focal length of 35 cm. The focusing of the laser beam produces the laser induced plasma of target which expands in the presence of background gas and finally gets deposited onto the substrate placed parallel to the target. The Si films were deposited under vacuum (~10^{-6} mbar) as a function of substrate

TH-1680_10612114

temperatures from room temperature (RT) to 700 °C. The SiO_x films were deposited in presence of oxygen gas ambient at a pressure ranging from 10^{-4} to 0.5 mbar at 400 °C. For this, the ablation chamber was pressurized with the desired pressure through a separate port via gas flow controller as shown in *Figure 2.2* and also marked in *Figure 2.3*. The gas flow rate was maintained in the range of 20-30 standard cubic centimeters per minute (sccm). For the deposition of SiC films similar PLD chamber having diameter of 18" (operated with non-corrosive gases only) was used to avoid any contamination. The SiC films were deposited at various substrate temperatures (RT to 750 °C) under vacuum (~10^{-6} mbar).

2.3 Characterization of thin films:

A variety of diagnostic techniques were employed to characterize the PLD thin films of Si, SiO_x and SiC as well as a-Si:SiO_2 nanostructures are detailed below.

2.3.1 Stylus Profilometer

In the present PLD system the substrate was placed intact on the substrate holder during deposition with the help of the two clips. These clips acted as masks and provided the substrate-film step. The profilometer (*Veco Dektak 150*) was scanned linearly at five different locations by a Diamond-tipped stylus across this step. The thickness of the films was calculated by taking the average over all the scanned locations of the film.

2.3.2 Scanning Electron Microscope and Energy Dispersive X-ray spectroscopy:

The surface morphology of the a-Si:SiO_2 nanostructures and SiO_x films was studied by Scanning Electron Microscope (SEM), model *Leo 1430VP*, operated at an accelerating voltage of 1 keV. The elemental composition was identified by Energy Dispersive X-ray (EDX) spectra recorded by Oxford energy dispersive spectrometer

TH-1680_10612114

attached to the SEM instrument. The films were coated with very thin gold layer prior to loading them inside the vacuum column to avoid the charging effect during measurement.

2.3.3 Field emission scanning electron microscopy:

The surface morphology of the PLD SiC films was also captured by Field Emission Scanning Electron Microscope (FESEM) (*ZEISS sigma*), operated at an accelerating voltage of 3 to 5 keV, in order to capture images at larger magnification as compared to that of SEM images. The films were coated with very thin gold layer prior to loading them inside the vacuum column to avoid the charging effect during measurement. The elemental composition of SiC films was identified by Energy Dispersive X-ray (EDX) spectra attached to this instrument.

2.3.4 Transmission electron microscopy:

The Transmission Electron Microscope (TEM) is a very powerful tool to analyze the quality, shape, size and distribution of particles, crystallinity, dislocations and grain boundaries. To capture the TEM images of films, it is generally deposited onto the uncoated Cu mesh grid. But in our case as the films were thick (> 250 nm), they were scratched out mechanically and transferred to Cu mesh grid. The measurements were performed with TEM (*Jeol, JEM 2100*) using electron source at an accelerating voltage of 200 keV. The TEM images and SAED pattern were analyzed for accessing the nanostructures, crystalline quality and estimation of inter-planner spacing using build in software "*Gatan digital micrograph*".

2.3.5 X-ray Diffraction:

X-ray Diffraction (XRD) technique was employed to investigate the crystal structure of the PLD thin films. The XRD patterns were recorded in thin film mode by

TH-1680_10612114

commercial *Seifert 3003TT* X-ray Diffractometer employing $Cu\text{-}K_\alpha$ (1.5418 Å) radiation at the grazing angle of incidence maintained between to 1°-2°.

2.2.6 Raman spectroscopy:

Raman shift corresponds to vibrational energy which are unique for each material and hence used to identify the molecules and their structural properties. Raman spectroscopy has been used to identify the amorphous or crystalline nature of the film. For Si-based materials, it has also been used to determine nanocrystal size distribution as well as for stress estimation. Raman spectroscopy had been extensively used in this work to unveil the bonding structure and crystallinity of all the films fabricated as well as that of a-Si:SiO_2 nanostructures. Raman spectra of the samples were recorded by the micro-Laser Raman spectrometer (*Horiba Jobin Yvon, LabRam HR800*) using a holographic grating of 1800 groves/mm. Ar-ion laser (488 nm and 514 nm) was used as an excitation source. The laser beam was focused on the sample, using 100X microscopic objective lens, to a spot size of ~1μm diameter on the film surface. The spatial resolution of the Raman spectrometer was 1 μm and spectral resolution was less than 1 cm^{-1}. Raman maps at several locations of the given film were also recorded to unveil various bonding structures present locally in structurally heterogeneous PLD Si and SiO_x films.

2.2.8 Fourier transform infrared spectroscopy:

Infrared spectroscopy is based on the absorption of infrared radiation by vibrational levels of molecule in a material. The vibrational energy levels are unique for a material and hence the infrared spectrum also serves as a fingerprint for a particular material. In the present work, a single beam Fourier Transform Infrared (FTIR) spectrometer (*Perkin Elmer BX*) was used to record the IR transmission spectra of PLD films to assess various bonding present in the films and nanostructures. For FTIR

TH-1680_10612114

measurement, PLD films were deposited onto undoped silicon (100) wafer. The spectrometer was operated with a resolution of 4 cm^{-1} and the spectra were averaged over twenty scans for each sample.

2.2.9 UV-Visible-Near Infrared spectroscopy

Transmission spectra of Si, SiO_x and SiC films deposited on glass substrates were recorded using a dual beam UV-Visible-Near Infrared (UV-Vis-NIR) spectrometer (*Shimadzu -UV3101 PC*). The Swanepole's envelop technique was employed to estimate the refractive index (n), absorption coefficient (α) and thickness (d) of the thin films from the respective transmission spectra exhibiting the interference fringes [13]. In this method, the transmission maxima and minima observed in the transmission spectra are interpolated to envelop all maxima and minima, represented as T_{max} and T_{min}, respectively as shown in *Figure 2.4*. The refractive index (n) of the films at each experimentally observed transmission maxima and minima in the weakly absorbing region can be calculated using the expression given below [13],

$$n = \left[N + (N^2 - n_s^2)^{1/2}\right]^{1/2} \quad (2.1)$$

$$\text{where} \quad N = 2n_s \frac{T_{max} - T_{min}}{[T_{max}T_{min}]} + \frac{n_s^2 + 1}{2} \quad (2.2)$$

Here n_s is the refractive index of the substrate (n_s=1.52 for fused silica). The calculated values of n, at various values of λ, were plotted as a function of ($1/\lambda^2$) and least square fitted to Cauchy dispersion relation (truncated up to second term),

$$n = A_0 + \frac{C_0}{\lambda^2} \quad (2.3)$$

where A_0 and C_0 are two Cauchy's parameter. A_0 is also denoted as static refractive index n_0. The thickness (d) of the films can be calculated using the following expression, [13]

$$d = \frac{\lambda_a \lambda_b}{2(\lambda_a n_a - \lambda_b n_b)} \quad (2.4)$$

TH-1680_10612114

where n_a and n_b are refractive indices corresponding to the wavelengths λ_a and λ_b of adjacent maxima or minima respectively and finally average thickness, d_{avg} was obtained.

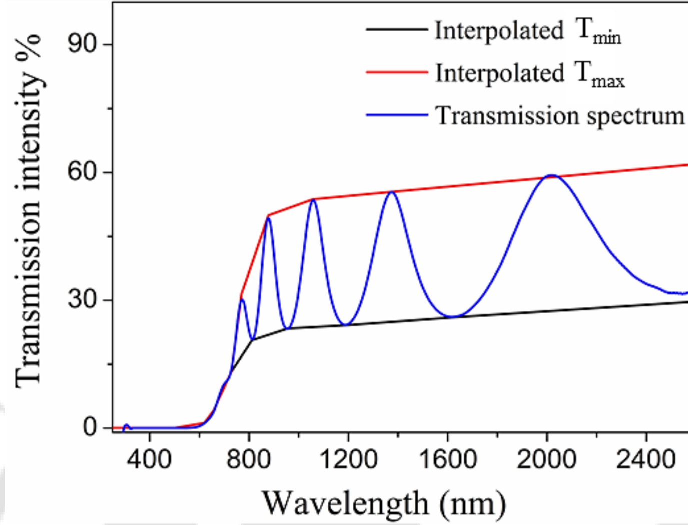

Figure 2.4 *UV-Vis-NIR transmission spectrum of PLD Si (~430 nm thickness) thin film exhibiting T_{max} and T_{min} curves.*

In amorphous materials, the absorption coefficient when plotted as a function of photon energy basically exhibit two regions- Tauc region and Urbach region, as depicted in *Figure 2.5*. The Tauc region is towards the higher photon energy side of absorption spectrum where absorption coefficient is parabolic w.r.t photon energy. While the Urbach region is situated toward the low photon energy side of low absorbing spectral region. In Urbach region the absorption coefficient shows an exponential dependence on photon energy and is given by [14],

$$\alpha = \alpha_0 exp\left(\frac{h\upsilon}{E_U}\right) \quad (2.5)$$

where α_o is a constant and E_U is Urbach energy which gives the measure of the width of the tails of localized states in the forbidden gap of the amorphous materials. The absorption coefficient of the films, in low absorbing spectral region, can be calculated using the following expression [13]:

TH-1680_10612114

$$\alpha = -\frac{1}{d} ln \frac{E_M - \left[E_M^2 - (n^2-1)^3 (n^2 - n_s^2)\right]^{\frac{1}{2}}}{(n-1)^3 (n - n_s^2)} \tag{2.6}$$

where $E_M = \frac{8n^2 n_s}{T_{max}} + (n^2 - 1)(n^2 - n_s^2)$

The absorption coefficient estimated from equation (2.6) can be plotted as a function of photon energy. From equation (2.5), the plot of *ln(α)* vs. *hv* exhibiting a linear relation within the Urbach region of absorption spectrum and the E_U for the films can be calculated from the slope of this plot.

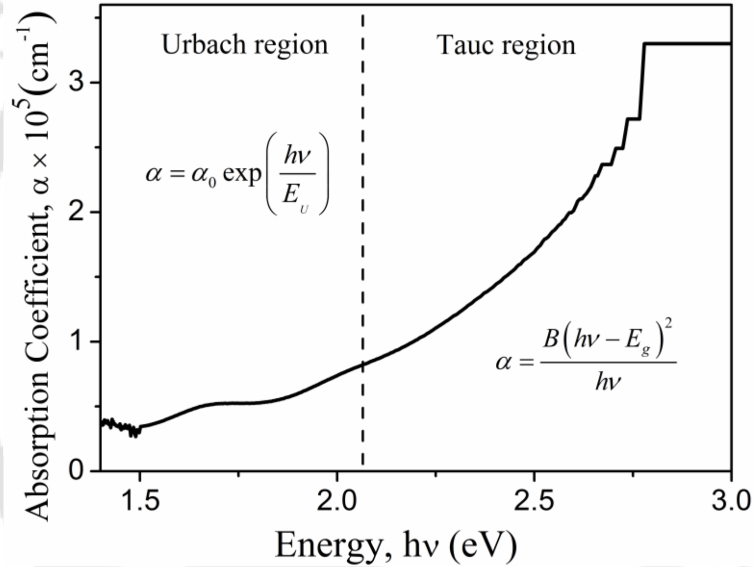

Figure 2.5 *Absorption coefficient of a PLD nanocrystalline Si film (~330 nm) exhibiting Tauc region and Urbach region.*

For highly absorbing spectral region, *α* is given as [13],

$$\alpha = -\frac{1}{d} ln \frac{(n+1)^3 (n + n_s^2)}{16 n^2 n_s} T_0 \tag{2.7}$$

where T_0 is the transmission in the strongly absorbing region where envelop curve for T_{max} and T_{min} merges together (*Figure 2.4*). The absorption coefficient, *α*, is related to photon energy (*hv*) by the following equation [14],

$$(\alpha hv) = B\left(hv - E_g\right)^m \tag{2.8}$$

TH-1680_10612114

where B is the Tauc slope (or B parameter), E_g is the energy of the optical band gap and m is the power factor dependent upon type of electronic transition (m=1/2, 3/2 and 2 for direct, forbidden and indirect transitions, respectively) determined by the nature of the material. For amorphous materials, indirect transitions are valid, m=2, and hence absorption coefficient in Tauc region is given as [15]

$$(\alpha h\upsilon)^{\frac{1}{2}} = B\left(h\upsilon - E_g\right) \qquad (2.9)$$

The linear region of the Tauc plot, $(\alpha h\nu)^{1/2}$ vs. $h\nu$, which lies in highly absorbing region is generally used to estimate the optical band gap of the films. The intercept estimated by extrapolating the linear region of the $(\alpha h\nu)^{1/2}$ *vs* $h\nu$ plot on the $h\nu$ axis gives the optical band gap, E_g for the amorphous thin films.

2.2.10 Spectroscopic Ellipsometry

Spectroscopic Ellipsometer (SE) is an optical instrument in which plane waves of light having known wavelength and polarization are directed onto a sample surface, and the change in polarization state of the wave upon specular reflection is analyzed to obtain the structural and the optical properties of the sample. In this technique, the change in polarization state of the reflected light with respect to the incident light is measured as a function of frequency (or wavelength) as well as angle of incidence. *Figure 2.6* shows the schematic depicting reflection of polarized light on film-substrate surface during SE measurement and geometrical interpretation of ellipsometric parameters (ψ, Δ). The *p*- and *s*- polarized light waves are the parallel and perpendicular components of the electric field vector of the light wave with respect to the plane of incidence. Here, $\overrightarrow{E_\iota}$ and $\overrightarrow{E_r}$ are incident and reflected electric field vectors, respectively, with Φ being the angle of incidence. $\overrightarrow{E_{\iota s}}$ and $\overrightarrow{E_{rs}}$ are incident and reflected electric field vectors for s-polarization

TH-1680_10612114

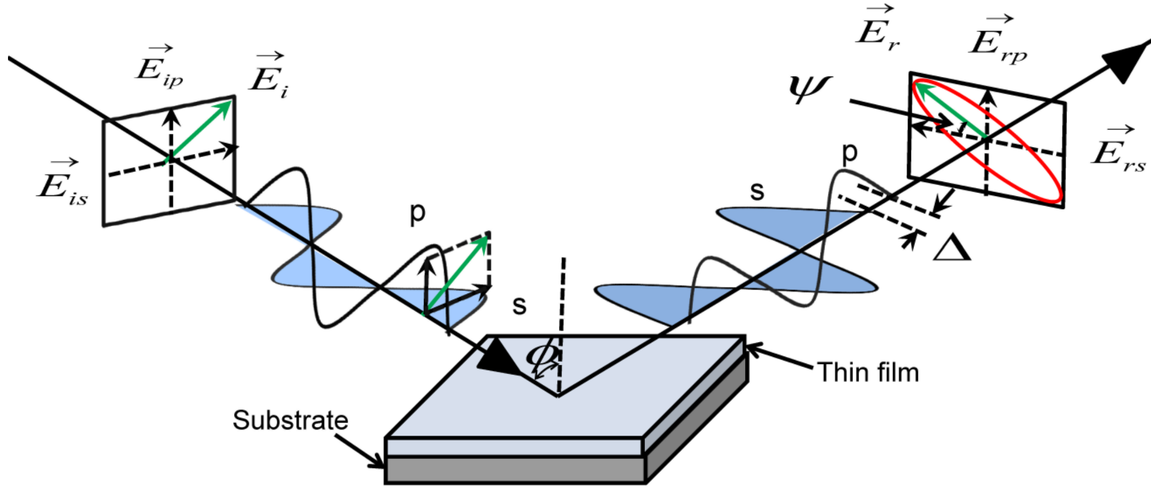

Figure 2.6 *Schematic depicting reflection of polarized light on film-substrate surface and geometrical interpretation of ellipsometric parameters (ψ, Δ).*

while $\overrightarrow{E_{ip}}$ and $\overrightarrow{E_{rp}}$ are that of p-polarization, respectively. The parameters 'Ψ', depicted in *Figure 2.6*, is the angle whose tangent gives the ratio of the reflection coefficients of electric field components along the p and s polarizations, and is given by, $tan\psi = \frac{|r_p|}{|r_s|}$, where $|r_p| = \frac{|\overrightarrow{E_{rp}}|}{|\overrightarrow{E_{ip}}|}$ and $|r_s| = \frac{|\overrightarrow{E_{rs}}|}{|\overrightarrow{E_{is}}|}$ are the amplitude of Fresnel reflection coefficient for *p*- and *s*- polarizations, respectively. For linearly polarized light incident at 45°, $|\overrightarrow{E_{ip}}| = |\overrightarrow{E_{is}}|$ and hence $tan\psi = \frac{|r_p|}{|r_s|} = \frac{|\overrightarrow{E_{rp}}|}{|\overrightarrow{E_{rs}}|}$. The another parameter 'Δ' gives the difference between the phase shifts of electric field components for p and s polarizations upon reflection given by Δ= δ_p - δ_s, where δ_p and δ_s are the phase of reflected *p*- and *s*- polarized light waves, respectively. The change in polarization are expressed in terms of two parameters, ψ and Δ, defined by the following equation [16, 17],

$$\rho = \frac{r_p}{r_s} = \left|\frac{r_p}{r_s}\right| e^{i(\Delta_p - \Delta_s)} = tan\psi e^{i\Delta} \quad (2.10)$$

TH-1680_10612114

The ellipsometric parameters, Δ and $\tan \psi$, are the directly measurable quantities which are recorded as a function of wavelength at various angle of incidences. In the particular case of an abrupt interface between two semi-infinite media, the ellipsometric data are related to the complex dielectric function ε by the following relation [16, 17],

$$\varepsilon = sin^2\Phi\{1 + [(1-\rho)/(1+\rho)]^2 tan^2\Phi\} = \varepsilon_1 + i\varepsilon_2 \qquad (2.11)$$

where $\varepsilon_1 = \varepsilon_\infty + \sum_i \varepsilon_{1,i}$ and $\varepsilon_2 = \sum_i \varepsilon_{2,i}$ with $\varepsilon_{1,i}$ and $\varepsilon_{1,i}$ are real and imaginary part of dielectric function of ith oscillator. Using equation 2.10 and 2.11, real and imaginary part of dielectric constant, ε_1 and ε_2, can be expressed as a function of Δ and $\tan \psi$. Using appropriate optical models and layered structure, the ε_1 and ε_2 values are simulated and compared with the measured ε_1 and ε_2 spectra. The unknown parameters in the optical model, such as film thickness, refractive index, extinction coefficient or parameters of the dispersion relation are varied and computed to obtain a "best fit" to the experimental data. The best fitted results will minimize RMSE value as given in equation 2.12 below, and then the physical parameters are obtained.

$$RMSE = \sqrt{\frac{1}{2p-q-1}\sum_{i=1}^{p}\left[\left(\frac{\varepsilon_{1i}^{cal}-\varepsilon_{1i}^{exp}}{\sigma_{\varepsilon_{1i}}^{exp}}\right)^2 w_1 + \left(\frac{\varepsilon_{2i}^{cal}-\varepsilon_{2i}^{exp}}{\sigma_{\varepsilon_{2i}}^{exp}}\right)^2 w_2\right]} \qquad (2.12)$$

where, the superscripts "exp" and "cal" represent the experimentally measured and simulated values, respectively. Here w_1 and w_2 are weighted terms while $\sigma_{\varepsilon_{1i}}^{exp}$ and $\sigma_{\varepsilon_{2i}}^{exp}$ are experimental errors in the determination of ε_1 and ε_2. In equation (2.12), p and q are the numbers of the measured data points and fitted model parameters, respectively.

The basic models relevant to the present work are Lorentz model, Tauc-Lorentz model and Tauc-Lorentz-Lorentz model. The Lorentz oscillator model is a classical dispersion model which assumes that the material can be described as a collection of non-

TH-1680_10612114

interacting oscillators. For this model, the imaginary part of the dielectric function ε_2 as a function of photon energy E is given by [16, 17],

$$\varepsilon_2^L(E) = \frac{AE_0^2CE}{(E_0^2-E^2)^2+C^2E^2} \tag{2.13}$$

where E_0 is the oscillator position, A is the oscillator amplitude and C is the broadening of the Lorentz oscillator. The Tauc–Lorentz (TL) oscillator model is widely used dispersion model to describe the optical properties of the amorphous materials having band structure and was proposed by Jellison and Modine [18]. It was formulated by combining the Tauc expression, $\varepsilon_2^T(E) = \left(E - E_g\right)^2/E^2$, for ε_2 near the band edge with the single classical Lorenz oscillator and is given by, [16, 17, 19]

$$\varepsilon_2^{TL}(E) = \begin{cases} \frac{AE_0C\left(E-E_g\right)^2}{\left(E^2-E_0^2\right)^2+C^2E^2}\frac{1}{E}, & E \geqslant E_g, \\ 0, & E \leqslant E_g \end{cases} \tag{2.14}$$

where E_g is the band gap of the material. In the present work, a model with a combination consisting dispersion laws of Tauc-Lorentz and Lorentz gave the best fit for Si films In this approach, the imaginary part of dielectric function ε_2 is considered to be the combination of TL oscillator model (for $E_0 > E_g$), and a Lorentz oscillator. Thus, the imaginary part of the dielectric function ε_2 in Tauc Lorentz-Lorentz (TLL) model is defined as,

$$\varepsilon_2(E) = \varepsilon_2^{TL}(E) + \varepsilon_2^L(E) \tag{2.15}$$

The real part of the dielectric function ε_1 for the Lorentz, Tauc–Lorentz and TLL oscillator models can be obtained by the Kramers–Kronig integration of the ε_2 functions described by the equations (2.13, 2.14 and 2.14) [16, 17],

$$\varepsilon_1(E) = \varepsilon_\infty + \frac{2}{\pi}P\int_{E_g}^{\infty}\frac{\xi\varepsilon_2(\xi)}{\xi^2-E^2}d\xi \tag{2.16}$$

TH-1680_10612114

where ε_∞ represents the value of real part of the dielectric function ε at infinite energy and it is an additional fitting parameter in the oscillator model, the P stands for the Cauchy principal part of the integral.

In the present thesis, the SE measurements for PLD Si films were carried out over the spectral range of 1.32–5.00 eV for incident angles ranging from 50° to 77° using Variable Angle Spectroscopic Ellipsometer (*Semilab SOPRA:GES-5E*) equipped with goniometer. The data was analyzed for incident angles of 65°, 70°, and 75° only. Data acquisition and analysis was performed using spectroscopy ellipsometry analyzer (*SEA*) software. In order to represent a mixed amorphous–crystalline phase for Si films, the Bruggeman's effective medium approximation (BEMA) was used [17, 20, 21]. The optical band gap, refractive index, extinction coefficient and thickness of the films were estimated from SE studies and compared with those of of UV-Vis-NIR transmission spectra studies.

2.4 Modified Z-Scan set-up for measurement of the third order NLO coefficients of Si, SiO_x and SiC thin films:

In Z-scan technique, the sample is translated longitudinally along the optic axis of a focused Gaussian laser beam. The translation of the sample leads to the change of irradiance in the sample, resulting in changes in the intensity dependent optical properties. The intensity transmitted through the sample is recorded as a function of sample location (z) with respect to the focus. The plot of transmitted intensity as a function of z gives the information about the order of the nonlinearity as well as its sign and magnitude. The technique includes open aperture (OA) and closed aperture (CA) Z-scan measurements which determine nonlinear absorption (NLA) coefficient and nonlinear refractive index

TH-1680_10612114

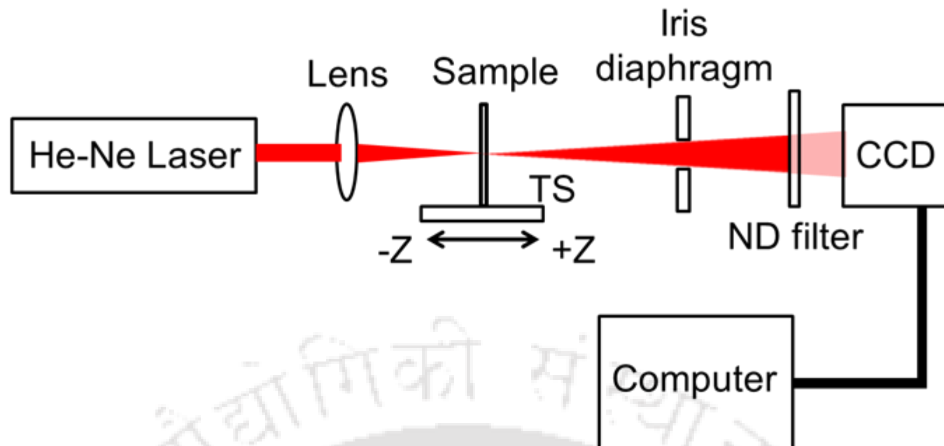

Figure 2.7 *Schematic of modified Z-scan setup.*

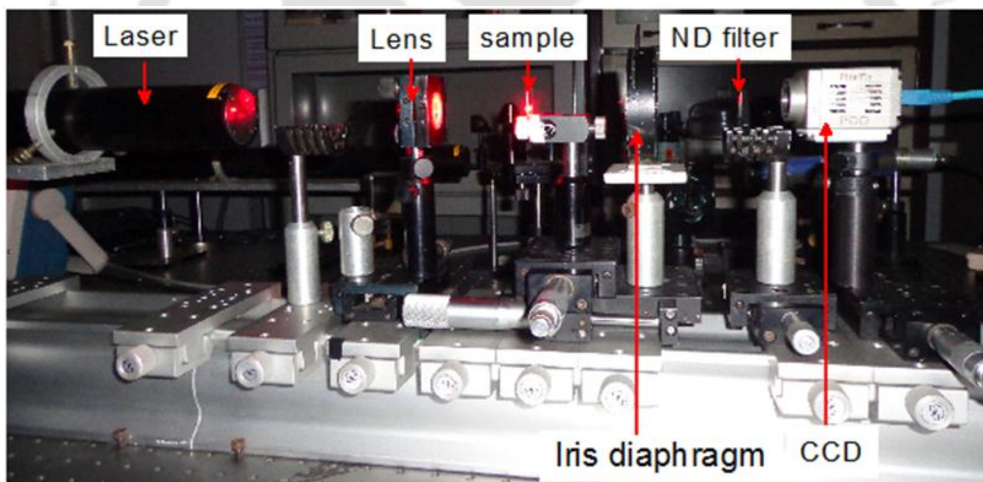

Figure 2.8 *Photograph of modified Z-scan setup.*

(NLR) coefficient, respectively. In the present work, modified *Z*-scan technique was used to measure the NLA and NLR coefficients of PLD films, [12]. *Figure 2.7* and *2.8* show the schematic of the modified *Z*-scan setup assembled in lab and its photograph. In this, a 32 mW cw He-Ne laser (*Melles Griot, 05-LHP-927*, 632.8 nm) was focused by a convex lens of the focal length of 5 cm on the thin film sample. The transmitted beam from the sample was imaged on a CCD detector (*PCO, PixelFly*), kept at a distance of ~25 cm

TH-1680_10612114

from the focusing lens. A neutral density (ND) filter was placed in front of CCD to avoid its saturation. An iris diaphragm of aperture size ~6 mm was placed before the ND filter to suppress the scattered light entering into the CCD. The beam waist at the focus of the lens was estimated to be ~21.8 μm. The transmitted power before the sample was around ~ 28 mW, which corresponds to a peak intensity of ~7.5×10^3 W/cm^2. But the intensity entering the thin film sample is estimated as 7.5×10^3 (1-R) W/cm^2 where R is the reflectance of the sample. The thin film was scanned to 15 mm on either side of the focus along beam direction in a step size of 1 mm, marked as –Z to +Z in *Figure 2.7*, and the transmitted beam imaged simultaneously by CCD as a function of *z*.

Z-scan experiments were conducted for determining the sign and magnitude of real and imaginary parts of third-order nonlinear susceptibility (χ). The intensity dependent nonlinear absorption and refraction are expressed by the equations, $a(I) = \alpha + \beta I$ and $n(I) = n + n_2 I$, where α is the linear absorption coefficient, n is the linear refractive index, β is the nonlinear absorption coefficient, n_2 is nonlinear refarctive index coefficient and I the intensity of the laser beam incident on the sample. For OA Z-scan, the transmitted inetnsity was obtained by integrating the grey values of the recorded images using Matlab. The CA *Z*-scan data was obtained by implementing a software aperture over the OA *Z*-scan images using the Matlab program for S=0.4 (where S is the ratio of transmittance intensity with aperture to that of without aperture). Thus, both open and closed aperture *Z*-scan data could be retrived by this single scan recording via CCD. In a *Z*-scan experiment, in accordance with Sheik-Bahae formalism (SBF), under the approximation that the sample thickness is less than the Rayleigh length, z_0, the far-field transmission intensity measured as a function of sample position (*z*) w.r.t the focal plane of the lens, accounting for purely intensity dependent nonlinear absorption and nonlinear

TH-1680_10612114

refraction are given by [22],

$$T_{op} = 1 - \frac{c}{(1+bz^2)} \quad (2.17)$$

$$T_{cl} = 1 + \frac{4az}{(1+bz^2)(9+bz^2)} \quad (2.18)$$

where, T_{op} and T_{cl} are the normalized transmittance for OA and CA Z-scan, respectively, with $c = \beta I L_{eff} / 2^{3/2}$, $a = 2\pi n_2 I L_{eff} / \lambda z_o$, $b = 1/z_o^2$ and L_{eff} is the effective thickness of the thin film given by equation ,

$$L_{eff} = \frac{1-exp(-\alpha L)}{\alpha} \quad (2.19)$$

where, α is the linear absorption coefficient and d is the film thickness. The normalized OA Z-scan transmittance curves exhibiting minimum transmission at focus indicates the presence of strong reverse saturation absorption (RSA). The experimental data points for OA Z-scan were fitted to the transmission profile given by equation (2.17) and β was calculated from the best fitted constant 'c'. The normalized transmittance through the closed aperture was normalized and fitted to equation (2.18). In the CA Z-scan, if the normalized transmission curves displays a transmittance minimum (valley) prior to focus followed by a transmittance maximum (peak) after focus, then it indicates the self focusing property, corresponding to a positive nonlinear refractive index n_2. On the other hand if peak apears prior to valley then it indicates the self defocusing property corresponding to negative nonlinear refractive index.The n_2 can be calculated by fitting the data of the CA Z-scan measurment to equation (2.18). The Rayleigh length z_o is given by,

$$z_0 = \frac{\pi w_0^2}{\lambda} \quad (2.20)$$

where w_o is the beam diameter at the focus (z=0) which was estimated using the relation,

TH-1680_10612114

$$w_0 = \frac{f\lambda}{D} \qquad (2.21)$$

where f is the focal length of the lens (= 5 cm), D is the laser beam diameter coming out of the laser (≈ 1.45 mm) and λ is the laser wavelength (= 632.8 nm). From this the value of z_0 comes out to be ~ 2.45 mm. The thickness of the films, in the present work, is less than 600 nm and hence it satisfies the thin film approximation.

The linear and nonlinear refractive indices (n and n_2 respectively) can be expressed as, $N = n + ik \text{ and } N_2 = n_2 + ik_2$, where, n and k (extinction coefficient) represent the real and imaginary parts of the complex linear refractive index while n_2 and k_2 that of real and imaginary part of the complex nonlinear refractive index, respectively. From these, the real and imaginary part of third order NLO susceptibility, $\chi^{(3)}{}_R$ and $\chi^{(3)}{}_I$, was calculated using the following equations [23, 24],

$$\chi_R^{(3)}(esu) = 10^{-7}\frac{nc}{12\pi^2}(nn_2 - kk_2) \qquad (2.22)$$

$$\chi_I^{(3)}(esu) = 10^{-7}\frac{nc}{12\pi^2}(nk_2 + kn_2) \qquad (2.23)$$

where, the linear extinction coefficient, k = ($\alpha\lambda$/4π) and imaginary part of the nonlinear refractive index k_2 = ($\beta\lambda$/4π). Finally the magnitude of third order susceptibility is calculated from following,

$$\chi^{(3)} = \sqrt{\left(\chi_R^{(3)}\right)^2 + \left(\chi_I^{(3)}\right)^2} \qquad (2.24)$$

2.5 Optical limiting set-up:

Optical limiting (OL) is a property exhibited by nonlinearly absorbing material where it has a linear transmission till certain incident laser power and beyond which the output begins to saturate [25, 26]. The point of onset of deviation from linearity of the plot of output laser power transmitted from the sample versus input laser power is termed

TH-1680_10612114

as optical limiting threshold. To test the optical limiting (OL) capability of all the thin film samples documented in the thesis, the experimental setup very similar to the OA Z-scan geometry was assembled and shown in *Figure 2.9*. The laser beam from a cw He:Ne

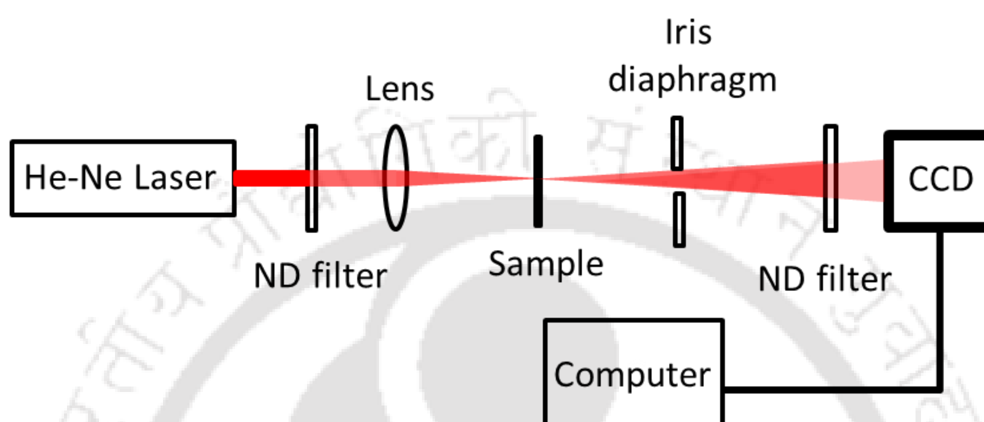

Figure 2.9 *Schematic of optical limiting measuring set-up.*

laser (*Melles Griot, 05-LHP-927*, 632.8 nm) was transmitted through a ND filter placed immediately after the laser and then focused on a sample by a 5 cm lens. The input power of the laser incident on the sample was varied by placing ND filters, of OD ranging from 0.1-1, immediately after the laser. Another ND filter was placed before the CCD to avoid its saturation. The laser beam transmitted through the sample was imaged on CCD. From the CCD images, the transmitted beam intensity was measured by integrating the grey values of the images. Prior to recording the OL data, CCD was calibrated by illuminating with a known power of laser later of which was measured from power meter (*Melles Griot, 13PEM001*). The plot of transmitted laser power as a function of incident laser power gives the OL curve.

2.6. Conclusion:

In this chapter, the experimental setup used for direct laser irradiation of Si wafer to fabricate a-Si:SiO_2 nanostructures locally as well as the PLD system for fabrication of

TH-1680_10612114

thin films of Si, SiO_x and SiC are presented. The various characterization techniques employed to study the structural, compositional and optical properties of PLD films are also presented briefly. Finally, the in-house developed modified *Z*-scan setup and OL setup employed to study the NLO properties of PLD films are also discussed.

TH-1680_10612114

Bibliography

[1] D.B. Chrisey, G.K. Hubler, Pulsed Laser Deposition of Thin Films, Wiley-VCH, USA, 2003.

[2] R. Eason, Pulsed Laser Deposition of Thin Films Applications, John Wiley & Sons, New Jersey, 2007.

[3] M. Filipescu, A.P. Papavlu, M. Dinescu, Functional Metal Oxide Thin Films Grown by Pulsed Laser Deposition, in: P. Mandracci (Ed.) Crystalline and Non-crystalline Solids, InTech, Rijeka, 2016, pp. 33-55.

[4] R.D. Vispute, S. Choopun, R. Enck, A. Patel, V. Talyansky, R.P. Sharma, T. Venkatesan, W.L. Sarney, L. Salamancariba, S.N. Andronescu, A.A. Iliadis, K.A. Jones, Pulsed laser deposition and processing of wide band gap semiconductors and related materials, Journal of Electronic Materials, 28 (1999) 275-286.

[5] A.T.T. Mostako, C.V.S. Rao, A. Khare, Mirrorlike pulsed laser deposited tungsten thin film, Review of Scientific Instruments, 82 (2011) 013101.

[6] D.H. Lowndes, D.B. Geohegan, A.A. Puretzky, D.P. Norton, C.M. Rouleau, Synthesis of Novel Thin-Film Materials by Pulsed Laser Deposition, Science, 273 (1996) 898.

[7] S. Kumari, A. Khare, Optical and structural characterization of pulsed laser deposited ruby thin films for temperature sensing application, Applied Surface Science, 265 (2013) 180-186.

[8] G. Shukla, P.K. Mishra, A. Khare, Effect of annealing and O2 pressure on structural and optical properties of pulsed laser deposited TiO2 thin films, Journal of Alloys and Compounds, 489 (2010) 246-251.

[9] B.P. Swain, R.O. Dusane, Effect of substrate temperature on HWCVD deposited a-SiC:H film, Materials Letters, 61 (2007) 4731-4734.

[10] H. ElGazzar, E. Abdel-Rahman, H.G. Salem, F. Nassar, Preparation and characterizations of amorphous nanostructured SiC thin films by low energy pulsed laser deposition, Applied Surface Science, 256 (2010) 2056-2060.

[11] M. Tabbal, A. Said, E. Hannoun, T. Christidis, Amorphous to crystalline phase transition in pulsed laser deposited silicon carbide, Applied Surface Science, 253 (2007) 7050-7059.

[12] I. Kumar, A. Khare, Modified Z-scan Set-up using CCD for Measurement of Optical Nonlinearity in PLD Carbon Thin Film, Optics and Laser Technology, 77 (2016) 51-54.

[13] R. Swanepoel, Determination of the Thickness and Optical Constants of Amorphous Silicon, J. Phys. E: Sci. Instrum. , 16 (1983) 1214-1222.

[14] I. Chambouleyron, S.D. Ventura, E.G. Birgin, J.M. Martínez, Optical constants and thickness determination of very thin amorphous semiconductor films, Journal of Applied Physics, 92 (2002) 3093-3102.

[15] J. Tauc, Amorphous and Liquid Semiconductors, Plenum, London, 1974.

[16] H.G. Tompkins, W.A. McGahan, Spectroscopic Ellipsometry and Reflectometry: A User's Guide, John Wiley & Sons Inc. , New York, 1999.

TH-1680_10612114

[17] H. Fujiwara, Spectroscopic Ellipsometry: Principles and Applications, John Wiley & Sons Ltd., Chichester, West Sussex, England, 2007.

[18] G.E. Jellison, F.A. Modine, Parameterization of the optical functions of amorphous materials in the interband region, Applied Physics Letters, 69 (1996) 371-373.

[19] J. Tauc, R. Grigorovici, A. Vancu, Optical Properties and Electronic Structure of Amorphous Germanium, Phy. Stat. Solidi B, 15 (1966) 627-637.

[20] D.A.G. Bruggeman, Berechnung verschiedener physikalischer Konstanten von heterogenen Substanzen. I. Dielektrizitätskonstanten und Leitfähigkeiten der Mischkörper aus isotropen Substanzen, Annalen der Physik, 416 (1935) 636-664.

[21] Y. Bouizem, C. Abbes, J.D. Sib, D. Benlakehal, R. Baghdad, L. Chahed, K. Zellama, S. Charvet, Ellipsometric and Raman spectroscopic study of nanocrystalline silicon thin films prepared by a rf magnetron sputtering technique, Journal of Physics: Condensed Matter, 20 (2008) 445221.

[22] M. Sheik-Bahae, A.A. Said, T.H. Wei, D.J. Hagan, E.W.V. Stryland, Sensitive measurement of optical nonlinearities using a single beam, IEEE Journal of Quantum Electronics, 26 (1990) 760-769.

[23] R.W. Boyd, Nonlinear Optics, 3rd ed., Academic Press, 2008.

[24] G.P. Bharti, A. Khare, Structural and Linear and Nonlinear Optical Properties of $Zn_{1-x}Al_xO$ ($0<x<0.10$) Thin Films Fabricated via Pulsed Laser Deposition Technique, Optical Materials Express, 6 (2016) 2063-2080.

[25] D.J. Harter, M.L. Shand, Y.B. Band, Power/Energy Limiter using Reverse Saturable Absorption, Journal of Applied Physics, 56 (1984) 865.

[26] E.W. Van Stryland, Y.Y. Wu, D.J. Hagan, M.J. Soileau, K. Mansour, Optical limiting with semiconductors, Journal of the Optical Society of America B, 5 (1988) 1980-1988.

TH-1680_10612114

TH-1680_10612114

Chapter 3
Fabrication of lumunescent Si:SiO2 nanostructures by direct laser irradiation of Si wafer in air

The nanostructured silicon, viz.; nano-crystalline (nc) Si, nanostructured amorphous Si (a-Si), nc Si or a-Si embedded in amorphous SiO_2 matrix, porous silicon (po-Si) etc. shows intense visible and near infrared photoluminescence (PL) [1-3]. PL properties make nanostructured Si potential candidate as emitters for field-emission based devices such as high-definition displays as well as other vacuum microelectronics devices [4], MEMS based memory devices [5] and light emitting devices [6]. The nanostructured Si-based thin films can be fabricated by magnetron sputtering [7], chemical vapor deposition [8], pulsed laser ablation [9, 10] etc. In some cases, it is desirable to grow nanostructured area locally on a silicon-based device or on assembled integrated chip. The nc-Si structures can be grown directly on Si substrate by direct irradiation of laser [2] or via chemical etching [11]. The local etching of a Si based film can be performed by nano second pulsed radiation from a laser with a high precision. It does not require any hazardous chemical and hence is contamination free as well as environment friendly. In the present chapter, the fabrication of a-Si:SiO_2 nanostructures via direct pulsed laser ablation of Si wafer and its room temperature PL properties are described.

3.1 Experimental details:

The a-Si:SiO_2 nanostructures were fabricated on polished crystalline Si (100) wafers by irradiating it with a loosely focused beam of second harmonic (532 nm) from a Q switched high power Nd: YAG laser (pulse duration of 8 ns and repetition rate of 10 Hz) in air at room temperature (RT) as shown in *Figure 2.1, Chapter 2*. The laser beam was

TH-1680_10612114

steered by a prism and irradiated on the target at an incident angle ~ 30° to avoid back reflection. The focal spot of laser beam onto the Si target was elliptical with major and minor axes of ~ 1.9 mm and 1.6 mm, respectively. The focusing of high power laser onto Si target in air results in the breakdown of the material and the atmospheric air in the neighborhood of focal region forming the laser produced plasma plume. This produces Si and oxygen ions which reacts and get deposited back onto the target around the periphery of the focal spot to yield a-Si:SiO_2. The effect of laser fluence on the fabrication of a-Si:SiO_2 was studied by varying the fluence in the range of 0.35 – 2.67 Jcm^{-2}. The Raman spectra of a-Si:SiO_2 were recorded at room temperature (RT) by micro-Raman spectrometer in back scattering geometry. The 488 nm line of Ar ion laser was used as an excitation source. The same laser was also used for PL studies of these samples. The surface morphology of the laser irradiated region was recorded by Scanning Electron Microscope (SEM) and the compositional analysis was performed by Energy Dispersive X-Ray (EDX). Fourier Transform Infrared (FTIR) transmission spectra of all the samples were recorded to get the confirmation of the presence of SiO_2 in the vicinity of focal region. Transmission Electron Microscopic (TEM) images were recorded for analyzing the size distribution of a-Si particle within the whitish clusters formed in the peripheral region of laser ablated crater. SAED patterns were also recorded for all the samples.

3.2 Results and discussions:

3.2.1 Study of morphological, structural and photoluminescence property of laser irradiated Si target at a laser fluence of ~ 1.46 Jcm^{-2} after 6,000 laser shots:

Figure 3.1 shows SEM image of the laser irradiated spot onto Si target at a laser fluence of 1.46 Jcm^{-2} after 6000 shots of laser. A central dark crater-like region surrounded by white clusters is clearly visible in the SEM image. Similar features were

TH-1680_10612114

observed at all other values of laser fluences. The crater size and amount of white cluster kept on increasing as a function of laser fluence from 0.35 to 2.67 Jcm^{-2}.

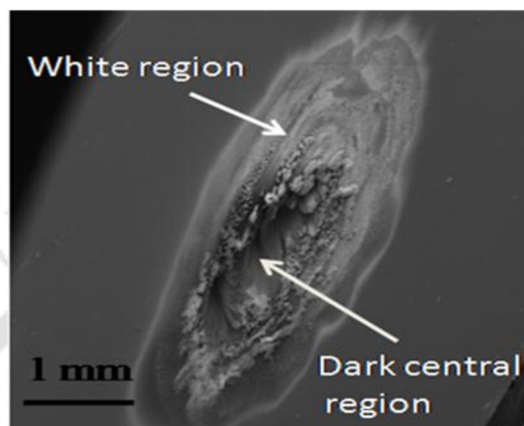

Figure 3.1 *SEM image of laser irradiated Si target at a laser fluence of ~ 1.46 Jcm^{-2} after 6,000 shots.*

The magnified view of whitish region is shown in *Figure 3.2(a)*. It shows the formation of cauliflower like structure having size distribution from 10 to 20 μm. The Raman spectrum (200-700 cm^{-1}) of these structures is shown in the *Figure 3.2(b)*. It displays a prominent band (400-550 cm^{-1}) and a shoulder toward the low energy tail (350-400 cm^{-1}) of this band. The 400-550 cm^{-1} band with broad peak at around 483 cm^{-1} (FWHM ~ 105.6 cm^{-1}) is attributed to first-order scattering of vibrational TO phonon modes of amorphous silicon [12, 13]. For comparison the Raman spectrum of unexposed Si target displaying a sharp intense peak at 521 cm^{-1}, a characteristic of bulk crystalline Si, is also shown in *Figure 3.2(b)*. It arises from the first-order Raman scattering of the longitudinal optical (LO) and the transverse optical (TO) phonon modes which are degenerate at the Brillouin zone centre in crystalline Si [14]. Figure 3.2(c) shows the RT PL spectrum of

TH-1680_10612114

above sample. It displays a broad asymmetric PL ranging from 1.6 – 2.2 eV, having band tail towards the blue region, with a peak around 1.82 eV [3, 14].

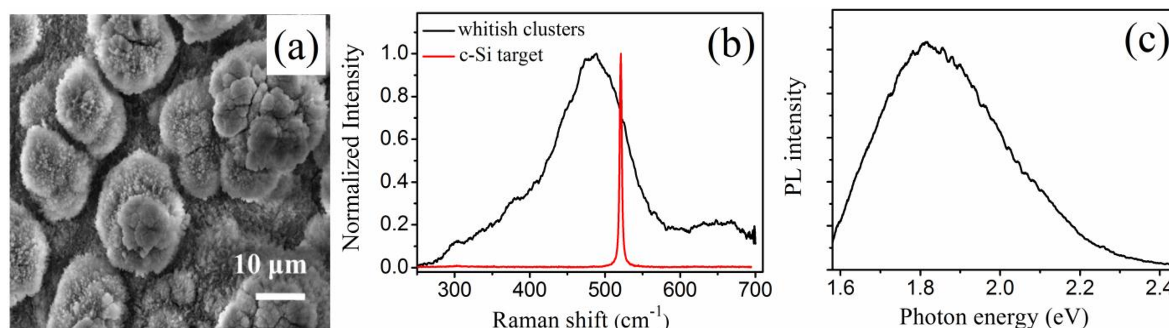

Figure 3.2 *(a) SEM image, (b) Raman spectrum and (c) RT Photoluminescence spectrum of whitish clusters formed at a laser fluence of 1.46 Jcm^{-2} (6000 laser shots).*

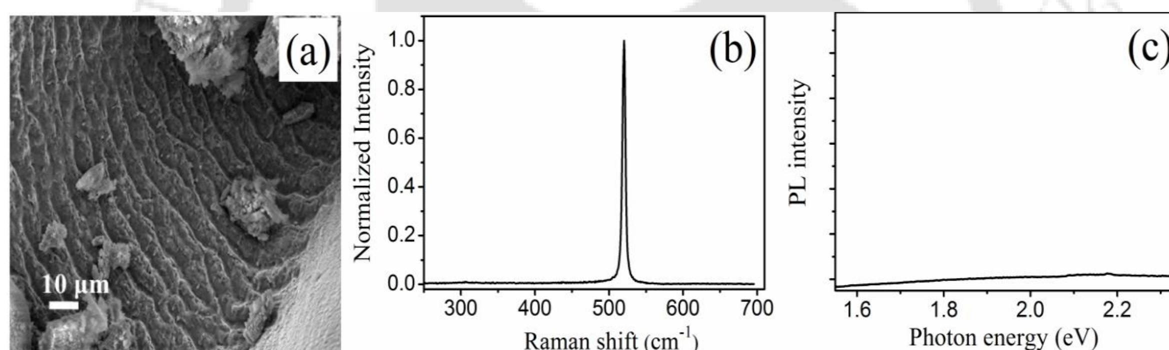

Figure 3.3 *(a) SEM image, (b) Raman spectrum and (c) RT Photoluminescence spectrum of dark central region formed at a laser fluence of 1.46 Jcm^{-2} (6000 laser shots).*

Figure 3.3(a), *3.3(b)* and *3.3(c)* shows magnified SEM image, Raman spectrum and PL spectrum of central dark region of the same sample, respectively. The SEM image displayed formation of micron sized rippled structures termed as laser-induced periodic surface structures (LIPSS) [15]. Its Raman spectrum exhibited a sharp high intense peak at 521 cm^{-1} similar to that of a bare target as shown in the *Figure 3.2(b)*. No detectable PL was observed in the dark central regions as evident from *Figure 3.3(c)*. The central dark

TH-1680_10612114

region surrounded by whitish region was formed by the re-deposition and nucleation of material onto the target from the expanding laser produced plasma plume. The laser beam spot being Gaussian has an intense central region with relatively less energy at periphery. The central region receives larger energy density and hence reaches higher temperatures compared to peripheral regions. Due to larger thermal diffusion length in the central regions the depth of molten mass is comparatively more. Therefore, central region has much larger amount of melt volume at relatively higher temperature compared to regions at periphery. In central region, the material has enough time to re-crystallize from the melt due to increased recalescence and higher temperature, hence providing sufficiently long period of cooling. The peripheral region, having low temperature and smaller amount of melt volume, cools much earlier to allow hardly any re-crystallization and hence resulted into the formation of amorphous phase [16, 17].

3.2.2 Compositional analysis of a-Si:SiO_2 nanostructures as a function of laser fluence:

Figure 3.4(a), *3.4(b)*, *3.4(c)* and *3.4(d)* show the EDX spectra of whitish region formed around the periphery of the laser irradiated spot at laser fluences of 0.35, 0.67 and 1.46 Jcm^{-2} after irradiation with 6000 shots and at 2.67 Jcm^{-2} after 3000 shots respectively. These spectra showed the presence of silicon and oxygen in the nanostructures indicating the SiO_2 matrix formation [18]. The atomic proportion of O_2 was found to have increased gradually from 44.9 % to 70.9 % with increasing laser fluence. The higher laser fluence favours the formation of larger amount of SiO_2 due to the breakdown of more and more ambient air at higher laser fluence. The reaction of ions of Si and oxygen in laser produced plasma results in subsequent SiO_2 formation during

TH-1680_10612114

cooling phase of plasma followed by the re-solidification onto the target surface.

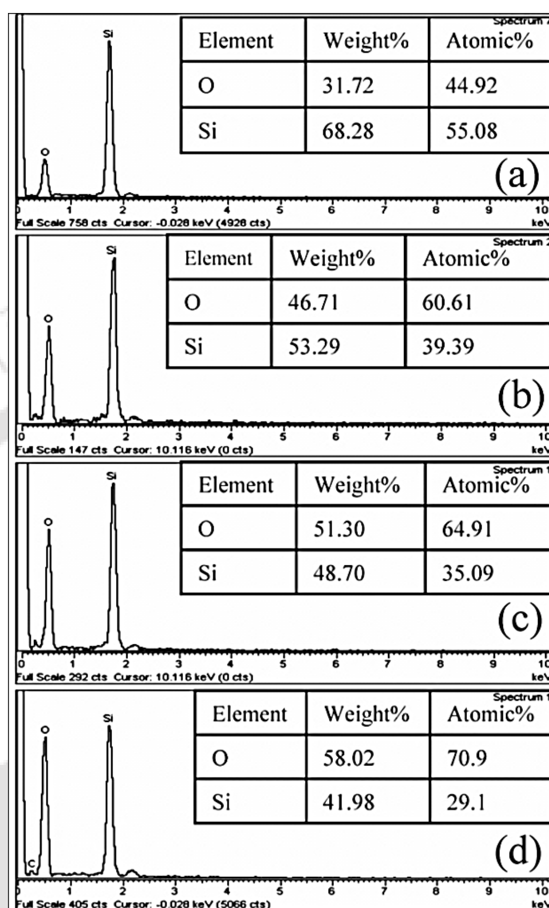

***Figure 3.4** EDX spectra of whitish area of sample fabricated at laser fluences of (a) 0.35 Jcm^{-2}, (b) 0.67 Jcm^{-2} and (c) 1.46 Jcm^{-2} with 6000 laser shots and (d) 2.67 Jcm^{-2} with 3000 laser shots.*

3.2.3 Structural characterization of a-Si:SiO_2 nanostructures as a function of laser fluence:

To study the effect of laser fluence on the formation of a-Si embedded in SiO_2 matrix, the Raman spectra of all the samples prepared at laser fluence of 0.35, 0.67 and 1.46 Jcm^{-2} after irradiation with 6000 shots and at 2.67 Jcm^{-2} after 3000 shots were recorded. At 2.67 Jcm^{-2} after 6000 shots a hole was drilled on the target, so its spectra could not be recorded. *Figure 3.5* shows the de-convoluted Raman spectra of the

TH-1680_10612114

periphery (white region) of the samples fabricated at (a) 0.35, (b) 0.67 Jcm^{-2} (c) 1.46 Jcm^{-2} and (d) 2.67 Jcm^{-2} to unveil the multiple peaks present in the spectra. After de-convolution five distinguishable peaks have been observed in Raman spectra of white region formed at a laser fluence of 0.35 Jcm^{-2} as shown in *Figure 3.5(a).* These five peaks observed at 615 cm^{-1}, 512 cm^{-1}, 478 cm^{-1}, 433 cm^{-1} and 333 cm^{-1} had been designated as peak 1, peak 2, peak 3, peak 4 and peak 5, respectively. Peak 1 is the least intense which corresponds to defect peak D_2 of SiO_2 matrix. Peak 2 observed at 512 cm^{-1} could be due to presence of small fraction of nc-Si. Peak 3 had the maximum intensity with broad FWHM~67 cm^{-1} peaking around 478 cm^{-1} which is attributed to first-order scattering of vibrational TO phonon modes of a-Si [12, 13]. Peak 4 observed at around 433 cm^{-1} has maximum FWHM of 116 cm^{-1} with peak intensity nearly half of that of peak 3. This peak is attributed to the six-membered rings (Si_2O_4) and presence of five-, seven- and higher member rings is responsible for broadening of this band [19]. Moreover, a blue shift of this peak is related to decrease of Si-O-Si bridging angle between different tetrahedral units forming the SiO_2 matrix. Finally, a broad peak 5 observed at 333 cm^{-1} is attributed to combination of LA and LO like modes of amorphous silicon [12, 13]. Similar Raman peaks were observed for the samples prepared at laser fluences of ~ 0.67, 1.46 and 2.67 Jcm^{-2}. In Figure 3.5(b), 3.5(c) and 3.5(d), D_2 peak was absent. In Figure 3.5(d), an additional peak at 491 cm^{-1} assigned as peak 2 was observed. This peak corresponds to D_1 peak of SiO_2 which though present in other spectra could not be de-convoluted due to close proximity and broadness of vibrational TO phonon modes of a-Si present around 480 cm^{-1}. D_1 and D_2 peaks are associated with in-phase breathing motions of oxygen atoms in three- and four- membered rings respectively [19]. Thus Raman spectra revealed the presence of both a-Si and disordered SiO_2 in the whitish micro-clusters. The data of

TH-1680_10612114

various de-convoluted peaks and respective FWHM of Raman spectra of whitish region formed around the periphery of the irradiated Si target at different laser fluences are listed in Table 1. The last column of the table lists the assignments of peaks to corresponding Raman active vibrational modes. The Raman spectra of dark central region of each sample exhibited sharp Lorenzian peak at 521 cm^{-1}, corresponding to Raman active mode of c-Si. While at few places a red shift w.r.t. this peak was also observed, which is a characteristic feature of nanocrystalline Si (nc-Si).

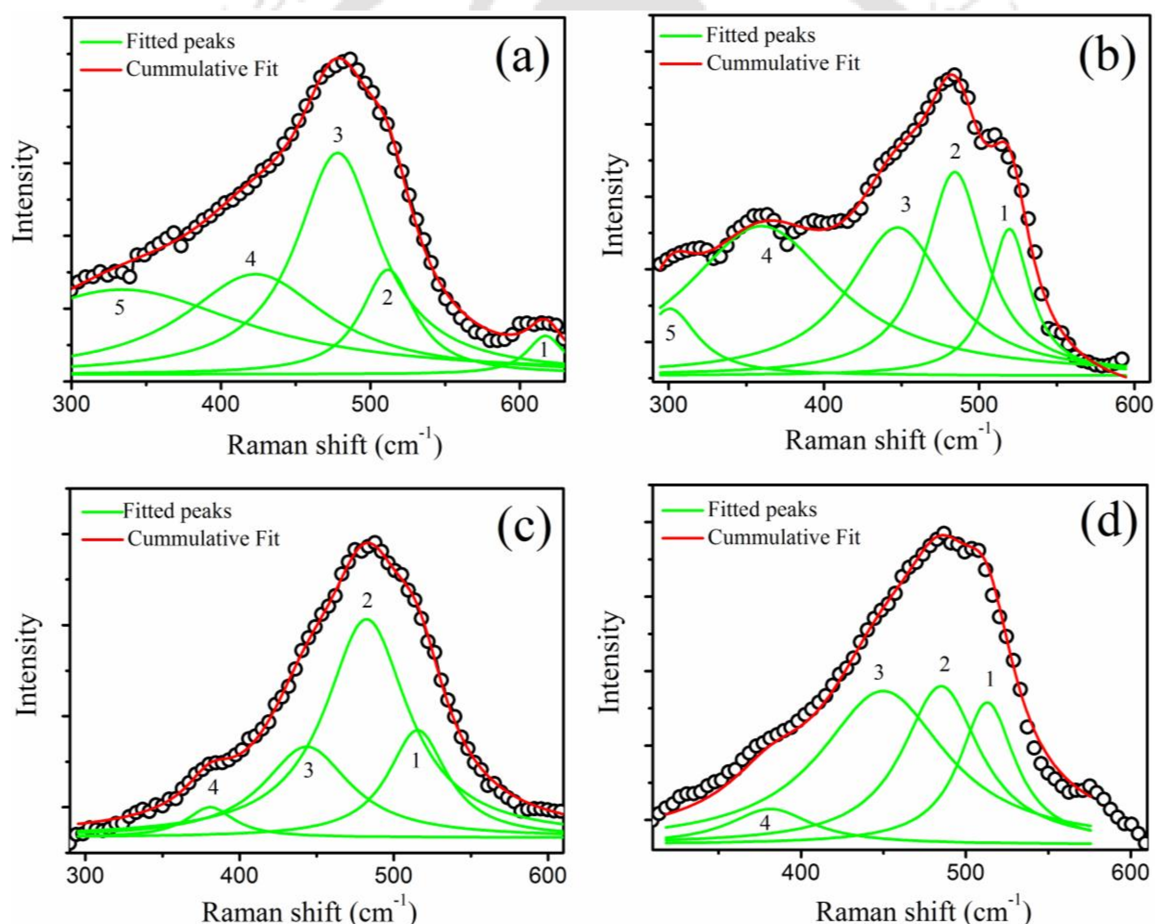

Figure 3.5 *The de-convoluted RT Raman spectra of whitish clusters of a-Si:SiO_2 formed at laser fluences of (a) 0.35 Jcm^{-2}, (b) 0.67 Jcm^{-2} and (c) 1.46 Jcm^{-2} with 6000 laser shots and (d) 2.67 Jcm^{-2} with 3000 laser shots.*

TH-1680_10612114

***Table** 3.1. Peak centers and FWHMs of de-convoluted RT Raman spectra of whitish clusters of a-Si:SiO_2 formed as a function of laser fluences along with appropriate peak assignments.*

Laser Fluences (Jcm^{-2})	Peak No.	Raman Peaks (cm^{-1})	FWHM (cm^{-1})	Peak Assignments
0.35	1	615	30	D_2 localised 3 membered Siloxine ring
	2	512	44	Red shifted LO and TO phonon modes of c-Si (Signature of nc-Si)
	3	478	67	TO phonon modes of a- Si
	4	433	116	6 membered ring in Silica network
	5	339	203	Combination of LA and LO modes of a-Si
0.67	1	519	32	LO / TO phonon modes of nc-Si
	2	483	47	TO phonon modes of a- Si
	3	445	77	6 membered ring in Silica network
	4	360	119	Combination of LA and LO modes of a-Si
	5	301	43	LA phonon modes of a- Si
1.46	1	515	45	LO / TO phonon modes of nc-Si
	2	482	65	TO phonon modes of a- Si
	3	443	68	6 membered ring in Silica network
	4	380	37	LO modes of a-Si
2.67	1	518	30	LO / TO phonon modes of nc-Si
	2	491	41	D_1 localised 4 membered Siloxine ring
	3	471	47	TO phonon modes of a- Si
	4	441	74	6 membered ring in Silica network
	5	384	50	LO modes of a-Si

TH-1680_10612114

Figure 3.6 shows the FTIR transmission spectra of laser irradiated region in c-Si wafer at all the laser fluences. The baseline correction was done w.r.t the FTIR transmission spectrum of unirradiated intrinsic c-Si target. The intensity of absorption band (a) located around 458 cm^{-1} which is attributed to rocking vibration of Si-O, increases with increasing laser fluence. For samples fabricated at higher laser fluences of 1.46 and 2.67 Jcm^{-2}, absorption bands marked as (b) and (c) evolved at 652 cm^{-1} and 789 cm^{-1}, respectively. The band at 652 cm^{-1} is attributed to Si-Si stretching vibration in a-Si. The band at 789 cm^{-1} is due to in plane Si-O-Si bending vibration in SiO_2 matrix. The absorption band ranging from 1000 cm^{-1} to 1300 cm^{-1} was the most prominent absorption feature observed in all these samples. This spectral region consisted of the most intense absorption band designated as (d) with a broad shoulder leveled as (e). The absorption

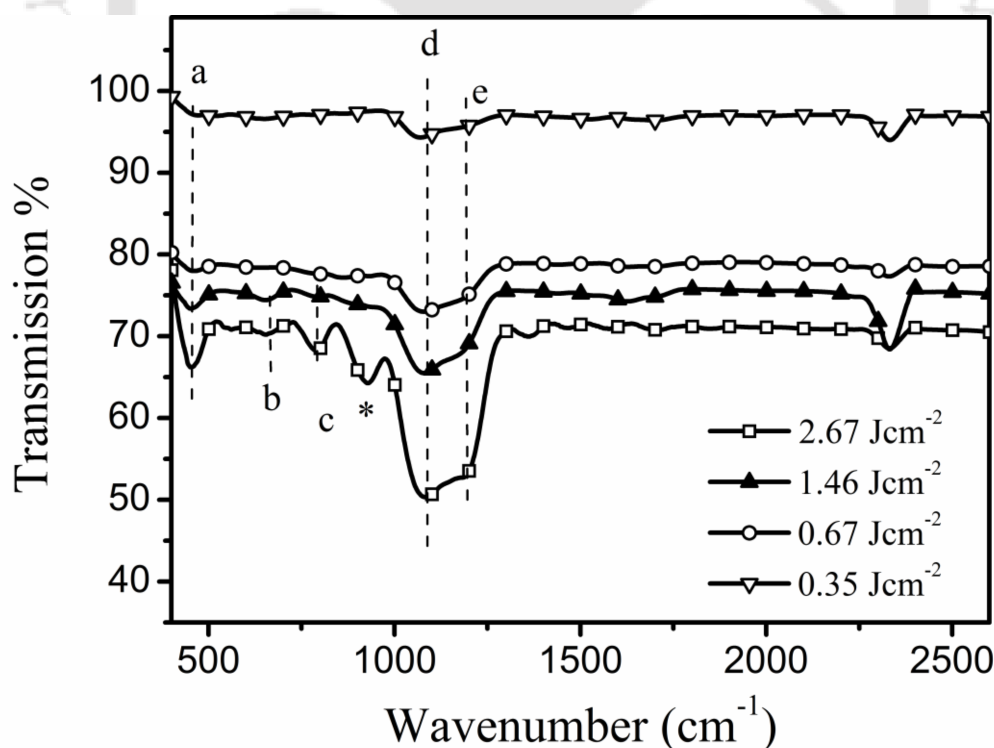

Figure 3.6 *FTIR transmission spectra of whitish clusters of a-Si:SiO_2 formed at different laser fluences.*

TH-1680_10612114

band (d) located around 1074 cm^{-1} for samples prepared at 0.35 Jcm^{-2} showed a gradual blue shift with increasing laser fluence. It shifted to 1081 cm^{-1} at maximum laser fluence of 2.67 Jcm^{-2}. The absorption shoulder found to be slightly blue-shifted with increasing laser fluence, from 1189 cm^{-1} to 1192 cm^{-1}. Both of these bands showed an increase in absorption intensity with increasing laser fluence and at higher fluences the shoulder becomes more pronounced. The absorption band at (d) is attributed to the in phase bond-stretching vibrations along Si-O bond and that of (e) are due to out-of-phase bond-stretching vibrations along Si-O bond [20]. The FTIR spectra for sample, prepared at laser fluence of 2.67 Jcm^{-2}, exhibited an additional absorption band marked as '*' around 930 cm^{-1}, attributed to Si-OH stretching vibration. The absorption bands associated with the rocking (a), bending (c) and stretching (d, e) vibration modes of the Si–O–Si bonds in SiO_2 reconfirms the formation of SiO_2 matrix in the Si target. The increase in absorption dip with the laser fluence further indicates the increase in proportion of SiO_2 in confirmation with the EDX results (*Figure 3.4*).

3.2.4 Surface morphology characterization of a-Si:SiO₂ nanostructures as a function of laser fluence:

Figures 3.7 displays the SEM images of whitish region formed around the periphery of the samples prepared at laser fluences of (a) 0.35, (b) 0.67 and (c) 1.46 Jcm^{-2} after irradiation with 6000 shots as well as that of (d) 2.67 Jcm^{-2} after 3000 shots. The images showed micron sized cauliflower-like clusters with a nanostructured envelop in all the samples.

TH-1680_10612114

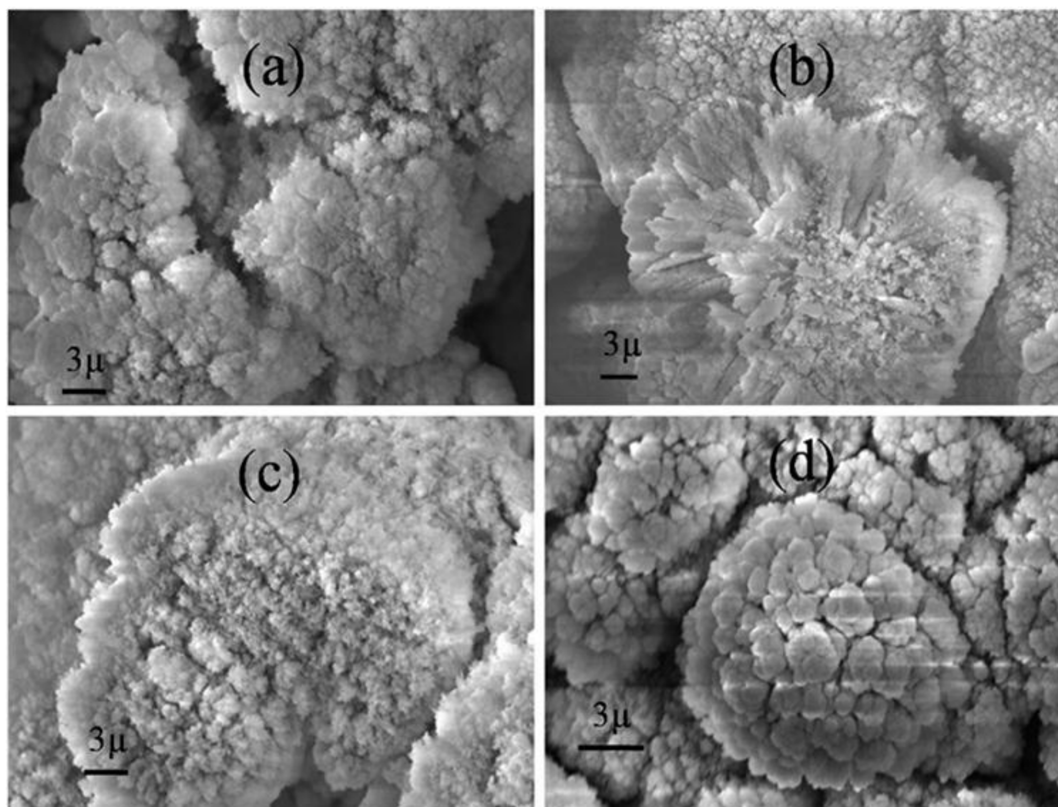

Figure 3.7 *SEM images of whitish clusters formed at different laser fluences (a) 0.35 Jcm*$^{-2}$*, (b) 0.67 Jcm*$^{-2}$ *and (c) 1.46 Jcm*$^{-2}$ *with 6000 laser shots and (d) 2.67 Jcm*$^{-2}$ *with 3000 laser shots.*

3.2.5 TEM analysis of a-Si:SiO$_2$ nanostructures as a function of laser fluence:

Figure 3.8 (a-d) show TEM micrographs and *Figure 3.8 (e-h)* show the corresponding SAED pattern of whitish clusters formed at different laser fluences. From these images, it was observed that at lowest laser fluence densely packed nanosized clusters of variable size were formed while at high laser fluences the particle were relatively less dense and more distinct. From the corresponding SAED pattern shown in *Figure 3.8 (e-h)*, it was observed that diffraction pattern of these nanostructures displayed diffuse ring, a characteristic of the amorphous material. The inset of *Figure 3.8 (c)* shows

TH-1680_10612114

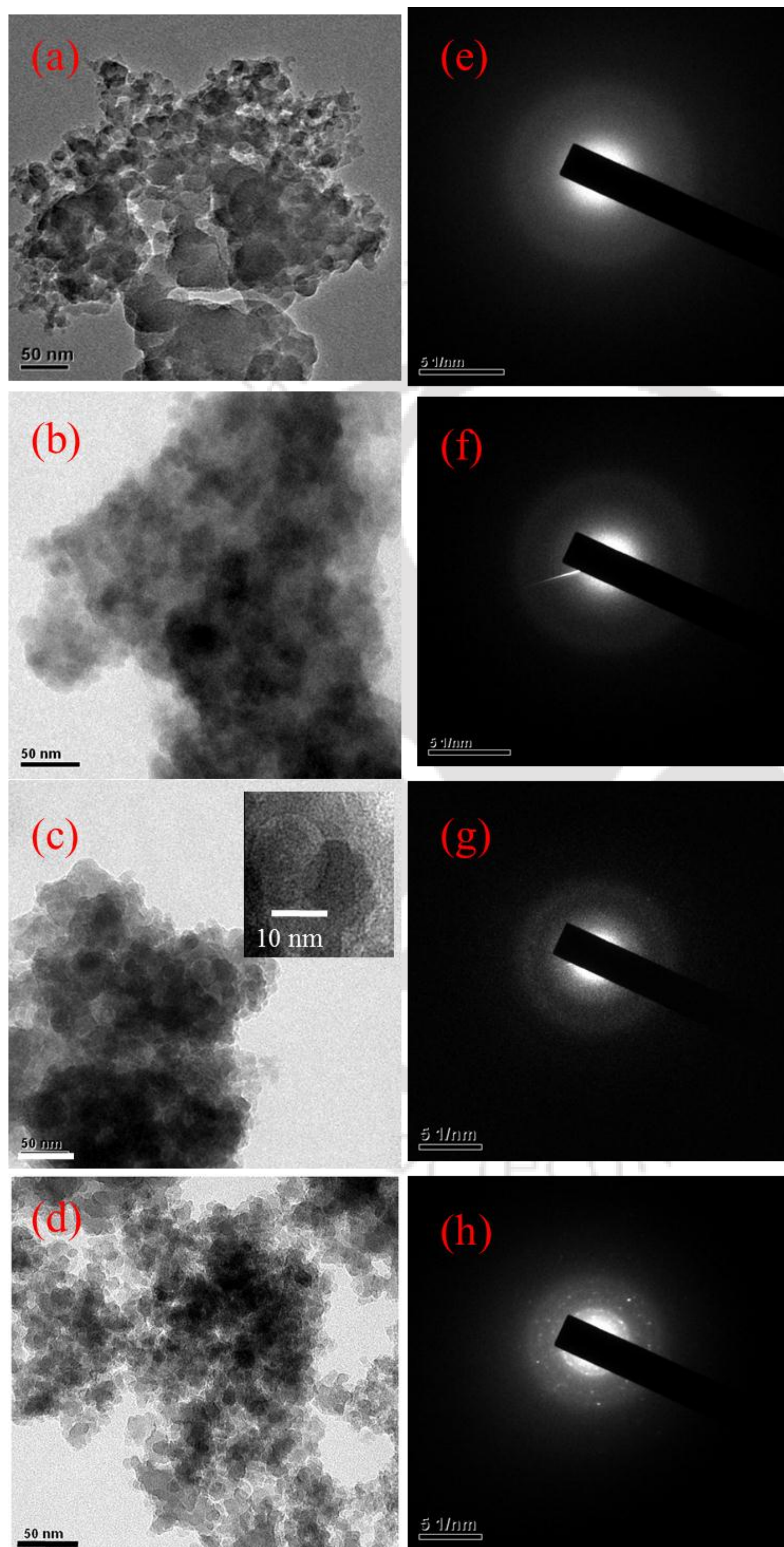

Figure 3.8 *TEM micrographs (a-d) and corresponding SAED pattern (e-h) of whitish clusters formed at laser fluences of 0.35 Jcm^{-2}, 0.67 Jcm^{-2} and 1.46 Jcm^{-2} with 6000 laser shots and 2.67 Jcm^{-2} with 3000 laser shots, respectively. Inset in (c) shows the HRTEM of nanostructures formed at laser fluence of 1.46 Jcm^{-2}.*

TH-1680_10612114

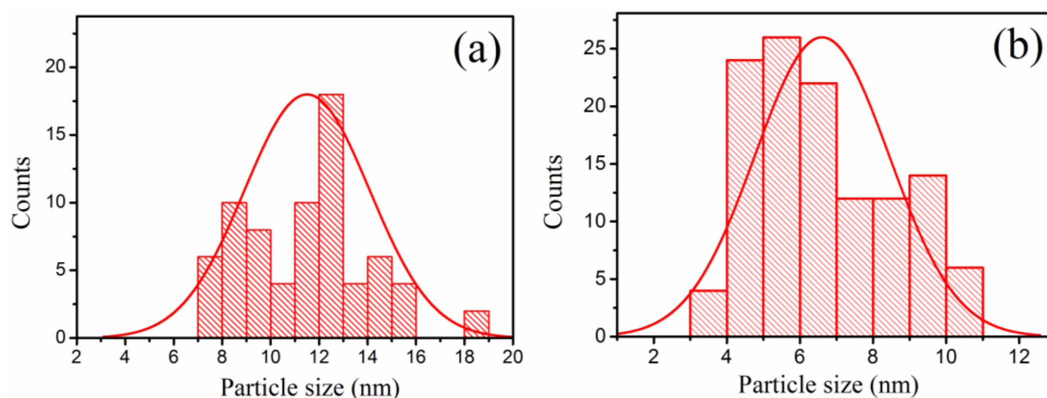

Figure 3.9 *Histograms depicting the particle size distribution estimated from TEM images of whitish clusters formed at laser fluences of (a) 1.46 and (b) 2.67 Jcm^{-2}.*

the HRTEM of white clusters formed at 1.46 Jcm^{-2}. It can be seen from the inset image that the clusters composed of nanospheres of nearly 15 nm diameter which was amorphous in nature as no crystal plane was visible. Hence there is hardly any significant formation of nanocrystallites within the whitish clusters of all these samples. These results are consistent with those of Raman studies which claimed that whitish clusters are basically composed of a-Si: SiO_2. The Figure 3.9 (a) and Figure 3.9 (b) show the histograms depicting the particle size distribution estimated from TEM images of whitish clusters formed at laser fluences of (a) 1.46 and (b) 2.67 Jcm^{-2}. It has been observed that with increased laser fluences from 1.46 Jcm^{-2} to 2.67 Jcm^{-2}, the average size of spherical nanoclusters decreased from nearly 12 nm to 5 nm.

3.2.6 Photoluminescence studies of a-Si:SiO_2 nanostructures as a function of laser fluence :

The PL spectra of the whitish region of all the samples fabricated at different laser fluence are shown in *Figure 3.10*. The room temperature PL spectra for all these samples show an asymmetric broad luminescence band having peak at around 1.82 eV. The

TH-1680_10612114

multiple peak fitting of PL spectra using Gaussian lineshape function are shown in *Figure 3.10*. After de-convolution, two peaks could be clearly distinguished on each of these curves as shown in *Figure 3.11*, one is low energy peak (peak 1) ranging from 1.6 – 1.8 eV and other is high energy peak (peak 2) ranging from 1.6 – 2.4 eV. The low energy peak was less intense as compared to that at higher energy in each spectrum. From *Figure 3.12*, plot of PL peak energy as a function of laser fluence, it is observed that the low energy PL peak had undergone a slight blue shift from 1.66 to 1.75 eV with increasing laser fluence while that for high energy peak was relatively constant at around 1.83 eV for all fluence except for white clusters formed at 2.67 Jcm^{-2} for 3000 laser shots whose PL peak 2 was observed at 1.95 eV. The origin of PL in the present case could be two fold. The bulk a-Si gives a near-infrared PL around 1.3–1.4 eV at room temperature due to

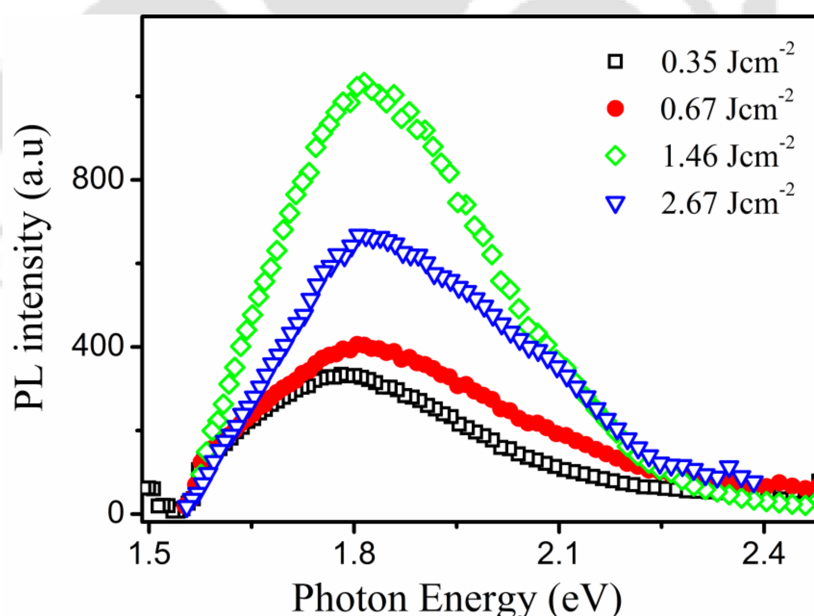

Figure 3.10 *RT Photoluminescence spectra of whitish clusters of a-Si:SiO$_2$ formed at different laser fluences~ 0.35 Jcm^{-2} (6000 shots), 0.67 Jcm^{-2} (6000 shots), 1.46 Jcm^{-2} (6000 shots), and 2.67 Jcm^{-2} (3000 shots).*

TH-1680_10612114

structural disorder and can get blue shifted to 2.7 eV in nanostructured form [21, 22]. The blue shift in peak 1 of the PL spectra of all the samples, w.r.t that of documented for bulk a-Si, is attributed to the nanostructured a-Si of size less than 20 nm as observed in TEM results (Figure 3.8) [23]. Unlike nc-Si, visible PL and related blue shift with decrease in size could not be explained by quantum confinement model in a-Si. This blue-shift in PL peak energy can be attributed to spatial confinement [22] in nanostructured a-Si clusters which depends on the statistical distribution of available bandtail states [3, 24]. With the

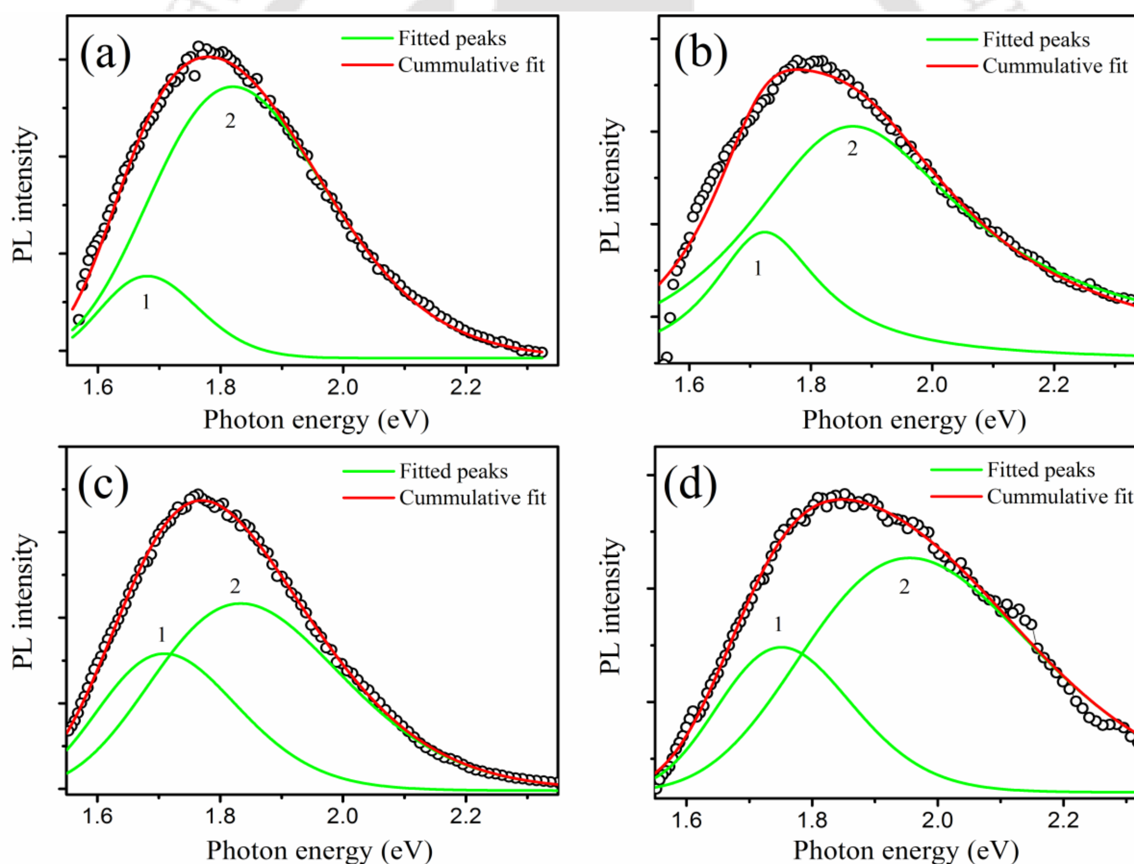

Figure 3.11 *Curve-fitted and de-convoluted RT Photoluminescence spectra of whitish clusters of a-Si:SiO_2 formed at different laser fluences (a) 0.35 Jcm^{-2} (6000 shots),(b) 0.67 Jcm^{-2} (6000 shots), (c) 1.46 Jcm^{-2} (6000 shots), and 2.67 Jcm^{-2} (3000 shots) showing two peak centers (in eV).*

TH-1680_10612114

reduction of the structure size, electron-hole (e-h) pairs get confined in a small dimension resulting in decrease of the available band-tail states. Hence, probability of e-h recombination is higher between the deeper states in the proximity to mobility edges of transition bands. Consequently, the lowest energy accessible for recombination of the e-h pairs is greater than that of bulk a-Si. The broad line width of the PL spectra, which were observed for all samples, could be mostly due to the statistical distribution of states in a-Si:SiO_2, though a distribution of structure sizes may also contribute further to broaden the peak [21]. Peak 1 also showed small but gradual blue shift with increase in laser fluence. A PL peak shift from 1.50 eV to 1.75 eV has been reported for a-Si spherical nanostructures of diameter from nearly 12 nm to 4 nm [22]. But in present case, PL peak is observed to be blue shifted from 1.71 eV to 1.75 eV for a-Si spherical nanostructures of average size of 12 nm and 5 nm formed in whitish clusters at laser fluence of 1.46 Jcm^{-2} and 2.67 Jcm^{-2} respectively. This reduction in particle size with increasing laser fluence can be explained in the following manner. At low laser fluence, the LPP was composed of less Si atoms while the plasma temperature and pressure were also low. So, the nucleation sites are very few. These nuclei continue to grow until nearby silicon clusters are completely consumed. The small number of nuclei formed accommodates all the surrounding Si clusters, forming large sized particles. With increase in laser fluence, plasma plume attains relatively high temperature and particle density resulting formation of large number of nucleation sites. Therefore, though there is an increment in Si atoms at high laser fluence the nucleation sites are too numerous, leading to formation of small sized nanostructures [25]. This decrease in size with laser fluence can also be explained in context of increase in O_2 content with laser energy. With the increase in laser fluence and subsequent oxidation of Si, oxygen content increases and more Si are consumed reducing

TH-1680_10612114

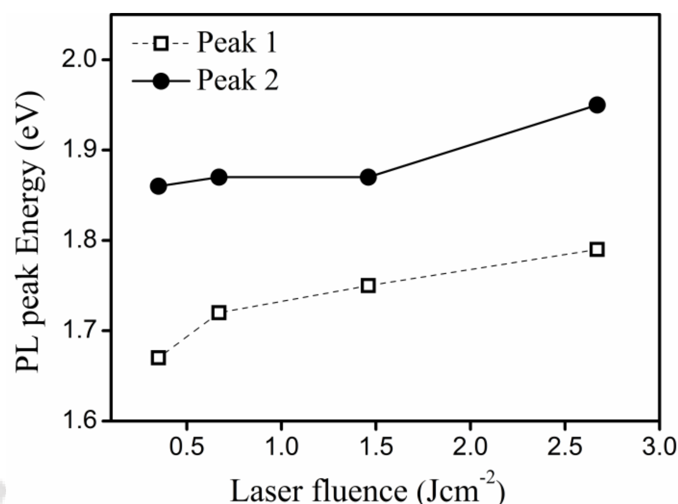

Figure 3.12 *Plot showing variation of PL peak energy of peak 1 (at low energy) and peak 2 (at high energy) versus increasing irradiating laser fluence.*

the size of a-Si clusters embedded in SiO_2 matrix. As the presence of SiO_2 is confirmed by EDX, FTIR and Raman spectra, the peak 2 in PL spectra could be due to oxygen defects [26]. Basically, excess O_2 and O_2 deficiency are major variety of oxygen defects which contribute to PL. The PL originating from oxygen deficient defect like ODC(I), ODC(II), E' center etc. were reported to have peak within 2.2-4.8 eV while excess oxygen related defect PL were reported to be observed between 1.8-2.0 eV [26, 27]. The PL spectra of white clusters for sample irradiated at laser fluence of 2.67 Jcm^{-2} showed high energy peaks (Peak 2) at 1.95 eV and that of other samples around 1.83 eV. The potential candidate for such PL could be the defect states like non-bridging oxygen hole center (NBOHC), interstitial O_2^-, O_3^- and their respective neutrals. NBOHC has absorption bands peaking at 1.97 and 4.8 eV while that of defect states due interstitial O, O_2 and O_3 is around 4.8 eV. So, as the excitation photon energy used in PL studies is 2.54 eV (488 nm) only, the probable reason for PL emission peaking around 1.83 eV could be

TH-1680_10612114

due to absorption of 2.54 eV photon resulting into electronic excitation to energy states formed by NBOHC defect corresponding to 1.97 eV absorption band and subsequent de-exitation from low lying emission level [26].

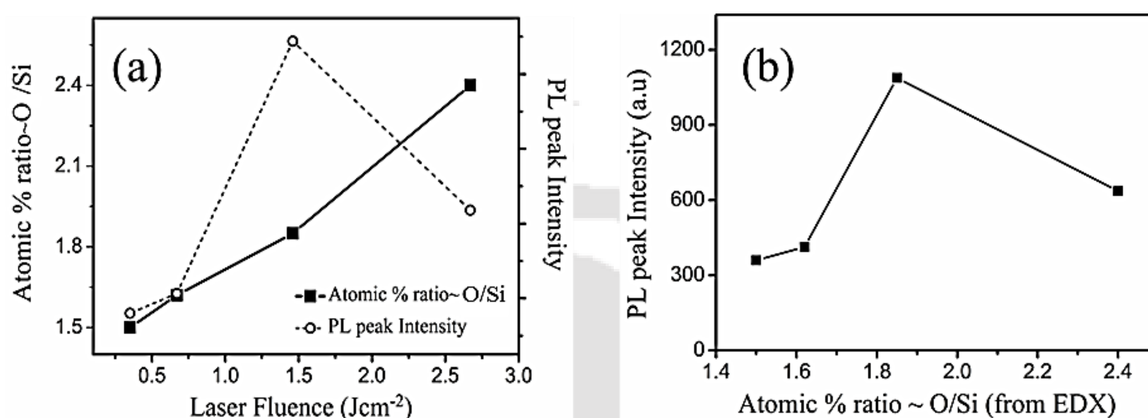

Figure 3.13 *(a) Variation of atomic percentage of O/Si (from EDX) and peak 2 PL intensity as a function of irradiating laser fluence and (b) variation in PL intensity of peak 2 as a function of atomic % of O/Si (from EDX).*

In *Figure 3.13(a)*, the variation of ratio of the atomic percentages of oxygen to silicon (O/Si) from EDX and PL intensity of peak 2 of white micro-clusters with increasing laser fluence are shown. The ratio of the atomic percentages of oxygen to silicon increased from nearly 1.52 to 2.4 with increasing laser fluence from 0.35 to 2.67 Jcm^{-2}. The increase in oxygen content with increasing laser fluence could be explained by the fact that with increasing laser fluence from 0.35 to 2.67 Jcm^{-2} the plasmas of Si and air get more ionized and denser enhancing the probability of oxidation of Si. The intensity of peak 2 is plotted as a function of O/Si from EDX in *Figure 3.13(b)*. It has been observed that PL intensity of peak 2 varies non- monotonically, first increased with increasing oxygen content in the a-Si:SiO_2 matrix and then decreased. With increasing laser fluence, deposited energy increases which may strain the undisturbed Si_2O_7 network

TH-1680_10612114

(≡Si─O─Si≡) finally breaking it to give ≡Si● (E' center) and ●O─Si≡ (NBOHC). The increased oxidation in a-Si:SiO_2 matrix with increasing laser fluence oxidizes ≡Si● to convert them into ●O─Si≡ creating additional NBOHC defects. This enhances the PL intensity with increasing laser fluence till 1.46 Jcm^{-2} [27, 28]. At 2.67 Jcm^{-2}, the oxidation of white clusters was too large that it might have passivated the defects reducing the PL intensity. Hence the origin of PL corresponding to peak 2 is attributed to electronic transition from states formed by NBOHC defects.

3.3 Conclusions

Micron sized amorphous silicon clusters embedded within SiO_2 matrix, a-Si:SiO_2, were fabricated by direct laser irradiation on crystalline Si target in air. The amorphous nature of the clusters was confirmed by Raman spectra as well as SAED patterns. Further both Raman and FTIR spectra showed the presence of a-Si and amorphous SiO_2. The EDX results showed increase of oxidation of Si with increasing laser fluence which is also confirmed by gradual increase in infrared absorption corresponding to Si-O-Si stretching vibration mode. These nanostructures exhibited an intense room temperature broad band PL ranging from 1.6 eV to 2.2 eV consisting of two peaks. The origin of luminescence in these structures is attributed to nanostructures of a-Si and NBOHC defects in SiO_2 matrix. This broad band luminescent property of a-Si: SiO_2 within visible range via such a simple fabrication technique may find applications in optoelectronic devices.

TH-1680_10612114

Bibliography

[1] A. Serpenguzel, A. Kurt, I. Inanc¸, J. Carey, E. Mazur, Luminescence of Black Silicon, Journal of Nanophotonics, 2 (2008) 021770-021770-021779.

[2] C. Wu, C.H. Crouch, L. Zhao, E. Mazur, Visible Luminescence from Silicon Surfaces Microstructured in Air, Applied Physics Letters, 81 (2002) 1999-2001.

[3] T.K. Chini, D.P. Datta, S. Facsko, A. Mücklich, Room Temperature Photoluminescence from the Amorphous Si Structure Generated under keV Ar-ion-induced Surface Rippling Condition, Applied Physics Letters, 92 (2008) 101919.

[4] B. Zeng, G. Xiong, S. Chen, S.H. Jo, W.Z. Wang, D.Z. Wang, Z.F. Ren, Field Emission of Silicon Nanowires, Applied Physics Letters, 88 (2006) 213108.

[5] K. Lilienthal, M. Fischer, M. Stubenrauch, A. Schober, Self-organized Nanostructures in Silicon and Glass for MEMS, MOEMS and BioMEMS, Materials Science and Engineering: B, 169 (2010) 78-84.

[6] V.T. Vu, D.C. Nguyen, H.D. Pham, A.T. Chu, T.H. Pham, Fabrication of a Silicon Nanostructure-based Light Emitting Device, Advances in Natural Sciences: Nanoscience and Nanotechnology, 1 (2010) 025006.

[7] F. Gourbilleau, X. Portier, C. Ternon, P. Voivenel, R. Madelon, R. Rizk, Si-rich/SiO_2 Nanostructured Multilayers by Reactive Magnetron Sputtering, Applied Physics Letters, 78 (2001) 3058.

[8] P. Photopoulos, A.G. Nassiopoulou, Photoluminescence from SiO_2 /Si/SiO_2 Structures, Journal of Physics: Condensed Matter, 15 (2003) 3641.

[9] D. Riabinina, C. Durand, J. Margot, M. Chaker, G.A. Botton, F. Rosei, Nucleation and Growth of Si Nanocrystals in an Amorphous SiO_2 matrix, Physical Review B, 74 (2006) 075334.

[10] X.Y. Chen, Y.F. Lu, Y.H. Wu, B.J. Cho, W.D. Song, D.Y. Dai, Optical Properties of SiO_x Nanostructured Films by Pulsed-laser Deposition at Different Substrate Temperatures, Journal of Applied Physics, 96 (2004) 3180.

[11] M. Li, Y. Li, W. Liu, L. Yue, R. Li, Y. Luo, M. Trevor, B. Jiang, F. Bai, P. Fu, Y. Zhao, C. Shen, J.M. Mbengue, Metal-assisted Chemical Etching for Designable Monocrystalline Silicon Nanostructure, Materials Research Bulletin, 76 (2016) 436-449.

[12] C. Smit, R.A.C.M.M. van Swaaij, H. Donker, A.M.H.N. Petit, W.M.M. Kessels, M.C.M. van de Sanden, Determining the Material Structure of Microcrystalline Silicon from Raman Spectra, Journal of Applied Physics, 94 (2003) 3582-3588.

[13] J. Won Dong, M.O. Ramirez, H. Kang, V. Gopalan, N.F. Baril, J. Calkins, J.V. Badding, P.J.A. Sazio, All-optical Modulation of Laser Light in Amorphous Silicon-filled Microstructured Optical Fibers, Appl. Phys. Lett., 91 (2007) 161112.

[14] M. Benyoucef, M. Kuball, J.M. Sun, G.Z. Zhong, X.W. Fan, Raman Scattering and Photoluminescence Studies on Si/SiO_2 Superlattices, Journal of Applied Physics, 89 (2001) 7903.

TH-1680_10612114

[15] B. Tan, K. Venkatakrishnan, A Femtosecond Laser-induced Periodical Surface Structure on Crystalline Silicon, Journal of Micromechanics and Microengineering, 16 (2006) 1080.

[16] J. Siegel, J. Solis, C.N. Afonso, C. García, Bulk solidification and recalescence phenomena in amorphous Ge films upon picosecond pulsed laser irradiation, Journal of Applied Physics, 80 (1996) 6677-6682.

[17] T. Sameshima, S. Usui, Mechanism of Pulsed Laser-induced Amorphization of Silicon Films, Applied Physics Letters, 59 (1991) 2724-2726.

[18] G. Kurumurthy, K.S. Alee, D.N. Rao, Photoluminescence Studies of Si/SiO_2 Nanoparticles Synthesized with Different Laser Irradiation Wavelengths of Nanosecond Pulse Duration, Optics Communications, 282 (2009) 3509-3512.

[19] Y. Borodko, J.W. Ager, G.E. Marti, H. Song, K. Niesz, G.A. Somorjai, Structure Sensitivity of Vibrational Spectra of Mesoporous Silica SBA-15 and Pt/SBA-15, The Journal of Physical Chemistry B, 109 (2005) 17386-17390.

[20] J.A.L. Lopez, J.C. Lopez, D.E.V. Valerdi, G.G. Salgado, T. Diaz-Becerril, A.P. Pedraza, F.J.F. Gracia, Morphological, Compositional, Structural, and Optical Properties of Si-nc Embedded in SiO_x Films, Nanoscale Res Lett, 7 (2012) 1-10.

[21] C. Tsang, R.A. Street, Recombination in Plasma-deposited Amorphous Si:H. Luminescence Decay, Physical Review B, 19 (1979) 3027-3040.

[22] M.J. Estes, G. Moddel, A Model of Size-dependent Photoluminescence in Amorphous Silicon Nanostructures: Comparison with Observations of Porous Silicon, Applied Physics Letters, 68 (1996) 1814-1816.

[23] C.X. Wang, P. Liu, H. Cui, G.W. Yang, Nucleation and Growth Kinetics of Nanocrystals Formed upon Pulsed-laser Ablation in Liquid, Applied Physics Letters, 87 (2005) 201913.

[24] R.B. Wehrspohn, J.-N. Chazalviel, F. Ozanam, I. Solomon, Spatial versus Quantum Confinement in Porous Amorphous Silicon Nanostructures, The European Physical Journal B - Condensed Matter and Complex Systems, 8 (1999) 179-193.

[25] P. Chewchinda, T. Tsuge, H. Funakubo, O. Odawara, H. Wada, Laser Wavelength Effect on Size and Morphology of Silicon Nanoparticles Prepared by Laser Ablation in Liquid, Japanese Journal of Applied Physics, 52 (2013) 025001.

[26] R. Salh, Defect Related Luminescence in Silicon Dioxide Network: a Review, in: S. Basu (Ed.) Crystalline Silicon - Properties and Uses, InTech, Rijeka, 2011, pp. 135-172.

[27] L. Skuja, Optically Active Oxygen-deficiency-related Centers in Amorphous Silicon Dioxide, Journal of Non-Crystalline Solids, 239 (1998) 16-48.

[28] L. Skuja, Time-resolved Low Temperature Luminescence of Non-bridging Oxygen Hole Centers in Silica Glass, Solid State Communications, 84 (1992) 613-616.

TH-1680_10612114

Chapter 4

Fabrication and Characterization of PLD Si and SiOx films

The thin films of Silicon (Si) and non stoichiometric silicon oxide (SiO_x) are nowadays an indispensable part of optoelectronics, photovoltaic, optical and non-linear optical (NLO) devices [1-5]. The band gap of nanocrystalline Si (nc-Si) thin films depends on crystallite size due to quantum confinement (QC) effect and hence photoluminescence emission from it can be tuned over a wide range of visible spectrum [2]. The SiO_x ($0 \leq x \leq 2$) films generally contain nc-Si embedded in a silicon oxide (SiO_2) matrix and hence also termed as nc-Si:SiO_2. The structural, optical and NLO properties of these films can be modulated by controlling the oxygen content (x) as well as the size of the nanocrystallites embedded in it [3]. It is foreseen as a potential candidate for the fabrication of light-emitting silicon-based devices [6]. The SiO_x layers have been used as protective coatings on metallic mirrors, antireflection coatings and low refractive index layers in the mid infrared spectral range [7-9]. It can also be used as insulating dielectric films, passivation layers, and interlayers in microelectronic devices [10, 11]. The thin films of Si and SiO_x have been fabricated by thermal or e-beam evaporation [12, 13], R.F. sputtering [14, 15], chemical vapor deposition [16, 17], pulsed laser deposition (PLD) techniques etc. [18, 19]. Among all the deposition techniques, PLD offers the advantages of fabrication of stoichiometric as well as non-stoichiometric thin films in a single step by controlling the deposition parameters. It does not require any hazardous gas and hence environmental friendly.

In this chapter fabrication and characterization of Si and SiO_x semiconductor thin films via PLD technique are presented. The effect of substrate temperature and O_2 ambient pressure on the stoichiometry and crystallinity, which in turn control their

TH-1680_10612114

structural as well as optical properties are studied. The room temperature (RT) photoluminescence properties of SiO_x films and their possible origins are also investigated.

4.1 Experimental Details:

The Si films were deposited by PLD technique onto Corning glass by varying substrate temperatures; RT, 200 ^{0}C, 400 ^{0}C, 600 ^{0}C and 700 ^{0}C. A pulsed high power Q-switched Nd:YAG laser (532 nm, 10 ns duration, 10 Hz) was focused, to provide a laser fluence of 2.5 J/cm^2, onto the Si (100) target under vacuum (~10^{-6} mbar) for depositing the films as discussed in section 2.2 of *Chapter 2*. The films were deposited for 30 minutes duration. SiO_x films were fabricated onto glass substrate via reactive PLD by ablating a c-Si target under oxygen ambient at deposition pressures of 10^{-4}, 10^{-3}, 10^{-2} and 0.5 mbar at a constant substrate temperature of 400 °C, keeping other deposition parameter fixed and are listed in *Table 4.1*. All these samples were characterized by XRD for analyzing their crystallinity using the Cu K_α line at a glancing incidence angle of 1.5°. The 2θ was scanned in between 20° and 70° in an angular step of 0.03°. The Raman spectra of Si and SiO_x thin films were recorded using micro-Raman setup in back scattering geometry. The 488 nm line of Ar ion laser was used as an excitation source. The Raman mapping was performed by scanning over an area of 30×30 μm^2 with a step size of 1×1 μm^2 area. The UV-Vis-NIR transmission spectrum of the films was recorded in the wavelength range from 200 to 3000 nm. The Swanepoel's envelop method was used to estimate the refractive index (n) and thickness of the films as described in *Chapter 2* [20]. The thickness of the thin films was also measured by stylus profilometer for comparison. The optical band gap of the films was estimated using Tauc plot after calculating absorption co-efficient from their respective UV-Vis-IR transmission spectra.

TH-1680_10612114

The Si films were also been subjected to ellipsometric measurements and the results are compared with that of obtained from UV-Vis-NIR spectra. SEM and EDX of SiO_x films were performed for the surface morphology as well as the compositional analysis, respectively. In addition, the steady-state PL spectra of the SiO_x films were recorded at RT using a commercial fluorimeter (Thermo Spectronic, *FA-357*) equipped with charge coupled detector. A diode laser providing wavelength of 405 nm is used as excitation source. The high-magnification surface morphologies and structures of the samples were studied by TEM, UHRTEM and SAED pattern.

4.2 Effect of substrate temperature and O_2 pressure on Si-based thin films via PLD:

The range of deposition parameters over which Si and SiO_x films were fabricated are listed in *Table 4.1*. In the following subsections the effect of substrate temperature and oxygen gas pressure is detailed.

Table 4.1: *Deposition parameters for the fabrication of Si-based films:*

Laser fluence (Jcm^{-2})	Deposition duration (min)	Ambient pressure (mbar)/type	Substrate temperature (°C)	Substrate
2.5	30	~10^{-6}	RT	Corning glass
			200	
			400	
			600	
			700	
		10^{-4}/ O_2	400	Glass (microscopic slide)
		10^{-3}/ O_2		
		10^{-2}/ O_2		
		10^{-1}/ O_2		
		0.5/ O_2		

TH-1680_10612114

4.2.1 Effect of substrate temperature on the properties of Si films:

The substrate temperature (T_s) controls the surface energy during nucleation of film and hence its variation may play a vital role in shaping up the structural and corresponding optical properties of Si films. Hence Si films were initially fabricated as a function of T_s. The Si films were deposited on Corning glass substrate at various T_s; RT, 200 °C, 400°C, 600 °C and 700 °C. The other deposition parameters were kept fixed and are listed in *Table 4.1*.

4.2.1.1 Structural properties of nc-Si thin films:

Figure 4.1 shows the XRD spectra of the Si thin film deposited at various T_s from RT to 700 °C. All the samples exhibited characteristic XRD peaks for the Si (111), Si (220) and Si (311) planes at 2θ ~ 28.45˚, 47.37˚ and 56.2˚, respectively [21]. It was observed that intensity of these peaks showed non-monotonous behavior as a function of T_s, initially increasing with T_s from RT to 400 °C and thereafter slightly decreased with increasing T_s till 700 °C. Figure 4.1 (b) exhibits the plot of integrated intensity for XRD peaks corresponding to Si (111), Si (220) and Si (311) as a function of T_s, indicating the

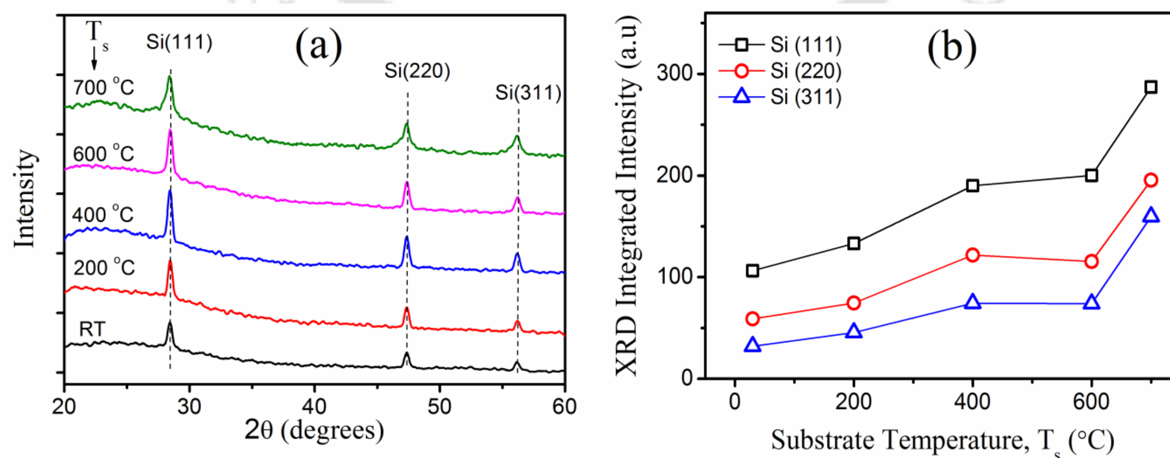

***Figure 4.1** (a) XRD spectra of the substrate and PLD nc-Si thin films fabricated at different T_s and (b) Plot of integrated intensity of respective peaks as a function of T_s.*

TH-1680_10612114

Table 4.2 *XRD peak positions, corresponding FWHMs and respective Si crystallite size for the Si thin films as a function of T_s.*

Substrate Temperature, T_s (^oC)	Si[111]		Si[220]		Si[311]		D_{ds} (nm), (Debye-Scherrer's)
	Peak position (˚)	FWHM (˚)	Peak position (˚)	FWHM (˚)	Peak position (˚)	FWHM (˚)	
RT	28.43	0.43	47.35	0.46	56.18	0.51	19.0
200	28.45	0.38	47.35	0.42	56.20	0.46	21.5
400	28.43	0.40	47.35	0.44	56.18	0.50	20.5
600	28.46	0.44	47.36	0.46	56.20	0.54	20.5
700	28.42	0.54	47.33	0.64	56.12	0.79	13.5

increase in crystallinity of the films with increasing T_s. The peak positions and corresponding full width half maxima (FWHM) of all the XRD peaks of the films deposited as a function of T_s are listed in *Table 4.2*. The average crystallite size (D_{ds}) was calculated from the prominent Si [111] peak and using Debye-Scherrer's formula, $D_{ds} = \frac{K\lambda}{\beta_{hkl} cos\theta}$, where K is the shape factor (0.9), β_{hkl} is the FWHM of XRD peak and λ is the wavelength of $Cu\text{-}k_{\alpha}$ radiation used for recording XRD spectra. The values of D are also listed in *Table 4.2*.

Figure 4.2 (a) shows microscopic images (30μm × 30μm) of Si thin films deposited at T_s = 400 ^0C. It clearly exhibits the formation of localized micron sized clusters against uniform background. In the PLD technique, the laser ablated material comprising of laser induced plasma (LIP) of target material (Si plasma in present case) was formed along with the direct ejection of molten droplets. The LIP of Si target, containing Si ions, neutrals and electrons, expands and cools down to finally deposit on the substrate rendering the smooth background of the film. The molten droplets deposited directly on the substrate appear in the form of micron sized clusters against uniform background [22, 23]. To unveil the structural inhomogeneity of the localized clusters and the background of the film, Raman map was recorded. *Figure 4.2 (b)* exhibits the Raman

TH-1680_10612114

map of 30μm × 30μm region of Si thin films. The Raman map was recorded over two different ranges; Raman shift from 500 - 525 cm^{-1} represented in green colour and that of 460-490 cm^{-1} in black colour. It is very clear that the Raman shift of the clusters lies in former range while that of the background in the later range. *Figure 4.2 (c)* shows the respective Raman spectra of both the regions, clusters in green and background in black for Si thin films deposited at T_s= 400°C. The Raman spectrum of cluster within the film shows a sharp highly intense peak at 520.5 cm^{-1}. The peak is asymmetric toward lower wavenumber side and red shifted w.r.t that of bulk c-Si at 521 cm^{-1} and hence is a feature of nanocrystalline Si. It arises from the first-order Raman scattering of the longitudinal optical (LO) and the transverse optical (TO) phonon modes which are degenerate at the Brillouin zone center [24, 25]. The Raman spectrum of the film background, *Figure 4.2 (c)*, (black in colour) displays one prominent band (400-550 cm^{-1}) with a highly intense peak around 480 cm^{-1} and shoulders toward the lower wavenumber (350-400 cm^{-1}). Another relatively less intense broad band in the range of 100-280 cm^{-1} having peak around 160 cm^{-1} has also been observed. These bands corresponds to Raman active TO, LO, longitudinal acoustic (LA) and transverse acoustic (TA) (marked in figure) phonon modes of amorphous Si (a-Si) [25]. Hence from the Raman studies it can be inferred that

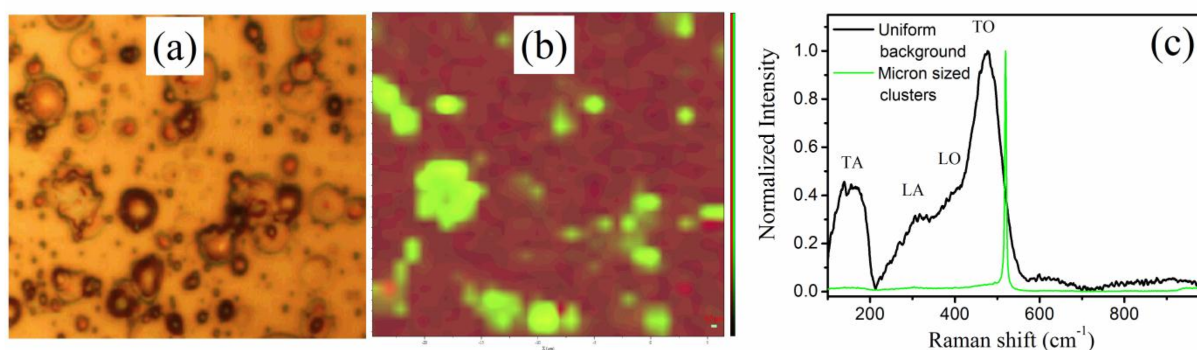

Figure 4.2 *(a) Optical micrograph images (30μm × 30μm), (b) corresponding Raman mapping and (c) Raman spectra of micron sized clusters and background of nc-Si thin film deposited at T_s of 400 °C.*

TH-1680_10612114

the thin films were composed of clusters of nc-Si embedded in otherwise uniform background of a-Si. The Raman maps of all the other films also exhibited similar behavior. *Figure 4.3(a-e)* shows the (i) optical micrograph images, (ii) Raman spectra of micron sized clusters and (iii) Raman spectra of background of the Si thin films deposited at T_s of (a) RT, (b) 200 ˚C, (c) 400 ˚C, (d) 600 ˚C and (e) 700 ˚C, respectively. The microscopic images, *Figure 4.3 (a-i) - (e-i)*, of all the samples displayed the micron sized clusters embedded in smooth background. The Raman spectra of the clusters within each film, *Figure 4.3 (a-ii) – (e-ii)*, exhibited a sharp highly intense peak asymmetric towards lower wavenumber side and was red shifted w.r.t. the peak arising at 521 cm^{-1} for that of bulk c-Si indicating the feature of nc-Si [26]. In addition, the Si films deposited at RT and 700 ˚C (*Figure 4.3a-ii and 4.3e-ii*), shows the presence of weak broad peaks corresponding to TA, LA, LO and TO Raman modes of amorphous Si within the clusters. The Raman spectra of the background, *Figure 4.3 (a-iii)-(e-iii)*, were de-convoluted into multiple peaks using Gaussian lineshape to analyze different bonding structures in the thin films. The de-convoluted spectra showed the presence of broad peaks corresponding to longitudinal acoustic (LA), transverse acoustic (TA), LO, TO and 2-LA phonon modes of a-Si in all the samples [24, 25]. The corresponding peak positions are mentioned in the respective figures. The film deposited at T_s of 700 ˚C showed a sharp intense peak at 519.2 cm^{-1} corresponding to nc-Si [26]. This red shift of 1.8 cm^{-1}, w.r.t. Raman modes of c-Si, was used to estimate the average cryatal size of nc-Si present in this film and was found to be ~ 5.3 nm [26]. This nano-crystalline feature depicted by background matrix of this particular film could be due to the crystallization of Si from LIP forming the background region which is fabricated at high substrate temperature. At higher substrate temperature, the surface energy was sufficiently high, providing required surface mobility to the adatoms so that they can diffuse through several atomic distances before sticking to

TH-1680_10612114

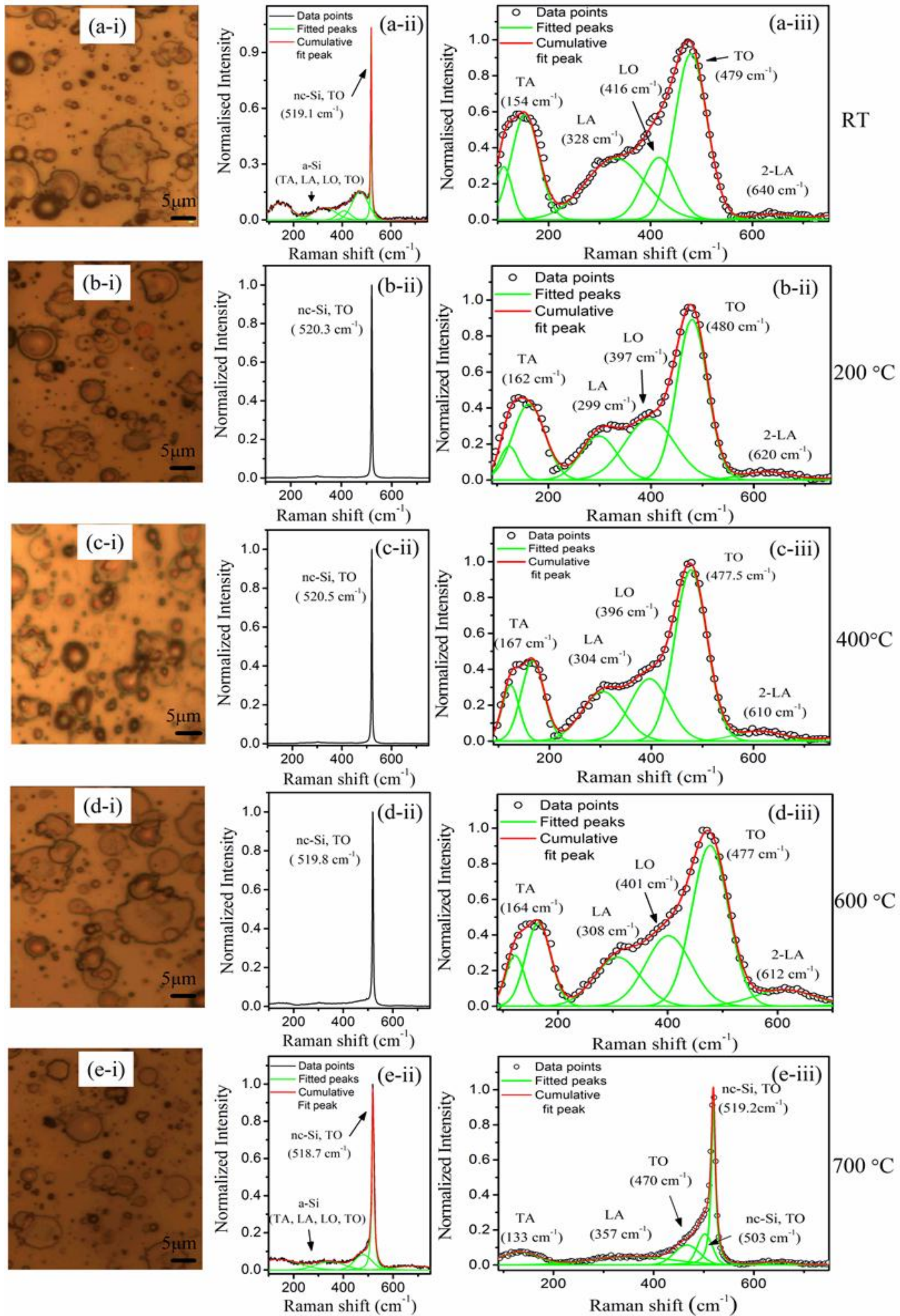

Figure 4.3 *(i) Optical micrograph, (ii) Raman spectra of micron sized crystalline clusters and (iii) Raman spectra of background amorphous matrix along with respective de-convoluted spectra of the PLD nc-Si thin films deposited at T_s of (a) RT, (b) 200 ˚C, (c) 400 ˚C, (d) 600 ˚C and (e) 700 ˚C.*

TH-1680_10612114

stable positions making long range ordered structures enhancing crystalline growth of the film.

4.2.1.2. Linear optical properties of Si thin films:

The UV-Vis-NIR transmission spectra of the Si films deposited at RT and other elevated T_s of 200 ˚C, 400 ˚C, 600 ˚C and 700 ˚C are shown in *Figure 4.4*. The transmission spectra of all the films exhibited interference fringes in far red to NIR spectral range and sharp absorption edge in the wavelength range of 500-750 nm. The Swanepoel's envelop method was employed for estimation of thickness, refractive index and absorption coefficient of these thin films [20]. In this method, two curves joining the transmission maxima (T_{max}) and transmission minima (T_{min}) in the transmission spectra are interpolated to get the values of T_{max} and T_{min} as a function of wavelength (λ) as described in section 2.2.9 of *Chapter 2*. The refractive index n for the Si films was calculated using the equation 2.1 [20], where n is a function of T_{max} and T_{min}. These calculated values of n as a function of λ (at transmission maxima and minima) were fitted

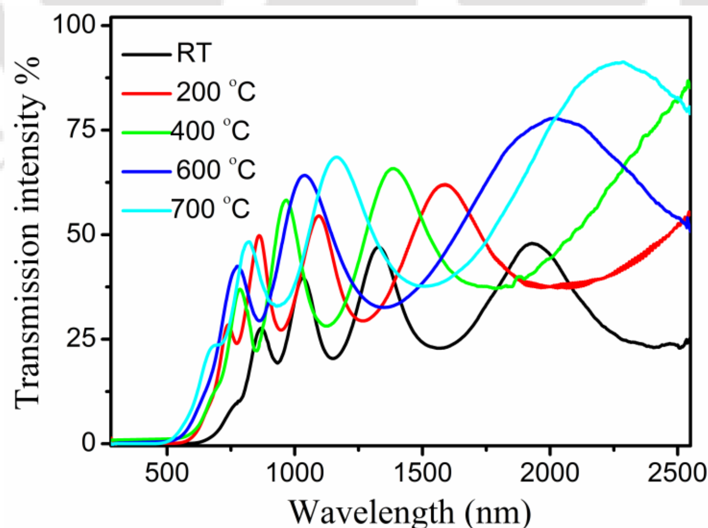

Figure 4.4 *UV-Vis-NIR Transmittance spectra of SiO_x thin films deposited at different T_s.*

TH-1680_10612114

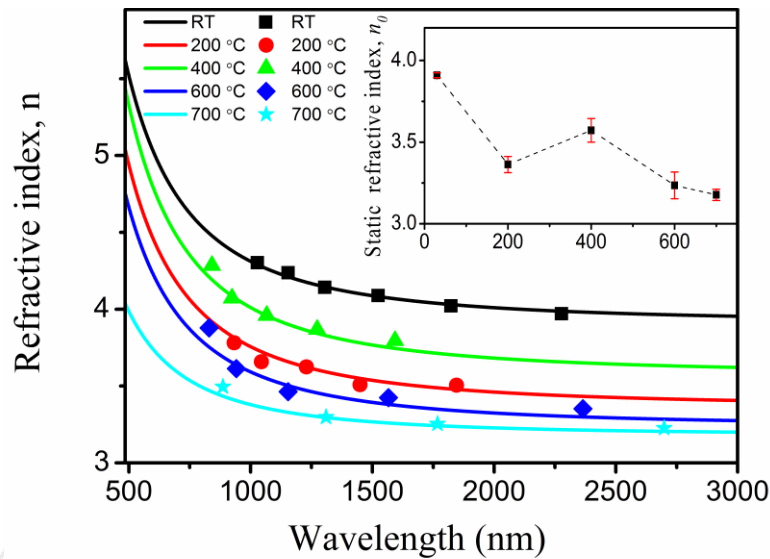

Figure 4.5 *Plot of refractive index as a function of wavelength for nc-Si films deposited at different T_s. Inset shows static refractive indices (n_0) for nc-Si thin films deposited as a function of T_s.*

to Cauchy dispersion relation (equation 2.3). The *n* was plotted as a function of wavelength in the region 500-3000 nm for each film and is shown in *Figure 4.5*. In this figure, the symbols represent the values of the *n* estimated from envelop method (equation 2.1) while the continuous line corresponds to the respective fitted curves using Cauchy dispersion relation (equation 2.3). The values of refractive index decrease with the increasing wavelength thus displaying normal dispersion behavior. The inset of *Figure 4.5* shows the variation of static refractive index, n_0 (Cauchy parameter, A_0) as a function of deposition temperature from RT to 700 ˚C. It showed that the n_0 of the film deposited at RT was found to be around 3.9 while that for films fabricated at elevated temperatures it decreased to around 3.4 for 250 ˚C. Thereafter it slightly rises to 3.6 for 400 ˚C film and then finally decreases to 3.3 for the film deposited at 700 ˚C [27]. The static refractive index of a-Si films has been reported to be in the range of 3.5-4.5 and that of polycrystalline Si films to be ~ 3. For nc-Si films it varies from ~ 2.8 to 4 depending on the proportion of amorphous content in these films [28, 29]. Thus, the

TH-1680_10612114

higher value of n_0 observed for the film deposited at RT is due to higher amorphous content as compared to those of other films. The film deposited at 700 ˚C exhibited minimum refractive index as the film was composed of nc-Si only as indicated in its Raman spectrum (*Figure 4.3-e*). The thickness (d) of the films was calculated by Swanepoel's envelop method using the equation 2.4 [15]. The thickness of films, d_{step}, was also measured using step profilometer and found to be nearly similar to that of estimated with envelop method. The d for all these films deposited at T_s of RT, 200, 400, 600 and 700 ˚C were found to be nearly 480, 448, 363, 300 and 348 nm, respectively. It is also observed that with increase in T_s from RT to 600 ˚C, the film thickness estimated from envelop method gradually decreases from around 480 nm to 300 nm and then slight increases to 348 nm with further increase in T_s to 700 ˚C. The decrease in film thickness with increasing T_s from RT to 600 ˚C could be due to temperature dependent erosion. The surface adatoms created by the particle bombardment from laser induced plasma are much loosely bounded to the surface compared to that of existing within a lattice structure. Hence they are more likely to effuse out at a temperature lower than actual sublimation temperature of the material [30]. The erosion rate increases with the increasing substrate temperature and results in subsequent thinning of the deposited film [31]. The absorption coefficient of these films was estimated from equation 2.7. The variation of $(\alpha h\nu)^{1/2}$ versus $h\nu$ for all the films were plotted in *Figure 4.6*. The optical band gap, E_g was obtained from the intercept of the linear region of this plot on the $h\nu$ axis. The inset of *Figure 4.6* displays the variation of E_g as a function of substrate temperature. The band gap was observed to be decreasing from 1.35 eV to 1.31 eV for films fabricated from RT to T_s= 400 ˚C and then increased to 1.56 eV at T_s of 700 ˚C. The presence of nc-Si clusters as well as a-Si matrix in the Si films, as confirmed by Raman studies, can affect the band structure of these thin films. This variation can be

TH-1680_10612114

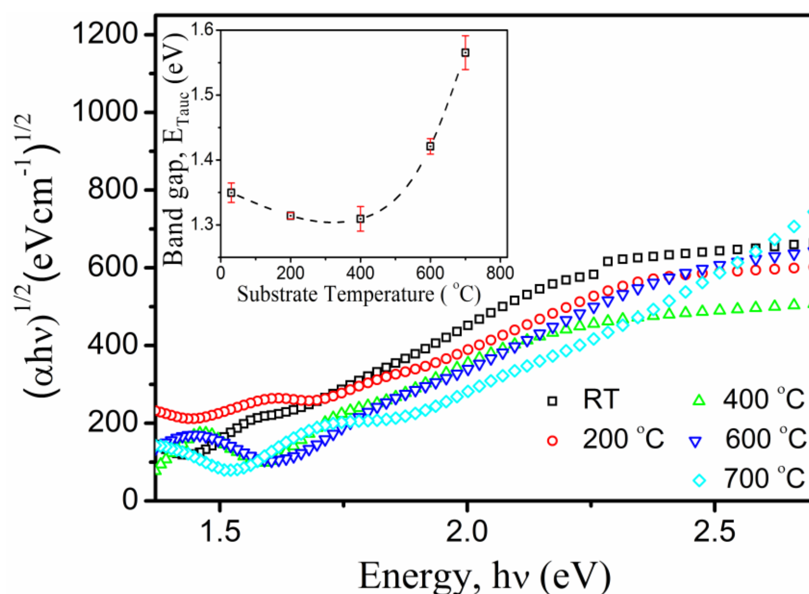

***Figure 4.6** Tauc plots for determining optical band gap of nc-Si films and the inset shows the variation of optical band gap (E_g) of the films with increasing T_s.*

explained in terms of crystallinity of the films. The bulk crystalline Si has an optical band gap of around 1.12 eV and that of bulk a-Si varies from 1.4-1.6 eV [32]. With increase in T_s from RT to 400 ˚C, the crystallinity increased and hence band gap drops from 1.35 eV to 1.31 eV. But with further increase in T_s, crystallinity decreased resulting in the increase in band gap. The band gap of Si film fabricated at 700 ˚C was observed to be around 1.56 eV which is close to the band gap of ~1.53 eV arising from quantum confined nc-Si of average size of 5.3 nm as estimated from Raman studies [33].

The PLD Si films were also subjected to spectroscopic ellipsometer which measures the pseudo dielectric function, ε, in terms of ellipsometric parameters; ρ, ψ and Δ as described in section 2.2.10 of *Chapter 2* of the present thesis. The real and imaginary parts, ε_1 and ε_2 of ε are determined by suitable structured dispersion model from which the refractive index, extinction coefficient, optical band gap and layer thickness are determined. In the present work, the fitting of ε_1 and ε_2 spectra of these Si films was

TH-1680_10612114

performed by considering a two layered structure with a perfectly flat top surface composed of silicon oxide (SiO_2) and a thick main dispersion layer of Si having Tauc gap (E_g) grown onto corning glass (SiO_2) substrate for each samples. Several dispersion laws were used for the main thin film layer in order to fit the ε_1 and ε_2 spectra with minimum RMSE values. Finally a model having a combination of dispersion laws of TL and Lorentz, depicted by equation 2.15, gave the best fit for Si films. *Figure 4.7(a)* and *4.7(b)* shows the real and imaginary part of the measured and fitted pseudo-dielectric function, ε_1 and ε_2 spectra w.r.t the photon energy (E) in the range of 1.4–5.0 eV for Si films deposited at various T_s measured by SE at $\varphi = 70^\circ$. The experimentally measured ε_2 spectra of Si thin films deposited at T_s of RT and 400 ºC display a broad peak around 3.3 eV and 3.35 eV, respectively. This broad distribution of ε_2 spectra with maximum photon energy at around 3.2-3.6 eV is a feature of *a*-Si [34]. There is a marked increase in peak value of ε_2 for the film deposited at 400 °C as compared to that of at RT, indicating the reduction in void formation at elevated temperature within the a-Si structure. In contrast to these two samples, film deposited at 700 ºC displays two broad peaks at photon energy of 3.3 eV and 4.1 eV in ε_2 spectra confirming its polycrystalline nature having micron- or nano-sized crystallites [34]. These peaks are attributed to a convolution of direct electronic transitions in Si resulting optical absorption in the UV region [34]. The fitted parameters, thicknesses of top surface layer of SiO_2 and main layer of Si, optical band gap (along with that of obtained via UV-vis-NIR spectra), refractive index, values of RMSE and regression coefficient R^2 are listed in *Table 4.3*. The E_g estimated from UV-Vis-NIR spectra is in good agreement with SE results. The film thickness obtained from both SE and profilometer are also in good agreement. The R^2 value for film deposited at 700 °C is below 0.9. Also the fitted curve for this particular sample is deviated from the experimental one. This is due to the presence of mixed phases of a-Si and polycrystalline

TH-1680_10612114

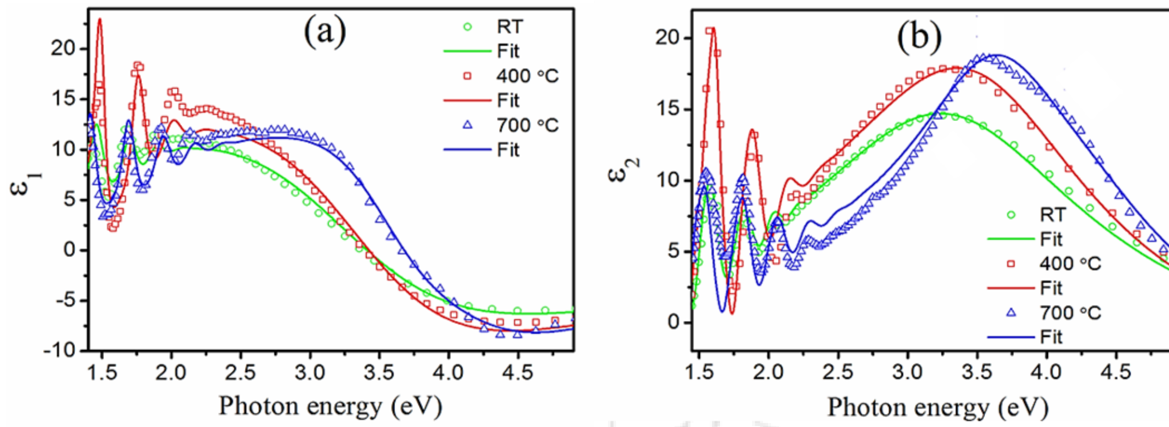

Figure 4.7 *Measured ellipsometric spectra for (a) real (ε_1) and (b) imaginary (ε_2) parts of dielectric functions of Si films deposited at various T_s. The solid lines depict the fitted curves.*

Table 4.3 *Measured film thickness and optical properties of thin Si films measured by means of SE and compared with other relevant techniques.*

Substrate Temperature, T_s (°C)	SE		Film thickness, d_{step} (using profilometer) (nm)	Optical Band gap, E_g (eV)		Refractive index, *n* (λ = 632 nm) SE	Errors	
	SiO_2 surface layer thickness (nm)	Bulk layer thickness (nm)		SE	UV-Vis-NIR		RMSE	R^2
RT	2.8	476	452-468	1.34	1.35	4.76	0.9	0.96
400	3.6	358	355-368	1.25	1.26	4.64	1.3	0.95
700	3.6	348	350-361	1.52	1.56	4.07	1.9	0.87

Si in the sample. Therefore, the numerical simulations of ε_1 and ε_2 spectra for the sample deposited at 700 °C were performed using BEMA. In this, the two layered structure similar to that of above was assumed. For the intermediate bulk layer, the effective complex dielectric function, ε, of the total system was assumed to be composed of *n* number of phases mixed together and are modeled in BEMA as, $\sum_{i=1}^{n} f_i \frac{\varepsilon_i - \varepsilon}{\varepsilon_i + 2\varepsilon} = 0$, where ε_i and f_i are the dielectric function and volume fraction of phases *i* [35, 36]. In the present

TH-1680_10612114

case, there are two phases; i=1 for a-Si (amorphous Si) and i=2 for poly-Si (polycrystalline Si). *Figure 4.8(a)* and *4.8(b)* shows the real and imaginary part of the pseudo-dielectric function, ε_1 and ε_2 spectra, along with BEMA fitted curves, for Si films deposited at 700°C measured by SE at φ = 65 ˚, 70˚ and 75˚ within the photon-energy range of 2.5–5 eV. The layered structure used in BEMA modeling is depicted in the inset of *Figure 4.8 (a)* where the thickness of each layer and respective refractive index at λ=632 nm as obtained via BEMA are also mentioned. The thickness of the top SiO_2 layer was ~1.47 nm and that of intermediate layer was ~ 340 nm which matches with that of obtained by profilometer listed in *Table 4.3*. These three spectra, for φ = 65 ˚, 70˚and 75˚, were simultaneously fitted to minimize error, thus RMSE and R^2 values in this case are 0.3 and 0.99, respectively confirming the good agreement with the experimental data.

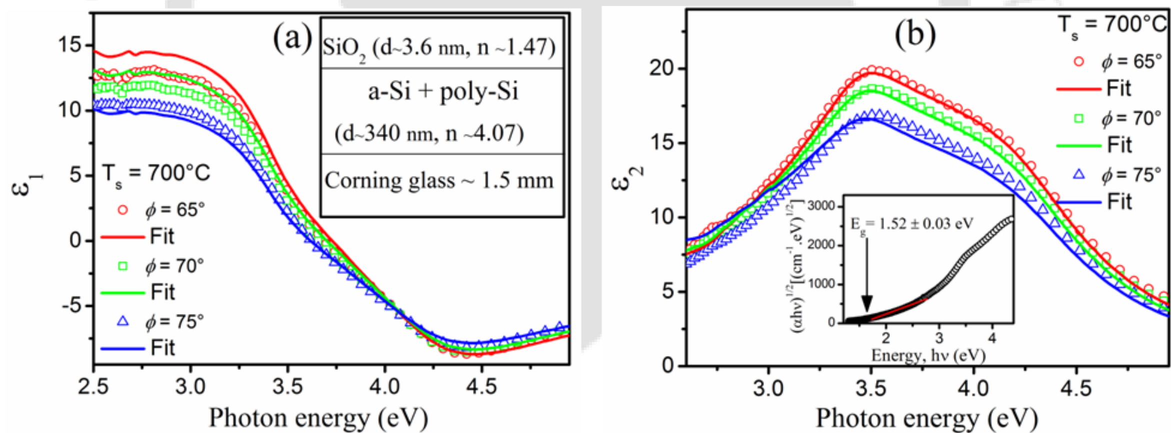

Figure 4.8 *Measured ellipsometric spectra for (a) real (ε_1) and (b) imaginary (ε_2) parts of dielectric functions of Si film deposited at 700 °C at different angle of incidence, Φ = 65°, 70° and 75°. The solid lines depict the fitted curves using BEMA. Inset of figure (a) and (b) show the layered structure used in BEMA modeling and Tauc plot of α (hν) estimated using BEMA, respectively.*

Using BEMA the constituent concentration of a-Si and poly-Si, i.e. $f_{a\text{-}Si}$ and $f_{p\text{-}Si}$, were evaluated and found to be 0.2 and 0.8, respectively. The inset of the *Figure 4.8 (b)* shows the Tauc plot for α ($h\nu$), estimated from values of k ($h\nu$) calculated from best fitted ε_1 and

TH-1680_10612114

ε_2 spectra using BEMA. The optical band gap of the Si film fabricated at T_s of 700°C was found to be ~ 1.52±0.03 eV which is again nearly in agreement with that of obtained from UV-Vis-NIR spectrum, *Table 4.3*. *Figure 4.9* shows the evolution of both refractive index, $n(\lambda)$ and extinction coefficient, $k(\lambda)$ for all the Si films deposited at RT, 400 °C and 700 °C obtained from SE data. For the comparison $n(\lambda)$ and $k(\lambda)$ spectra of both bulk a-Si and poly-Si available from SE software package, SEA, is also displayed in both these figures. It clearly confirms that the films deposited at RT and 400 °C are by and large composed of a-Si while that at 700 °C is dominated by polycrystalline Si. In present case, the value of the refractive index (within visible to infrared region) is slightly reduced compared to that of bulk a-Si and the falling edge of the extinction coefficient is shifted towards shorter wavelengths with the increase in T_s, as evident from *Figure 4.9*. This observed behavior is indication of change in the silicon film structure from amorphous to nano-crystalline Si at higher deposition temperature [29, 37] as was also confirmed by Raman studies, *Figure 4.3*.

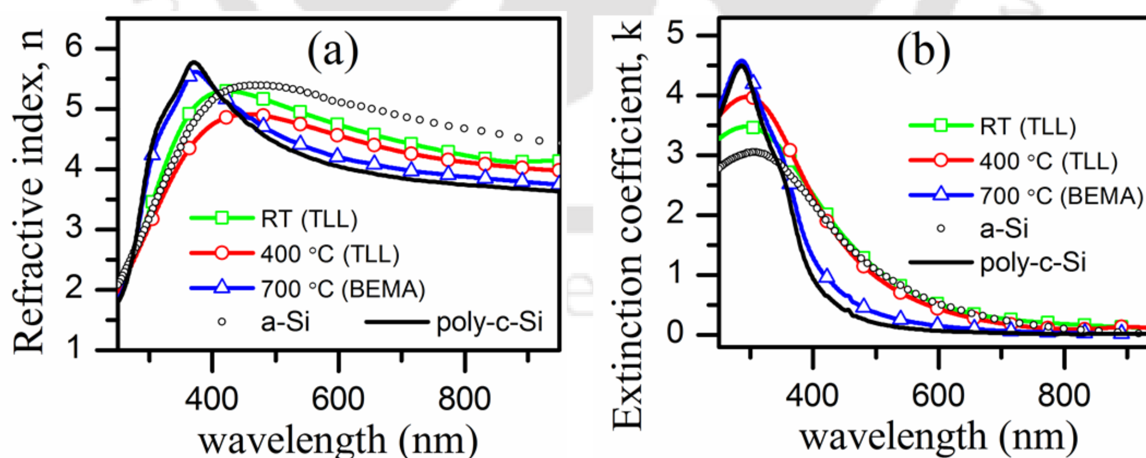

Figure 4.9 *(a) The refractive index and (b) extinction coefficient as a function of wavelength of the Si films deposited at RT, 400 and 700 ºC.*

TH-1680_10612114

4.2.2 Effect of background oxygen pressure during deposition on the properties of SiO_x films:

The structural, morphological, and optical properties can be modulated easily by changing the stoichiometry of SiO_x film. The control over the size and structure of Si nanoparticles as well as the oxygen content in the SiO_x films enable the fabrication of suitable structures with desired electrical and optoelectronic properties for device applications. Keeping this in mind, SiO_x thin films with varied oxygen concentration were deposited by ablating c-Si wafer in O_2 ambient via PLD at O_2 pressure ranging from 10^{-4} to 0.5 mbar. The other deposition parameters were kept fixed and listed in *Table 4.1*.

4.2.2.1 Structural and Compositional properties of SiO_x thin films:

Figure 4.10 shows the XRD spectra of the SiO_x thin films deposited in presence of O_2, pressure from 10^{-4} to 0.5 mbar and also that of a bare glass substrate. All the thin films exhibited characteristic XRD peaks for the Si (111), Si (220) and Si (311) planes at around 2θ ~ 28.45˚, 47.37˚ and 56.2˚, respectively reflecting the polycrystalline nature of these films [21]. It is observed that intensity of these peaks gradually increased with

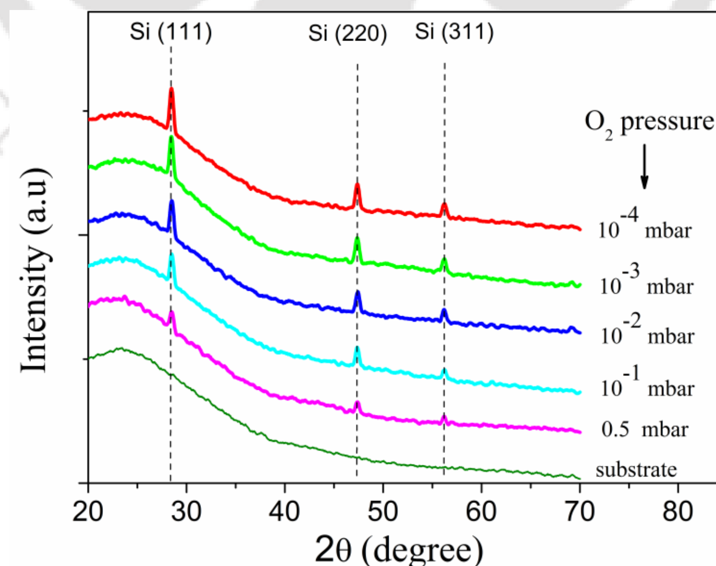

***Figure 4.10** XRD spectra of the substrate and PLD SiO_x thin films fabricated at various ambient O_2 pressure.*

TH-1680_10612114

Table 4.4 *XRD peak positions, corresponding FWHMs and respective Si crystallite size (D) for the SiO_x thin films as a function of O_2 pressure.*

O_2 pressure (mbar)	Si[111]		Si[220]		Si[311]		crystallite size D_{ds} (nm)
	Peak position	FWHM	Peak position	FWHM	Peak position	FWHM	
10^{-4}	28.47°	0.38°	47.35°	0.43°	56.25°	0.47°	20.8
10^{-3}	28.45°	0.44°	47.35°	0.5°	56.20°	0.54°	18.6
10^{-2}	28.45°	0.42°	47.35°	0.47°	56.20°	0.52°	19.2
10^{-1}	28.44°	0.40°	47.36°	0.46°	56.20°	0.52°	20.2
0.5	28.48°	0.42°	47.38°	0.48°	56.20°	0.55°	19.5

decreasing O_2 pressure. The peak positions and corresponding full width half maxima (FWHM) of observed peaks in the XRD spectra and crystallite size of Si within the films (calculated for Si(111) peak) as a function of O_2 pressure are listed in *Table 4.4*. There were hardly any significant changes observed in any of these parameters with the deposition pressure.

Figure 4.11(a-c) and *Figure 4.11(d-f)* show SEM images and EDX spectra of the SiO_x thin films deposited at O_2 pressure of 10^{-4}, 10^{-2} and 0.5 mbar, respectively. The SEM images clearly show micron sized clusters (droplets) embedded otherwise against the uniform background in all the films. The number of clusters on the film surface increases with increasing O_2 pressure. During PLD, the laser ablated material comprising of LIP of Si and oxygen plasma was formed along with the direct ejection of molten droplets. The LIP containing Si and oxygen ions, their neutrals and electrons expands, reacts and cools down to finally deposit on the substrate rendering the smooth background of the film. The molten droplets deposited directly on the substrate appear in the form of micron sized clusters against uniform background [22, 23]. The molten droplets during their dynamics through LPP could not be oxidized easily as their surfaces were only available for oxidation excluding the bulk of the structure. The chances of their oxidation are feeble as

TH-1680_10612114

they were hardly ionized. The EDX spectra showed the presence of silicon and oxygen in the thin film indicating the SiO_2 matrix formation [38]. The EDX spectra, *Figure 4.11 (d-f)*, were recorded over various regions of each film and hardly any significant changes in the composition, was observed within the given film, indicating that stoichiometry of the films is uniform throughout. The formation of SiO_2 is due to the reaction of Si and oxygen in laser produced plasma (LPP) during adiabatic cooling followed by the nucleation and growth onto the substrate surface. The atomic percentage of oxygen is found to be 3.5 (±1) %, 13.5 (±2) % and 68.2 (±2) % for the SiO_x thin films corresponding to x=0.03, 0.15 and 2.1, deposited at O_2 pressure of 10^{-4}, 10^{-2} and 0.5 mbar, respectively. Thus, increase in O_2 concentration in the SiO_x thin films with increasing deposition pressure is due to the increase in oxygen in LPP facilitating the formation of more Si-O bonds before deposition.

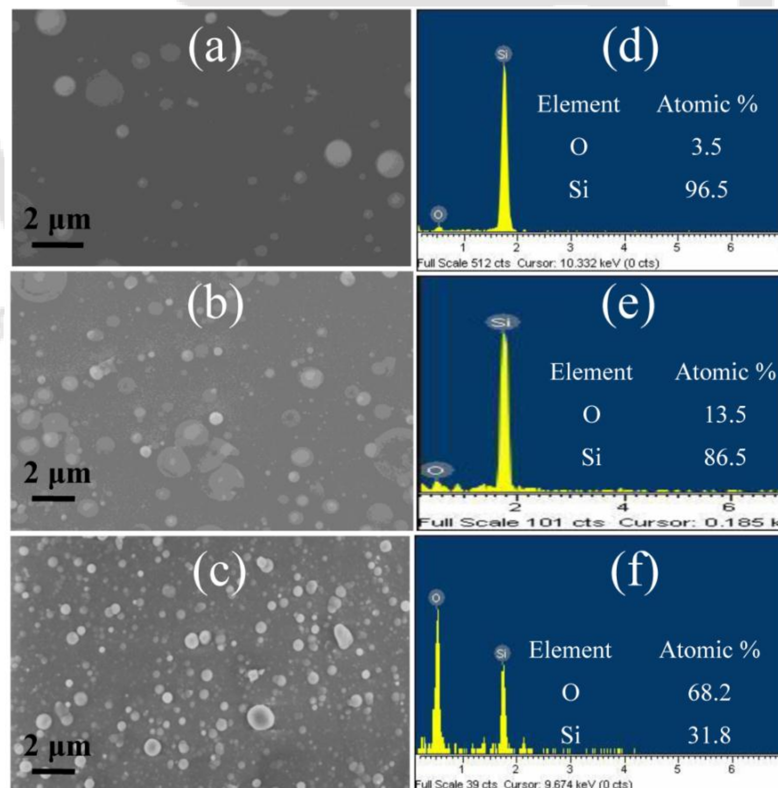

Figure 4.11 *SEM images (a-c) and corresponding EDX spectra (d-f) of SiO_x thin films deposited at O_2 pressure of 10^{-4}, 10^{-2} and 0.5 mbar, respectively.*

TH-1680_10612114

Figure 4.12 (a-c) display optical microscopic images (30μm × 30μm) and *Figure 4.12 (d-f)* corresponding Raman maps of SiO_x thin films deposited at O_2 pressure of 10^{-4}, 10^{-2} and 0.5 mbar, respectively. The microscopic images exhibit nearly spherical clusters embedded against uniform background. The number of clusters in the films increases though their size decreases with increase in O_2 pressure, which is consistent with SEM images (*Figure 4.11*). The Raman maps shown in *Figure 4.12 (d- f)* were recorded over two different ranges; Raman shift from 500 - 525 cm^{-1} represented in green colour and that of 460-490 cm^{-1} in black colour. It is very clear that the Raman shift of the clusters

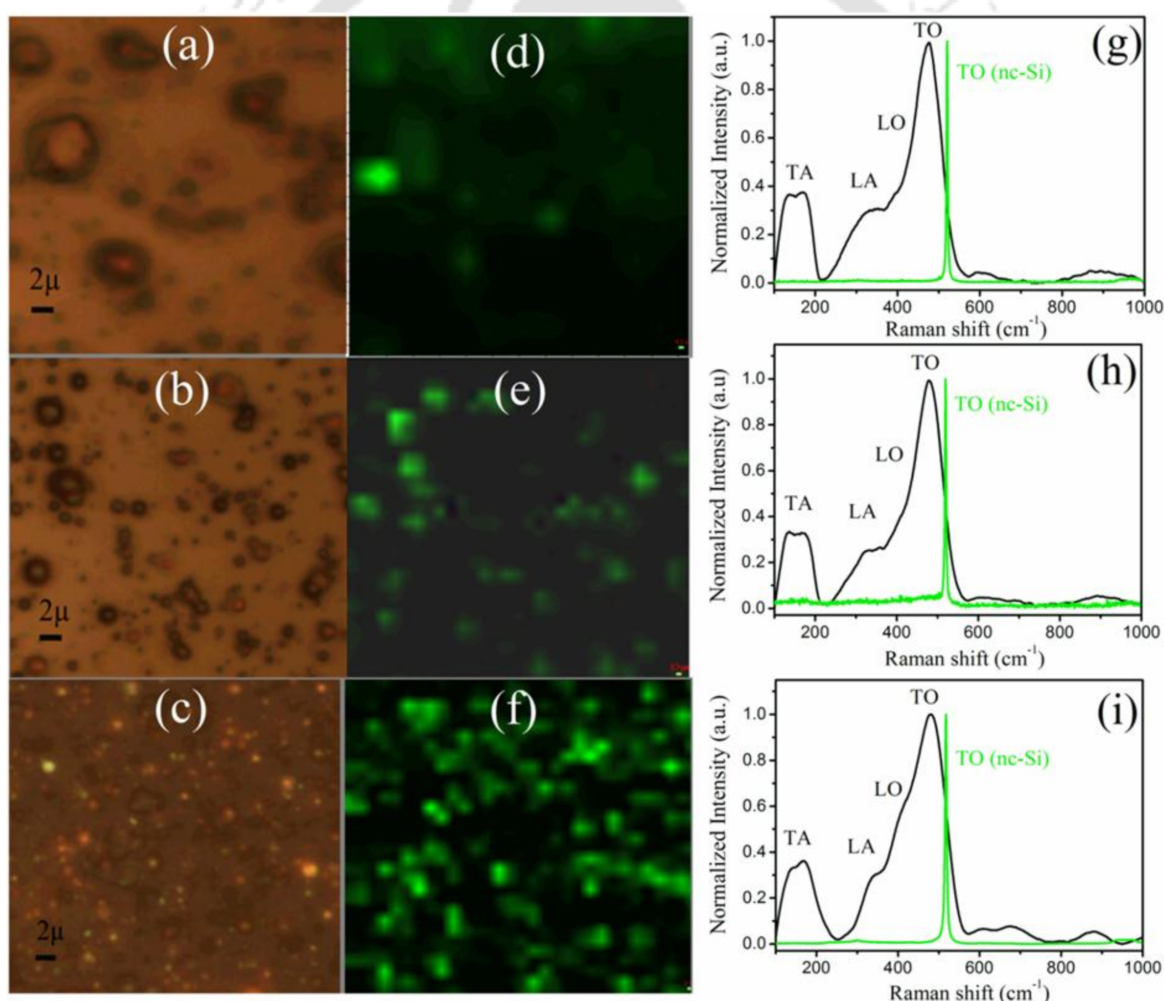

Figure 4.12 *Optical micrograph (a-c), corresponding Raman map (d-f) and Raman spectra of micron sized clusters and background (g-i) of SiO_x thin films deposited at O_2 pressure of 10^{-4}, 10^{-2} and 0.5 mbar, respectively.*

TH-1680_10612114

lies in former range while that of the background in the later range. *Figure 4.12 (g-i)* show the respective Raman spectra of both the regions, clusters in green and background in black colour. The Raman spectra of clusters in the films deposited at O_2 pressure of 10^{-4}, 10^{-2} and 0.5 mbar, *Figure 4.12 (g-i)*, show a sharp highly intense peak around 520.7, 519.5 and 517.4 cm^{-1}, respectively. The peaks are asymmetric toward lower wavenumber side and red shifted w.r.t that of bulk c-Si at 521 cm^{-1}, thus indicating the presence of nc-Si. This peak arises from the first-order Raman scattering of the longitudinal optical (LO) and the transverse optical (TO) phonon modes which are degenerate at the Brillouin zone center [24, 25]. The Raman spectra of the film background, *Figure 4.12 (g-i)*, (black in colour) display one prominent band (400-550 cm^{-1}) having intense peak around 480 cm^{-1} and shoulders toward the lower wavenumber (350-400 cm^{-1}). Another relatively less intense broad band in the range of 100-280 cm^{-1} having peak around 160 cm^{-1} has also been observed. These bands correspond to Raman active TO, LO, longitudinal acoustic (LA) and transverse acoustic (TA) phonon modes of amorphous Si (a-Si) [25]. Hence, from the Raman studies it can be inferred that the thin films were composed of clusters of nc-Si embedded in otherwise uniform background comprising of a-Si and SiO_2 (as revealed in EDX results). The formation of micron-sized clusters consisting of nc-Si is due to the direct deposition of molten droplets of Si ablated from the target.

For details, the Raman spectra of the cluster region of all the SiO_x thin films fabricated at different O_2 pressures (plotted with Y-offset), in the range of 510-530 cm^{-1}, are enlarged in *Figure 4.13*. The observed red shift w.r.t 521 cm^{-1} peak of bulk c-Si, was 0.3, 0.8, 1.5, 1.8 and 3.6 cm^{-1} for the films fabricated at O_2 pressure of 10^{-4}, 10^{-3}, 10^{-2}, 10^{-1} and 0.5 mbar, respectively. The red shift and asymmetric broadening of these peaks could originate due to quantum confinement (QC) effect of phonon, tensile strain, laser heating or combinations of all these. In order to avoid the effect of laser heating, the Raman

TH-1680_10612114

spectra of the samples were recorded at a very low excitation intensity of 0.01 mW/μm^2. From XRD studies using William-Hall method [39], it was found that the strain observed were compressive and of the order of 100 MPa and it corresponds to a Raman shift of less than 0.1 cm^{-1}. Thus, the effect of strain on the Raman spectra, in the present case, is ruled out and only possible contribution could be due to QC effect. Unlike bulk crystals, where only optical phonons at wave vector, $q = 0$ (zone center) are allowed, in the nanocrystals, additional phonon modes corresponding to the discrete allowed wave vectors, $q > 0$ (due to Heiseignberg uncertainity principle) also contribute in vibrational excitations. This results in asymmetric broadening of the TO mode toward lower wave number region of

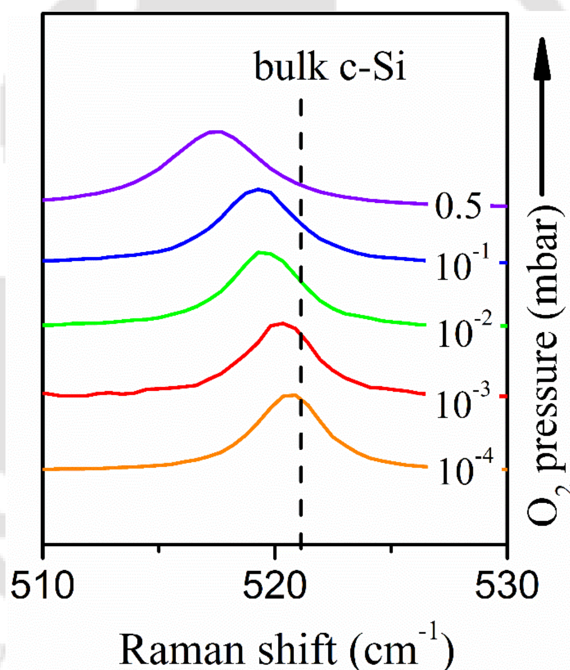

Figure 4.13 *Enlarged view of Raman spectra of micron sized clusters of* SiO_x *thin films deposited at* O_2 *pressure of* 10^{-4} *mbar to 0.5 mbar. Peak position of TO mode of bulk c-Si is marked as broken line at 521 cm*$^{-1}$.

Raman spectrum, depicting the feature of nc-Si in the micron sized clusters of SiO_x film. In order to understand the Raman spectrum of Si nanocrystals several models have been developed [40, 41]. The simplest model was originally proposed by Richter, Wang, and Ley [40] and is referred to as RWLM which is appropriate for Si nanocrystals of

TH-1680_10612114

dimension larger than 3 nm. For smaller nc-Si, bond-polarizability model (BPM) [41] is more appropriate. The size of the Si nanocrystallites in the SiO_x films can be estimated using the observed red shift in wavenumber of the nc-Si Raman peak. The relation between average crystal size (*D*) and observed Raman shift of nc-Si with respect to that of crystalline Si at 521 cm^{-1}, $\Delta\omega$ (in cm^{-1}), is given by [26],

$$D = a\left(\frac{A}{\Delta\omega}\right)^{1/\gamma} \quad (4.1)$$

where A=52.3 cm^{-1} and 47.41 cm^{-1}, γ=1.586 and 1.44 for RWLM and BPM respectively, and a=0.543 nm, the lattice parameter of c-Si. The estimated values of *D* from equation 4.1 using RWLM as well as BPM, are plotted as a function of O_2 pressure in *Figure 4.14*. It indicated that the average crystallite size of nc-Si gradually reduced from around 14 to 2.9 nm (using RWLM) and 18 to 3.2 nm (using BPM) with increasing O_2 pressure from 10^{-4} mbar to 0.5 mbar, respectively. The nc-Si size estimated by both these models needs to be complemented by other observations and then only conclusion on best suited model can be made.

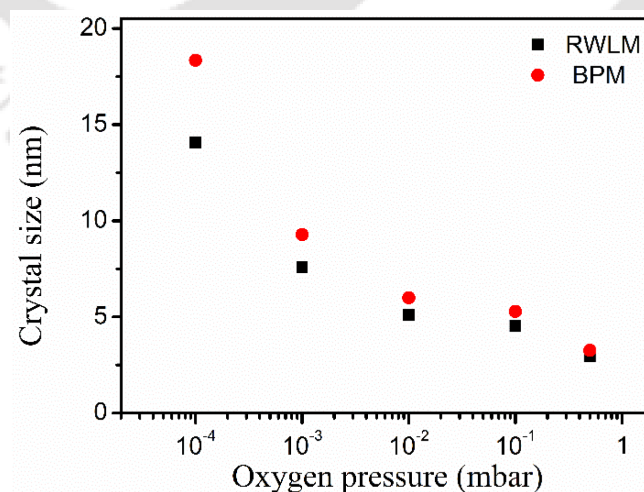

Figure 4.14 *Variation of crystal size (D) of nc-Si present withinthe micron sized clusters of SiO_x thin films as a function of O_2 pressure.*

TH-1680_10612114

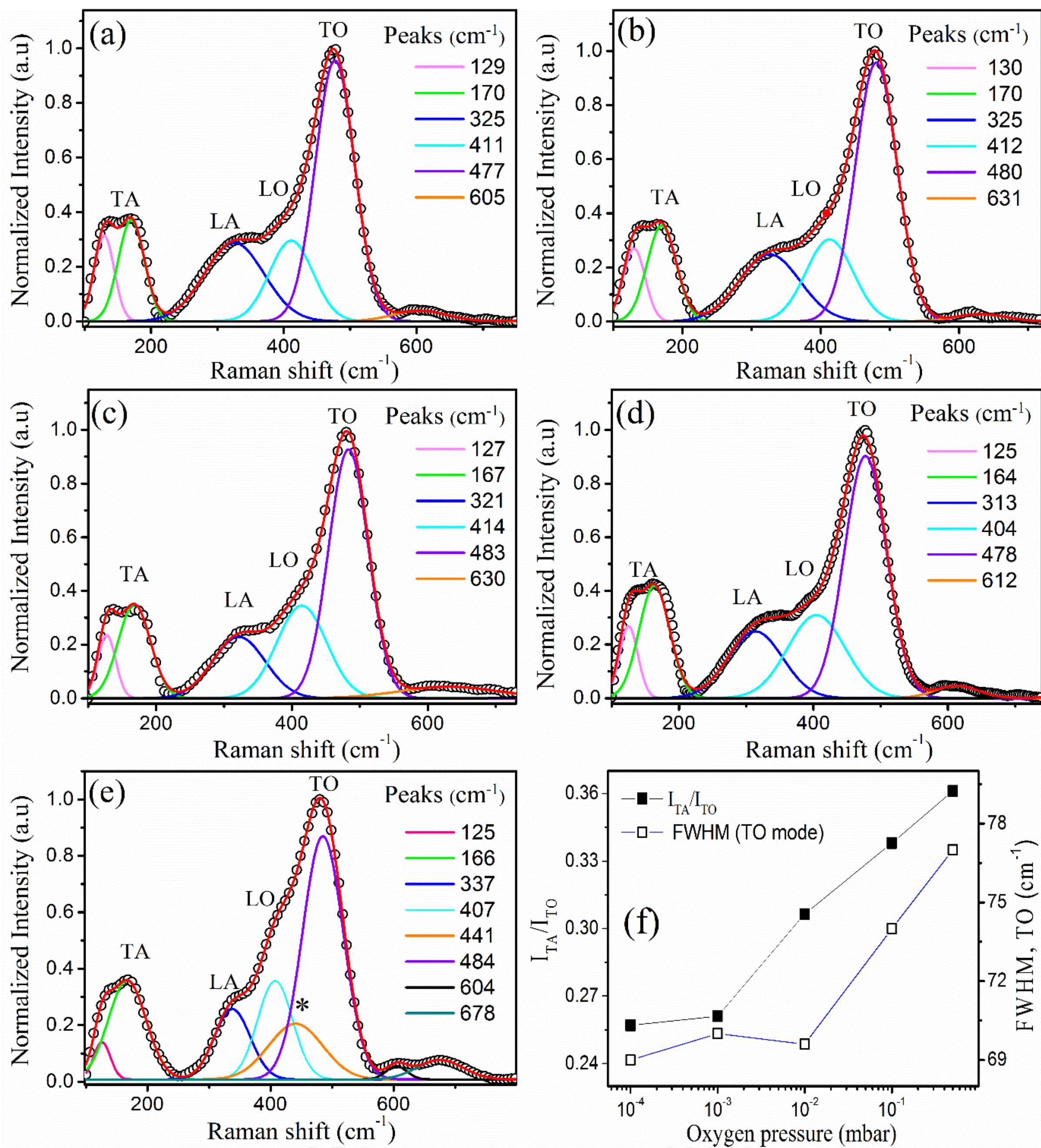

***Figure 4.15** De-convoluted Raman spectra of background amorphous matrix of SiO_x thin films deposited at O_2 pressure of (a) 10^{-4}, (b) 10^{-3}, (c) 10^{-2}, (d) 10^{-1} and (e) 0.5 mbar, respectively. Open circle and solid lines represents experimental data and fitted data respectively. (f) the variation of I_{TA}/I_{TO} and FWHM of TO Raman peak of SiO_x films as a function of different O_2 pressure.*

Figure 4.15 shows normalized Raman spectra (open circle) of the background amorphous matrix of SiO_x thin films deposited at O_2 pressure of (a) 10^{-4}, (b) 10^{-3}, (c) 10^{-2},

TH-1680_10612114

(d) 10^{-1} and (e) 0.5 mbar. These spectra were de-convoluted by multiple peak-fitting using Gaussian lineshape and peak positions (in cm^{-1}) are mentioned on the right side of each spectrum. In the Raman spectrum of SiO_x film deposited at O_2 pressure of 10^{-4} mbar, *Figure 4.15 (a)*, several peaks were observed. The five significant peaks, observed at 477 cm^{-1}, 411 cm^{-1}, 325 cm^{-1} and 170 cm^{-1} along with 129 cm^{-1} corresponds to TO, LO, LA and TA Raman modes of a-Si respectively [25]. The Raman spectra of the background matrix of all other films, *Figure 4.15 (b-e)*, also exhibited similar features. The Raman spectra of amorphous background matrix of SiO_x thin films deposited at O_2 pressure of 0.5 mbar (*Figure 4.15-e*) showed an additional prominent broad shoulder peaking at 441 cm^{-1} (marked as '*'). This additional peak is attributed to the six-membered rings (Si_2O_4) and presence of five-, seven- and higher member rings is responsible for broadening of this band [42]. The signature of this peak was absent in other films due to lower oxygen content as was indicated in EDX spectra of film, *Figure 4.11*. The ratio of the integrated intensity of TA to TO modes (I_{TA}/I_{TO}) provides the measure of bonding disorder in the a-Si material. *Figure 4.15 (f)* shows the variation of I_{TA}/I_{TO} and full width at half maximum (FWHM) of the TO mode (Γ_{TO}) as a function of deposition O_2 pressure. An increase in I_{TA}/I_{TO} was observed from 0.19 to 0.36 with increasing deposition O_2 pressure from 10^{-4} to 0.5 mbar. The peak position (ω_{TO}) and Γ_{TO} of the TO mode are associated with the force constant of the stretching vibration and the bond-angle deviation in tetrahedrally bonded Si atoms. On the other hand, the TA mode is associated with bond bending which reflects dihedral angle variations. Hence, the increase in I_{TA}/I_{TO} with increasing oxygen pressure reflects an enhancement in variation of bond bending w.r.t. the stretching vibrations, indicating the increase in structural disorder in the films [25]. The r.m.s bond angle deviation $\Delta\theta$ from the tetrahedral angle of 109°28″ is related to Γ_{TO}, and given by Γ_{TO}= 15 + 6$\Delta\theta$ [43]. A small and gradual increase in Γ_{TO} from 66 cm^{-1} to 71 cm^{-1} was

TH-1680_10612114

observed, which reflects increase in *Δθ* from 8.5° to 9.1°, for films fabricated at O_2 pressure from 10^{-4} to 10^{-2} mbar. Thereafter, Γ_{TO} increases sharply to 77 cm^{-1} giving *Δθ* ~ 10.3° at O_2 pressure of 0.5 mbar. Hence the increasing trend of Γ_{TO} and corresponding *Δθ*, with increasing O_2 pressure also indicates the increase in bonding disorder in the films with the increase in oxygen content.

4.2.2.2 Linear optical properties of SiO_x thin films:

The UV-Vis-NIR transmission spectra of the SiO_x films, shown in *Figure 4.16*, depict sharp absorption edge in the wavelength range of 270-640 nm. In general it was observed that the transmittance of the SiO_x films increases with increasing O_2 pressure. The increase in the transmittance with the increase in O_2 pressure can be attributed to shift in film stoichiometry from Si rich to oxygen rich resulting reduction in the optical density of the films with increasing O_2 content. *Figure 4.17* shows the transmission spectrum of SiO_x thin film deposited at 10^{-4} mbar of O_2 pressure whose maxima and minima are enveloped by curves T_{max} and T_{min}, plotted by interpolation as per

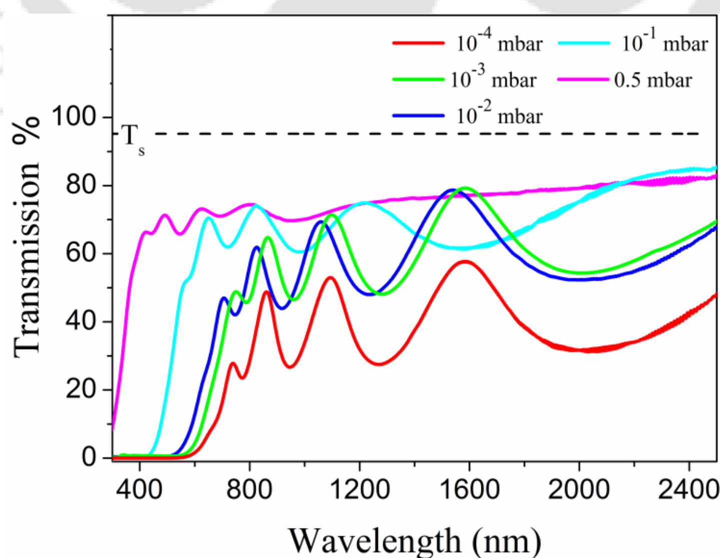

Figure 4.16 *UV-Vis-NIR Transmission spectra of SiO_x thin films deposited at different O_2 pressure*

TH-1680_10612114

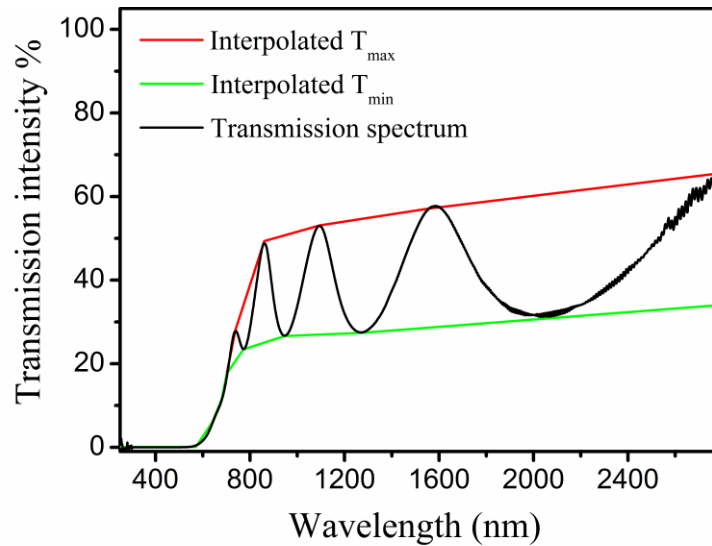

Figure 4.17 *UV-Vis-NIR transmission spectrum of SiO_x thin film deposited at 10^{-4} mbar of O_2 pressure showing T_{max} and T_{min} curves plotted by interpolation to envelop transmission maxima and minima.*

Swanepoel's envelop method, discussed in *Chapter 2*. The refractive index n for the SiO_x films was calculated using equation (2.1) [20]. These calculated values of n as a function of λ (at transmission maxima and minima) were fitted to Cauchy dispersion relation (eq. 2.3). *Figure 4.18* shows the refractive indices for all the five SiO_x thin films as a function of wavelength exhibiting normal dispersion behavior [27]. The inset shows the variation of $x\left(=\frac{\text{atomic \% of O}}{\text{atomic \% of Si}}\right)$ and n_0 of the SiO_x films (estimated by envelope method), as a function of O_2 pressure. The values of n_0 was found to decrease from 3.57 to 1.57 with increase in O_2 pressure from 10^{-4} to 0.5 mbar, the corresponding increase in x from 0.03 to 2.1, respectively. This refractive index change is attributed to the shift in stoichiometry from Si-like to SiO_2-like material [44]. The thickness, d, of the films was estimated from equation (2.4) [15], using Swanepoel's envelop method and also measured using step profilometer (d_{step}). Both the results are in agreement with each other. The film thickness estimated by the envelop method for the films fabricated at O_2 pressure of 10^{-4}, 10^{-3}, 10^{-2}, 10^{-1} and 0.5 mbar were found to be 452, 578, 585, 590 and 519 nm, respectively. The

TH-1680_10612114

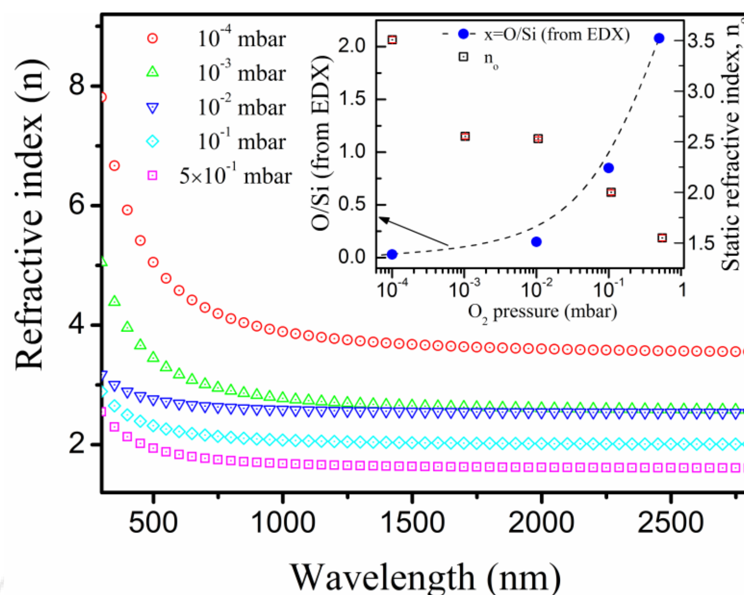

Figure 4.18 *Refractive index as a function of wavelength for SiO_x films deposited at various O_2 pressure. Inset shows variation of x in SiO_x films and corresponding static refractive index as a function of O_2 pressure.*

increase in thickness of the films with increasing O_2 pressure is due to confinement of LPP which in turn increases the particle flux resulting in higher deposition rates and hence increasing the thickness but at 0.5 mbar, pressure was too high causing over confinement of the plasma and thus restricting the incoming particle flux from LPP towards the substrate resulting in reduction in film thickness.

The absorption coefficient was estimated from equation (2.7) and variation of $(\alpha h\nu)^{1/2}$ as a function of $h\nu$ for all the films were depicted in *Figure 4.19 (a)*. The optical band gaps, E_g was obtained from the intercepts of the linear region of this plots on the $h\nu$ axis. *Figure 4.19 (b)* shows a gradual blue shift in E_g from 1.55 - 2.80 eV of the films fabricated with increasing ambient O_2 pressure from 10^{-4} to 0.5 mbar, respectively. Though a small increase of E_g from 1.55 to1.62 eV was observed in films fabricated at low pressure range from 10^{-4} to 10^{-2} mbar but it rises sharply to 2.80 eV for the film fabricated at 0.5 mbar. The nc-Si present in the SiO_x films, as confirmed by Raman

TH-1680_10612114

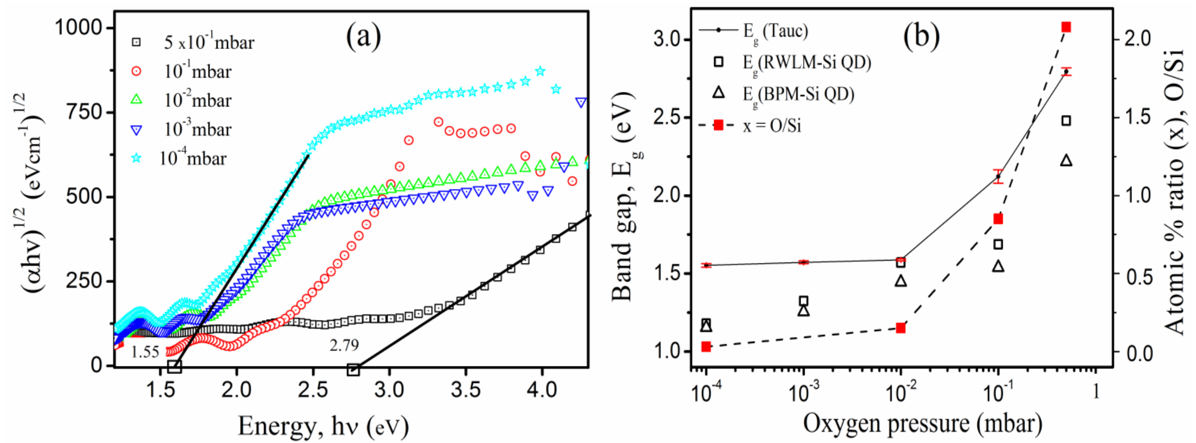

Figure 4.19 *(a) Tauc plots for determining optical band gaps of SiO_x films and (b) variation of optical band gaps (E_g) of SiO_x films as a function of different O_2 pressure.*

studies, can affect the band structure of the thin films. Though a crystalline bulk Si have an indirect band gap of 1.12 ev , but the nc-Si can have larger band gap which can be of quasi direct nature and size dependent due to quantum confinement (QC) effect. A blue shift in optical band gap is observed with decrease in nanocrystal size. The optical band gap of quantum confined spherical nc-Si is given as [33],

$$E_g = E_{g(bulk)} + \frac{1171.1}{D^2} \quad (4.2)$$

where, $E_{g\,(bulk)}$ is optical band gap of bulk c-Si and D is the size of Si nanocrystals in Å. If the optical band gap is assumed to be solely determined by QC of nc-Si, the expected E_g of nc-Si in the present case can be determined from D estimated using equation (4.1). *Figure 4.19 (b)* also displays the variation of optical band gap (E_g) of the SiO_x thin films with increasing O_2 pressure estimated from equation (4.2) in which crystallite size (D) was determined from equation (4.1) using RWLM (□) as well as BPM (Δ). In *Figure 4.19 (b)*, the ratio of atomic percentage of oxygen to that of Si (x = O/Si), measured from EDX spectra, is also plotted as a function of O_2 pressure. It shows similar variation as that of optical band gap. Hence, optical band gap of SiO_x films varies almost proportionally

TH-1680_10612114

with *x*. Some mismatch between band gap estimated from Tauc plot and that considering only the contribution of the QC of nc-Si was observed which can be explained in the following manner. The nc-Si clusters were thinly distributed over the a-Si:SiO_2 matrix as depicted in Raman maps, *Figure 4.12 (d-f).* Thus the background of the films, i.e. a-Si:SiO_2 matrix, actually determines the optical band gap of the SiO_x films. This observation enumerates the efficacy of Raman map in analyzing structurally inhomogeneous films containing nc-Si.

The absorption coefficient, α, for each SiO_x thin films, in the weakly to medium absorption spectral region, is given by equation (2.6) and are shown in *Figure 4.20 (a)*. In these films, the absorption coefficient near the band edge showed an exponential dependence on photon energy and this dependence can be represented by equation (2.5). The $ln(\alpha)$ vs. $h\nu$ curves shown in *Figure 4.20 (b)* displays a linear region. From the slope of these linear regions the Urbach energy, E_U, was estimated. E_U is interpreted as the width of the tails of localized states, associated with the amorphous state, in the forbidden gap. *Figure 4.21* displays the variation of Urbach energy (E_U) and *B* factor (Tauc slope) with increasing O_2 pressure from 10^{-4} to 0.5 mbar. The increase in E_U from 336 meV to 400 meV with the O_2 pressure from 10^{-4} to 0.1 mbar was small, but thereafter it acquires a value of 660 meV at 0.5 mbar. It has been reported that the E_U is related to the local structural disorder in the films [45]. The absorption band falls exponentially with decreasing photon energy at band edges in distorted amorphous materials, equation (2.5). A material with higher structural disorder has a larger tail in the absorption edge. The larger E_U at higher O_2 pressure is related to larger band tails, indicating increase in structural disorder with increase in oxygen content in the SiO_x thin films. The *B* factor decrease from 781 $(cm.eV)^{-1/2}$ to 607 $(cm.eV)^{-1/2}$ for thin films deposited at O_2 pressure of 10^{-4} to 0.01 mbar, then it increases marginally to 611 $(cm.eV)^{-1/2}$ for film fabricated at O_2

TH-1680_10612114

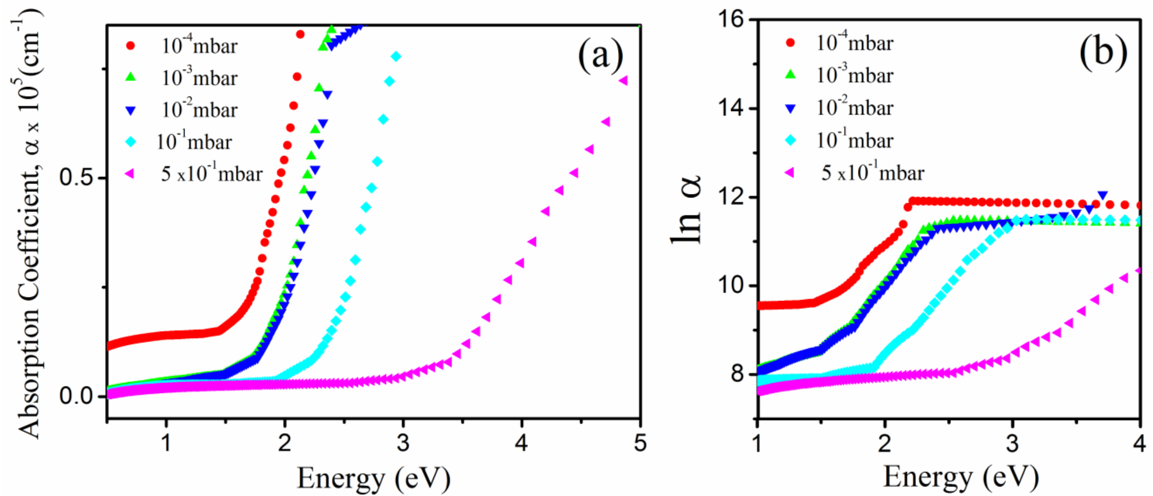

Figure 4.20 *(a) Plot of absorption coefficient as a function of photon energy for SiO_x thin films deposited at different O_2 pressure and (b) showing the plot of ln α vs hυ of SiO_x thin films.*

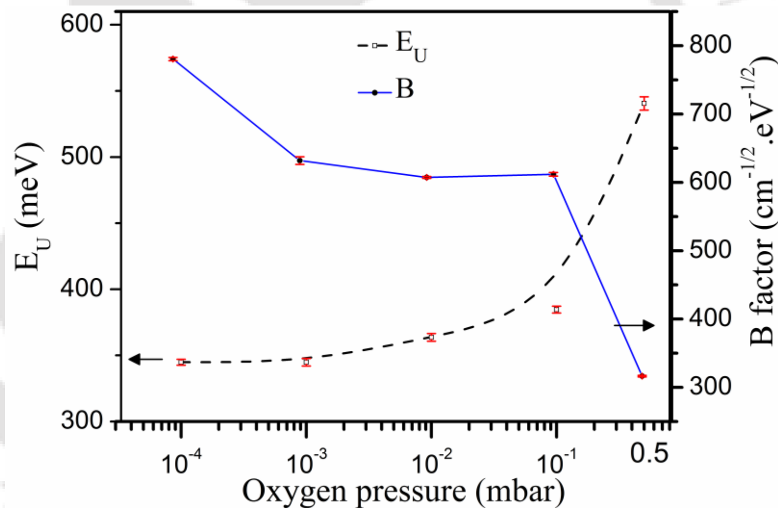

Figure 4.21 *Variations of E_U and B parameter of SiO_x thin films fabricated with increasing O_2 pressure from 10^{-4} to 0.5 mbar.*

pressure of 0.1 mbar and finally decreases abruptly to 317 $(cm.eV)^{-1/2}$ for that at 0.5 mbar. As the increase in *B* parameter is related to the reduction in overall structural disorder in the films [45], the observed decrease in *B* parameter with increasing deposition pressure of oxygen reconfirms the fact that with the increment in oxygen content in the films, the bonding structure becomes more disordered. These results are consistent with Raman

TH-1680_10612114

results (*Figure 4.15-f*) which also established the fact that the structural disorder depicted by I_{TA}/I_{TO}, increases with increase in oxygen content in the SiO_x thin films.

4.2.2.3 Photoluminescence studies of SiO_x films:

There are three main mechanisms accounting for PL emission in SiO_x films. These are related to near band edge emission (NBE), quantum confinement effect-induced (QCE) optical emission, and emission from defect states. The PL peak arising due to the NBE lies around the optical band gap of the material. For a QCE PL emission, blue shift of the peak occurs with the decrease in size of the nanocrystals [46]. Lastly, for the defect states-related PL, the peak positions remain unchanged irrespective of the band gap of the films. In the present case, the SiO_x films consists of nc-Si embedded in a-Si:SiO_2 matrix, hence it is expected to have several O_2 related defects. The O_2 deficient defects like ODC(I), ODC(II), E' center etc. exhibit PL peaks within 2.2-4.8 eV while defect states formed by non-bridging oxygen hole center (NBOHC); interstitial O_2^-, O_3^- and their respective neutrals show PL around 1.7-2 eV in Si based materials [47]. *Figure 4.22* shows the RT PL spectra, in the range of 1.2-3 eV, for all the PLD SiO_x thin films deposited in presence of various O_2 pressure. All the PL spectra were recorded at a fixed excitation laser power of 20 mW. There was hardly any signature of PL for the films deposited at lower O_2 pressure of 10^{-4} and 10^{-3} mbar. These films contain nc-Si of lager dimensions (*Figure 4.14*) as compared to the exitonic Bohr diameter of Si nanocrystals (~ 9 nm) [48], thus making them less likely to exhibit QCE PL. Moreover, these two films hardly contained any oxygen, and thus PL originated from oxygen related defects was also absent. A less intense symmetric broad band PL peak, E_{PL}, around 1.43 eV was observed for SiO_x film deposited at 10^{-2} mbar O_2 pressure. The estimated average size of nc-Si present within the micron sized clusters of this film was ~ 6 nm using BPM model (*Figure 4.14*). The band gap of QC nc-Si, $E_{g(QC)}$, obtained using eq. (4.2) for this film was

TH-1680_10612114

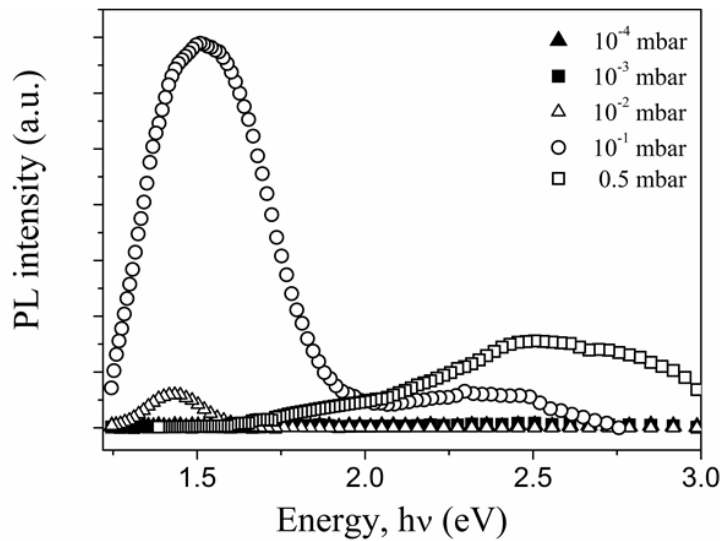

Figure 4.22 *PL spectra of SiO_x thin films fabricated at different O_2 pressure from 10^{-4} to 0.5 mbar.*

found to be 1.44 eV (*Figure 4.19(b)*) which matches with the peak energy of its PL emission (~1.43 eV), i.e. $E_{PL} = E_{g(QC)}$. Hence, the origin of PL in this case is attributed to emission due to transition between energy states produced by QC Si nanocrystals. For the films deposited at higher O_2 pressures of 0.1 and 0.5 mbar, highly intense broad PL peaks were observed having peaks around 1.52 eV and 2.45 eV, respectively. Both these PL spectra exhibit multiple structures and hence were de-convoluted into multiple peaks using Gaussian lineshape to understand their possible origin. The de-convoluted PL spectrum of SiO_x thin films deposited at 0.1 mbar of O_2 pressure, *Figure 4.23(a)*, shows four peaks at 1.38 eV (FWHM ~0.15 eV), 1.53 eV (FWHM~ 0.34 eV), 1.76 eV (FWHM~ 0.36 eV) and 2.36 eV (FWHM~ 0.51 eV). The most intense PL peak observed at 1.53 eV in this sample matches with its corresponding $E_{g(QC)}$ value, obtained using eq. (4.2), confirming its origin from QC nc-Si of average size ~ 5.2 nm. The relatively weak PL at 1.38 eV could also be due to QC nc-Si of larger sizes, as observed in TEM images discussed in later part of this section. The PL peak at 1.73 eV could be attributed to

TH-1680_10612114

NBOHC. The NBOHC (●O─Si≡) has been reported to have absorption bands peaking at 1.97 and 4.8 eV while that of interstitial states of O, O_2 and O_3 are around 4.8 eV [47]. As the excitation photon energy, used for PL measurement, was 3.06 eV (λ~405 nm) which could only be absorbed by NBOHC defect state corresponding to 1.97 eV absorption band, causing electronic excitation to higher energy and subsequent de-excitation resulting PL at 1.73 eV in the SiO_x film. The green PL emission around 2.36 eV observed in this film is attributed to the neutral oxygen vacancy (V_O) related defects present in the SiO_2 matrix [49]. The general schematic of possible PL mechanism involved in emission from the SiO_x film is shown in *Figure 4.23(b).* As discussed earlier (*Figure 4.19(b)*) the band structure in the SiO_x film, comprising of nc-Si embedded in a-Si:SiO_2 matrix, has two kinds of band gaps, one is the E_g (E_{Tauc}~2.11 eV, in case of SiO_x film fabricated at 0.1 mbar) due to background matrix and other one due to QC in nc-Si, $E_{g(QC)}$ (~ 1.53 eV). On excitation with 3.06 eV photons, electron-hole pairs are generated within the energy bands of SiO_x films. The photo-generated electrons (e^-) and holes (h^+) undergoes thermalization to reach the lowest states of conduction band (E_c) and highest states of valence band (E_v) respectively, of both a-Si:SiO_2 as well as nc-Si [50]. Most of the carriers after thermalization to band edges of a-Si:SiO_2 might undergo non-radiative transition to the low lying band edges of QC nc-Si as well. While thermalizing, some of the e^- could be trapped by V_0 defect states and had undergone radiative transitions emitting $E_{PL}^{V_0}$(~ 2.36 eV) photons. The carriers thermalized to band edges of QC nc-Si via different non-radiative channels undergo recombination via radiative transition yielding E_{PL}^{QC} peaking at 1.53 eV. Moreover some excited carriers while thermalizing along the energy bands of of both a-Si:SiO_2 as well as nc-Si or via non-radiative down transitions get trapped in 1.97 eV absorption band of NBOHC defects followed by another non-radiative transition to low lying emission level. From there they get de-exited emitting

TH-1680_10612114

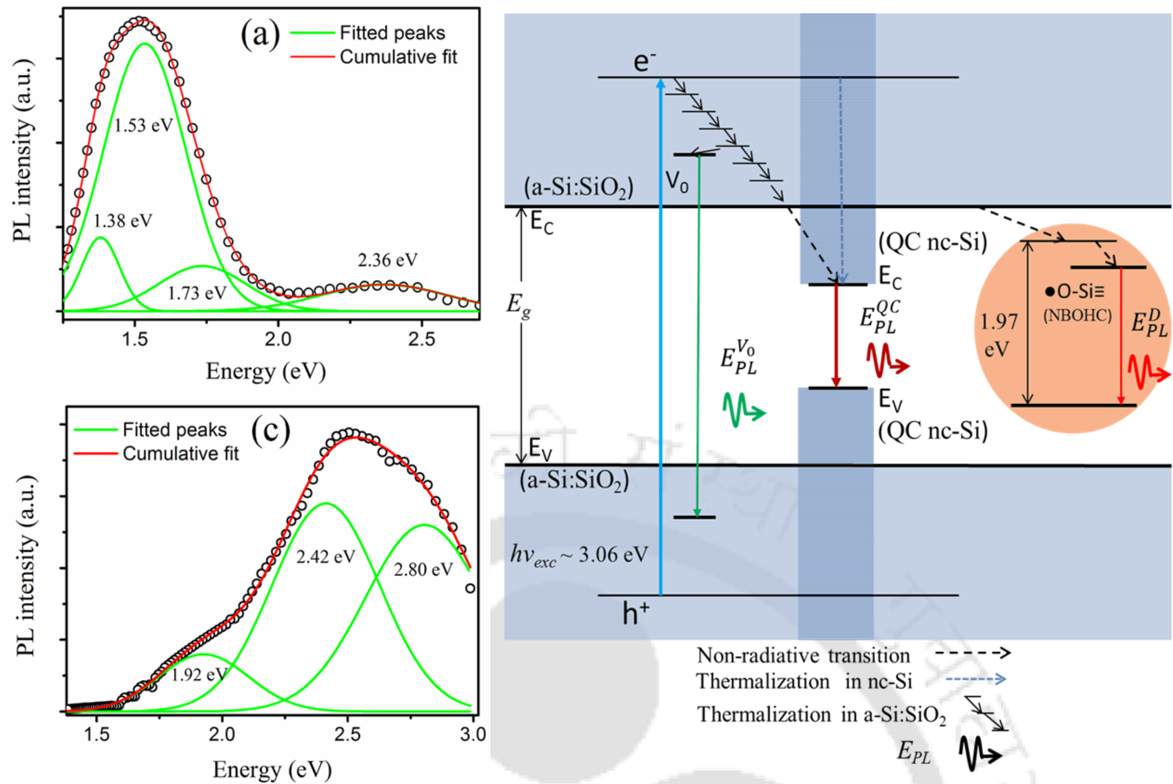

Figure 4.23 *(a) De-convoluted PL spectra of SiO_x thin film fabricated at O_2 pressure of 0.1 and (b) the energy level schematic of possible PL mechanism while (c) shows de-convoluted PL spectra of the film fabricated at O_2 pressure of 0.5 mbar.*

photons E_{PL}^{D} having peak energy of 1.73 eV [47, 51]. The PL spectrum of SiO_x thin films deposited under 0.5 mbar of O_2 pressure (*Figure 4.23(c)*) also shows three component peaks at 1.92 eV (FWHM~ 0.42 eV), 2.42 eV (FWHM~ 0.52 eV) and 2.8 eV (FWHM~ 0.5 eV). The PL peaks at 1.92 eV and 2.42 eV could be attributed to transitions from NBOHC and V_O defect levels yielding E_{PL}^{D} and $E_{PL}^{V_O}$ photons respectively, *Figure 4.23(b)*, as similar energy level structure exists in this film as well. Due to increased oxygen content in SiO_x films fabricated at 0.5 mbar as compared to that for 0.1 mbar, the V_O defects might have increased and it resulted into comparatively stronger PL peak at 2.42 eV in highly oxidized film. The intense PL peak exhibited at 2.8 eV (*Figure 4.23(c)*) for this sample is attributed to defects related to nanostructured a-SiO_2 matrix [47, 52].

TH-1680_10612114

The effect of increasing excitation laser power on PL emission of SiO_x film fabricated under 0.1 mbar O_2 pressure was studied as this particular sample exhibited the most intense PL emission due to QC effect. *Figure 4.24* shows the PL spectra of this thin film as a function of excitation laser power from 5 to 100 mW. With increase in excitation laser power the shape of PL spectra remained unchanged though there was a slight shift in its peak position and change in intensity. The variation of peak position and integrated intensity of E_{PL}^{QC} peak (~1.53 eV) was plotted as a function of excitation laser power in *Figure 4.25*. The PL peak position was observed to be nearly constant around 1.52 eV at incident laser power of 10 to 15 mW then it shifted slightly to 1.53 eV at 20 mW and remained nearly constant till 30 mW. After that it gradually blue shifted to 1.57 eV at 80 mW and then remained unchanged till 100 mW. The origin of the observed blue shift could be due to oxidation of nc-Si in atmosphere caused by increased laser heating with increasing incident cw-laser power. With increased laser heating the exterior of Si nanocrystals embedded in the film could have been oxidized resulting into reduction in the crystallite size, thereby exhibiting slight blue shift in PL due to QC effect. There was a sharp increase in integrated intensity of this PL peak with the incident laser power from 10 to 20 mW. Then, beyond that it increases slowly and reaches a maximum at 60 mW, after which it remains nearly constant till 70 mW displaying saturation behavior followed by slight decrease till 100 mW. The initial sharp increase in PL intensity with excitation laser intensity is due to increase in e-h pair generation, which is a linear function of incident photon density, electronic density of states of valence band and optical absorption cross section, followed by subsequent photon emission via radiative recombination. At high excitation intensity, the PL saturation behavior is expected as maximum emissivity of nanocrystals is limited by one photon per e-h pair [53]. This behavior can be explained by power law behavior of the PL intensity (I_{PL}) described for

TH-1680_10612114

Si nanocrystals by the following equation [53],

$$I_{PL} = \frac{N\sigma I_{ex}}{1+\sigma I_{ex}\tau_R(h\nu)} \quad (4.3)$$

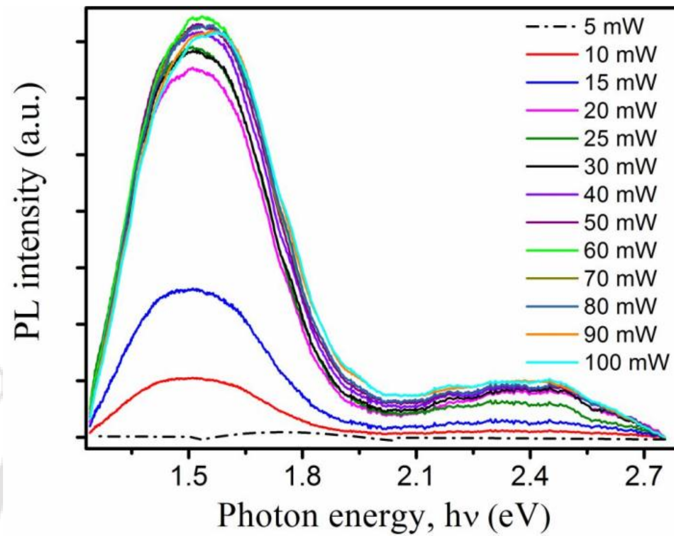

Figure 4.24 *PL spectra of SiO_x thin film fabricated at 0.1 mbar O_2 pressure as a function of excitation laser power.*

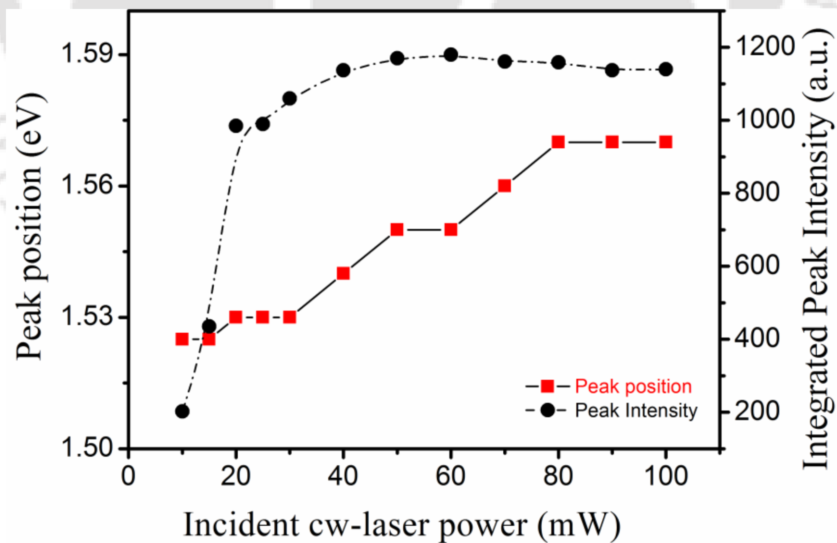

Figure 4.25 *Variation of QC PL peak position (E_{PL}^{QC}) and corresponding integrated intensity in SiO_x thin film fabricated at O_2 pressure of 0.1 mbar as a function of excitation laser power.*

TH-1680_10612114

where N is the total number of luminescent nanocrystals, $\tau_R(h\nu)$ is the radiative lifetime of an e-h pair, σ is the cross section for absorption of photons, and I_{ex} is the intensity of the exciting laser light. At low intensity, $\sigma I_{ex}\tau_R << 1$ and hence I_{PL} is linearly proportional to I_{ex} while at high excitation intensity, $1+\sigma I_{ex}\tau_R \sim \sigma I_{ex}\tau_R$ making I_{PL} independent of I_{ex}. But *Figure 4.25* also shows slight quenching of PL beyond $I_{ex} = 70$ mW which could be due to excessive laser heating causing oxidation, thereby increasing certain oxygen defects which traps the photo-excited electrons facilitating more non-radiative transitions.

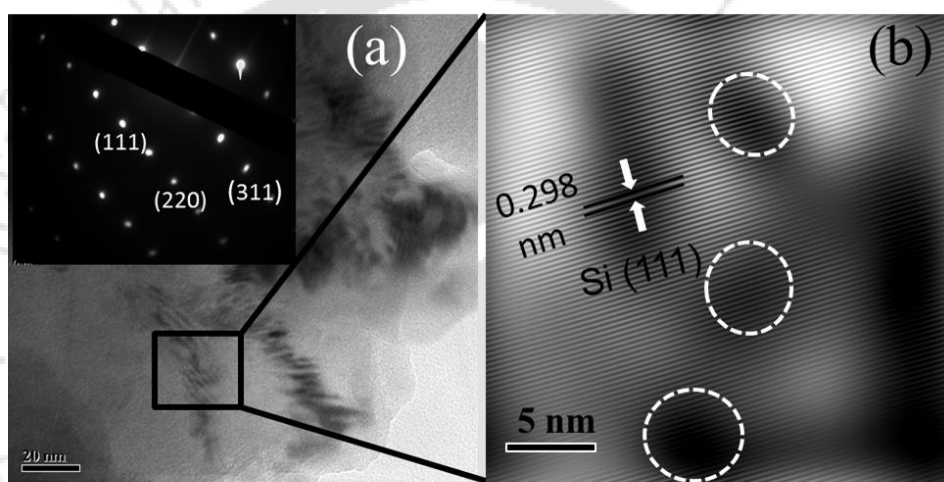

Figure 4.26 *(a) TEM image with inset containing corresponding SAED pattern and (b) UHRTEM of selected region of SiO_x thin film fabricated at O_2 pressure of 0.1 mbar.*

Figure 4.26(a) shows the TEM image of SiO_x thin film deposited at 0.1 mbar of O_2 pressure. It reveals the presence of darker nano-sized clusters embedded in grayish matrix. The SAED pattern of the dark region (marked by a rectangular box) is shown in the inset of the *Figure 4.27(a)*. It clearly exhibits well-ordered intense diffractions spots depicting the crystalline feature. The diffraction spots corresponding to Si (111), Si (220) and Si (311) were observed and also detected by XRD measurements, *Figure 4.10*. For further analyses of the crystalline phase present in those nanostructures, UHRTEM was recorded and shown in *Figure 4.26(b)*. It confirmed the presence of nearly spherical

TH-1680_10612114

nanocrystals of diameter of ~ 5 nm along with few larger nanocrystals. The magnified image showed the presence of lattice planes with d = 2.98 Å which corresponds to [111] planes of Si. The presence of Si nanocrystals of size nearly around 5 nm within this film as probed by TEM supports average size (~5.2 nm) of Si nanocrystals determined by using eq.(4.1) from Raman spectra (*Figure 4.14*) by BPM. Both these results reinforce the fact that it was indeed the QC nc-Si embedded in amorphous matrix which was responsible for exhibiting intense PL peak at 1.52 eV in the PL spectrum observed for SiO_x films deposited at 0.1 mbar O_2 pressure.

4.3 Conclusions:

In the first part of this chapter, the effect of substrate temperature on structural as well as linear optical properties of PLD nanocrystalline Si thin films, were studied. XRD spectra, exhibiting characteristic peaks for the Si (111), Si (220) and Si (311) planes, confirmed the polycrystalline nature of the films. The Raman maps showed the formation of nc-Si clusters embedded in uniform background composed of amorphous Si. The static refractive indices were found to be in the range of 3.3 - 3.9 and observed to be dependent on the substrate temperature. Band gap of the Si thin films were found to be controlled by crystallinity of the films which in turn was found to be dependent on substrate temperature. But SE studies showed that the Si film deposited at 700 °C was nanocrystalline while that deposited at lower T_s were overwhelmingly amorphous. Both the $n(\lambda)$ and $k(\lambda)$ spectra of the Si films showed their optical properties to be changing from a-Si-like to poly-Si-like with increasing T_s. The optical band gap, refractive index and film thickness estimated from SE were found to be in good agreement with UV-Vis-NIR results.

TH-1680_10612114

In the second part of this chapter the effect of oxygen pressure on the PLD SiO_x thin films is presented. The Raman maps showed that the SiO_x films were grown with nc-Si clusters embedded in uniform background composed of amorphous Si and SiO_2. The XRD showed that the SiO_x films were polycrystalline in nature. The films was found to be composed of Si and O_2 as confirmed by EDX where atomic percentage of O_2 increased from 3.5 % to 68 % for films deposited under O_2 pressure of 10^{-4} mbar to 0.5 mbar, respectively. The optical properties were studied by UV-Vis-IR transmission and absorption spectroscopy. The static refractive index of SiO_x films were found to be decreasing from 3.57 to 1.57 with increasing oxygen content. The optical band gap of the films calculated using Tauc plot was found to be blue shifted from 1.55 eV to 2.80 eV approximately with increasing O_2 pressure. The increasing oxygen content in the films increased the structural disorder, depicted by increase in both Urbach energy studied from absorption spectra and I_{TA}/I_{TO} from Raman spectra. Laser excited PL were only observed for films fabricated at oxygen pressure of 0.01, 0.1 and 0.5 mbar only, exhibiting peak around 1.43, 1.53 and 2.51 eV. These PL spectra exhibited multi-component peaks originated due to quantum confined nc-Si as well as oxygen related defects like NBOH and V_o centers. The presence of nc-Si responsible for QC PL peak was also confirmed by TEM and UHRTEM images. This chapter also highlights the efficacy of Raman mapping over XRD and ellipsometry in analyzing the structure of heterogeneous films containing nc-Si clusters embedded against a-Si or a-SiO_2 matrix.

TH-1680_10612114

Bibliography

[1] H.S. Nalwa, Silicon-Based Material and Devices, Academic Press, Burlington, 2001.

[2] F. Priolo, T. Gregorkiewicz, M. Galli, T.F. Krauss, Silicon Nanostructures for Photonics and Photovoltaics, Nature Nanotechnology, 9 (2014) 19-32.

[3] N. Tomozeiu, Silicon Oxide (SiO_x, $0<x<2$): a Challenging Material for Optoelectronics in: P. Predeep (Ed.) Optoelectronics-Materials and Techniques, InTech Published online, 2011.

[4] H. Morkoç, S. Strite, G.B. Gao, M.E. Lin, B. Sverdlov, M. Burns, Large-band-gap SiC, III-V nitride, and II-VI ZnSe-based semiconductor device technologies, Journal of Applied Physics, 76 (1994) 1363-1398.

[5] D.E. Milovzorov, Nonlinear Optoelectronic Devices Based on Nanocrystalline Silicon Films: Acoustoelectrical Switches for Optical Modes, Nonliear Optical Switches and Lasers, in: Y. Masuda (Ed.) Nanocrystal, InTech, Rijeka, 2011, pp. Ch. 18.

[6] V.T. Vu, D.C. Nguyen, H.D. Pham, A.T. Chu, T.H. Pham, Fabrication of a Silicon Nanostructure-based Light Emitting Device, Advances in Natural Sciences: Nanoscience and Nanotechnology, 1 (2010) 025006.

[7] G. Hass, C.D. Salzberg, Optical Properties of Silicon Monoxide in the Wavelength Region from 0.24 to 14.0 Microns, Journal of the Optical Society of America, 44 (1954) 181-187.

[8] K.W. Wecht, Large-range Refractive-index Control of Silicon Monoxide Antireflection Coatings using Oblique Incident Thermal Evaporation, Applied Optics, 30 (1991) 4133-4135.

[9] J.A. Savage, Infrared Optical Materials and their Antireflection Coatings, Adam Hilger Ltd. , Bristol, 1985.

[10] H. Shibayama, S. Hasuo, T. Yamaoka, Formation of low defect density SiOx films for Josephson integrated circuits, Applied Physics Letters, 47 (1985) 429-430.

[11] O. Engström, B. Raeissi, J. Piscator, I.Z. Mitrovic, S. Hall, H.D.B. Gottlob, M. Schmidt, P.K. Hurley, K. Cherkaoui, Charging Phenomena at the Interface between High-k Dielectrics and SiO_x Interlayers, Journal of Telecomunication and Information Technology, 1 (2010) 10-19.

[12] D. Nesheva, C. Raptis, A. Perakis, I. Bineva, Z. Aneva, Z. Levi, S. Alexandrova, H. Hofmeister, Raman Scattering and Photoluminescence from Si Nanoparticles in Annealed SiO_x Thin Films, Journal of Applied Physics, 92 (2002) 4678-4683.

[13] C. Becker, T. Sontheimer, S. Steffens, S. Scherf, B. Rech, Polycrystalline silicon thin films by high-rate electronbeam evaporation for photovoltaic applications – Influence of substrate texture and temperature, Energy Procedia, 10 (2011) 61-65.

[14] H. Miyazaki, T. Goto, SiOx Films Prepared using RF Magnetron Sputtering with a SiO Target, Journal of Non-Crystalline Solids, 352 (2006) 329-333.

[15] M. Ito, K. Imakita, M. Fujii, S. Hayashi, Nonlinear optical properties of silicon nanoclusters/nanocrystals doped SiO2 films: Annealing temperature dependence, Journal of Applied Physics, 108 (2010) 063512.

[16] F. Iacona, G. Franzò, C. Spinella, Correlation between Luminescence and Structural Properties of Si Nanocrystals, Journal of Applied Physics, 87 (2000) 1295-1303.

TH-1680_10612114

[17] Y. Choi, J.-H. Park, M.R. Kim, W. Jhe, B.K. Rhee, Direct observation of self-focusing near the diffraction limit in polycrystalline silicon film, Applied Physics Letters, 78 (2001) 856.

[18] S. Vijayalakshmi, F. Shen, H. Grebel, Artificial dielectrics: Nonlinear optical properties of silicon nanoclusters at λ=532 nm, Applied Physics Letters, 71 (1997) 3332.

[19] D. Riabinina, C. Durand, J. Margot, M. Chaker, G.A. Botton, F. Rosei, Nucleation and Growth of Si Nanocrystals in an Amorphous SiO_2 matrix, Physical Review B, 74 (2006) 075334(075331-075337).

[20] R. Swanepoel, Determination of the Thickness and Optical-Constants of Amorphous-Silicon, Journal of Physics E-Scientific Instruments, 16 (1983) 1214-1222.

[21] D. Comedi, O.H.Y. Zalloum, E.A. Irving, J. Wojcik, T. Roschuk, M.J. Flynn, P. Mascher, X-ray Diffraction Study of Crystalline Si Nanocluster Formation in Annealed Silicon-rich Silicon Oxides, Journal of Applied Physics, 99 (2006) 023518(023511-023518).

[22] Ž. Andreić, V. Henč-Bartolić, D. Gracin, M. Stubičar, Droplet formation during laser sputtering of silicon, Applied Surface Science, 136 (1998) 73-80.

[23] W.O. Siew, W.K. Lee, H.Y. Wong, T.K. Yong, S.S. Yap, T.Y. Tou, Investigation of droplet formation in pulsed Nd:YAG laser deposition of metals and silicon, Applied Physics A, 101 (2010) 627-632.

[24] C. Smit, R.A.C.M.M. van Swaaij, H. Donker, A.M.H.N. Petit, W.M.M. Kessels, M.C.M. van de Sanden, Determining the Material Structure of Microcrystalline Silicon from Raman Spectra, Journal of Applied Physics, 94 (2003) 3582-3588.

[25] J. Won Dong, M.O. Ramirez, H. Kang, V. Gopalan, N.F. Baril, J. Calkins, J.V. Badding, P.J.A. Sazio, All-optical Modulation of Laser Light in Amorphous Silicon-filled Microstructured Optical Fibers, Applied Physics Letters, 91 (2007) 161112(161111-161113).

[26] V. Paillard, P. Puech, M.A. Laguna, R. Carles, B. Kohn, F. Huisken, Improved One-Phonon Confinement Model for an Accurate Size Determination of Silicon Nanocrystals, Journal of Applied Physics, 86 (1999) 1921.

[27] N.A. Bakr, A.M. Funde, V.S. Waman, M.M. Kamble, R.R. Hawaldar, D.P. Amalnerkar, S.W. Gosavi, S.R. Jadkar, Determination of the optical parameters of a-Si:H thin films deposited by hot wire–chemical vapour deposition technique using transmission spectrum only, Pramana, 76 (2011) 519-531.

[28] J.H. Ho, C.L. Lee, T.F. Lei, T.S. Chao, Ellipsometry Measurement of the Complex Refractive Index and Thickness of Polysilicon Thin Films, Journal of the Optical Society of America A, 7 (1990) 196-205.

[29] D. Das, A. Samanta, Quantum Size Effects on the Optical Properties of nc-Si QDs Embedded in an a-SiO_x Matrix Synthesized by Spontaneous Plasma Processing, Physical Chemistry Chemical Physics, 17 (2015) 5063-5071.

[30] R.P. Doerner, S.I. Krasheninnikov, K. Schmid, Particle-induced erosion of materials at elevated temperature, Journal of Applied Physics, 95 (2004) 4471-4475.

[31] S.A.-J. Jassim, A.A.R.A. Zumaila, G.A.A. Al Waly, Influence of substrate temperature on the structural, optical and electrical properties of CdS thin films deposited by thermal evaporation, Results in Physics, 3 (2013) 173-178.

TH-1680_10612114

[32] W. Futako, T. Kamiya, C.M. Fortmann, I. Shimizu, The structure of 1.5–2.0 eV band gap amorphous silicon films prepared by chemical annealing, Journal of Non-Crystalline Solids, 266–269, Part 1 (2000) 630-634.

[33] G. Conibeer, Applications of Si Nanocrystals in Photovoltaic Solar Cells, in: L. Pavesi, R. Turan (Eds.) Silicon Nanocrystals: Fundamentals, Synthesis and Applications, Wiley-VCH, Weimheim (Germany) 2010, pp. 555-582.

[34] Y. Bouizem, C. Abbes, J.D. Sib, D. Benlakehal, R. Baghdad, L. Chahed, K. Zellama, S. Charvet, Ellipsometric and Raman spectroscopic study of nanocrystalline silicon thin films prepared by a rf magnetron sputtering technique, Journal of Physics-Condensed Matter, 20 (2008) 445221.

[35] D.A.G. Bruggeman, Berechnung verschiedener physikalischer Konstanten von heterogenen Substanzen. I. Dielektrizitätskonstanten und Leitfähigkeiten der Mischkörper aus isotropen Substanzen, Annalen der Physik, 416 (1935) 636-664.

[36] H. Fujiwara, Spectroscopic Ellipsometry: Principles and Applications, John Wiley & Sons Ltd., Chichester, West Sussex, England, 2007.

[37] D. Amans, S. Callard, A. Gagnaire, J. Joseph, G. Ledoux, F. Huisken, Ellipsometric study of silicon nanocrystal optical constants, Journal of Applied Physics, 93 (2003) 4173-4179.

[38] G. Kurumurthy, K.S. Alee, D.N. Rao, Photoluminescence Studies of Si/SiO_2 Nanoparticles Synthesized with Different Laser Irradiation Wavelengths of Nanosecond Pulse Duration, Optics Communications, 282 (2009) 3509-3512.

[39] V.S.S. Kumar, K.V. Rao, X-ray Peak Broadening Analysis and Optical Studies of ZnO Nanoparticles Derived by Surfactant Assisted Combustion Synthesis Journal of Nano- and Electronic Physics, 5 (2013) 2026(2021-2026).

[40] H. Richter, Z.P. Wang, L. Ley, The One Phonon Raman Spectrum in Microcrystalline Silicon, Solid State Communications, 39 (1981) 625-629.

[41] J. Zi, K.M. Zhang, X.D. Xie, Comparison of Models for Raman Spectra of Si Nanocrystals, Physical Review B, 55 (1997) 9263-9266.

[42] Y. Borodko, J.W. Ager, G.E. Marti, H. Song, K. Niesz, G.A. Somorjai, Structure Sensitivity of Vibrational Spectra of Mesoporous Silica SBA-15 and Pt/SBA-15, The Journal of Physical Chemistry B, 109 (2005) 17386-17390.

[43] D. Beeman, R. Tsu, M.F. Thorpe, Structural Information from the Raman Spectrum of Amorphous Silicon, Physical Review B, 32 (1985) 874-878.

[44] Y. Zhang, S. Vijayalakshmi, M. Ajgaonkar, H. Grebel, C.W. White, Optical properties of an ordered array of silica nanospheres embedded with silicon nanoclusters, Journal of the Optical Society of America B, 17 (2000) 1967-1972.

[45] V. Chu, J.P. Conde, J. Jarego, P. Brogueira, J. Rodriguez, N. Barradas, J.C. Soares, Transport and photoluminescence of hydrogenated amorphous silicon–carbon alloys, Journal of Applied Physics, 78 (1995) 3164.

[46] J.A.L. Lopez, J.C. Lopez, D.E.V. Valerdi, G.G. Salgado, T. Diaz-Becerril, A.P. Pedraza, F.J.F. Gracia, Morphological, Compositional, Structural, and Optical Properties of Si-nc Embedded in SiO_x Films, Nanoscale Res Lett, 7 (2012) 1-10.

TH-1680_10612114

[47] R. Salh, Defect Related Luminescence in Silicon Dioxide Network: a Review, in: S. Basu (Ed.) Crystalline Silicon - Properties and Uses, InTech, Rijeka, 2011, pp. 135-172.

[48] E.G. Barbagiovanni, D.J. Lockwood, P.J. Simpson, L.V. Goncharova, Quantum Confinement in Si and Ge Nanostructures, Journal of Applied Physics, 111 (2012) 034307.

[49] B.S. Swain, B.P. Swain, S.S. Lee, N.M. Hwang, Microstructure and Optical Properties of Oxygen-Annealed c-Si/a-SiO_2 Core–Shell Silicon Nanowires, The Journal of Physical Chemistry C, 116 (2012) 22036-22042.

[50] W.D.A.M. de Boer, D. Timmerman, K. Dohnalova, I.N. Yassievich, H. Zhang, W.J. Buma, T. Gregorkiewicz, Red Spectral Shift and Enhanced Quantum Efficiency in Phonon-free Photoluminescence from Silicon Nanocrystals, Nature Nanotechnology, 5 (2010) 878-884.

[51] P.P. Dey, A. Khare, Fabrication of luminescent a-Si:SiO_2 structures by direct irradiation of high power laser on silicon surface, Applied Surface Science, 307 (2014) 77-85.

[52] G. Vaccaro, S. Agnello, G. Buscarino, M. Cannas, L. Vaccaro, Structural and Luminescence Properties of Amorphous SiO_2 Nanoparticles, Journal of Non-Crystalline Solids, 357 (2011) 1941-1944.

[53] D. Kovalev, J. Diener, H. Heckler, G. Polisski, N. Kunzner, F. Koch, Optical Absorption Cross Sections of Si Nanocrystals, Physical Review B, 61 (2000) 4485-4487.

TH-1680_10612114

Chapter 5
Fabrication and characterization of PLD amorphous SiC films

Amorphous (a-SiC) and nanocrystalline silicon carbide (nc-SiC) thin films have potential applications in solar cells, light-emitting diodes, image sensors, photodiodes etc. [1-4]. Amorphous SiC is being also used as a durable thermally stable surface passivation material for high efficiency thin silicon photovoltaic applications [5]. The ratio of atomic percentage of silicon to that of carbon as well as hybridization of C-C bonds in the film are responsible in shaping up the structural, electrical and optical properties of the a-$Si_{1-x}C_x$ films. By varying the x in the a-$Si_{1-x}C_x$ or nc-$Si_{1-x}C_x$ films, the optical band gap can be tuned over a wide range [6]. Anderson *et al.* [7] showed that the optical band gap of the a-$Si_{1-x}C_x$:H films increases from about 1.6 eV to 2.8 eV with carbon content from x= 0 to x =0.7 and decreases thereafter to 2.2 eV with further increase in x. Similar trend in the variation of optical band gap was observed by Shimada *et al.* [8] for reactive sputtered films where it was varying from 1.7-1.4 eV within full range of x, but the maximum band gap of 2.2 eV was observed for x = 0.4. The fabrication of SiC films have been reported by various techniques. Among them, PLD technique can be considered to be favorable for deposition of SiC films for being capable of control over stoichiometric as well as ease of growing the crystalline film at low temperature due to high kinetic energy of ablated neutral and ions which can easily enhance the surface diffusion, nucleation, chemical bonding and sticking probability. The quality of the films fabricated via PLD process depends on substrate, laser wavelength, laser fluence, background gas and substrate temperature [9, 10]. In the present chapter the effect of substrate temperature on the stoichiometry with consequent modification on their optical properties are reported.

TH-1680_10612114

5.1 Experimental details:

A schematic of PLD system used for the deposition of SiC thin films is shown in *Figure 2.1* (*Chapter 2*). The thin films were deposited on fused silica as well as undoped crystalline Si (100) substrates simultaneously via PLD by focusing a 2nd harmonic of a Q-switched Nd:YAG laser (pulse duration - 10 ns and repetition rate - 10 Hz) at a laser fluence of ~ 6 J/cm^2 on polycrystalline SiC sputtering target for 30 minutes under vacuum (~ 10^{-6} mbar). The films were deposited from room temperature (RT) to 750 °C of substrate temperature. The target was continuously rotated and rastered during deposition so as to provide fresh surface for every laser shot. The surface morphology of SiC films was captured by FESEM images. TEM images were captured to observe the nanoparticle formation while the SAED pattern were recorded for analyzing the modification in crystalline structure of the thin films as a function of T_s. XRD measurements were carried out with the Cu K_α line of an X-ray diffractometer at a grazing incidence angle of ω = 1° in thin film mode. The 2θ was scanned in the range of 20° to 70° in an angular step of 0.02°. Raman spectra of these thin films were recorded by micro-Raman setup by exciting with 488 nm line of Ar ion laser. The bonding structures and bond density of Si-C bonds in the films were studied from FTIR spectra. For recording the FTIR spectra, SiC thin films were deposited onto undoped c-Si wafer along with fused silica. The compositional analysis was performed by EDX diffraction. The transmission spectra of SiC thin films were recorded by a UV-Vis-NIR spectrometer within the wavelength range of 250 nm to 3000 nm to estimate the refractive index (n), absorption co-efficient and thickness (d) and optical band gap of these thin films as discussed in the sub-section 2.2.9, *Chapter 2*. The thickness of the films was also measured by stylus profilometer.

TH-1680_10612114

5.2 Effect of substrate temperature on the properties of SiC films:

As the substrate temperature controls the surface energy during nucleation of film, the substrate temperature variation may play vital role in shaping up the structural and corresponding optical properties of a film. Hence a-SiC films were fabricated as a function of substrate temperature at RT, 250 °C, 500 and 750 °C, under vacuum (~10^{-6} mbar) at a laser fluence of ~ 6 Jcm^{-2}. All these films were deposited for 30 minutes duration.

5.2.1 Surface morphology of PLD a-SiC thin films by FESEM images:

Figure 5.1 shows the FESEM images of a-SiC thin films fabricated, on c-Si substrate, at T_s of (a) RT, (b) 250°C, (c) 500°C and (d) 750°C, and the inset shows the corresponding images at higher magnification. The images of different regions of each thin film were captured and the morphology was found to be uniform over the surface for all the samples irrespective of the imaged region. The images revealed the particulate formation on the surface of the film with gradual increase in particle size with the increasing T_s. The a-SiC thin film deposited at RT showed some blemishes (white regions) over otherwise uniform background. Magnified image showed the presence of 10 nm sized particles in it. The film deposited at 250 °C also showed uniformly distributed particles of slightly larger size. At elevated T_s the granular structure of the surface becomes more prominent. The surface of thin films deposited at 500 °C and 750 °C displayed irregular shaped particles distributed uniformly over the entire film surface. The particle size of these thin films, grown at elevated T_s, was observed to be increased to around 20 nm. The observed increase in particle size in the thin films with increasing T_s could be due to the increase in surface energy enhancing the surface diffusion and hence coalescing several nucleated sites forming larger sized particles.

TH-1680_10612114

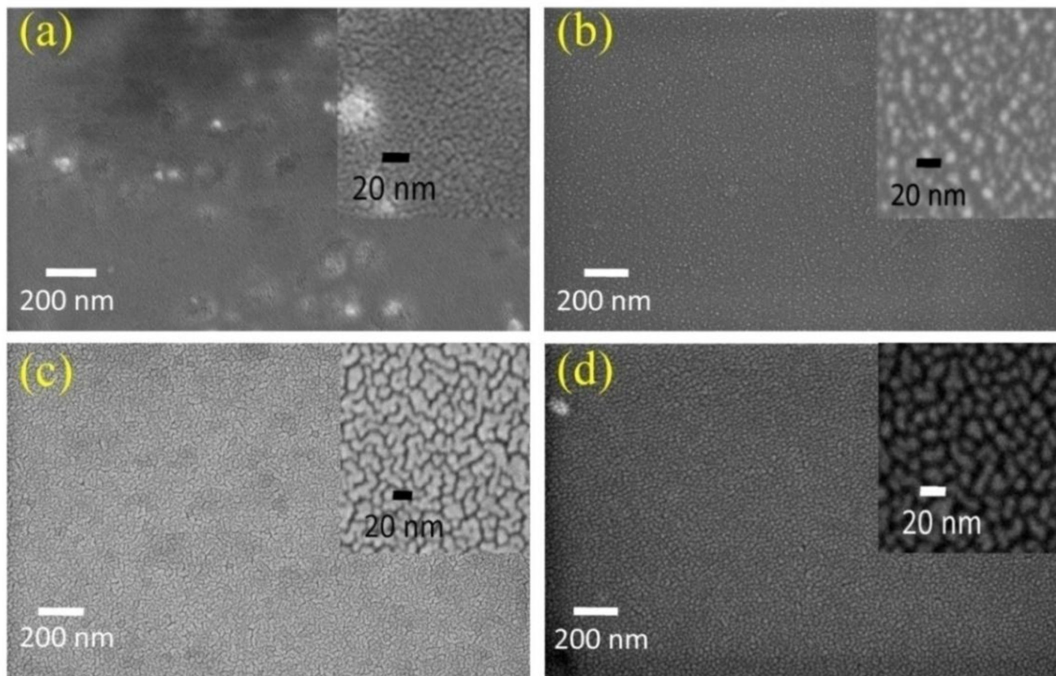

Figure 5.1 *FESEM images of PLD a-SiC thin films fabricated at (a) RT, (b) 250°C, (c) 500°C and (d) 750°C, respectively. The inset shows the corresponding images at higher magnification.*

5.2.2 TEM images and SAED patterns of PLD a-SiC thin films:

Figure 5.2 (a) and *(b)* show TEM images of a-SiC thin films deposited at RT and 750 ^{o}C, respectively. Insets show corresponding SAED patterns. TEM image of the film deposited at RT showed cluster of irregular shaped nano-sized particles having sizes less than 10 nm. The SAED pattern, in the inset of *Figure 5.2 (a)*, shows diffused diffraction pattern confirming the amorphous nature of the film. The TEM image of the film fabricated at an elevated temperature of 750 ^{o}C (*Figure 5.2-b*) reveals the presence of larger nanosized clusters of size around 20-30 nm embedded in grayish matrix. The SAED pattern of these particles shows diffraction ring superimposed with symmetric diffraction spots indicating the nano-crystalline nature of the film at elevated T_s which is also supported by XRD results (*Figure 5.3*) discussed in the next section.

TH-1680_10612114

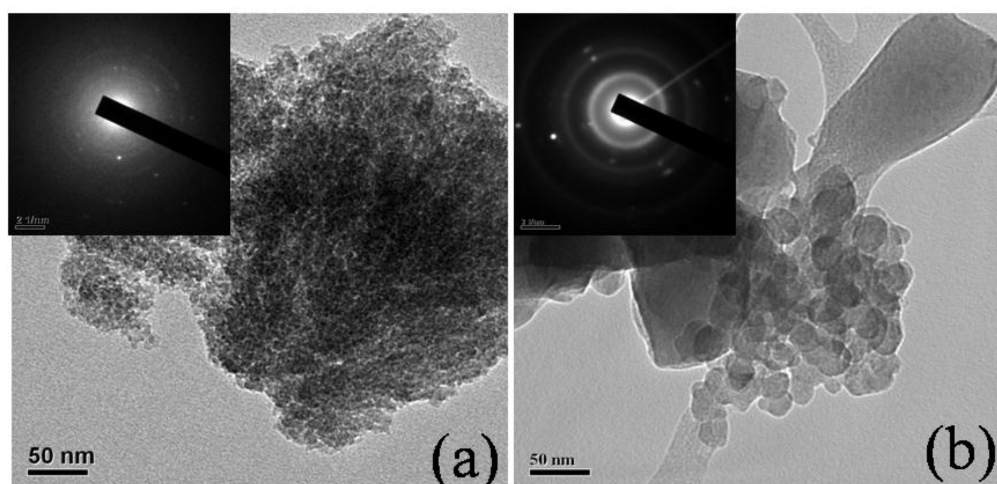

Figure 5.2 *TEM images of PLD a-SiC thin films deposited at (a) RT and (b) 750 °C. Inset shows corresponding SAED patterns.*

5.2.3 *Structural and compositional studies of PLD a-SiC thin films:*

Figure 5.3 shows the XRD spectra of the SiC thin films fabricated at T_s of RT, 250°C, 500 °C and 750 °C on fused silica. No prominent sharp peaks of crystalline SiC were observed for films deposited at RT and 250 °C indicating the amorphous nature of the films. A broad and weak characteristic XRD peak at 2θ ~ 35.7 ° was observed for SiC thin films deposited at elevated T_s of 500 °C and 750 °C, which corresponds to [111] plane of the 3C-SiC having cubic lattice structure [10]. The broad band feature ranging from 2θ ~ 20° to 30° was observed in all the films due to the fused silica substrate. The size of SiC crystallite, estimated using Debye Scherrer's formula, was observed to be nearly around 9.2±0.6 nm for the film deposited at 750°C.

TH-1680_10612114

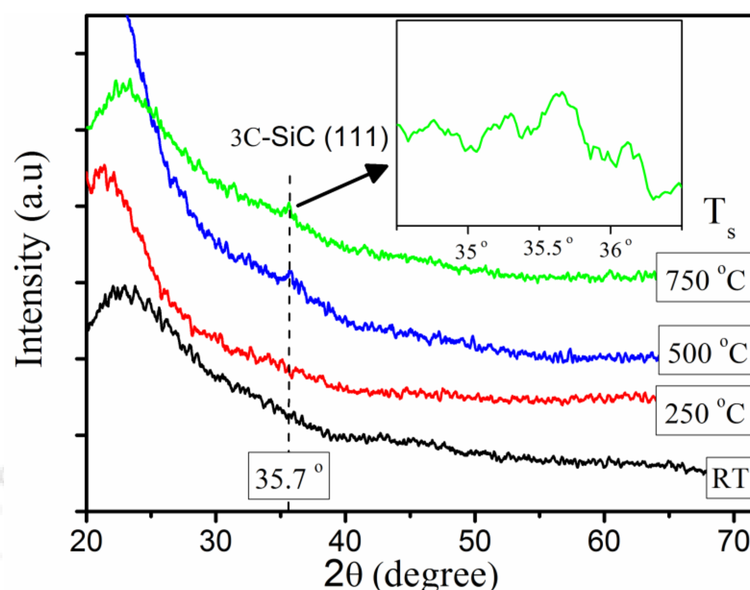

Figure 5.3 *XRD spectra of PLD SiC thin films fabricated at different substrate temperatures (T_s) from RT to 750 °C. Inset shows the zoomed view of 3C-SiC (111) XRD peak for SiC deposited at 750 °C.*

Figure 5.4 (a) shows the Raman spectra (Y-offset) of PLD deposited a-SiC thin films fabricated at T_s of RT, 250°C, 500 °C and 750 °C. These Raman spectra showed three obvious broad bands in the regions of 200-600 cm^{-1}, 700-1100 cm^{-1} and 1300-1600 cm^{-1}. The first band corresponds to various Raman modes of amorphous silicon (a-Si) (stretching of Si-Si bonds) [11] or Raman active acoustic phonon modes of a-SiC [12, 13] or both. The second band corresponds to Raman optical modes of SiC. In the literature, it has been reported that the main Raman peaks (sharp lorenzian) for crystalline SiC are centered at around 790 and 960 cm^{-1}, corresponding to the transverse (TO) and longitudinal (LO) optical modes respectively, of the cubic 3C-SiC (β SiC). Any other crystal lattice symmetry for SiC that displays either hexagonal or rhombohedral lattice symmetry is called as α-SiC. The α-SiC structure shows satellite peaks around 766 cm^{-1} [12]. In the present case, the Raman band being broad indicates that the SiC network is

TH-1680_10612114

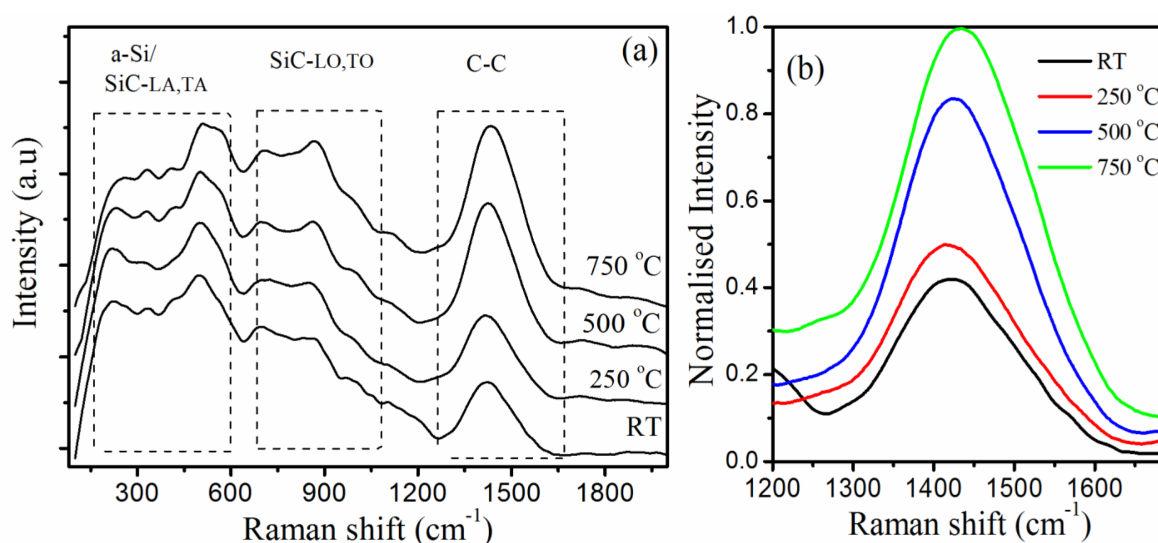

Figure 5.4 *(a) Raman spectra of PLD a-SiC thin films at different T_s and (b) corresponding C-C band of Raman spectra.*

amorphous and is highly disordered in nature. The third band corresponds to Raman active modes arising due to highly disordered C-C bonds [13]. An increase in peak intensity of C-C band is observed with increasing T_s, as shown in *Figure 5.4 (b)*. The Raman spectrum of sample deposited at T_s of 750 ^{o}C (*figure 5.4(b)*) showed maximum enhancement of C-C peak intensity relative to those of the other samples. To analyze the multiple peak features arising from the bonding structure in the SiC thin films, the Raman spectra for all the samples were de-convoluted and fitted to multiple peaks of Gaussian lineshape. The de-convoluted Raman spectra of all the a-SiC thin films are shown in the *Figure 5.5 (a-d)*. The wavenumbers for each and every peak are listed on the right hand side of the respective figure. In the Raman spectrum of a-SiC thin film deposited at RT (*Figure 5.5 (a)*), the prominent peaks were observed at 212, 328, 490, 702, 861, 981 and 1415 cm^{-1}. The broad multi-peak pattern below wavenumber of 600 cm^{-1} could be due to overlapping of Raman modes of a-Si (TO, LO, LA and TA) and acoustic Raman modes of a-SiC [12, 13]. The peak at 498 cm^{-1} (TO mode) was of maximum intensity. The other

TH-1680_10612114

broad bands observed at ~702, 861 and 981 cm^{-1} corresponds to optical modes (TO and LO) of the a-SiC. Another prominent broadband peak was observed around 1417 cm^{-1} which is attributed to the random covalent network of tetrahedral-trigonal bonding consisting of mixed phase of sp^3-sp^2 amorphous C with distorted bond angles and bond lengths [13]. The Raman spectrum of SiC thin film deposited at 250 °C, *Figure 5.5 (b)*, displayed the prominent peaks at 196, 308, 498, 715, 869, 982 and 1417 cm^{-1}. These features correspond to Raman modes of a-Si, a-SiC and C-C similar to that of the sample fabricated at RT. Here also, the peak corresponding to Si-Si bond observed at 498 cm^{-1} was prominent one and that corresponding to C-C bond was comparatively of low intensity. For the film deposited at 500 °C (*Figure 5.5 (c)*), similar peaks but with different relative intensities were observed. In this film, the peak at 1426 cm^{-1} was observed to have higher intensity than that of the earlier two samples indicating the presence of higher amount of C-C bonds compared to that of fabricated at lower T_s. For this film, optical modes (TO and LO) of the a-SiC were observed at ~698, 851 and 981 cm^{-1}. *Figure 5.5 (d)* shows the Raman spectrum of SiC thin film deposited at 750 °C where prominent peaks were observed at 220, 338, 497, 704, 877, 989 and 1438 cm^{-1}. For this film, peaks corresponding to optical modes (TO and LO) of the a-SiC were observed at ~704, 877 and 989 cm^{-1}. The peak at 1438 cm^{-1} was prominent among all other de-convoluted peaks, *Figure 5.5 (d)*, indicating the presence of higher amount of C-C bonds in it compared to all other films fabricated at lower T_s. The Raman peak positions of C-C band in all samples were shifted more toward the 1332 cm^{-1} diamond mode than the 1580 cm^{-1} of G band of perfect graphite crystal indicate relatively higher sp^3 content [13]. This large red shift of C-C band observed w.r.t the G band at 1415 cm^{-1}, 1417 cm^{-1}, 1427 cm^{-1} and 1438 cm^{-1} for the thin films fabricated at T_s of RT, 250 °C, 500 °C and 750 °C,

TH-1680_10612114

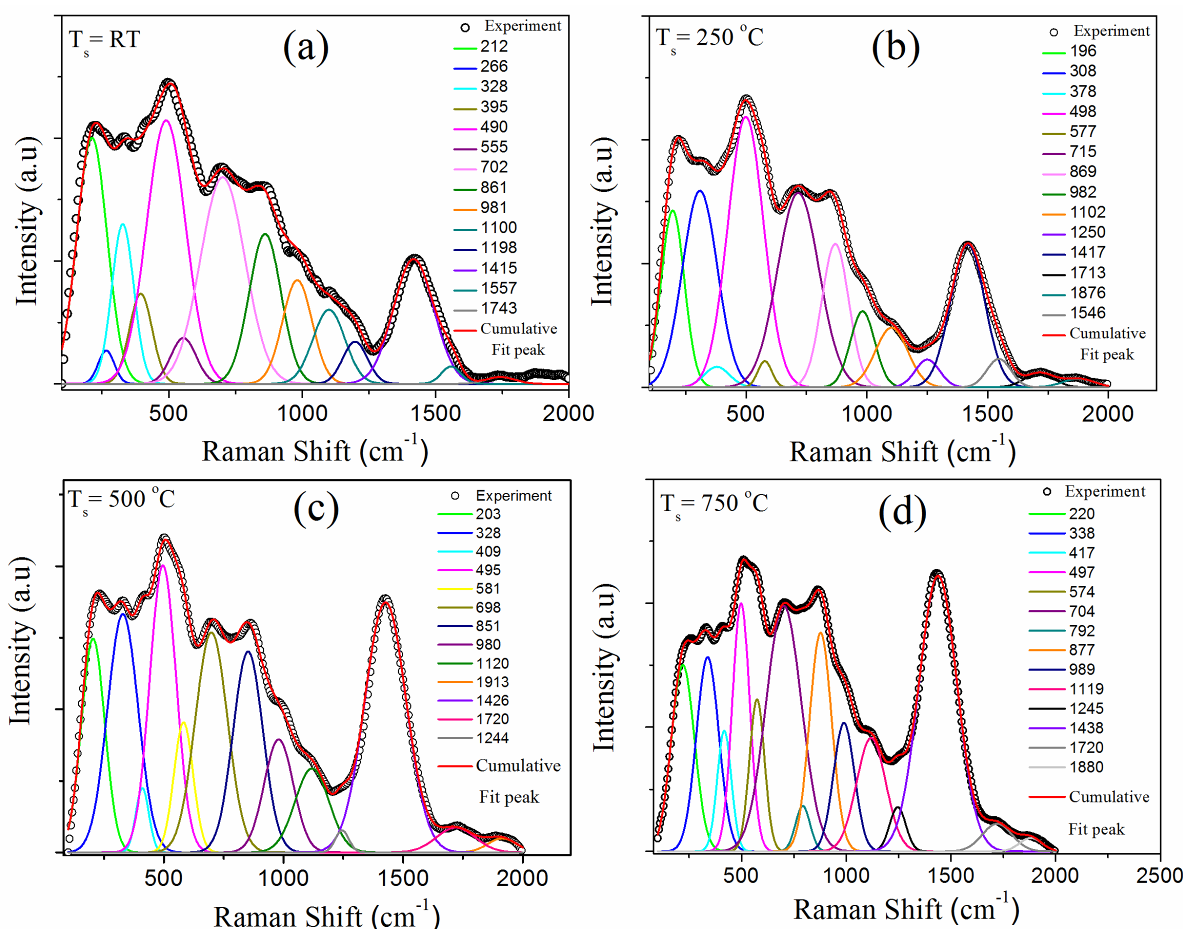

Figure 5.5 *De-convoluted Raman spectra of PLD a-SiC thin films at T_s–(a) RT, (b) 250 °C, (c) 500 °C and (d) 750 °C. The peak positions (in cm^{-1}) are listed on right side (colour coded) in the graphs.*

respectively, could also be due to the presence of heavier Si atoms attached to C atoms and highly disordered C- C bonds [14]. Also, the regular blue shift of C-C Raman peak observed from 1415 cm^{-1} to 1438 cm^{-1} with increasing T_s from RT to 750 °C, respectively is attributed to the replacement of heavier and weakly bonded Si atoms attached to C-C matrix by lighter and strong bonded C atoms as well as the increase in sp^2 carbon bonding. The sp^2 bonded carbon could be dispersed in film matrix as very small clusters or isolated sp^2 bonds which results in increase in sp^2/sp^3 ratio [14]. The integrated peak intensities of acoustic Raman modes of a-SiC ($I_{SiC,\ LA+TA}$) overlapped with Raman modes

TH-1680_10612114

of a-Si ($I_{a\text{-}Si}$) together, optical modes of a-SiC ($I_{SiC,\ LO+TO}$) and that of C-C ($I_{C\text{-}C}$) with respect to the total integrated intensity were estimated for each thin film from deconvulated spectra (*Figure 5.5*) and plotted as a function of T_s in *Figure 5.6*. In this plot, it was observed that with the increase in T_s from RT to 750 °C, the $I_{a\text{-}SiC,\ LA+TA} + I_{a\text{-}Si}$ decreases from 0.47 to 0.34 and $I_{a\text{-}SiC,\ LO+TO}$ is almost constant at around 0.29-0.3 and $I_{C\text{-}C}$ gradually increases from around 0.1 to 0.21. Hence SiC content was almost invariant w.r.t T_s whereas there is an increment in C-C bonds indicating the change in stoichiometry of a-SiC films from Si-rich to more stoichiometric SiC with increasing T_s.

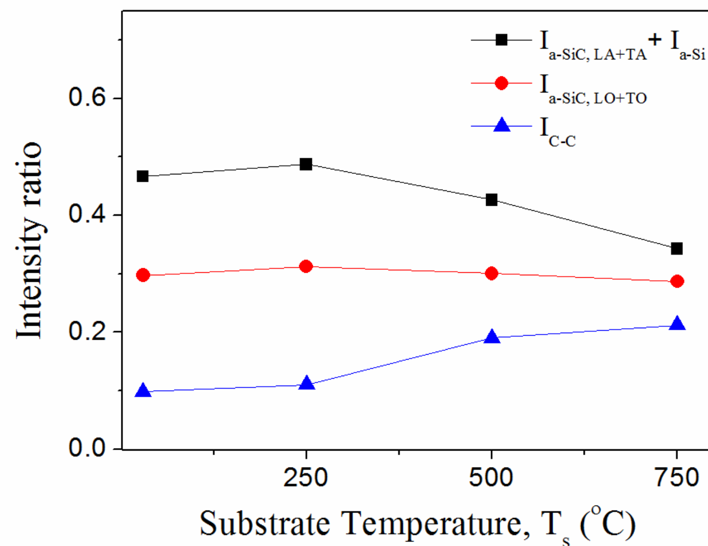

Figure 5.6 *Normalized integrated intensities of acoustic modes of a-SiC ($I_{SiC,\ LA+TA}$) overlapped with Raman modes of a-SiC, optical modes of a-SiC ($I_{SiC,\ LO+TO}$) and C-C ($I_{C\text{-}C}$) in a-SiC films as a function of substrate temperature, T_s.*

Figure 5.7 shows the dependence of FTIR absorbance spectra of SiC thin films, as a function of substrate temperature, deposited on undoped c-Si. A broad absorption peak was observed in the range of 500-1200 cm^{-1} peaking around 760 cm^{-1} in all the samples. From this, the absorption coefficient (α) for these films was determined using the Beer-Lambert's law:

TH-1680_10612114

$$\alpha(\omega) = 2.303\left(\frac{A}{d}\right) \tag{5.1}$$

where *d* is the film thickness and *A* is the absorbance. The inset of the *Figure 5.7* shows the FTIR absorption coefficients of each sample as a function of wavenumber depicting the multiple peak structure corresponding to different vibrational modes. The de-convoluted FTIR spectra of a-SiC films fabricated at different T_s were fitted with Gaussian functions and are shown in *Figure 5.8*. In *Figure 5.8 (a)*, three peaks were observed at 760 cm^{-1}, 982 cm^{-1} and 1076 cm^{-1}, where first peak is attributed to stretching vibration of Si-C bond and other two correspond to in phase Si-O-Si stretching vibrations [15]. It has been reported that the peak position and the shape of the absorption peak of the stretching vibration mode of Si-O-Si depend on the composition. It shifts from around ~ 940 cm^{-1} to 1083 cm^{-1} for SiO_x structure with x varying from 0.1 to 2 due to the increase in the oxygen content. For larger value of x, (x>1.2), a shoulder appears around1150 cm^{-1}, which becomes more and more pronounced when the oxygen content increases [16, 17]. So, peaks at 982 cm^{-1} and 1076 cm^{-1} could arise from similar Si-O-Si stretching but with later arising from more oxidized domain of smaller proportion. For other samples (*Figure 5.8b-d*), similar peaks corresponding to stretching vibration modes of Si-C and Si-O-Si were observed. The peak positions and respective peak assignments are marked in the figures. The integrated intensity of absorption coefficient of Si-O-Si vibration was found to be drastically decreasing at elevated substrate temperature while that of Si-C was increasing gradually. Hence with increasing T_s, a-SiC thin films were getting devoid of oxygen. *Figure 5.9* shows the variation of FTIR peak position attributed to Si-C bonding and corresponding FWHM with T_s. The peak is shifted gradually from 760 cm^{-1} to 770 cm^{-1} while the FWHM decreased from 267 cm^{-1} to 228 cm^{-1} with increasing T_s from RT to 750°C, respectively. The shift in vibrational frequency of an IR

TH-1680_10612114

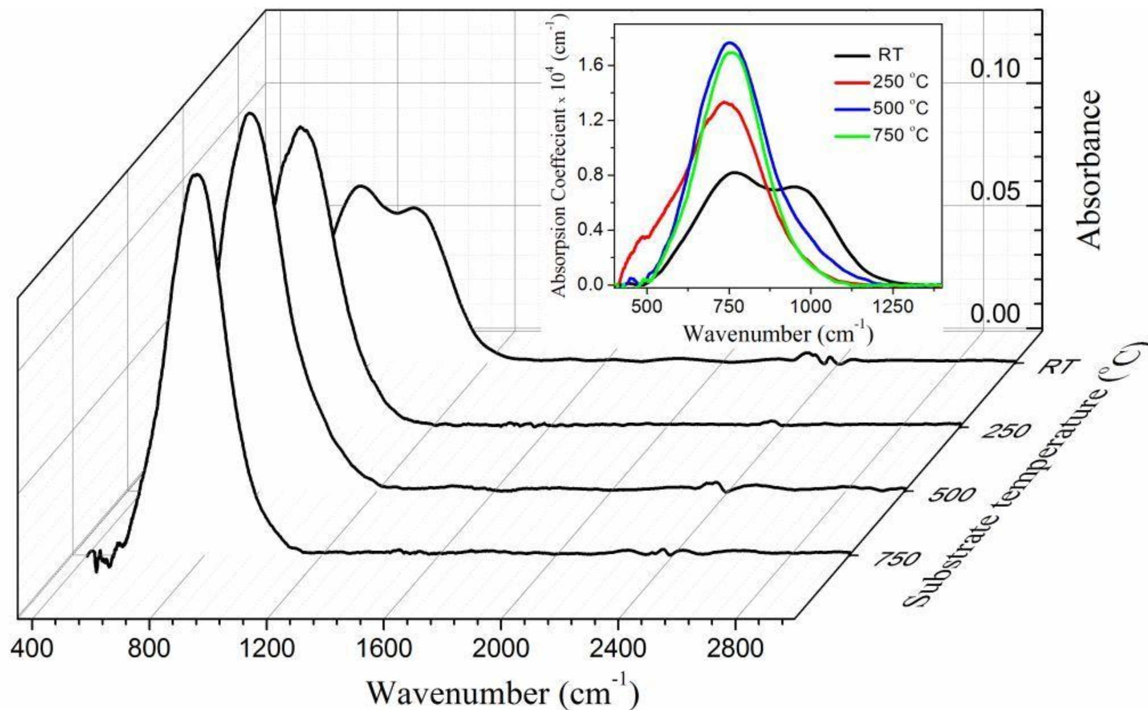

Figure 5.7 *FTIR absorbance spectra of PLD a-SiC thin films fabricated at T_s from RT to 750 °C. The inset shows the corresponding absorption coefficients (Y-axis scale = 10^4 cm^{-1}).*

active Si-C bond is due to the inductive effects of the nearest neighboring atoms. Mohr *et al.* [18] had reported that the various Si-C stretching modes of IR spectra observed between 650 and 780 cm^{-1} could be explained by back bonding variations. When a Si atom tetrahedrally bonded to another three Si atoms and a single C atom, it has IR active peak at 650 cm^{-1} due to their stretching vibration. The back bonding of C to Si is expected to shift the peak to higher wavenumber, while the effect of back bonding of C to C isexpected to have little effect. Hence when Si atom is bonded with all four tetrahedrally placed C atoms, which is more ordered SiC structure, its IR peak due to stretching vibration is blue shifted to 780 cm^{-1}[18]. Hence with increasing T_s the a-SiC thin films become more ordered as indicated by the blue shift in FTIR peak and their narrow FWHM. The concentration of the bond density which is directly proportional to the

TH-1680_10612114

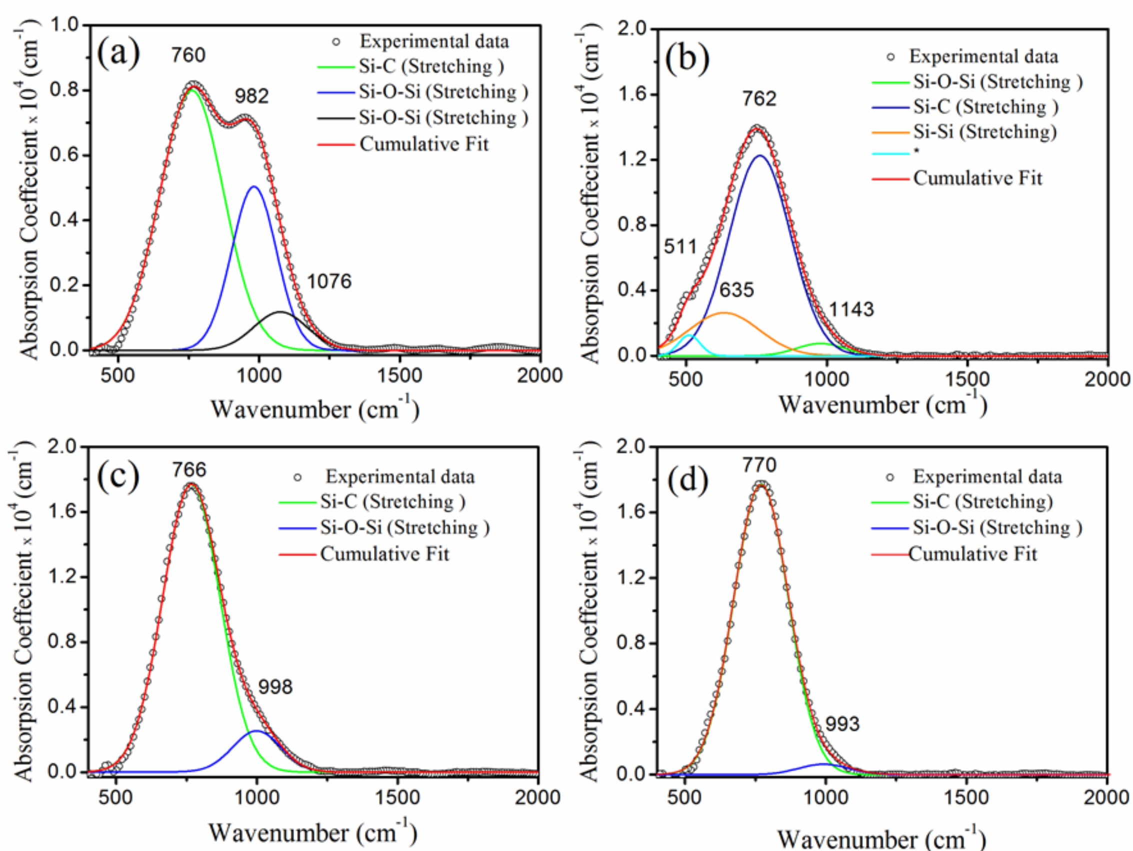

Figure 5.8 *Absorption coefficient of PLD a-SiC thin films fabricated at different T_s - (a) RT, (b) 250°C, (c) 500°C and (d) 750°C, respectively.*

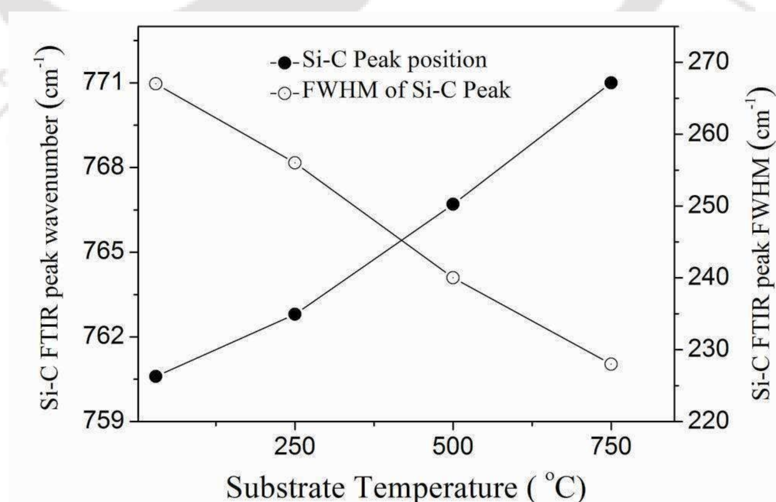

Figure 5.9 *Variation of FTIR (a) peak wavenumber and (b) corresponding FWHM of Si-C peak in a-SiC thin films as a function of T_s.*

TH-1680_10612114

integrated intensity of absorption of the band is given by the following relation [15],

$$N = N_0 \int \left(\frac{\alpha(\omega)}{\omega}\right) d\omega \qquad (5.2)$$

where N_o is the proportionality constant and $\alpha(\omega)$ is the absorption coefficient at a wavenumber ω. For Si-C the value of N_o is 2.13×10^{19} cm^{-2}. This relation was used to estimate the bond density from the FTIR measurements. *Figure 5.10* shows the variation of estimated Si-C bond density ($N_{Si\text{-}C}$) with T_s. The bond density of SiC thin films increases with increasing T_s and attains a maximum of 13.3×10^{22} cm^{-3} at 500°C and then slightly reduces to 12.2×10^{22} cm^{-3} at 750°C. The increase in $N_{Si\text{-}C}$ of the samples at higher T_s could be because of the increased probability of recombination of Si and C atoms due to increased surface mobility at higher surface temperatures. Hence from FTIR results it can be inferred that at high temperature of 500°C and 750°C, a-SiC with better stoichiometry and improved crystallinity was formed. This is also confirmed by Raman spectra (*Figure 5.5*), XRD results (*Figure 5.3*) as well as SAED patterns, *Figure 5.2*.

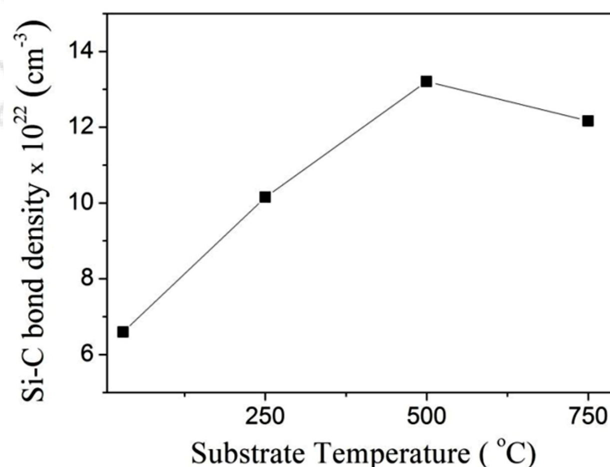

Figure 5.10 *Variation of Si-C bond density of PLD a-SiC thin films as a function of T_s.*

TH-1680_10612114

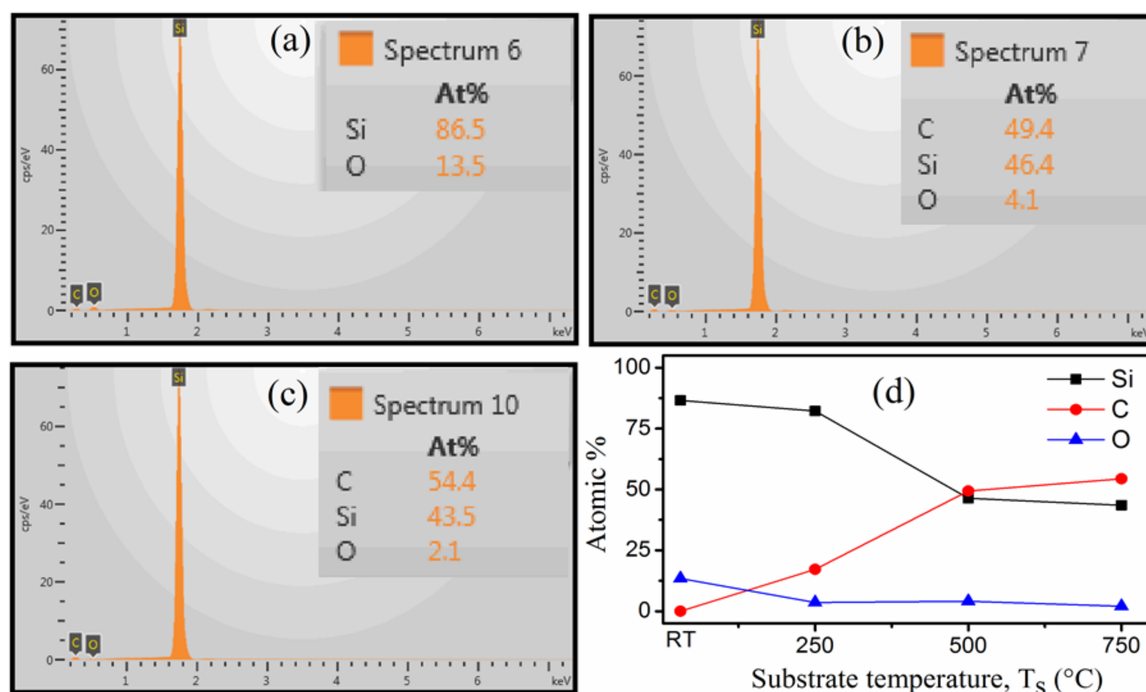

Figure 5.11 *EDX spectra of PLD a-SiC films deposited at T_s of (a) RT, (b) 500°C and (c) 750°C respectively, while (d) shows the variation of atomic percentages of Si, C and O with increasing T_s.*

Figure 5.11(a), *5.11(b)* and *5.11(c)* show the EDX spectra of a-SiC films deposited at T_s of RT, 500°C and 750°C, respectively. These spectra show the presence of silicon (Si), carbon (C) and oxygen (O) with respective atomic percentage listed at upper right corner of each spectrum. The variation of atomic percentages of Si, C and O with T_s is depicted in *Figure 5.11(d)*. The spectra were recorded at several locations within an approximate area of 100 µm × 200 µm in each film. A small change (±2-3%) was observed in atomic percentages of the Si and C. With the increasing T_s from RT to 750 °C, the atomic percentage ratio C/Si was observed to be increasing from 0 to 1.25 indicating transition of stoichiometry of the a-SiC films from Si-rich to nearly stoichiometric a-SiC films. The content of oxygen which was already minimal was observed to reduce with increasing T_s.

TH-1680_10612114

5.2.4 Linear optical properties of PLD a-SiC thin films:

The UV-Visible transmission spectra of the PLD a-SiC films deposited on fused silica substrate as shown in *Figure 5.12*, exhibit the interference fringes indicating good quality optically flat films. The refractive index (n), extinction coefficient (k) and thickness (d) of the a-SiC films were determined from the respective transmission spectra. The transmission spectra of the a-SiC films exhibited an absorption edge in the wavelength range of 250-600 nm. As the transmission fringes were visible for all the films, Swanepole's envelop method [19] was employed for estimation of refractive index and thickness. *Figure 5.13* shows the UV-Vis-IR transmission spectrum along with interpolated transmission maxima (T_{max}) and transmission minima (T_{min}) for SiC thin film deposited at 750 °C as an example. Here, T_{max} and T_{min}, at each wave length, is taken from interpolated envelop data coinciding every experimentally observed maxima and minima of transmission spectra.

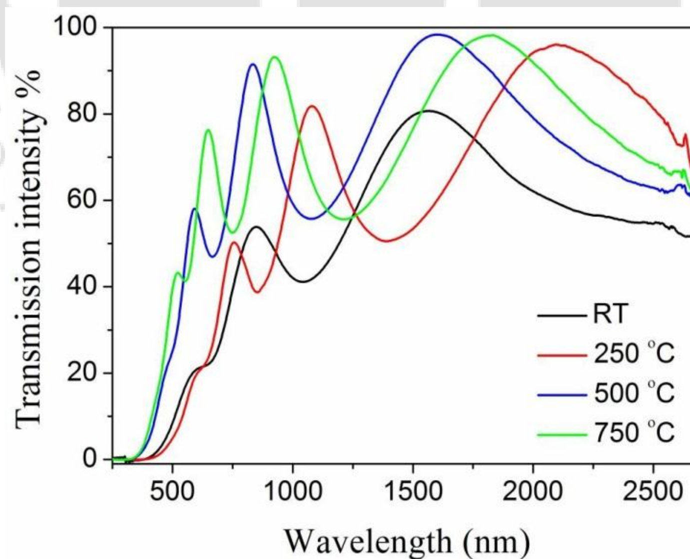

Figure 5.12 *UV-Vis-IR transmission spectra of PLD a-SiC thin films deposited at different T_s.*

TH-1680_10612114

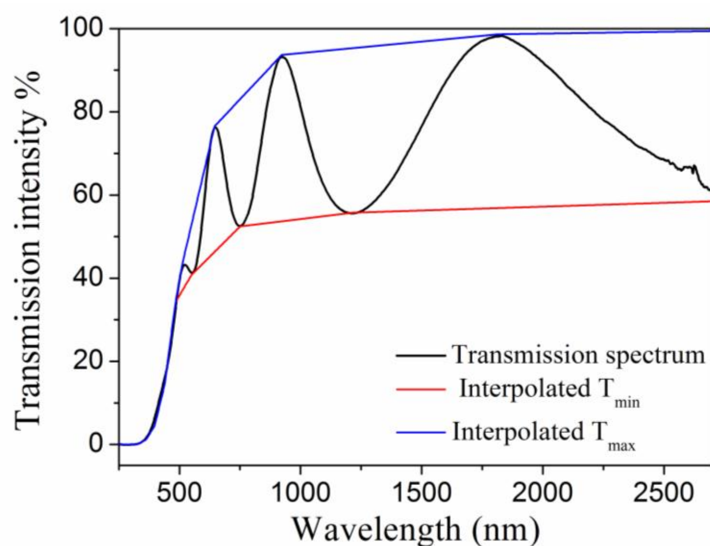

Figure 5.13 *UV-Vis-NIR transmission spectrum of PLD a-SiC thin film deposited at 750 °C substrate temperature along with interpolated* T_{max} *and* T_{min} *curves.*

Table 5.1 *Static refractive indices (*n_0*), film thicknesses estimated by envelop method (d) and measured by step profilometer (*d_{step}*) for PLD a-SiC thin films as a function of* T_s*.*

T_s (°C)	n_0	*d* (nm)	d_{step} (nm)
RT	2.99	255	215-245
250	2.85	360	322-330
500	2.63	300	288-297
750	2.55	330	320-336

The static refractive index (n_0) and film thickness were estimated using equation 2.1 and 2.4, respectively as discussed in *Chapter 2*. The thickness of films d_{step} was also measured directly using step profilometer. The n_0, d and d_{step} are listed in the *Table 5.1*. The variation of n as a function of wavelength in the spectral range of 250 nm-3000 nm is shown in *Figure 5.14*. The refractive index decreases with the increasing wavelength indicating normal dispersion behavior. The value of n_0 is found to be decreasing from 2.99 to 2.55, with the increase in the T_s from RT to 750 °C. As the growth temperature

TH-1680_10612114

increases the film composition is found to be changing from Si-rich to near stoichiometric SiC, hence refractive index decreases.

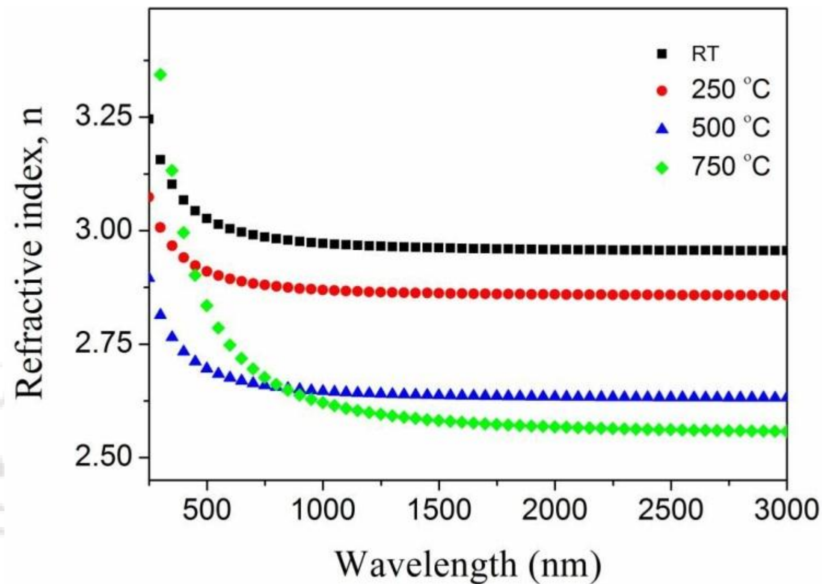

Figure 5.14 *Variation of refractive index as a function of wavelength for PLD a-SiC films deposited at different* T_s.

The absorption coefficient estimated from equation (2.6) for the a-SiC thin films was plotted as a function of photon energy in *Figure 5.15* and the inset shows the *ln*(α) vs. *hν* plots for all the samples. A gradual shift of absorption edge toward higher photon energy was observed with increasing T_s. The plot has a linear region within 1.5 to 3 eV which corresponds to Urbach tail of absorption coefficient. The slope of this linear region was calculated by least square fitting and corresponding Urbach Energy (E_U) was estimated for all the films. The *α* for Tauc region was estimated using equation 2.7 and $(\alpha h\nu)^{1/2}$ vs. *hν* was plotted for all the films as depicted in *Figure 5.16 (a)*. The intercept estimated by extrapolating the linear region of the $(\alpha h\nu)^{1/2}$ vs. *hν* plot on the *hν* axis gave the optical band gap, E_g for the SiC thin film. A gradual blue shift in E_g from 1.58 (±0.02)

TH-1680_10612114

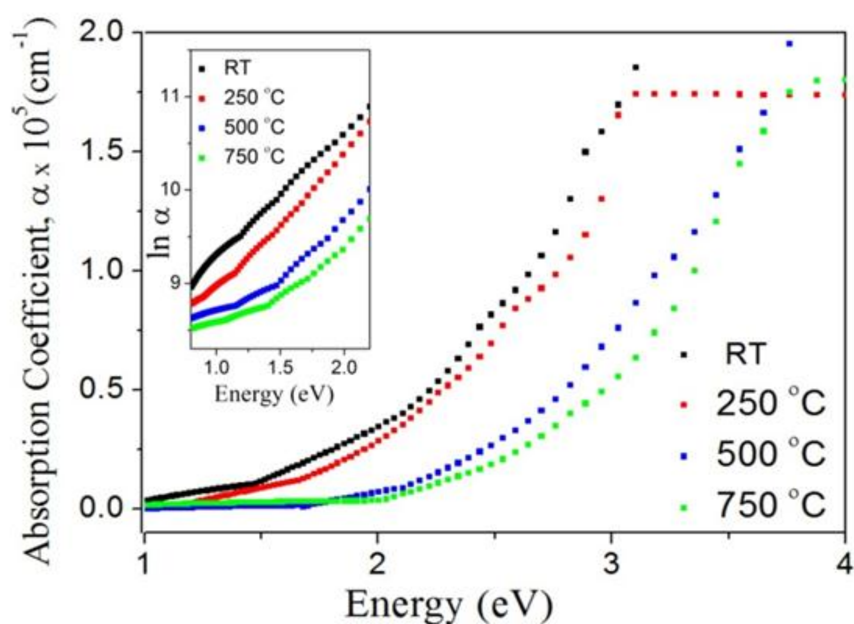

***Figure 5.15** Plot of absorption coefficient as a function of photon energy for PLD a-SiC films deposited at different T_s. Inset shows the plot of ln α vs hν at different T_s.*

to 2.32(±0.03) eV was observed in the films with increasing substrate temperature from RT to 750 °C as shown in the *Figure 5.16 (b)*.The observed blue shift of band gap can be explained on basis of ratio of C/Si content of films. With increasing growth temperature, the film composition changes from Si- rich to near stoichiometric a-SiC, as confirmed by Raman studies (*Figure 5.4*) as well as EDX studies (*Figure 5.11d*) and hence the optical band gap increases. The maximum optical band gap reported for sp^3 rich a-C films is around 3 eV and that of stoichiometric a-SiC is around 2.3 eV. These are much higher than that of a-Si (1.5-1.6 eV at RT). The thin film deposited at RT which was Si-rich, though had more sp^3 fraction of carbon in it, but Si content was much larger than C as evident from Raman spectrum (*Figure 5.4a*) as well as EDX results, *Figure 5.11*. The valence band maxima and conduction band minima was dominated by Si–Si bonding and antibonding levels, respectively hence it reflects Si like low optical band gap. In the film deposited at 750 °C, where ratio of $I_{c\text{-}c}$ to $I_{Si\text{-}Si}$ increased, the conduction band minima was

TH-1680_10612114

determined by Si–C and C-C antibonding levels. The energy of the Si–C and sp^3 rich C-C antibonding level is higher than that of Si–Si antibonding level (indicated by the large optical band gaps of c- SiC as well as sp^3 rich C) resulting in higher optical band gap of the a-SiC film deposited at 750 °C.

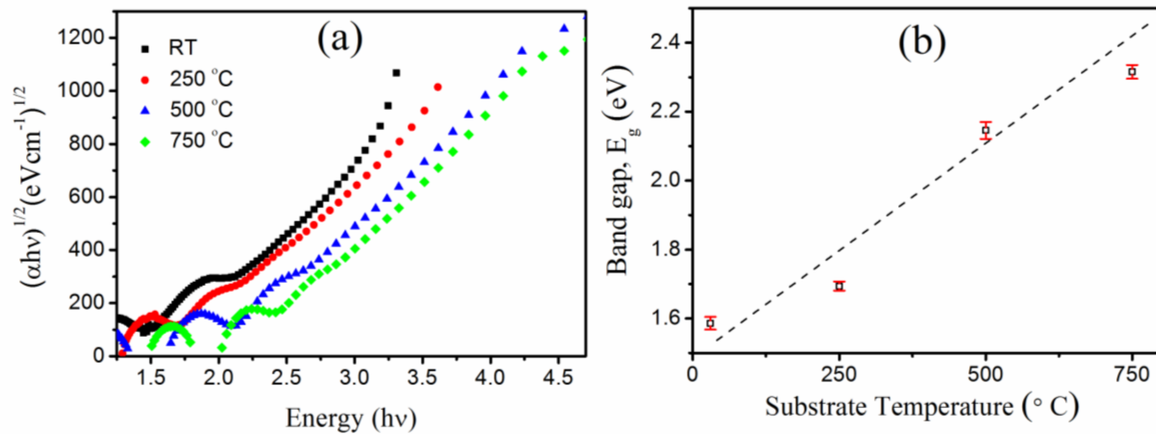

Figure 5.16 *(a) Tauc plots for determining optical band gap (E_g) of a-SiC films deposited at different T_s and (b) variation of E_g of PLD a-SiC thin films with T_s.*

Figure 5.17 shows the changes in E_U and *B* parameter (equation 2.9) with increasing T_s. It has been reported that the E_U and the *B* parameter are related to the local and overall structural disorder in the films, respectively [20]. The E_U of the a-SiC thin films decreases gradually from 760 to 600 meV with the increase in T_s. The decrease in E_U at higher T_s reflects the steep fall of absorption curve resulting smaller band tails. A material with higher structural disorder has a larger tail in absorption edge. Hence smaller band tail in a-SiC, deposited at higher T_s, reflect relatively low structural disorder. The *B* parameter first slightly decreased from 502 $(eVcm)^{-1/2}$ for film deposited at RT to 480 $(eVcm)^{-1/2}$ for that of deposited at 250 °C and then gradually increased to 540 $(eVcm)^{-1/2}$ for T_s = 750 °C. In most of the earlier published results, it has been reported that *B* parameter of a-SiC films reduces as C content increases beyond stoichiometric point of

TH-1680_10612114

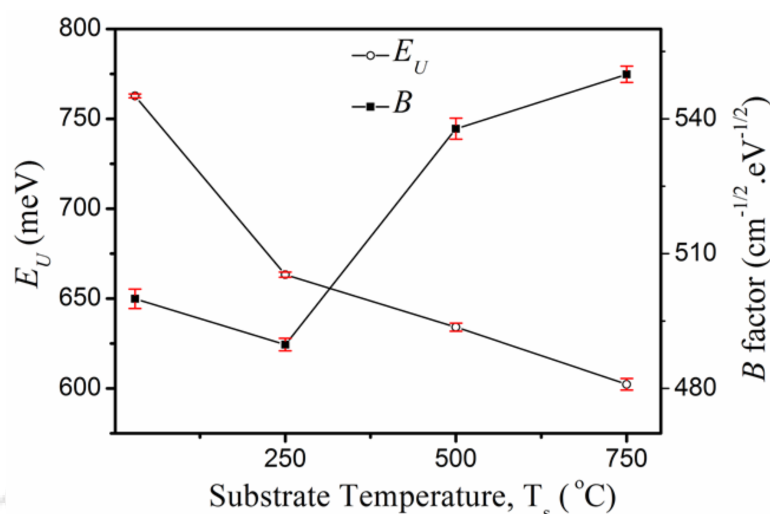

Figure 5.17 *Variations of E_U and B parameter of PLD a-SiC thin films fabricated with increasing T_s from RT to 750°C.*

SiC (C-rich SiC film). Sussman *et al.* [21] had reported that a decrease in the *B* parameter is due to a pronounced widening of the localized tail states as the carbon concentration is increased. This widening of the localized band tail states, in turn, is indicative of the increased disorder in the film [20, 22, 23]. In present case, the *B* parameter increased with increasing T_s indicating definite reduction in disorder. This could be due to the fact that the films fabricated at lower T_s were Si-rich a-SiC thin films which have higher structural disorder due to lack of stoichiometry. With increasing T_s there was a transition of a-SiC films from being Si-rich to nearly stoichiometric a-SiC, but not C-rich and hence less disordered as indicated by higher value of B parameter, which is in confirmation with XRD, Raman spectra as well as EDX spectra.

5.3 Conclusion:

Nanostructured amorphous SiC thin films were fabricated by PLD technique as a function of T_s. The role of T_s in changing the structural, composition, optical properties

TH-1680_10612114

and surface morphology of a-SiC PLD thin films were studied. The SiC thin films showed amorphous feature as confirmed by XRD and Raman studies. The thin films exhibited slight improvement in crystallinity at higher T_s as reflected by the appearance of XRD peak corresponding to *β*-SiC (111) plane. The stoichiometry of a-SiC films was observed to be changing from Si-rich to more stoichiometric a-SiC with increasing T_s from RT to 750 °C as confirmed by Raman spectra as well as EDX spectra. The refractive index in UV-Vis-NIR region measured from the transmission spectra is found to be decreasing with increasing T_s. Band gap calculated using Tauc plot was found to be blue shifted from 1.59eV to 2.33eV with increasing growth temperature which is due to the gradual increase in carbon content at elevated temperatures and transforming them to near stoichiometric a-SiC. FTIR results showed that the films basically composed of Si-C bonds and that fabricated at elevated temperatures were more ordered. TEM images showed increase in particle size while SAED pattern confirmed slight improvement in crystallinity of films with increase in T_s. The FESEM results showed the uniform growth of nanostructure with particles size increasing with increase in T_s.

TH-1680_10612114

Bibliography

[1] S.Y. Myong, S.S. Kim, K.S. Lim, In situ ultraviolet treatment in an Ar ambient upon p-type hydrogenated amorphous silicon–carbide windows of hydrogenated amorphous silicon based solar cells, Applied Physics Letters, 84 (2004) 5416.

[2] T. Ma, J. Xu, J. Du, W. Li, X. Huang, K. Chen, Full color light emission from amorphous SiC_x:H with organic–inorganic structures, Journal of Applied Physics, 88 (2000) 6408.

[3] M. Fernandes, M. Vieira, I. Rodrigues, R. Martins, Large area image sensing structures based on a-SiC:H: a dynamic characterization, Sensors and Actuators A: Physical, 113 (2004) 360-364.

[4] M. Akiyama, M. Hanada, H. Takao, K. Sawada, M. Ishida, Excess Noise Characteristics of Hydrogenated Amorphous Silicon p-i-n Photodiode Films, Japanese Journal of Applied Physics, 41 (2002) 2552-2555.

[5] Y.H. Joung, H.I. Kang, J.H. Kim, H.S. Lee, J. Lee, W.S. Choi, SiC formation for a solar cell passivation layer using an RF magnetron co-sputtering system, Nanoscale research letters, 7 (2012) 22.

[6] T. Ma, J. Xu, K. Chen, J. Du, W. Li, X. Huang, Red–green–blue light emission from hydrogenated amorphous silicon carbide films prepared by using organic compound xylene as carbon source, Applied Physics Letters, 72 (1998) 13.

[7] D.A. Anderson, W.E. Spear, Electrical and optical properties of amorphous silicon carbide, silicon nitride and germanium carbide prepared by the glow discharge technique, Philosophical Magazine, 35 (1977) 1-16.

[8] T. Shimada, Y. Katayama, K.F. Komatsubara, Compositional and structural properties of amorphous Si_xC_{1-x} :H alloys prepared by reactive sputtering, Journal of Applied Physics, 50 (1979) 5530.

[9] A. Keffous, K. Bourenane, M. Kechouane, N. Gabouze, T. Kerdja, Morphological, structural and optical properties of thin SiC layer growth onto silicon by pulsed laser deposition, Vacuum, 81 (2007) 632-635.

[10] M. Tabbal, A. Said, E. Hannoun, T. Christidis, Amorphous to crystalline phase transition in pulsed laser deposited silicon carbide, Applied Surface Science, 253 (2007) 7050-7059.

[11] J. Won Dong, M.O. Ramirez, H. Kang, V. Gopalan, N.F. Baril, J. Calkins, J.V. Badding, P.J.A. Sazio, All-optical Modulation of Laser Light in Amorphous Silicon-filled Microstructured Optical Fibers, Appl. Phys. Lett., 91 (2007) 161112.

[12] P. Colomban, SiC, from Amorphous to Nanosized Materials, the Exemple of SiCFibres Issued of Polymer Precursors, in: M. Mukherjee (Ed.) Silicon Carbide - Materials, Processing and Applications in Electronic Devices, Intech, Rijeka, Croatia, 2011, pp. 169-185.

[13] C.G. Jin, X.M. Wu, L.J. Zhuge, Room-Temperature Growth of SiC Thin Films by Dual-Ion-Beam Sputtering Deposition, Research Letters in Physical Chemistry, 2008 (2008) 1-5.

[14] A.L. Baia Neto, S.S. Camargo, R. Carius, F. Finger, W. Beyer, Annealing effects on near stoichiometric a-SiC:H films, Surface and Coatings Technology, 120 (1999) 395-400.

TH-1680_10612114

[15] T. Rajagopalan, X. Wang, B. Lahlouh, C. Ramkumar, P. Dutta, S. Gangopadhyay, Low temperature deposition of nanocrystalline silicon carbide films by plasma enhanced chemical vapor deposition and their structural and optical characterization, Journal of Applied Physics, 94 (2003) 5252.

[16] N. Tomozeiu, Silicon Oxide (SiO_x, 0<x<2): a Challenging Material for Optoelectronics in: P. Predeep (Ed.) Optoelectronics-Materials and Techniques, InTech Published online, 2011.

[17] J.A. Luna-López, G. García-Salgado, T. Díaz-Becerril, J.C. López, D.E. Vázquez-Valerdi, H. Juárez-Santiesteban, E. Rosendo-Andrés, A. Coyopol, FTIR, AFM and PL properties of thin SiOx films deposited by HFCVD, Materials Science and Engineering: B, 174 (2010) 88-92.

[18] W.C. Mohr, C.C. Tsai, R.A. Street, Properties And Local Structure Of Plasma-Deposited Amorphous Silicon-Carbon Alloys, Materials Issues in Amorphous Semiconductor Technology, 70 (1986) 319-324.

[19] R. Swanepoel, Determination of the Thickness and Optical Constants of Amorphous Silicon, J. Phys. E: Sci. Instrum. , 16 (1983) 1214-1222.

[20] V. Chu, J.P. Conde, J. Jarego, P. Brogueira, J. Rodriguez, N. Barradas, J.C. Soares, Transport and photoluminescence of hydrogenated amorphous silicon–carbon alloys, Journal of Applied Physics, 78 (1995) 3164.

[21] R.S. Sussmann, R. Ogden, Photoluminescence and optical properties of plasma-deposited amorphous Si x C1–x alloys, Philosophical Magazine Part B, 44 (1981) 137-158.

[22] Y. Catherine, A. Zamouche, J. Bullot, M. Gauthier, Ion bombardment effects in plasma deposition of hydrogenated amorphous silicon carbide films: A comparative study of d.c. and r.f. discharges, Thin Solid Films, 109 (1983) 145-158.

[23] N. Saito, T. Yamada, T. Yamaguchi, I. Nakaaki, N. Tanaka, Structural, optical and electronic properties of amorphous SiC: H alloys prepared by magnetron sputtering of silicon in methane-argon gas mixtures, Philosophical Magazine Part B, 52 (1985) 987-995.

TH-1680_10612114

Chapter 6
Third order Nonlinear optical properties of PLD Si, SiOx and a-SiC thin films

Nanostructured Si-based materials have exhibited some superlative linear and nonlinear optical properties in the recent years which have attracted attention for potential applications in variety of optoelectronics devices. It also has the advantage of compatibility with well-established Si-based micro-electronics technology. Nonlinear optical (NLO) materials are being recently explored with great interest for potential applications in optical switching, optical waveguide, optical limiting (OL), harmonic generation, information storage etc. [1]. Self-focusing displayed due to positive nonlinear refraction phenomena may be useful in reducing the optical beam-spot size below the diffraction limit and hence can be applied for enhanced density of optical data storage [2]. The bulk crystalline Si, SiC and SiO_2 possess weak NLO effect thereby restricting its applications [3, 4]. In the nano scale dimensions, spatially confined exitons are formed due to quantum confinement effect, and have been reported to play a major role in the enhancement of nonlinear optical property of nanocrystalline thin films [4, 5]. A nonlinear media can also exhibit OL behaviour by means of various nonlinear optical mechanisms which includes self-focusing, induced scattering, induced-refraction, induced aberration, excited state absorption, two-photon absorption, photo-refraction and free-carrier absorption [6]. The optical limiters are suitable for laser pulse shaping applications, passive mode locking, pulse smoothening, safety devices for sensors or eyes etc. [7, 8]. Though several forms of Si-based materials and SiC, as described in *Section 1.5* of *Chapter 1*, have been reported for NLO behaviour but the OL property has rarely

TH-1680_10612114

been reported. The NLO behavior of the Si-based films, controlled by its linear absorption and optical band gap, is reported to be dependent on the film microstructures, deposition technique and host dielectric [9, 10]. The NLO properties of thin films have been investigated experimentally by various techniques [11-15]. Among them, *Z*-scan technique has emerged as a very handy tool for measurement of third order nonlinear absorption (NLA) and nonlinear refraction (NLR) coefficients [15].

In Chapter 4 and 5 it was demonstrated that crystalline structure, surface morphology, stoichiometry and the linear optical properties of nc-Si, SiO_x and SiC thin films via PLD are influenced by deposition parameters, hence it is expected that the NLO properties will also display some dependence on these parameters. Therefore in this chapter, the measurement of the NLO coefficients using modified *Z*-scan setup under cw laser irradiation, of various nanostructured Si-based films (nc-Si, SiO_x and a-SiC) fabricated by PLD over a range of deposition parameters are presented. The NLA coefficient (β) and NLR coefficient (n_2) of these thin films have been measured by open aperture (OA) and closed aperture (CA) *Z*-scan, respectively. The third order optical susceptibility of each film was estimated from β and n_2. The OL studies were also carried out for these films. Finally a comparison of stoichiometric dependent third order susceptibility is made toward the end of this chapter.

6.1 Experimental details:

The third order NLA and NLR coefficient of PLD films was measured using modified *Z*-scan setup. The Z-scan set-up and OL set-up are detailed in Chapter 2. Both of these are briefly summarized below. For NLO studies, Si, SiO_x and a-SiC films were deposited by the PLD as detailed in *Chapter 2* and the deposition parameters for the fabrication of Si

TH-1680_10612114

along with SiO_x and a-SiC thin films are listed in *Table 4.1 (Chapter 4)* and *Table 5.1 (Chapter 5)*, respectively. In the modified Z-scan set-up, used in present thesis, a He-Ne laser was focused on the PLD thin film using a convex lens of focal length of 50 mm. The film was translated from -15 mm to +15 mm w.r.t. focal plane of the lens in a step size of 1 mm and at each step images of transmitted beam is recorded by CCD. The recorded CCD image of the transmitted beam through the thin film positioned at 10 mm from the focal point is shown in *Figure 6.1 (a)* for OA Z-scan and *(b)* corresponding masked image for CA *Z*-scan for S~ 0.40 by implementing a software aperture [16]. The transmitted intensity through the film at each location (z) was obtained by integrating the grey values of the recorded respective CCD image using a Matlab program [16]. These OA and CA *Z*-scan data were fitted to equations, 2.17 and 2.18, to obtain the β and n_2 values of the thin films.

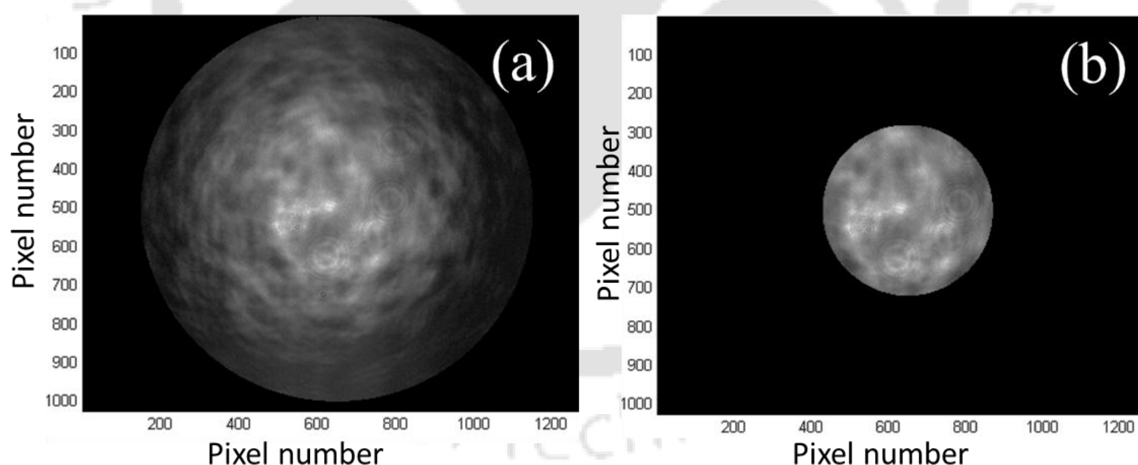

Figure 6.1 *CCD image of transmitted beam through PLD nc-Si film, fabricated at T_s=400 °C, positioned at 10 mm from the focal point: (a) open aperture and (b) closed aperture Z-scan for S~0.40.*

The OL experimental setup used was very similar to the open Z-scan geometry but the input power here was varied by using ND filters and sample was positioned fixed

TH-1680_10612114

at focus of the lens. The 32 mW power laser beam was used. The incident laser power on the sample was varied by ND filters. The images of transmission beam for each film as a function of input powers were recorded by CCD and finally output power was estimated after calibrating the CCD with the direct input laser beam. The plot of output power as a function of input power displayed the OL behavior.

6.2 Effect of substrate temperature on the third order NLO response and OL property of PLD nc-Si thin films:

In this section the results of the third order NLO and OL properties, under cw laser irradiation of nc-Si films fabricated via PLD are described.

6.2.1 Third order NLA and NLR coefficients of PLD nc-Si films:

The physical origin of NLR in any sample can be electronic, molecular, electrostrictive or thermal in nature. In the present case, in the *Z*-scan measurements a cw-laser was used, therefore optical nonlinearity induced in the films could be dominated by thermal effect. *Figure 6.2(a-e)* shows the normalized transmittance plot for OA Z-scan as a function of the sample position (z) w.r.t focus of the lens for nc-Si thin films deposited at substrate temperature (T_s) of (a) RT, (b) 200 ^{0}C, (c) 400 ^{0}C, (d) 600 ^{0}C and (e) 700 ^{0}C. The normalized OA Z scan transmittance curves for all the films exhibit minimum transmission at focus indicating the presence of strong reverse saturation absorption (RSA) in each of these Si films. The experimental data points of OA Z scan were fitted to the transmission profiles given by SBF, equation (2.17) [15] and β was calculated from the best fitted constant ‘c’. *Figure 6.2(f)* shows variation of β as a function of T_s. *Figure 6.3(a-e)* show the normalized transmittance plot for CA Z-scan as a function of the

TH-1680_10612114

sample position (z) w.r.t focus of the lens for nc-Si thin films deposited at different T_s (a) RT, (b) 200 ^{0}C, (c) 400 ^{0}C, (d) 600 ^{0}C and (e) 700 ^{0}C. All the CA z-scan spectra, show a transmittance minimum (valley) prior to focus followed by a transmittance maximum (peak) after focus. This valley-peak signature indicates the self focusing property, which corresponds to positive nonlinear refractive index n_2. The n_2 was calculated from the CA Z-scan measurment after fitting to equation (2.18) and shown in *Figure 6.3(f)* as a function of T_s. The measured value of Rayleigh length, z_o for the He:Ne laser focused by convex lens of focal length 5 cm in the present case is ~ 2.45 mm. The measured valley-to-peak separation, Δz_{pv}, is ~ 4.2 mm, close to $1.71z_0$ confirming the third order nonlinearity. Similar effects of RSA and self-focusing in refraction for Si films under cw laser and pulsed laser radiations has been reported by other researchers [17]. As the cw-laser was used in *Z*-scan experiment, the origin of optical nonlinearity is attributed mainly to the thermal effects. The nc-Si thin films being an indirect band gap material, the probability of optical transition is a function of phonon population density also. The rise in sample temperature, caused by cw laser heating, leads to shrinkage in the band gap of silicon and increase in phonon density [3, 17]. In the focal region, the laser intensity being maximum results in maximum laser induced heating in the sample. But while moving away from the focal region, on either side, laser induced heating gets curtailed due to the gradual fall of laser intensity. Therefore, the generated phonon density within the material is larger at the focus compared to that of at other locations. Hence the probability of phonon mediated optical absorption in this indirect band gap Si thin film is maximum (minimum transmission) at focus while the absorption decreases as the sample moves away from focus on either side, resulting RSA. Another major contribution for RSA could be phonon assisted free carrier absorption. Moreover, as the Gaussian beam

TH-1680_10612114

from a cw laser propagates through an absorbing sample, light is absorbed and immediately gives rise to local heating producing spatially varying temperature field. The refractive index which depends linearly on temperature forms a spatially varying

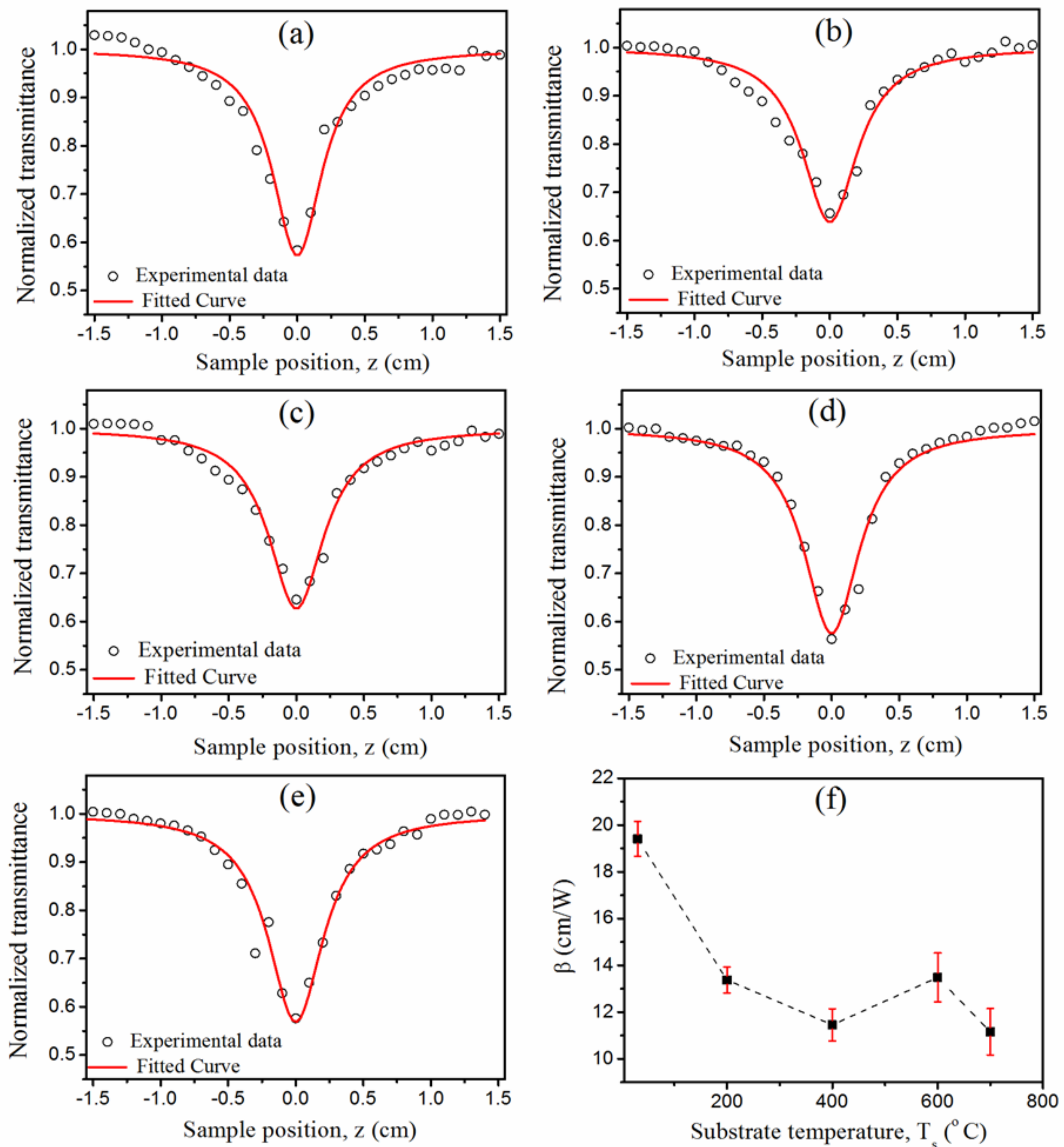

Figure 6.2 *Open aperture Z-scan Normalized Transmittance curve of nc-Si thin films deposited at substrate temperature of (a) RT, (b) 200 °C, (c) 400 °C, (d) 600 °C and (e) 700 °C while (f) shows variation of β as a function of substrate temperature.*

TH-1680_10612114

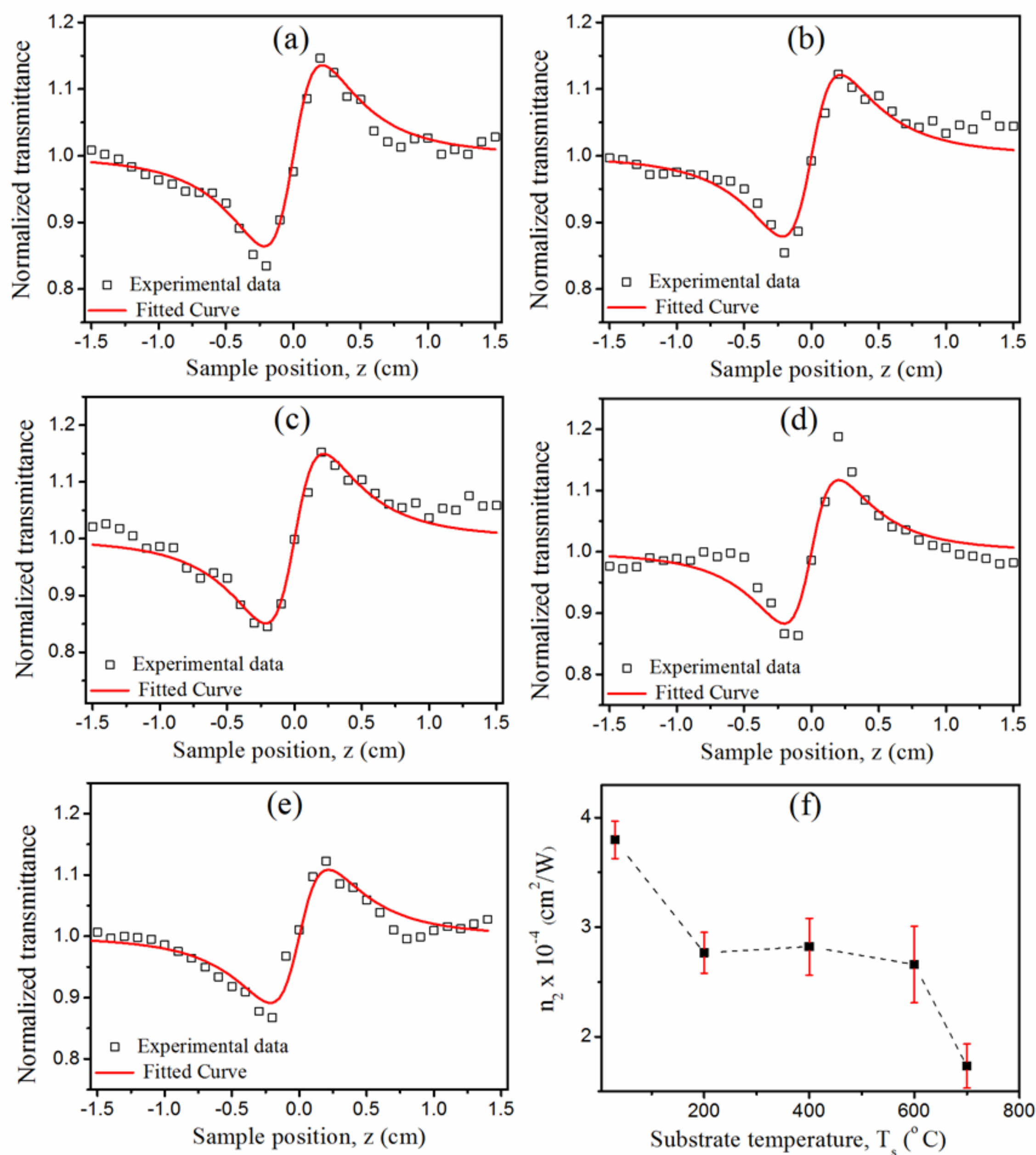

***Figure 6.3** Closed aperture Z-scan Normalized Transmittance curve of nc-Si thin films deposited at substrate temperature of (a) RT, (b) 200 °C, (c) 400 °C, (d) 600 °C and (e) 700 °C while (f) shows variation of n_2 as a function of substrate temperature.*

refractive index region forming a thermal lens and hence the films exhibited self-focusing effect [18, 19]. The β and n_2 of the nc-Si thin films as a function of deposited T_s is

TH-1680_10612114

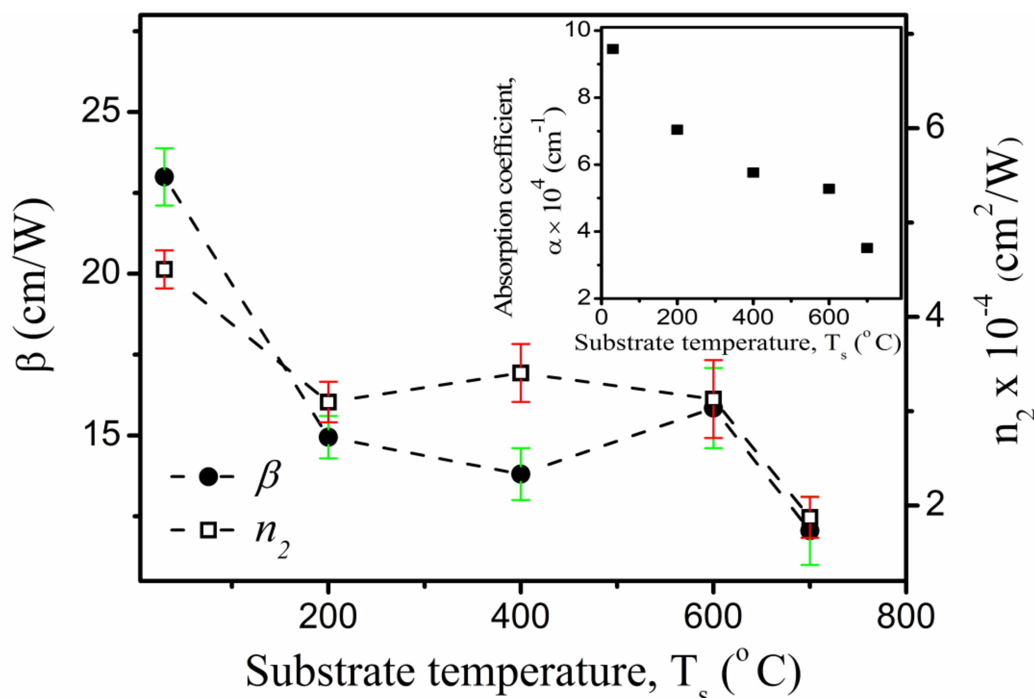

Figure 6.4 *Variation of nonlinear absorption coefficient (β) and nonlinear coefficient of refraction (n_2) of nc-Si thin films as a function of T_s. Dotted lines are not fitted lines but are only guide for eyes. Inset shows the variation of linear absorption coefficient (α) at λ = 632 nm, with increasing T_s.*

depicted again in *Figure 6.4*. The value of *β* for the nc-Si films was observed to be decreasing from 22.9 cm/W to 13.8 cm/W as T_s increases from RT to 400 ˚C, then it slightly increases to 15.8 cm/W for Si film deposited at 600 ˚C while finally decreasing to 12 cm/W at 700 ˚C. The n_2 for the nc-Si films was observed to be decreasing from 4.5 × 10^{-4} cm^2/W to 3.1 × 10^{-4} cm^2/W as T_s increases from RT to 200 ˚C, then it becomes nearly invariant with increasing T_s while finally decreasing to 1.9 × 10^{-4} cm^2/W at 700 ˚C. This change in the values of *β* and n_2 of Si films as a function of T_s can be corelated with the linear absorption coefficient, *α* (at λ = 632.8 nm) which changes in similar manner with increasing T_s as shown in the inset of *Figure 6.4*. The decrease in *α* reduces laser

TH-1680_10612114

heating in the films resulting in reduced production of phonon. This decline in phonon density reduces the probability of optical absorption in these indirect band gap Si thin films resulting in the decrease in RSA coefficient, β, with decreasing α and vice versa. The effective thermal nonlinear refractive index of the medium can be written as [19],

$$n_2^{th} = \left(\frac{dn}{dT}\right)\left(\frac{w_0}{2}\right)^2\left(\frac{\alpha}{k}\right) \quad (6.1)$$

where $k = D\rho C_p$, D is thermal diffusivity, ρ is material density and C_p is specific heat of the thin films. For small changes of linear refractive index w.r.t. temperature (dn/dT), the n_2 solely depends on the ratio of α/k. In the present work, the values of α in these thin films were found to change with the T_s, explaining the similar trend of n_2 as a function of T_s.

The real and imaginary part for $\chi^{(3)}$ of all the nc-Si thin films were calculated from the respective values of n_0, n_2 and β_{eff} obtained from the experiments using equations (2.22) and (2.23). The calculated values of n_0, n_2, α, β, $\chi^{(3)}_R$ and $\chi^{(3)}_I$ for the PLD nc-Si thin films deposited at different T_s are listed in *Table 6.1*. The significant large nonlinear third order optical susceptibility was observed in the nc-Si thin films in present case as compared to that of bulk Si. For all the films, positive nonlinearity was observed. The $\chi^{(3)}_R$ and $\chi^{(3)}_I$ observed were of the order of 10^{-1} esu and 10^{-2} esu, respectively, which is 10^9 times higher than that of observed in bulk Si [3]. This can be attributed to limitations imposed by the quantum size effects. In smaller dimension the oscillator strength enhances and interaction of the local electric field of the light with nanostructures in these films becomes stronger. The observed values of $\chi^{(3)}_R$ and $\chi^{(3)}_I$ of the nc-Si thin films fabricated by PLD were one order of magnitude higher than that of polycrystalline 300 nm Si thin film reported by Choi *et al* [17].

TH-1680_10612114

Table 6.1. *n_2, α, β, $\chi_R^{(3)}$, $\chi_I^{(3)}$ and $\chi^{(3)}$ for the PLD nc-Si thin films deposited at different T_s.*

Substrate Temperature, T_s (^{0}C)	Non linear Refractive index, n_2 (cm^2/W) $\times 10^{-4}$	Linear absorption coefficient, α (cm^{-1}) $\times 10^4$	Nonlinear absorption coefficient, β (cm/W)	$\chi_R^{(3)}$ (esu) $\times 10^{-1}$	$\chi_I^{(3)}$ (esu) $\times 10^{-1}$	$\chi^{(3)}$ (esu) $\times 10^{-1}$
RT	4.50±0.20	9.45	22.99±0.88	2.68	0.97	2.86±0.15
200	3.09±0.21	7.04	14.94±0.65	1.45	0.48	1.53±0.14
400	3.33±0.30	5.75	13.80±0.80	1.85	0.50	1.92±0.23
600	3.12±0.41	5.27	15.84±1.23	1.32	0.43	1.39±0.23
700	1.87±0.21	3.50	12.05±1.05	0.63	0.24	0.67±0.09

6.2.2 Optical limiting in PLD nc-Si thin films:

The materials with large nonlinear RSA can be used as optical limiters. An ideal optical power limiter has a linear transmission below a particular threshold and above this the output becomes constant. This property could be used for providing safety to sensors or eye. The OL can be achieved by means of various NLO mechanisms, including self-focusing, self-defocusing, induced scattering, induced-refraction, induced aberration, excited state absorption, two-photon absorption, photo-refraction and free-carrier absorption in nonlinear optical media [6]. The OL behavior of all the films was studied under cw laser illumination using the set-up shown in 2.10. *Figure 6.5* shows the characteristic optical limiting curves for the nc-Si films deposited at various T_s. In the present case, the OL is due to RSA induced by local heating caused by absorption of laser in these semiconducting films [6]. It is shown clearly in *Figure 6.4* that at low incident laser power, the output varies linearly with input power and deviates from it displaying the signature of saturation at higher laser powers. The point of onset of deviation from linearity of the plot of output laser power versus input laser power is termed as optical limiting threshold. The deviations from linearity began at around 8 mW for all the films

TH-1680_10612114

except that of deposited at 700 ˚C for which threshold was observed at slightly higher power of around 12 mW. This is due to the fact that this particular sample, fabricated at 700 ˚C had minimum value of *β*.

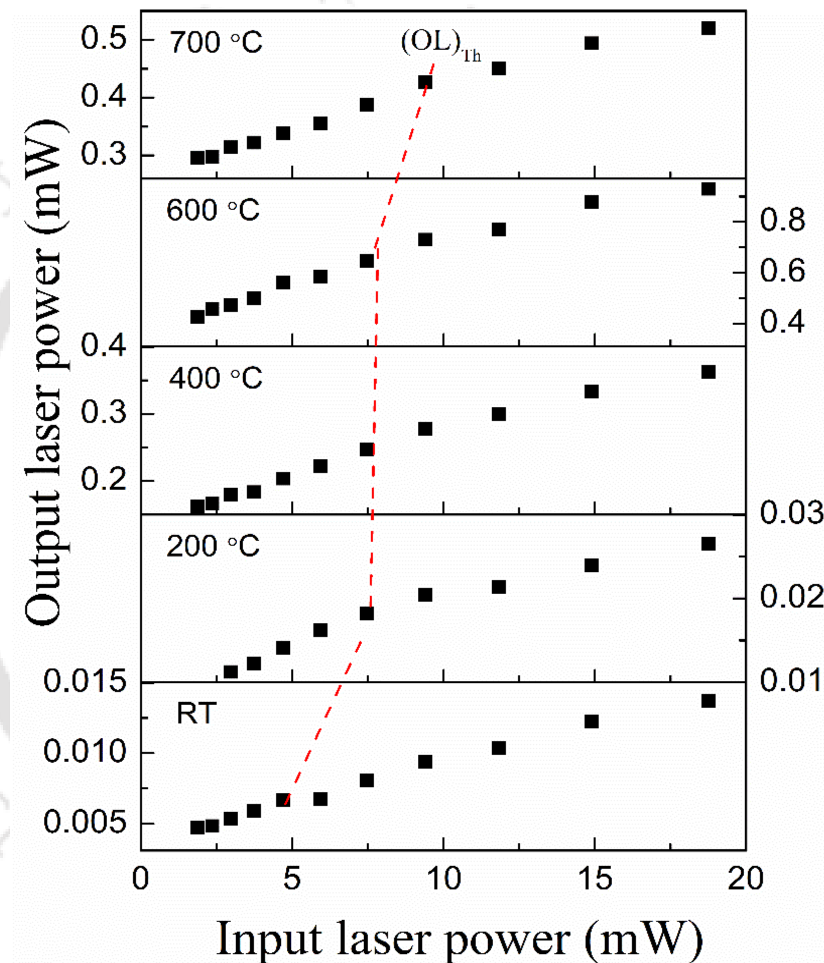

Figure 6.5 *Optical limiting response of nc-Si films deposited at various T_s. The variation of OL threshold as a function T_s is depicted by broken red line.*

TH-1680_10612114

6.3 Effect of oxygen pressure on the third order NLO response and OL property of PLD SiO_x thin films:

The SiO_x films fabricated via PLD comprised of nc-Si embedded in SiO_2 matrix as was confirmed by Raman and EDX studies, *Chapter 4*. Therefore these films are expected to exhibit NLO properties similar to that of nc-Si films as described in *Section 6.2*. The stoichiometry of SiO_x films was found to be dependent on background oxygen pressure during PLD and hence it is expected that same may get reflected in NLO properties too. In this section stoichiometric dependent NLO propertries of SiO_x (x~0.01 to 2.14) films is detailed along with their OL properties.

6.3.1 Third order NLA and NLR coefficients by modified Z-scan technique:

The normalized OA *Z*-scan transmittance curves for all the SiO_x films, reported in Chapter 4, are shown in *Figure 6.6 (a)*. Except the film deposited under O_2 pressure of 0.5 mbar (*Figure 6.6-e*), all the other films clearly exhibited minimum transmission at focus indicating the presence of strong reverse saturation absorption (RSA). The experimental data points for open *Z*-scan were fitted to the transmission profile given by equation (2.17) and β was calculated from the best fitted constant 'c'. The β values for the SiO_x thin films as a funtion of O_2 pressure are listed in *Table 6.2*. In the CA *Z*-scan, *Figure 6.6(b)*, normalized transmission curves showed a transmittance minimum (valley) prior to focus followed by a transmittance maximum (peak) after focus for all the films, indicating positive nonlinear refraction coefficient. The value of n_2 was calculated by fitting the data of the closed aperture *Z*-scan measurment to equation (2.18) and are listed in *Table 6.2* as a function of O_2 pressure. The measured valley-to-peak separation, $\Delta z_{pv} \sim$ 4.2 mm which amounts to ~1.71 times of Raleigh length (z_0 ~ 2.45 mm) indicating the

TH-1680_10612114

presence of third order nonlinearity [15]. The similar NLO behavior; self-focusing and reverse saturation absorption had been reported for Si films (fabricated by PECVD) under femto second and cw laser radiation [4, 17] as well as PLD films of nc-Si as discussed in the previous *Section 6.2*. The rise in sample temperature, caused by cw laser heating resulting in the RSA effect similar to that of Si films discussed in the *Section 6.2*.

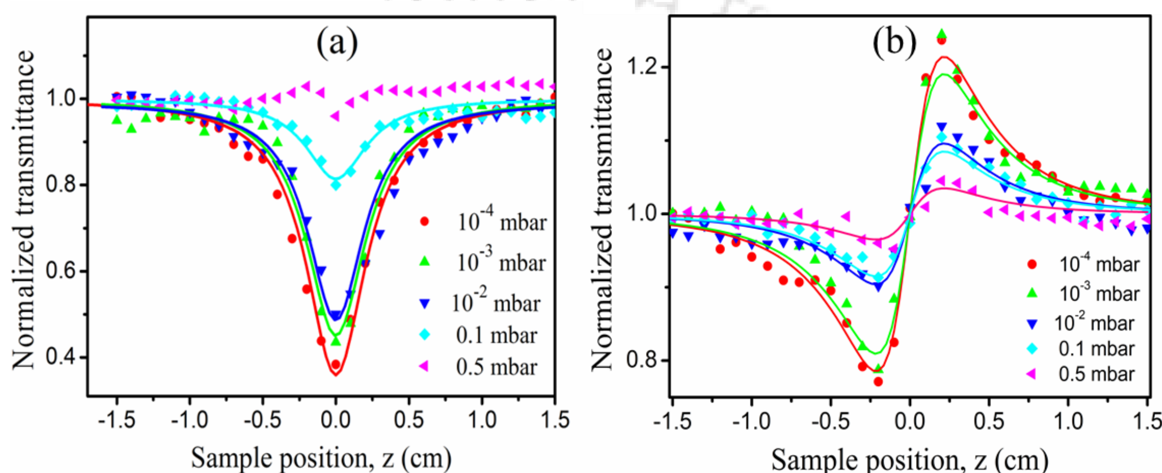

Figure 6.6 *Z scan spectra of SiO_x films (a) Open aperture and (b) Closed aperture (Symbols: measured data points, continuous line: fitted curve).*

The values of $\chi^{(3)}_R$, $\chi^{(3)}_I$ and $\chi^{(3)}$calculated using equations (2.22), (2.23) and (2.24) respectively, for the PLD SiO_x thin films as a function of O_2 pressure are listed in *Table 6.2*. For all the films, positive nonlinearity was observed. The values of $\chi_R^{(3)}$ and $\chi_I^{(3)}$ observed were of the order of 10^{-1} - 10^{-3} *esu* and 10^{-2} - 10^{-3} *esu*, respectively, with increasing oxygen content, and is 10^9 times higher than that of observed in bulk Si [3]. This again can be attributed to limitations imposed by the quantum size effects as described for the case of nc-Si films in *Section 6.2* [5]. The observed values of $\chi_R^{(3)}$ and $\chi_I^{(3)}$ of SiO_x thin films fabricated at O_2 pressure of 10^{-3} to 0.1 mbar were of the same order of magnitude as that of 300 nm thick polycrystalline Si film reported by Y. Choi *et al*.

TH-1680_10612114

Table 6.2 *n_2, α, β, $\chi_R^{(3)}$, $\chi_I^{(3)}$ and $\chi^{(3)}$ for the PLD SiO_x thin films deposited at different O_2 pressure.*

Oxygen pressure (mbar)	Nonlinear Refractive index, n_2 (cm^2/W) × 10^{-5}	Linear absorption coefficient, α (cm^{-1}) × 10^4	Nonlinear absorption coefficient, β (cm/W)	$\chi_R^{(3)}$ (esu) × 10^{-3}	$\chi_I^{(3)}$ (esu) × 10^{-3}	$\chi^{(3)}$ (esu) × 10^{-3}
10^{-4}	44.18±7.30	5.09	21.44±3.37	219.79	67.29	229.8±44.06
10^{-3}	19.92±3.80	2.12	9.23±1.61	48.49	13.08	50.22±10.62
10^{-2}	8.41±1.58	1.91	8.31±1.52	19.04	10.24	21.61±4.52
10^{-1}	6.61±1.53	0.43	2.08±0.46	8.08	1.36	8.19±2.07
0.5	1.98±0.63	0.28	-	1.52	--	1.52±0.61

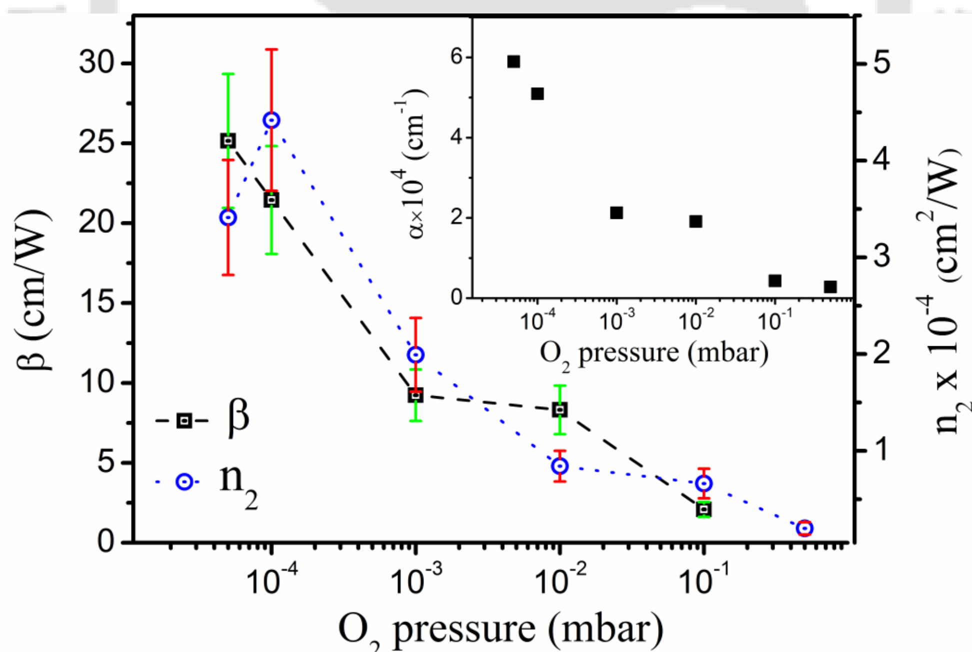

Figure 6.7 *Variation of nonlinear absorption coefficient (β) and nonlinear coefficient of refraction (n_2) of SiO_x thin films with increasing O_2 pressure (broken lines are not fitted lines but are only guide for eyes). Inset shows the variation of linear absorption coefficient (α) at λ = 632 nm, with increasing O_2 pressure.*

TH-1680_10612114

[17]. But the observed values of these NLO coefficients of the SiO_x thin films deposited at lower O_2 pressure of 10^{-4} mbar, in the present case, was one order of magnitude higher.

Figure 6.7 shows the variation of values of β and n_2 of SiO_x thin films with increasing O_2 pressure. The β for the SiO_x films was observed to be decreasing from 21.44 cm/W to 2.08 cm/W, with increase in O_2 pressure from 10^{-4} to 10^{-1} mbar. The values of n_2 for the SiO_x films was observed to be decreasing from 44.18×10^{-5} cm^2/W to 1.98×10^{-5} cm^2/W, with increase in O_2 pressure from 10^{-4} to 0.5 mbar. The decline in the values of β and n_2 with increasing deposition O_2 pressure can be corelated with the linear absorption coefficient, α, at λ = 632.8 nm (*Figure 4.18 (a)*, *Chapter 4*) which also decreases from 5.09×10^4 cm^{-1} to 0.28×10^4 cm^{-1} with increasing O_2 pressure from 10^{-4} to 0.5 mbar, respectively, as shown in the inset of *Figure 6.6* and is also presented in *Chapter 4*. This decrease in linear absorption with increase in O_2 pressure is solely due to the stoichiometric changes of the SiO_x films from Si-rich to oxygen rich. The decrease in α reduces the linear absorption induced heating in the films resulting in reduced phonon density. This decline in phonon density reduces the probability of optical absorption in the indirect band gap of SiO_x thin films resulting in the decrease in RSA coefficient, β. The *Z*-scan for these thin films was performed under cw laser illumination which can induce considerable heating in the samples producing thermally induced optical nonlinearities in SiO_x thin films as discussed in section 6.4 and equation (6.1).

6.3.2 Optical limiting in PLD SiO_x thin films:

Figure 6.8 shows the optical limiting response of the SiO_x films deposited at various O_2 pressures from 10^{-4} to 0.5 mbar. The variation of OL threshold is marked in red line. The OL threshold of SiO_x films was found to be increasing from 0.34 to 1.86

TH-1680_10612114

kW/cm^2 with increasing O_2 pressure from 10^{-4} to 10^{-1} mbar, where x changes from 0.03 to 0.85 respectively. For the film fabricated at 0.5 mbar, no clear signature of OL was observed, as SiO_x films fabricated at this pressure did not display any measureable nonlinear absorption behavior. The increase in OL threshold of the SiO_x films with increase in oxygen pressure is attributed to decrease in their β which is caused by the shift in stoichiometry of the films from Si-rich (x~0.03) to oxygen rich (x~0.85).

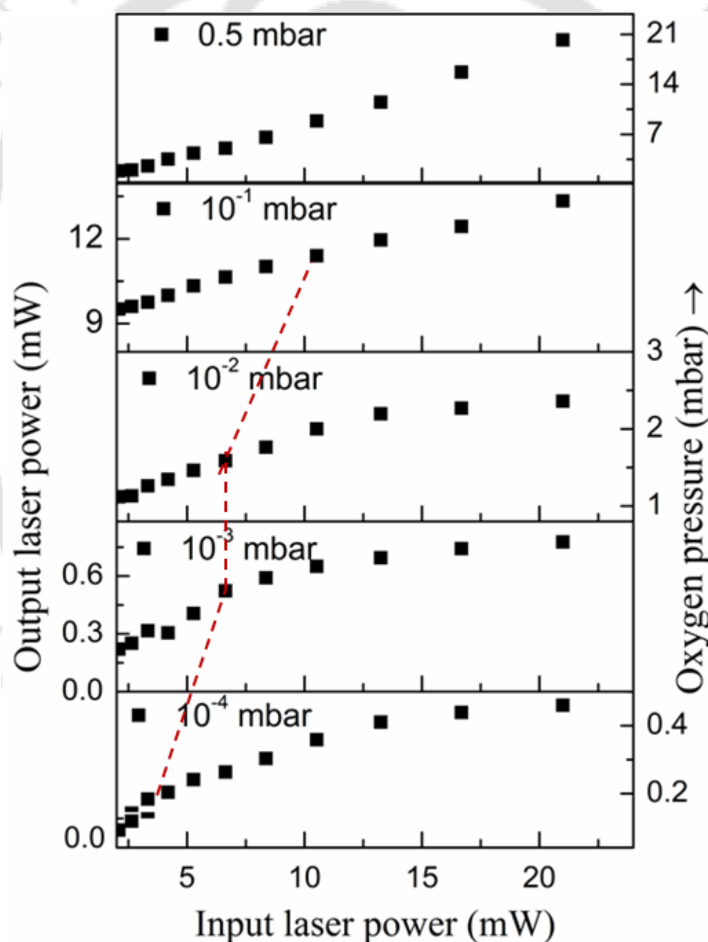

Figure 6.8 *Optical limiting response of SiO_x thin films. The red line shows the OL threshold variation as a function O_2 pressure.*

TH-1680_10612114

6.4 Effect of substrate temperature on the third order NLO properties of a-SiC thin films:

In *Chapter 5* the effect of deposition temperature (T_s) on the properties of PLD a-SiC films were presented. It is also expected that the NLO properties of these films may also exhibit some dependence on T_s. *Figure 6.9* and *Figure 6.10* show the normalized transmittance plot for open and closed aperture Z-scan as a function of the sample position w.r.t focus of the lens for a-SiC thin films deposited at various T_s. The OA Z-scan of all the films show minimum transmittance at the focus thus dispalying RSA, an indication of NLA. The NLA coefficient, β, was calculated from the nomalized

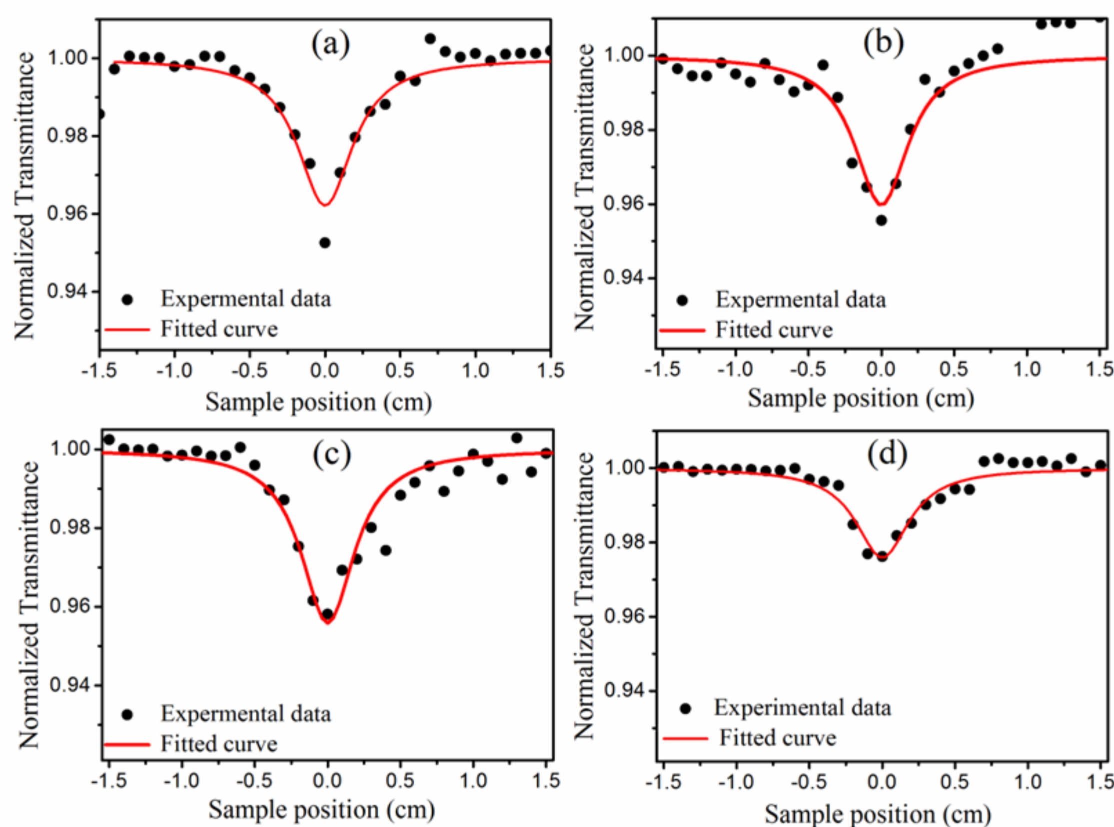

Figure 6.9 *Open Z-scan Normalized Transmission intensity for a-SiC thin films deposited at T_s = (a) RT, (b) 250 ^{0}C, (c) 500 ^{0}C and (d) 750 ^{0}C.*

TH-1680_10612114

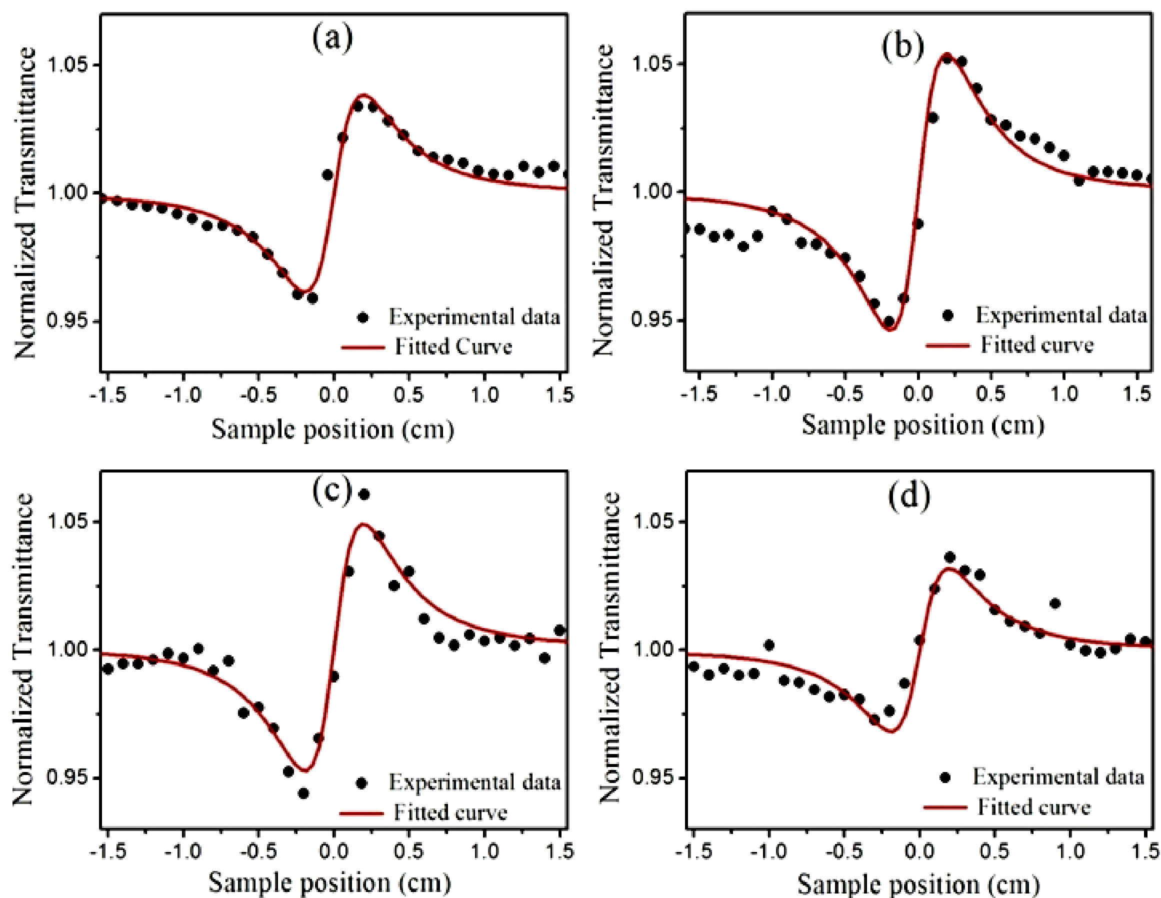

Figure 6.10 *Closed Z-scan Normalized Transmission intensity of PLD a-SiC thin films deposited at T_s = (a) RT, (b) 250 ^{0}C, (c) 500 ^{0}C and (d) 750 ^{0}C.*

transmittance data of the OA Z-scan measurement after being fitted to the equation (2.17). In the CA Z-scan, normalized transmission curves show a transmittance minimum (valley) prior to focus followed by a transmittance maximum (peak) after focus for all the films confirming the presence of positive nonlinear refractive index in these films. The CA Z-scan data was fitted to the equation (2.18). The measured valley-to-peak separation of 4.2 mm is ~ 1.7 times of Raleigh length (z_0 = 2.45 mm), confirms the presence of positive third order non linearity in the SiC films. The calculated values of n_2, α, β, $\chi_R^{(3)}$, $\chi_I^{(3)}$ and $\chi^{(3)}$ for the PLD a-SiC thin films as a function of T_s are listed in *Table 6.3*. The $\chi^{(3)}$ observed were of the order of 10^{-3} esu which is 10^{10} times higher than that of bulk SiC

TH-1680_10612114

under femtosecond laser irradiation [20]. This can be attributed to limitations imposed by the quantum size effects as described in section 6.2. Also values of $\chi^{(3)}_R$ observed in this report were 10^4 times higher than that of nanocrystalline SiC under ns-pulsed Nd-YAG laser irradiation as reported by Brodyn *et al.* [5]. In the present work, a gradual reduction in n_2 was observed with increasing T_s (*Table 6.3*). The values of α of these thin films were found to decrease with the increasing T_s, *Figure 5.15* , *Chapter 5*, due to transition of the film from Si-rich to near stoichiometric a-SiC, and hence resulting in the decrease of the n_2 (equation 6.1) of the a-SiC films with increasing T_s. In this case also the contribution of thermally induced nonlinearity is dominating one due to the cw laser induced heating.

Table 6.3 *n_2, α, ß, $\chi_R^{(3)}$, $\chi_I^{(3)}$ and $\chi^{(3)}$ for PLD a-SiC thin films deposited at different T_s.*

Substrate Temperature, T_s (^{0}C)	Non linear Refractive index, n_2 (cm^2/W) × 10^{-5}	Linear absorption coefficient, α (cm^{-1}) × 10^4	Non linear absorption coefficient, ß (cm/W)	$\chi_R^{(3)}$ (esu) × 10^{-2}	$\chi_I^{(3)}$ (esu) × 10^{-4}	$\chi^{(3)}$ (esu) × 10^{-2}
RT	7.68±2.22	4.64	0.75±0.23	1.73	8.4	1.73±0.50
250	7.55±1.97	4.16	0.81±0.23	1.59	8.5	1.59±0.41
500	5.64±1.53	2.15	0.75±0.20	1.01	6.7	1.01±0.27
750	3.14±0.87	1.39	0.34±0.08	0.58	2.8	0.58±0.16

Figure 6.11 shows a comparison of values of $\chi^{(3)}$ for all the sets of band gap engineered PLD Si-based thin films deposited over a range of parameters. These values of $\chi^{(3)}$ were solely dependent on the linear absorption coefficient which was controlled by

TH-1680_10612114

stoichiometry and crystallinity of the films, later two of which were dependent on the deposition parameters of PLD technique.

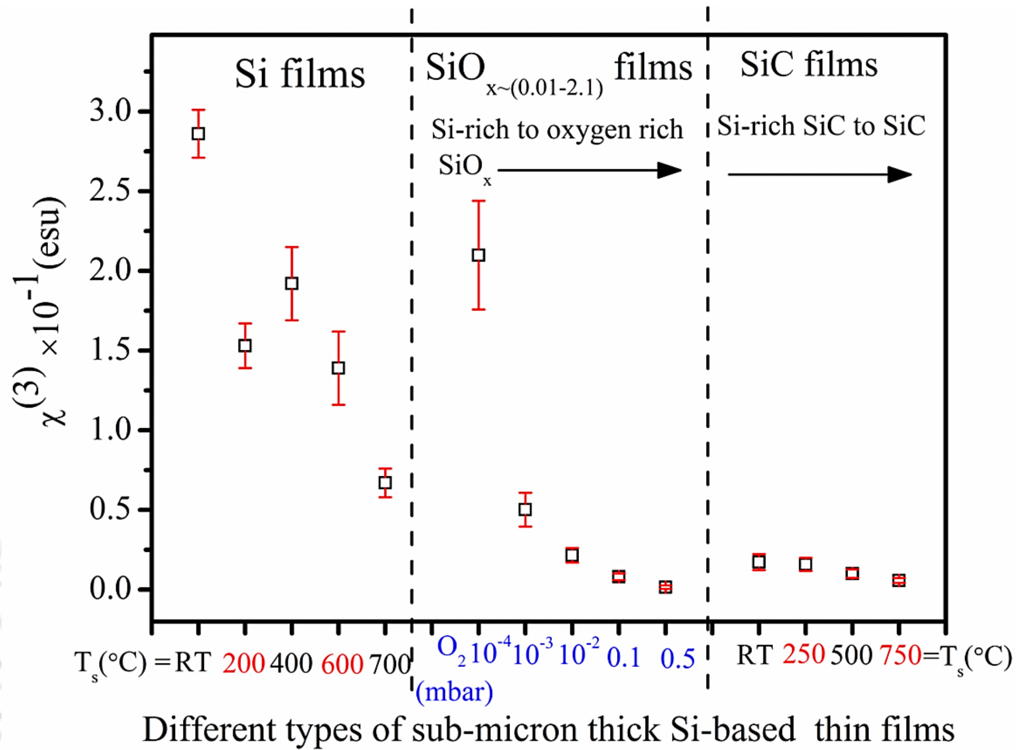

Figure 6.11 *$\chi^{(3)}$ values for the different band gap engineered PLD Si-based thin films deposited under different deposition parameters.*

6.5 Conclusion:

The third order NLO properties of Si, SiO_x and a-SiC thin films deposited via PLD were studied using modified Z-scan technique under cw He-Ne laser irradiation. The origin of optical nonlinearity in all these PLD Si-based thin films; Si, SiO_x and a-SiC, is due to the thermal effect induced by cw laser illumination. The OA Z-scan of all the Si-based thin films in present case indicated strong RSA while CA Z-scan exhibited self-focusing property confirming the positive NLR. The values of β for the nc-Si films was observed to be of the order of 10 cm/W. The n_2 for the Si films was observed to be of the

TH-1680_10612114

order of 10^{-4} cm^2/W. A large third order NLO susceptibility of the order of 10^{-1} *esu* was observed in these PLD nc-Si films, which is 10^9 times higher as compared to that of a bulk Si. The optical limiting was observed in all these nc-Si films where limiting threshold power was observed to be increasing with growth temperature due to decrease in values of β.

The $SiO_{x\ (\sim 0.03-2.14)}$ films fabricated as a function of background O_2 pressure, from 10^{-4} to 0.5 mbar also exhibited third order NLO. The value of β was observed to be decreasing from 21.4 - 2.0 cm/W, with increase in the O_2 pressure, changing x from 0.01 to 2.14. The value of n_2 was found to be decreasing from 44.2×10^{-5} - 1.9×10^{-5} cm^2/W, with similar increase in O_2 pressure. The significantly large NLO susceptibility of the order of 10^{-1}-10^{-3} *esu* was observed in these films. The SiO_x films except the one containing maximum oxygen content exhibited OL. The OL effect in these films were due to RSA and optical limiting threshold was found to increase with increasing oxygen content. Thus these results indicate that a tunable NLO and OL films can be fabricated by controlling the stoichiometry of SiO_x films which in case of PLD technique can be performed simply by controlling the background oxygen pressure.

The values of β and n_2 for PLD a-SiC thin films were found to be decreasing from 0.75 - 0.34 cm/W and 7.68 - 3.14×10^{-5} cm^2/W respectively with increasing T_s from RT to 750 °C, following similar decreasing trend of α. This is due to the change in stoichiometry from Si-rich to nearly stoichiometric a-SiC with increasing T_s from RT to 700° C during deposition. The NLO susceptibility of the order of 10^{-2} *esu* was observed in these films.

TH-1680_10612114

Bibliography

[1] D. Cotter, R.J. Manning, K.J. Blow, A.D. Ellis, A.E. Kelly, D. Nesset, I.D. Phillips, A.J. Poustie, D.C. Rogers, Nonlinear Optics for High-Speed Digital Information Processing, Science, 286 (1999) 1523.

[2] J. Tominaga, T. Nakano, N. Atoda, An Approach for Recording and Readout beyond the Diffraction Limit with an Sb Thin Film, Applied Physics Letters, 73 (1998) 2078.

[3] M. Ito, K. Imakita, M. Fujii, S. Hayashi, Nonlinear Optical Properties of Silicon Nanoclusters/nanocrystals Doped SiO_2 Films: Annealing Temperature Dependence, Journal of Applied Physics, 108 (2010) 063512.

[4] G.V. Prakash, M. Cazzanelli, Z. Gaburro, L. Pavesi, F. Iacona, G. Franzò, F. Priolo, Nonlinear optical properties of silicon nanocrystals grown by plasma-enhanced chemical vapor deposition, Journal of Applied Physics, 91 (2002) 4607-4610.

[5] M.S. Brodyn, V.I. Volkov, V.R. Lyakhovetskii, V.I. Rudenko, V.M. Puzilkov, A.V. Semenov, Nonlinear-optical and Structural Properties of Nanocrystalline Silicon Carbide Films, Journal of Experimental and Theoretical Physics, 114 (2012) 205-211.

[6] L.W. Tutt, T.F. Boggess, A Review of Optical Limiting Mechanisms and Devices using Organics, Fullerenes, Semiconductors and Other Materials, Progress in Quantum Electronics, 17 (1993) 299-338.

[7] D.J. Harter, M.L. Shand, Y.B. Band, Power/Energy Limiter using Reverse Saturable Absorption, Journal of Applied Physics, 56 (1984) 865.

[8] Y.B. Band, D.J. Harter, R. Bavli, Optical pulse compressor composed of saturable and reverse saturable absorbers, Chemical Physics Letters, 126 (1986) 280-284.

[9] S. Vijayalakshmi, F. Shen, H. Grebel, Artificial Dielectrics: Nonlinear Optical Properties of Silicon Nanoclusters at λ=532 nm, Applied Physics Letters, 71 (1997) 3332.

[10] Y.J. Ma, J.I. Oh, D.Q. Zheng, W.A. Su, W.Z. Shen, Tunable Nonlinear Absorption of Hydrogenated Nanocrystalline Silicon, Optics Letters, 36 (2011) 3431-3433.

[11] S.R. Friberg, P.W. Smith, Nonlinear optical glasses for ultrafast optical switches, IEEE Journal of Quantum Electronics, 23 (1987) 2089-2094.

[12] M. Moran, S. Chiao-Yao, R. Carman, Interferometric measurements of the nonlinear refractive-index coefficient relative to CS_2 in laser-system-related materials, IEEE Journal of Quantum Electronics, 11 (1975) 259-263.

[13] A. Owyoung, Ellipse rotation studies in laser host materials, IEEE Journal of Quantum Electronics, 9 (1973) 1064-1069.

[14] W.E. Williams, M.J. Soileau, E.W. Van Stryland, Optical switching and n_2 measurements in CS_2, Optics Communications, 50 (1984) 256-260.

[15] M. Sheik-Bahae, A.A. Said, T.H. Wei, D.J. Hagan, E.W.V. Stryland, Sensitive Measurement of Optical Nonlinearities using a Single Beam, IEEE Journal of Quantum Electronics, 26 (1990) 760-769.

TH-1680_10612114

[16] I. Kumar, A. Khare, Modified Z-scan Set-up using CCD for Measurement of Optical Nonlinearity in PLD Carbon Thin Film, Optics and Laser Technology, 77 (2016) 51-54.

[17] Y. Choi, J.-H. Park, M.R. Kim, W. Jhe, B.K. Rhee, Direct Observation of Self-focusing Near the Diffraction Limit in Polycrystalline Silicon Film, Applied Physics Letters, 78 (2001) 856.

[18] C.A. Carter, J.M. Harris, Comparison of Models Describing the Thermal Lens Effect, Applied Optics, 23 (1984) 476-481.

[19] F.L.S.A. Cuppo, A.M. Figueiredo Neto, S.L. Gómez, P. Palffy-Muhoray, Thermal-lens Model Compared with the Sheik-Bahae Formalism in Interpreting Z-scan Experiments on Lyotropic Liquid Crystals, Journal of the Optical Society of America B, 19 (2002) 1342-1348.

[20] J.L. Ding, Y.C. Wang, H. Zhou, Q. Chen, S.X. Qian, Z.C. Feng, W.J. Lu, Nonlinear Optical Properties and Ultrafast Dynamics of Undoped and Doped Bulk SiC, Chinese Physics Letters, 27 (2010) 124202.

TH-1680_10612114

TH-1680_10612114

Chapter 7

Conclusions

The present research work was aimed towards the fabrication and characterization of nc-Si, SiO_x and SiC semiconductor thin films via PLD technique in order to study the effect of substrate temperature and background gas pressure on their stoichiometry and crystallinity, which in turn control structural as well as optical properties. In addition a-Si:SiO_2 nanostructures were also fabricated by direct laser irradiation of Si wafer as a function of laser fluence. The room temperature (RT) photoluminescence properties of these films and nanostructures along with their possible origins were investigated. The effect of film stoichiometry on the third order NLO properties and optical limiting (OL) properties were studied as well.

Initially, the a-Si:SiO_2 nanostructures were fabricated directly on crystalline Si (c-Si) substrate by irradiating it with nearly focused beam of a second harmonic (532 nm) of a Q switched high power Nd: YAG laser (pulse duration of 8 ns and repetition rate of 10 Hz). The laser ablation was performed in air at RT as a function of laser fluence approximately from 0.35 to 2.67 Jcm^{-2}. This resulted in the formation of crater-like central crystalline region surrounded by the micron sized cauliflower-like clusters of a-Si embedded within SiO_2 matrix. The amorphous nature of the clusters, which were composed of a-Si as well as amorphous SiO_2, was confirmed by Raman spectra, FTIR spectra and SAED patterns. The EDX spectroscopy results showed increase in oxidation of Si with increasing laser fluence which was also confirmed by infrared absorption of Si-O-Si stretching vibration mode. TEM images showed that with increasing laser fluence, the size of the nanoparticles decreases while their SAED pattern indicated the amorphous structure. These nanostructures exhibited an intense RT broad band PL ranging from 1.6 to 2.2 eV with twin peaks around red region. The origin of luminescence in these

TH-1680_10612114

structures was attributed to nanostructures of a-Si and predominantly to non-bridging oxygen hole center (NBOHC) defects in SiO_2 matrix. The PL peak intensity was found to be a function of oxygen content.

The nc-Si thin films were fabricated onto Corning glass substrate by PLD at a laser fluence of ~ 2.5 Jcm^{-2} under vacuum (~10^{-6} mbar) as a function of substrate temperatures (T_s), from RT to 700 ˚C. The effect of T_s on the structural as well as linear and nonlinear optical properties was studied. These films were polycrystalline in nature as was confirmed by the characteristic XRD peaks for the Si (111), Si (220) and Si (311) planes. The Raman maps indicated the presence of nc-Si clusters embedded in uniform background of amorphous Si for the films deposited at RT and 200 ˚C to 600 ˚C of substrate temperature. The film deposited at 700 ˚C exhibited nc-Si feature by and large. The thickness, refractive index and absorption coefficient of films were measured from interference pattern of the UV-Vis-NIR transmission spectra using Swanepoel's envelop method. The thickness of the films was found to be in the range of 480-348 nm. The static refractive index were found to be in the range of 3.3- 3.9. The optical band gap of the Si thin films was observed to be in the range of 1.3-1.55 eV for the T_s from RT to 700 ˚C, respectively. The thickness, optical constants and band gap of the films were also estimated from Spectroscopic Ellipsometry spectra using Tauc-Lorentz-Lorentz dispersion model along with BEMA and were observed to be consistent with the values obtained from UV-Vis-NIR spectroscopic studies.

The direct laser ablation of c-Si target resulted in photoluminescent a-Si:SiO_2 structures. But from the device point of view it is also required to be grown in the form of thin film geometry. Therefore, the films of nc-Si:SiO_2 (or simply SiO_x) were fabricated via PLD on glass substrate. All the films were deposited at a laser fluence of ~ 2.5 Jcm^{-2} and substrate temperature of 400 °C for 30 min duration. The stoichiometry of the SiO_x

TH-1680_10612114

films was controlled by background pressure of oxygen during deposition in the range of 10^{-4} to 0.5 mbar. XRD spectra confirmed the polycrystalline nature of these films. The EDX results indicated the increase in oxygen content, x= 0.03 to 2.1, with increasing O_2 pressure from 10^{-4} to 0.5 mbar, respectively. Scanning electron microscopic images of SiO_x films exhibited the micron-sized clusters embedded in otherwise uniform background. The Raman maps confirmed that these micron-sized clusters contained nc-Si embedded in uniform matrix composed of oxidized amorphous Si. The average crystallite size of nc-Si, estimated from Raman shift of nc-Si, was observed to be reducing from around 18.3 nm to 3.2 nm (using bond-polarizability model) with increasing O_2 pressure from 10^{-4} mbar to 0.5 mbar, respectively. The static refractive index was found to reduce from 3.57 to 1.57 while band gap energy blue shifted from 1.55 to 2.80 eV approximately with increasing O_2 pressure in these films. This is due to shift in stoichiometry from Si-rich to oxygen rich SiO_x films. Urbach energy estimated from absorption spectra and I_{TA}/I_{TO} obtained from Raman spectra of amorphous Si matrix was found to increase with increasing oxygen content in SiO_x films indicating increase in the structural disorders in a material. Laser excited PL spectra were observed for films fabricated at oxygen pressure of 0.01, 0.1 and 0.5 mbar only, exhibiting peak around 1.43, 1.53 and 2.51 eV, respectively. These PL spectra have multi-component peaks originated due to quantum confined nc-Si as well as oxygen related defects; NBOH and V_o centers. The QC-related PL peak was observed to be blue shifted for smaller sized crystallites. These studies also emphasizes on the efficacy of Raman mapping to probe structural heterogeneity of Si-based thin films which helped in explaining the origin of multicomponent structure in the PL spectra.

Nanostructured amorphous SiC thin films of sub-micron thickness were also fabricated onto fused silica and undoped c-Si substrates by PLD technique at T_s of RT,

TH-1680_10612114

250 °C, 500 °C and 750 °C with a laser fluence of 6 J/cm^2 under vacuum (~ 10^{-6} mbar). The SiC thin films showed amorphous feature as confirmed by XRD and Raman studies. The thin films exhibited slight improvement in crystallinity at higher T_s as reflected by the appearance of small XRD peak corresponding to β-SiC (111) plane. The stoichiometry of a-SiC films was observed to be changing from Si-rich to more stoichiometric a-SiC with increasing T_s from RT to 750 °C as confirmed by Raman spectra as well as EDX spectra. The thickness of the films was found to be in the range of ~255-330 nm. The refractive index in UV-Vis-NIR region measured from the transmission spectra is found to be decreasing from 3 to 2.64 with increasing T_s. The band gap was found to be blue shifted from 1.59 to 2.33eV with increasing growth temperature which is due to the gradual increase in carbon content at elevated temperatures resulting in change in stoichiometry from Si- rich to near stoichiometric a-SiC films. The FTIR results showed that the films basically composed of Si-C bonds and that fabricated at elevated temperatures were more ordered. TEM images showed increase in particle size while SAED pattern confirmed improvement in crystallinity of films with increase in T_s. The FESEM images displayed the uniform growth of nanostructure with particles size increasing with increase in T_s.

The third order NLO characteristics of all the PLD thin films of Si, SiO_x and a-SiC was performed by modified Z-scan set up using cw He-Ne laser at 632.8 nm wavelength. The nonlinear absorption (NLA) coefficient, β and nonlinear refraction (NLR) coefficient, n_2, were determined from open aperture (OA) and closed aperture (CA) Z-scan, respectively. Finally from these coefficients the NLO susceptibilities of the films were calculated. The OA Z-scan spectra of all the three kinds of films; nc-Si, SiO_x and a-SiC, showed feature of strong reverse saturation absorbtion (RSA) and their CA Z-scan spectra indicated self-focussing property. The value of β of nc-Si films was observed to be of the order of 10 cm/W. The n_2 values for the nc-Si films was estimated to be of the

TH-1680_10612114

order of 10^{-4} cm^2/W. These high NLO coefficients had resulted significantly large values of $\chi^{(3)}$ of the order of 10^{-1} *esu* in the nc-Si films, which is 10^9 times higher as compared to that of a bulk Si. The optical limiting (OL) property was also observed in the nc-Si thin films. The values of β for SiO_x thin films decreased from 23.5 cm/W to 1.64 cm/W while n_2 decreased from 28.3×10^{-5} cm^2/W to 1.70×10^{-5} cm^2/W with the increase in O_2 pressure from 10^{-4} to 0.5 mbar, respectively. The values of $\chi^{(3)}$ for SiO_x was observed to be of the order of 10^{-1} to 10^{-3} esu with increasing oxygen content. The SiO_x films also exhibited OL properties where the OL threshold (varies inversely with β) increases with increasing oxygen content. The NLO behaviour of a-SiC films was similar to that of SiO_x films with $\chi^{(3)}$ observed to be of the order of 10^{-3} esu, which is two order of magnitude smaller than that of Si films. The origin of the optical nonlinearity in all the samples reported in the thesis was overwhelming due to thermo-optic effects, induced by cw laser irradiation. Hence the behavior of β and n_2 of these films as a function of deposition parameters were observed to vary in the manner similar to that of linear absorption coefficient as a function of respective deposition parameters.

Future scopes:

The films exhibiting photoluminescence can be subjected to time-resolved PL and temperature dependent PL studies for detailed understanding of the possible emission mechanism involved.

The a-SiC films can be used to fabricated nanocrystalline SiC film by annealing them at high temperatures under vacuum and their structural as well as PL property can be extensively studied. In PLD stoichiometry the films can be controlled by the background gas pressure. Therefore, SiC films can be fabricated in presence of some inert

TH-1680_10612114

gas environment and thus stoichiometric dependent linear, nonlinear and PL properties can be studied to obtain the optimized parameter of the film for device application.

The third order optical nonlinearity of nc-Si, SiO_x and SiC thin films using cw laser is presented in this thesis. These films can also be subjected to nanosecond and femtosecond laser for studying their NLO behavior. Apart from this, the nc-Si and Si-rich SiO_x films which exhibited strong RSA can be tried for optical switching and modulation applications.

TH-1680_10612114

List of Publications

Journal Papers: *Related to thesis work*

i. *'Non-linear optical and optical limiting response of PLD nc-Si thin film',* **Partha P. Dey** and Alika Khare, ***J. Mat. Chem. C**,* 5 (2017) 12211 – 12220.

ii. '*Fabrication of Photoluminescent nc-Si:SiO_2 Thin Films prepared by PLD*', **Partha P. Dey** and Alika Khare, - ***Phys. Chem. Chem. Phys***.,19 (2017) 21436-214345.

iii. '*Stoichiometry-dependent linear and nonlinear optical properties of PLD SiO_x thin films*', **Partha P. Dey** and Alika Khare, ***J. Alloys and Comp***. 706 (2017) 370-376.

iv. '*Stoichiometric dependent optical limiting in PLD SiO_x thin films*', **Partha P. Dey** and Alika Khare, ***Adv. Mat. Lett***. 8 (2017) 331-335.

v. '*Effect of substrate temperature on structural and linear and nonlinear optical properties of nanostructured PLD a-SiC thin films*', **Partha P. Dey** and Alika Khare, ***Mat. Res. Bull.*** 84 (2016) 105-117.

vi. *'Nd-YAG Ns-Pulsed Laser Induced Structural and Compositional Modification of Silicon Surface: Formation of Photoluminescent a-Si nanostructures*', **Partha P. Dey** and Alika Khare, ***Adv. Sci. Lett***. 20 (2014) 1364-1368.

vii. '*Structural and optical properties of nanostructured a-SiC thin films by pulsed laser deposition at different substrate temperatures*', **Partha P. Dey** and Alika Khare, ***J. Nanosci. Lett***. 2014, 4: 29

viii. '*Fabrication of luminescent a-Si:SiO_2 structures by direct irradiation of high power laser on Silicon surface'*, **Partha P. Dey** and Alika Khare, ***Appl. Surf. Sci***. 307 (2014) 77–85.

TH-1680_10612114

ix. *'Efficacy of Raman mapping over ellipsometric spectroscopy and XRD for structural characterization of PLD ns-Si thin film'*, **Partha P. Dey**, Rahul Kesarwani and Alika Khare – **Under review**.

Journal Papers: *Not related to thesis work*

x. *'Pulsed laser deposited $Zn_{1-x}Ti_xO$ (0=x=0.050) thin films for tunable refractive index and nonlinear optical applications,* Gyan Prakash Bharti, **Partha P. Dey** and Alika Khare – **Under review**.

xi. *'Anomalous scaling behavior and surface roughening of Cu film under Pulsed Laser deposition',* Rahul Kesarwani, **Partha P. Dey** and Alika Khare – To be communicated.

xii. *'Effect of He pressure on structural, optical and photoluminescence properties of nanostructured PLD a-SiC thin films.* **Partha P. Dey** and Alika Khare*',* - Manuscript under preparation.

Conference Presentations

i. 'Structural and optical properties of Silicon Carbide thin films fabricated via PLD', **Partha P. Dey** and Alika Khare, National Laser Symposium (**NLS-23**), Sri Venkateshwara University, Tirupati, A. P. (India), 3-6 December, 2014.

ii. 'Nd-YAG ns-pulsed laser induced Structural and compositional modification of Silicon surface : Formation of Photoluminescent a-Si:SiO_2 nanostructures.', **Partha P. Dey** and Alika Khare, National Conference on Nanotechnology and Renewable Energy (**NCNRE-14**), New Delhi, India, April 28-29, 2014.

iii. 'Third order Nonlinear optical properties of PLD deposited nanostructured SiC Thin Films', **Partha P. Dey**, G. P. Bharti and Alika Khare, International conference of Optics and Optoelectronics (**ICOL-2014**), IRDE Dehradun, India, 5-8 March 2014.

iv. 'Fabrication of SiO_x thin films by pulsed laser deposition at different O_2 ambient pressure', **Partha P. Dey** and Alika Khare, conference paper of DAE-BRNS 7th

TH-1680_10612114

National Symposium on Pulsed Laser Deposition of Thin Films and Nanostructured Materials (**PLD 2013**), organized by Dept. of Physics, Indian Institute of Technology Kharagpur, Kharagpur, India, 14-16 November, 2013.

v. 'Structural and optical properties of nanostructured a-Sic thin films by pulsed laser deposition at different substrate temperatures', **Partha P. Dey** and Alika Khare, conference paper of International conference on Nanotechnology (**ICNT 2013**), organized by Dept. of Chemical Engineering, Haldia Institute of Technology, Haldia, West Bengal, India, 25-26 October 2013.

vi. 'Micro structuring of Silicon surface by high power pulsed Laser irradiation', **Partha P. Dey** and Alika Khare, conference paper of 21th International Symposium on Processing & Fabrication of Advanced Materials (**PFAM XXI 2010**) organized by Dept. of Mechanical Engineering, Indian Institute of Technology Guwahati, Guwahati, India, December 10-13, 2012.

School/Workshops attended

i. SERC school on 'Laser Produced Plasmas: Physics and Applications' held during 7-21 July 2012 by RRCAT, Indore, India.

ii. IEEE Workshop on Compressive Sensing and Technical Writing held during 6-7 April 2013, organized by IEEE Student Branch, IIT Guwahati, Guwahati, India.

iii. National Workshop on Advanced Probing Techniques in TEM (APTTEM-2016) during 15-16 February, 2016, organized by IIT Guwahati, Guwahati, India.

iv. SPIE Workshop on Vacuum Technology and its Application in Optical Science held on 19th August, 2017, organized by SPIE IIT Guwahati student chapter and Pfeiffer Vacuum Pvt. Ltd. In association with Dept. of Physics, IIT Guwahati, Guwahati, India.

TH-1680_10612114

TH-1680_10612114